UNIVERSITY OF ROME "ROMA TRE"

Department of Mathematics and Physics

CAIXA-A:
a Catalogue of AGN In the XMM-*Newton* Archive - Absorbed

Candidate:
Ilaria De Angelis

Supervisor:
Dr. Stefano Bianchi

January 2014

Contents

Introduction

Active galaxies are galaxies which have a small core of emission embedded in an otherwise typical galaxy. This core may be highly variable and very bright compared to the rest of the galaxy. For ”normal” galaxies, we can think of the total energy they emit as the sum of the emission from each of the stars found in the galaxy. For the ”active” galaxies, usually called Active Galactic Nuclei (AGN), this is not true. There is a great deal more emitted energy than there should be and this excess energy is found in the infrared, radio, UV, and X-ray regions of the electromagnetic spectrum. Models of active galaxies concentrate are based on the presence of a supermassive black hole which lies at the center of the galaxy. The dense central galaxy provides material which accretes onto the black hole (ranging from $10^6 - 10^9$ solar masses) releasing a large amount of gravitational energy. Accretion occurs via an accretion disc that efficiently converts gravitational energy into radiation.

There are several types of active galaxies: Seyferts, quasars, and blazars. A further classification is based on their optical/UV spectra: broad and narrow emission lines are both present in AGN 1s while only the latters are visible in AGN 2s.

The standard Unification Model for AGN assumes the same internal structure for both Seyfert 1 and Seyfert 2 galaxies (Antonucci 1993), with all observational differences ascribed to an axisymmetric distribution of gas, located between the Broad Line Region (BLR) and the Narrow Line Region (NLR), in order to obscure the former, but not the latter. A natural geometrical and physical scenario is that of a homogeneous torus on a parsec scale (Krolik & Begelman 1988). If the so-called torus intercepts our line of sight the primary emission and the BLR are obscured with a resulting lack of broad lines in the optical/UV spectrum and a classification as Seyfert 2. On the contrary, if the nucleus is unobscured, the source is classified as a Seyfert 1 and every component of the spectrum is visible. This classification holds true also in X-rays, where Seyfert 2s look usually absorbed, as expected. Besides, in X-ray spectra a number of other components arise as reprocessing of the primary emission from the circumnuclear material. The most striking effect is the absorption from intervening neutral matter. The column density of the absorber discriminates between two kinds of sources: *Compton-*

thick if it exceeds the value $N_H > \sigma_T^{-1} = 10^{24}cm^{-2}$ (i.e. when the optical depth for Compton scattering equals unity), completely blocking the nuclear continuum up to 10 keV or more; *Compton-thin* if it is lower, allowing only photons more energetic than a certain threshold to pierce through the material.

Absorbed AGN represent ideal laboratories to study the emission components which originate in circumnuclear matter outside the absorbing regions, because in this case they are not outshined by the nuclear emission. The high energy spectrum is dominated by Compton reflection and a strong iron fluorescence line which are likely to be produced in a compact (parsec-scale), Compton-thick and low ionized material, traditionally identified with the absorber along the line of sight (the torus envisaged in the Seyfert unification scenario). On the other hand, the soft X-ray spectrum had to await the high resolution spectrometers aboard XMM-Newton and Chandra to reveal its real nature. The spectrum is dominated by emission lines, mainly from He- and H-like K transitions of light metals and L transitions of Fe (Kinkhabwala et al. 2002; Sambruna et al. 2001b; Sako et al. 2000). The continuum observed in lower resolution CCD spectra was mainly due to the blending of these features. Different diagnostic tests seem to suggest that in these sources the observed lines are produced in a gas photoionized by the AGN, rather than in a hot gas in collisional equilibrium. The unprecedented high spatial resolution of Chandra added another key ingredient to the puzzle revealing that the soft X-ray emission of bright obscured Seyfert galaxies was actually extended on hundreds of pc, thus being clearly produced in a gas well beyond the torus (Young, Wilson & Shopbell 2001; Sambruna et al. 2001a; Sako et al. 2000).

In the framework of this scenario, we selected and analyzed a sample of obscured AGN observed by the XMM-Newton in order to study the soft X-ray band of obscured AGN. With the aim to analyze large numbers of AGN with good-quality X-ray spectra and to perform statistical studies we have built the catalogue CAIXA-A, a Catalogue of AGN In the XMM-*Newton* Archive - Absorbed. All the EPIC pn spectra of the sources in CAIXA-A were extracted homogeneously, and a baseline model was applied in order to derive their basic X-ray properties and select only those sources absorbed by column density larger than 10^{22} cm^{-2}. At the end of the selection procedure, CAIXA-A consists of all the radio-quiet, X-ray obscured ($N_H > 2{\times}10^{22} cm^{-2}$) AGN observed by XMM-Newton in targeted observations, whose data were public as of November 22, 2011. With its 109 sources, this is the largest catalog of high signal-to-noise X-ray spectra of obscured AGN. We then focused on the analysis of the high resolution soft X-ray RGS spectra of CAIXA-A sources, adopting different, complementary, methods of analysis with both phenomenological and self-consistent approaches. The observational evidence discussed in this thesis leads to think that the CAIXA-A sources seems to be dominated by the photoionization, although collisionally ionized plasma may play a significant role in some sources.

The structure of this thesis is as follows. Chapter 1 introduces the reader to Active Galactic Nuclei and their classification, to the Spectral Energy Distribution (SED) of AGN across the whole electromagnetic spectrum. In Chapter 2 the main mechanisms involved in the production and absorption of X-rays, in order to understand the physics behind AGN emission in this band, will be briefly explained. Chapter 3 is devoted to the description of the sample and the analysis of the spectra in the soft X-ray band. Finally, a discussion of the results of this thesis can be found in the Conclusions.

Chapter 1

Active Galactic Nuclei

The term Active Galactic Nuclei (AGN) refers to a few percent of galaxies whose emission from the inner region cannot be ascribed to stars. The 'zoo' of galaxies that fits this definition is wide and varied, and the classification, mainly based on luminosity and spectroscopical features, is complex and not always straightforward. AGN are powered by accretion of matter onto a Super Massive Black Hole (SMBH), lying at the center of a galaxy, which accretes matter from the galaxy itself (gas and stars). BHs are very simple objects, defined by only three independent parameters: the mass, the angular momentum (the spin) and the electric charge.[1] The mass of the BH (in the range $10^6 - 10^{10} M_\odot$ for AGN) and especially the circumnuclear matter can produce different phenomena and alter properties such as the luminosity and the spectral energy distribution.

The main and common trait of AGN is their huge luminosity, typically in the range $10^{42} - 10^{48}$ erg s^{-1}, that spans over $\sim$ 20 decades of the electromagnetic spectrum, making them among the most luminous objects in the sky from radio to gamma rays. Any source can reach a maximum value of luminosity called 'Eddington luminosity' when the continuum radiation force outwards balances the gravitational force inwards in hydrostatic equilibrium. If the luminosity exceeds this limit, then the radiation pressure drives an outflow. Whatever the emission mechanism is involved, the limit Eddington Luminosity relation (for fully ionized hydrogen gas: see Sect. 1.1.2.)

$$L_{Edd} = \frac{4\pi G M m_p c}{\sigma_T} \cong 1.3 \times 10^{38} \left(\frac{M}{M_\odot}\right) \frac{erg}{s} \tag{1.1}$$

tells us that a mass of the order $M \approx 10^8 M_\odot$ is required to achieve the typical AGN luminosity.

[1] It is usually assumed that the electric charge is negligible for astrophysically relevant BHs.

1.0.1 AGN Taxonomy

The taxonomy of AGN tends to be rather confusing as we do not yet fully understand the physics underlying this phenomenon. Undoubtedly some of the differences we see between various types of AGN are due more to the way we observe them than to intrinsic differences; this theme represents the basis of the unification models (see Sect. 1.2.).

In Figure 1.1, a summarizing scheme shows some of the various ‘species’ of the rich AGN family.

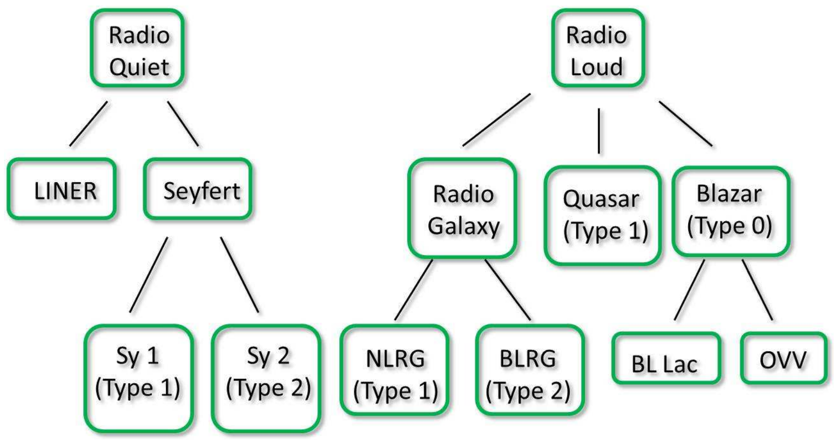

Figure 1.1: *AGN taxonomy scheme*

A detailed description of all the different types of AGN does not fall in the purposes of this thesis. We just want to broadly give an idea of the classification and introduce the Unification Model for AGN. A first classification comes from two main parameters of the spectrum of an AGN:

1. **Radio Emission:** AGN show a large distribution of radio (L_R) and optical (L_O) luminosities with a bimodal distribution of the ratio between the two luminosities, with $\frac{L_R}{L_O} \sim 10$ as the dividing value. Objects below this value are called Radio-Quiet AGN, sources with a $\frac{L_R}{L_O} > 10$ are indicated as Radio-Loud AGN. This last class of galaxies is 10-15% of the total. The intense radio emission in Radio-Loud AGN is believed to be related with the presence of relativistic, collimated flows of matter (jets). Since we will investigate only radio-quiet objects in this thesis, in the following we will focus on the characteristics of this subclass.

2. **Emission lines:** in the optical/UV spectrum of AGN emission lines much more intense and broader than in usual galaxies are usually present. They can be divided into:

- Broad Emission Lines: lines corresponding to permitted transitions with Full Width at Half Maximum (FWHM) of thousands of km s^{-1};
- Narrow Emission Lines: lines from permitted and forbidden transitions with FWHM of hundreds of km s^{-1}

Broad lines observed in the optical/UV spectra of Seyfert Galaxies have typical widths of $\simeq$ 5000 km s^{-1}, but can be as large as 10 000 km s^{-1} or more. Such widths are interpreted as being due to the Keplerian velocities of a large number of clouds (the Broad Line Region: BLR) rotating around the BH at a distance of 0.01-0.1 pc (see figure 1.4). The density of this gas is believed to be very high, of the order of $10^9 - 10^{11}$ cm^{-3}, as required by the observed lack of forbidden transitions. Still under debate is the origin of these clouds and several models have been proposed (see Sect. 1.2). The narrow lines have much smaller widths, typically a few times 100 km s^{-1}. This is easily explained if they are produced by gas (the Narrow Line Region: NLR) farther away from the BH, extending on $\sim$ 100 pc scale (see figure 1.4), as often directly observed in the images. The gas has a density of $10^3 - 10^6$ cm^{-3}, lower than that required for the BLR and low enough to explain the presence of forbidden lines. It is likely composed by the inner part of the Galactic disc, photoionized by the nuclear continuum (Bianchi & Guainazzi 2007).
A further classification depends on the presence or absence of Broad Emission Lines. Two different class of sources can be introduced:

1. Type 1 AGN: Broad Emission Lines and Narrow Emission Lines are both present in the optical spectrum;

2. Type 2 AGN: only narrow emission lines are present.

The column density of the absorbing matter around the central nucleus (N_H) can be used as a further classification criterium:

1. Obscured AGN: evidence of intrinsic cold absorption in the X-ray band in excess to that due to the Milky Way;

2. Unobscured AGN: there is no excess cold absorption in the X-ray band.

A good correlation between this classification and the previous one is observed: type 2 AGN are usually X-ray absorbed, while type 1 AGN are not. Among the unobscured AGN a further discrimination can be introduced: even if classified as type 2 AGN, these objects have a nuclear luminosity which may not completely absorbed in X-rays by the circumnuclear material. The following classification is based on the column density of the absorbing circumnuclear material (N_H):

- **Compton Thin sources:** present a typical $N_H < 10^{24}$ cm^{-2}. They have a nuclear flux much higher than a Compton Thick object's one because the circumnuclear material is transparent to the radiation in the 2-10 keV band.
- **Compton Thick sources:** present a typical $N_H > 10^{24}$ cm^{-2}. Most of the radiation coming from the inner part of the galaxy is absorbed by the circumnuclear material.

1.1 Fueling the central engine

One of the main characteristics of AGN is their extreme luminosities, typically ranging between 10^{42} and 10^{48} erg s^{-1} and produced in a very small region. Since the first quasar's (3C 273) redshift was measured in 1963 by Marteen Schmidt (Schmidt 1963) great efforts have been spent in understanding what mechanisms could be involved in producing such a great amount of radiation in such compact regions, without exceeding the Eddington luminosity to keep the process effective. The extreme compactness (M/R) of the nuclei of active galaxies leads almost unambiguously to postulate the presence of supermassive black holes (SMBHs), in the range $10^6 - 10^9 M_\odot$.
In the following we will discuss the process of accretion, thought to be responsible for fueling the central engine of AGN and compact systems in general, through the conversion of gravitational energy into radiation.

1.1.1 Accretion efficiency

The mechanism of accretion on a supermassive black hole should be very efficient in order to produce such high luminosities in active galaxies. If the energy is converted so that $E = \eta mc^2$, the efficiency η needs to be very high. If we consider the standard nuclear processes that fuel stars we can only reach a maximum value of $\eta = 0.007$, in the case of Hydrogen burning. In the following we will show that the process of accretion can reach $\eta = 0.42$.
Let us consider an object with mass m which is falling onto a much more massive body with mass M. If the object of mass m is in a free-falling regime from infinity it gains kinetic energy at the expense of gravitational energy. If we consider a proton with mass m_p :

$$\frac{1}{2}m_p v_{ff}^2 = \frac{GMm_p}{r} \tag{1.2}$$

When matter reaches the surface of the compact object kinetic energy is transformed into heat, with a consequent irradiation. If the accretion rate is $\dot{m}$, the kinetic energy dissipation is $\frac{1}{2}\dot{m}v_{ff}^2$ and hence the luminosity, $L = \frac{dE}{dt}$ is:

$$L = \frac{1}{2}\dot{m}v_{ff}^2 = \frac{GM\dot{m}}{r}. \tag{1.3}$$

It is convenient to introduce the Schwarzschild's radius for an object with mass M:

$$r_s = \frac{2GM}{c^2}, \tag{1.4}$$

which corresponds roughly to 3×10^{13} cm or 0.01 light days for a 10^8 $M_\odot$ black hole. Inserting r_s in the expression 1.3 we get:

$$L = \frac{1}{2}\dot{m}c^2(\frac{r_s}{r}) \tag{1.5}$$

Defining $\frac{r_s}{2r} = \eta$, then:

$$L = \eta\dot{m}c^2. \tag{1.6}$$

It would then seem natural to assume that the accretion efficiency reaches its higher values in the vicinity of a BH. However, this is not necessarily true, because BHs do not have a surface and the accretion mechanism must be induced by the presence of an accretion disc of gas rotating around the BH.

The value of the efficiency factor η is of the order of 0.1 for a neutron star and it is very easy to show that it is proportional to the compactness of the hidden object. Considering a spinning BH, with a non null angular momentum, the accretion takes place not beyond the so called 'radius of marginal stability' r_{ms}. Since r_{ms} in a Kerr metric is strongly dependent from the BH spin we have $\eta \simeq 0.06$ for a non-rotating BH and $\eta \simeq 0.42$ for a maximally rotating BH. We refer the reader to Shapiro, Teukolsky & Lightman (1983) for a very elegant mathematical approach.

1.1.2 Eddington Luminosity

In order to have a stable system, the outward force due to the radiation pressure cannot exceed the inward gravitational force. The outflowing flux of energy at a distance r is $F = L/4\pi r^2$, where L is the luminosity (erg/s) of the source. Since the momentum of a photon with energy $E = h\nu$ is $p = E/c$, the total outflowing momentum will be:

$$P_{rad} = \frac{F}{c} = \frac{L}{4\pi r^2 c}.$$

The outward radiation force on a single photon can be obtained multiplying P_{rad} times the interaction cross section of the photon:

$$F_{rad} = \sigma_e \frac{L}{4\pi r^2 c} \tag{1.7}$$

where σ_e is the Thomson cross section. The gravitational force on a proton-electron couple by an object with mass M is:

$$F_{grav} = \frac{-GM(m_p + m_e)}{r^2} \approx \frac{-GMm_p}{r^2}. \tag{1.8}$$

Since the gravitational force acting on the gas has to balance or exceed the outflowing radiation force to keep the system stable, from equation 1.7 and 1.8 we have:

$$|F_{rad}| \leq |F_{grav}|$$
$$\sigma_e \frac{L}{4\pi r^2 c} \leq \frac{GMm_p}{r^2}$$
$$L_{\mathrm{Edd}} \leq \frac{4\pi Gcm_p}{\sigma_e} M \approx 1.26 \times 10^{38} (M/M_\odot)\ \mathrm{erg/s} \tag{1.9}$$

The equation 1.9 is known as *Eddington luminosity* and it can be used to determine the minimum mass (M_{Edd}) to produce a luminosity L_{Edd}. The Eddington luminosity can also be interpreted as the maximum luminosity of a source with mass M fueled by a spherical accretion.

Whatever the emission mechanism is involved the limit Eddington Luminosity relation (for fully ionized hydrogen gas)

$$L_{Edd} = \frac{4\pi GMm_p c}{\sigma_T} \cong 1.3 \times 10^{38} \left(\frac{M}{M_\odot}\right) \frac{erg}{s} \tag{1.10}$$

tell us that a mass of the order $M \approx 10^8 M_\odot$ is required to achieve the typical AGN brightness.

Another important characteristic shared among AGN is their variability timescale, of the order of days, which implicates a sub-parsec scale size of the emitting region

$$R_{AGN} \approx c \times t_{day} < 1\ pc \ll R_{Galaxy} \approx 10^4\ pc$$

as confirmed by many observations showing an unresolved emission core in all electromagnetic bands. The extreme compactness $\left(\frac{M}{R}\right)$ of AGN leads naturally to consider supermassive black holes (SMBHs) liable for the huge luminosity. After all is well-known that 'normal' galaxies, like our own, host SMBHs at their core with masses of $10^6 M_\odot - 10^8 M_\odot$, directly estimated by stellar kinematics (see Schödel et al. 2002, 2006, for details) for details. The 'SMBH paradigm' is nearly unanimously accepted among the scientific community and represents the starting point to understand the AGN physics.

If a SMBH converts mass to energy at a rate of $\dot{M}$, it must do it with high efficiency η to produce the immense luminosity observed

$$L = \eta \dot{M} c^2 \tag{1.11}$$

Low efficiency stellar nuclear reactions like pp-chain, $\eta = 0.007$, or triple-alpha process, $\eta = 0.00062$ are ruled out. The only plausible alternative is accretion, a process where matter around the black hole slowly spirals inward converting gravitational potential energy in kinetic energy. As we will see in the next section this kinetic energy, converted in internal energy, can be dissipated and produce a lot of radiation, with efficiency in the range $\eta \approx 0.06 - 0.4$.

With a prudential value of $\eta = 0.1$, from (1.2), it is possible to reach Eddington luminosity with an accretion rate of

$$\dot{M}_E \equiv \frac{L_E}{\eta c^2} \cong 10^{-8} M_8 \frac{M_\odot}{yr} \tag{1.12}$$

a quite reasonable value if compared to the typical black hole masses involved, $M_{BH} = 10^8 M_\odot = M_8$.

1.1.3 Accretion physics

Accretion can take place in different ways and the final result depends on many factors like the geometry of the system, the presence of a magnetic field, the optical depth of the accreting material, and so on. The simplest model of accretion was developed between 50s and 60s by Bondi and is based on spherical accretion approximation. Although instructive, this model does not find practical application because accreting material always have some angular momentum that breaks spherical symmetry and especially it does not work with objects without a solid surface, like black holes. The right symmetry we need to consider is the cylindrical one, with matter orbiting around the central compact object and forming an accretion disk.

From the point of view of energetics the question is very simple. By the law of conservation of energy, a portion of gas with mass m falling on a compact object with mass M and radius R, satisfies

$$\frac{1}{2} m v_{ff}^2 = \frac{GMm}{R} \tag{1.13}$$

Assuming that all of the energy is converted into radiation

$$E_{tot} = \frac{1}{2} m v_{ff}^2 = \frac{GMm}{R} = E_{rad} \tag{1.14}$$

Differentiating the previous equation we get the luminosity

$$L = \frac{dE_{rad}}{dt} = \frac{dU}{dt} = \frac{GM}{R}\frac{dm}{dt} = \frac{GM\dot{m}}{R} \tag{1.15}$$

Therefore luminosity is proportional to the accretion rate, $\dot{m}$, and to the compactness, $\left(\frac{M}{R}\right)$, and that is the reason why accretion is so efficient for collapsed objects like black holes. Indeed, recalling equation 1.12 and the definition of 'Schwarzschild radius', efficiency can be written as

$$\begin{aligned} R_S &\equiv 2\frac{GM}{c^2} \Rightarrow L = \frac{1}{2}\left(\frac{R_S}{R}\right)\dot{m}c^2 = \eta\dot{m}c^2 \Rightarrow \\ \Rightarrow \eta &= \frac{1}{2}\left(\frac{R_S}{R}\right) \end{aligned} \tag{1.16}$$

Obviously not all of the energy is transformed into radiation and 1.16 represents an upper limit to the efficiency. In equation 1.16, for black holes, we can replace R with the last stable orbit radius R_{lso} which is $R_{lso} = 3R_S$ for non-rotating BHs and $R_{lso} \simeq R_S$ for maximally rotating ones, obtaining

$$\begin{aligned} \eta(a=0) &= \frac{1}{6} \backsimeq 0.16 \\ \eta(a \sim M) &\simeq \frac{1}{2} = 0.5 \end{aligned}$$

where $a \in [0, M)$ is the adimensional spin of the black hole. Actually we cannot neglect relativistic effects and we should solve the entire calculus in Schwarzchild metric for a non-rotating BH and in Kerr metric for a rotating one, obtaining

$$\begin{aligned} \eta(a=0) &\backsimeq 0.057 \\ \eta(a \sim M) &\backsimeq 0.42 \end{aligned} \tag{1.17}$$

A maximally rotating black hole forces the surrounding portion of spacetime to co-rotate with it, allowing matter to reach a radius three times smaller than in the case of a Schwarzchild black hole, and bringing to an efficiency of an order of magnitude larger.

The main problem with accretion is to find a clear way to let the gas loose angular momentum (considering that the system is isolated) and to convert gravitational energy into radiation. In a classical approach, both problems are resolved invoking viscosity forces between disk annuli, originated by the differential disk rotation. The nature of this mechanism is still under debate, but useful results can be obtained confining all our ignorance about kinematic viscosity arising from turbulent motions in a dimensionless parameter α (the so called 'α-prescription') as proposed by Shakura & Sunyaev (1973). Leaving the details to the beautiful review by Pringle (1981) we will briefly describe the main concepts behind Shakura and Sunyaev approach showing the most important equations and the results.

The first problem to solve, as we mentioned before, is the angular momentum loss: the idea is that viscosity forces act to decrease velocity difference between annuli. If we consider only two annuli, the outermost slow his neighbour down letting it lose rotational kinetic energy and letting it fall in the potential well produced by the black hole. At the same time the angular momentum is transferred to the outer part of the disk. Since the last stable orbit is circular, and assuming that gas can radiate efficiently[2], the falling material will form a thin accretion disk.

Let us consider an annulus at radius R with surface mass density Σ, orbiting with Keplerian angular velocity[3] around the BH. Making use of mass conservation (continuity equation) and angular momentum conservation it is possible to obtain a differential equation that describes how Σ varies with radius

$$\frac{\partial \Sigma}{\partial R} = \frac{3}{R} \frac{\partial \left\{ \sqrt{R} \frac{\partial \left(\nu \Sigma \sqrt{R} \right)}{\partial R} \right\}}{\partial R} \tag{1.18}$$

Generally, kinematic viscosity ν is a function of local properties of the disk like Σ, R and t and therefore (1.9) is a non-linear (and not analytically solvable) diffusion equation for surface density Σ. Instead, assuming ν as constant, equation (1.9) can be solved and $\Sigma(R, t)$ can be written in an integral form using the Bessel function $J_{\frac{1}{4}}$. In Figure 1.2 the time evolution of a disk annulus is shown. When $t = 0$ the whole mass is confined around R_0 and $\Sigma_0(t_0) = \delta(R - R_0)$; then, as time goes by, viscosity forces cause the energy loss and the gas flows toward $R = 0$ while a small fraction moves outward carrying the angular momentum and guaranteeing the conservation.

In order to obtain a complete description of our accreting annulus, we should solve Navier-Stokes equations considering all forces involved (gravitational, centrifugal and viscous) and, as previously, we would have to do with the 'viscosity uncertainty'. In their enlighten paper Shakura and Sunyaev, making use of the thin disk approximation, were able to find an easy-to-handle expression for viscosity and adopting the 'steady disk' approximation (i.e. $\dot{m} = const$), which is satisfied in many situations of astrophysical interest, were capable of achieve a simple expression for the rate of energy dissipated by one side of the disk

[2] Time scale for viscous processes, responsible for angular momentum redistribution, is larger than radiative and dynamic (orbital) time scale

[3] $\Omega = \sqrt{\frac{GM}{R^3}}$

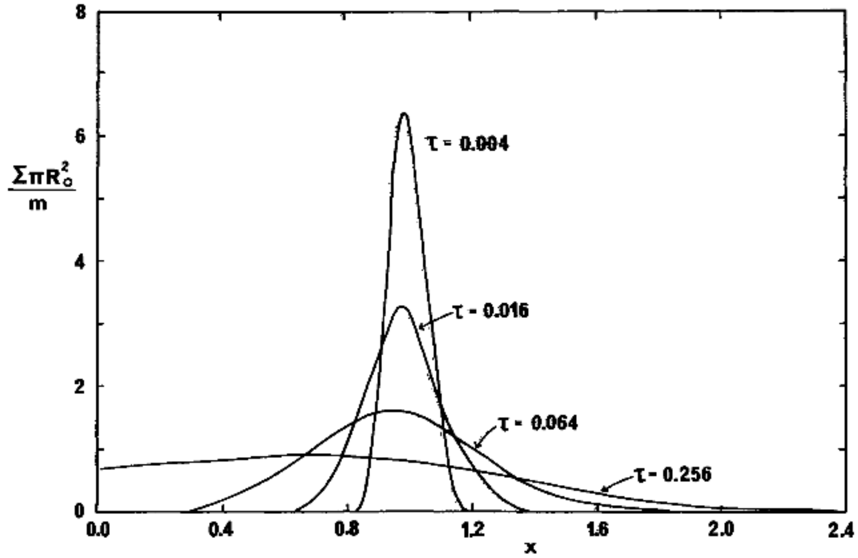

Figure 1.2: *The viscous evolution of a ring of matter of mass m. The surface density* Σ *is shown as a function of dimensionless radius* $x = \frac{R}{R_0}$*, where* R_0 *is the initial radius of the ring, and dimensionless time* $\tau = 12\frac{\nu t}{R_o^2}$ *where* ν *is the viscosity. (from Shakura & Sunyaev, 1973)*

$$\dot{Q} = \frac{3GM\dot{m}}{8\pi R^3}\left(1 - \sqrt{\frac{R_0}{R}}\right) \tag{1.19}$$

Assuming that the dissipated energy is entirely converted into radiation, the total luminosity of the disk is simply

$$L = \int_{R_0}^{\infty} 2\left(-\dot{Q}\right) \cdot 2\pi R dR = \frac{1}{2}\frac{\dot{m}GM}{R_0} \tag{1.20}$$

Thus, during radial motion half of the liberated potential energy goes into increasing the kinetic energy and half goes into heat and then into radiation. In order to obtain the emission spectrum we should be able to predict the emission from any part of the disk and than integrate over the whole surface or, in other words, we should solve the radiative transfer equation for any radius. Otherwise, if the disk were optically thick, every part would emit like a black body with its radius-dependent temperature $T_S(R)$ and, from the Stefan-Boltzmann law, the energy flux density might just be

$$U = \sigma T_S^4(R) \tag{1.21}$$

As for the steady disk approximation, the optically thick disk approximation extremely simplify our problem. Equating 1.19 with 1.21 we get the temperature at each radius

$$\dot{Q} = U \Rightarrow$$

$$\Rightarrow T_S(R) = \left[\frac{3GM\dot{m}}{8\pi R^3\sigma}\left(1 - \sqrt{\frac{R_0}{R}}\right)\right]^{\frac{1}{4}} \tag{1.22}$$

A typical value for AGN would be $T_S \simeq 10^5 K$ while for stellar-mass black holes $T_S \simeq 10^7 K$, respectively corresponding to UV and X-ray bands, as successfully confirmed by observations. The overall spectrum is simply the sum on the entire disk surface of single black body radius-dependent emission

$$S_\nu \propto \int_{R_0}^{R_{out}} B_\nu(T_S(R)) 2\pi R dR \tag{1.23}$$

where R_{out} is the outer radius of the disk and B_ν the Planckian photon distribution. The spectrum, shown in Figure 1.3, is the so-called 'multi-temperature black body'. At low frequencies the emission is due to the outer and cooler (T_{out}) part of the disk and the spectrum follows the typical $S_\nu \propto \nu^2$ Rayleigh-Jeans tail; the Planck exponential cut-off is clearly visible at high frequencies, while in the middle the characteristic $S_\nu \propto \nu^{\frac{1}{3}}$ trend for accretion spectra can be seen.

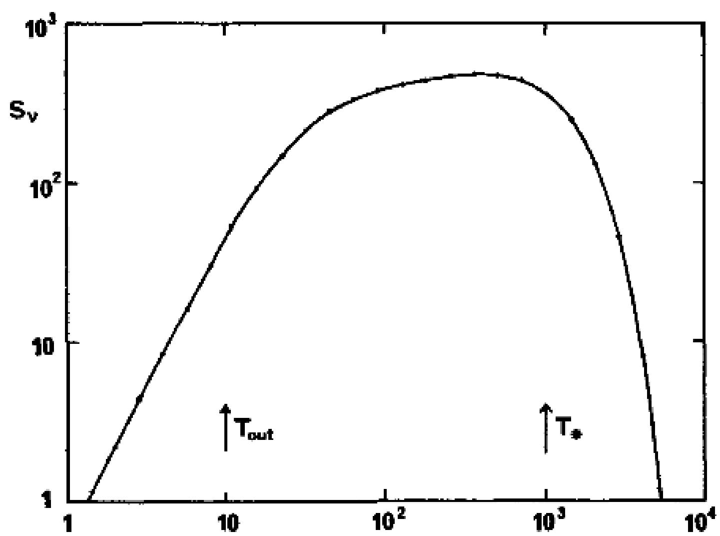

Figure 1.3: *Integrated spectrum of a steady, geometrically thin and optically thick accretion disk. The units are arbitrary but the frequencies corresponding to T_{out} and T_* are labelled. (from Shakura & Sunyaev, 1973)*

The accretion model of geometrically thin and optically thick disk we have just considered fits quite well the AGN case. As anyone can easily imagine there is a vast literature on accretion physics and a lot of different model arising from almost all the possible combinations between geometrically thin/thick and optically thin/thick conditions. One among all models that deserve to be mentioned is the 'Advection Dominated Accretion Flows' (ADAF) accretion model[4]. In ADAF models the accretion rate is so low that the surface mass density of the disk is not high enough to keep ions and electrons thermally coupled via Coulomb interactions. As a consequence, the energy associated to ions, which are poor radiators, cannot be locally emitted and it is advected together with the accretion flow beyond the black hole event horizon. Therefore a large fraction of the available energy turns into internal energy and the gas becomes hot and optically thin, with a very low radiative efficiency. Great attention has been focused on ADAF models thanks to their success in explaining the emission from the Galactic Center (see Narayan, Yi & Mahadevan 1995).

1.2 Unification Model

In 1985 when Antonucci & Miller (1985) observed the Seyfert 2 NGC 1068 in polarized light, they noticed that broad lines, completely absent in the total spectrum, were clearly visible and similar to those observed in Seyfert 1s. This result led them to suggest that type 2 objects harbour a type 1 nucleus, which is obscured by intervening gas. Its presence may be indirectly observed thanks to a reflecting 'mirror' (such as a gas of electrons) which scatters part of the nuclear radiation towards the line of sight, introducing a detectable degree of polarization. Therefore, the basic assumption of what was called the 'Unification Model' (see Antonucci 1993) is that type 1 and type 2 objects are absolutely equivalent, the only difference being whether the absorbing gas intercepts the line of sight to the nucleus or not. The absorbing medium assumes clearly the fundamental role in this scenario. It is usually envisaged as an optically thick 'torus' embedding the nucleus and the 'Broad Line Region' (BLR) (see Figure 1.4). If we observe the torus edge-on, all the nuclear radiation, including lines from the BLR which is inside it, is completely blocked and we classify the source as a type 2. The narrow lines are still visible, because the 'Narrow Line Region' (NLR) is located farther away from the nucleus, outside the torus. On the other hand, if the torus does not intercept our line of sight, we observe every component of the spectrum and the object is classified as a type 1.

The basic idea behind the Unification Model, i.e. that geometrical effects play a fundamental role in the classification of AGN, is probably correct, but a number of observational evidence suggests that some complications should be introduced.

[4]ADAFs are a subclass of 'Radiatively-Inefficient Accretion Flows' (RIAF) disks, characterized by a sub-Eddington accretion rate that brakes down radiative efficiency

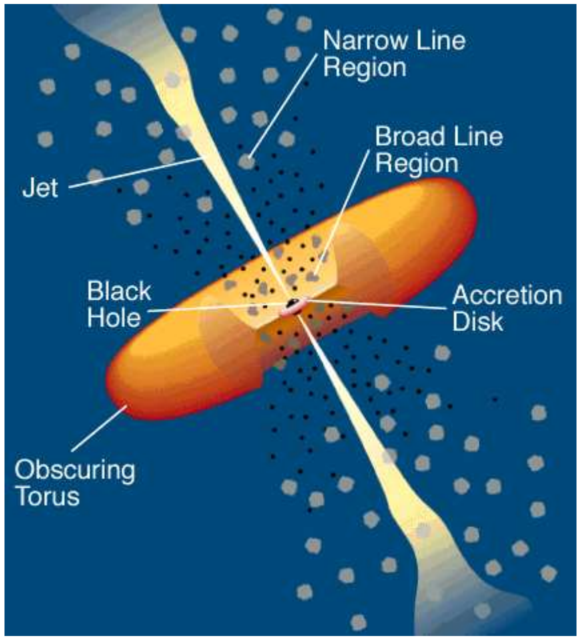

Figure 1.4: *AGN unification model sketch: a cartoon illustrating the Unification Model. Credit: M. Polletta, Laurea Thesis, 1996, adapted from Urry and Padovani, 1995*

Since the first work by Antonucci & Miller (1985), polarized broad lines have been observed in several other Seyfert 2s, but there are also many examples of type 2 objects which, observed in polarized light, still do not present broad lines (see Tran 2001, 2003). Moreover, simple extrapolations of the optical/UV scenario to the X-ray emission do not easily fit the observations, leading sometimes to different classifications between the two bands. Indeed, a number of obscured objects in X-rays turn out to be type 1 AGN when observed in the optical band (Maiolino et al. 2001; Fiore et al. 2001, 2002). There is also evidence for the existence of unobscured Seyfert 2s (Panessa & Bassani 2002; Bianchi et al. 2012). A major issue about misclassification in X-ay and optical arises for the non-simultaneous data available in both wavelengths. However, a number of cases of unabsorbed type 2 and absorbed type 1 AGNs have been confirmed with an observational simultaneous campaign in X-rays and optical.

The great success of the classical Unification Model, together with the problems it cannot explain, justify all the efforts spent to propose a number of alternatives. Among them, one of the most promising is the one advanced Elvis (2000). In the proposed scenario, a funnel-shaped thin shell outflow substitutes the torus and offers the possibility to explain many other features observed in AGN (see Figure 1.5).

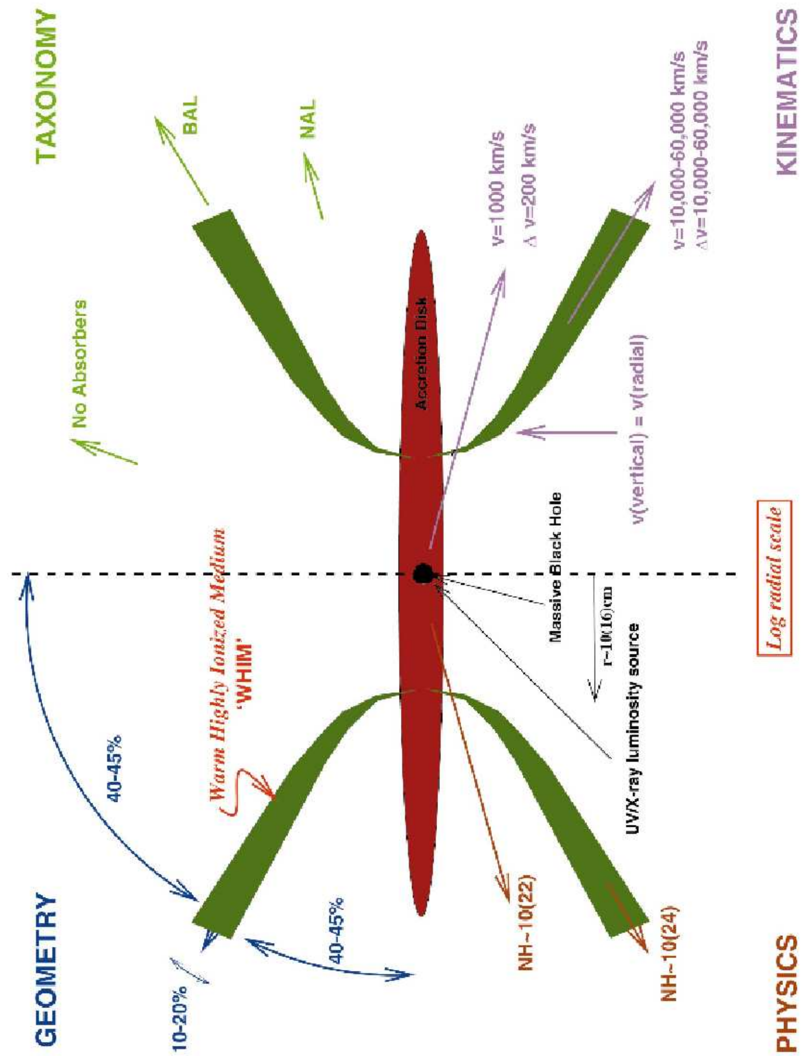

Figure 1.5: *A cartoon depicting the alternative Unification Model proposed by Elvis (Elvis 2000). The figure is divided in four quadrants which illustrate (clockwise from top left): the geometrical angles involved in the structure, the resulting classification for a distant observer, the outflow velocities for each line of sight and typical radii and column densities. (from Elvis, 2000)*

1.3 AGN Spectral Energy Distribution

AGN shine over ~ 10 decades of the electromagnetic spectrum, from the radio to the gamma rays and in most of this wide energy range they are the brightest objects in the sky. In the following sections we will describe the Spectral Energy Distribution (SED, shown in Fig. 1.6) of Seyfert galaxies, in the context of the Unification Model, in the different energy bands of the electromagnetic spectrum. It should be noted that the following description applies well to all radio quiet AGN, once accounted for the characteristic properties of each subclass. Moreover, the same consideration holds true for radio loud objects (at least those not dominated by jet emission), even if, in this case, the differences are clearly better defined in some electromagnetic bands, such as the radio emission, naturally larger in this class, and the γ ray spectrum, typically observed only in blazars.

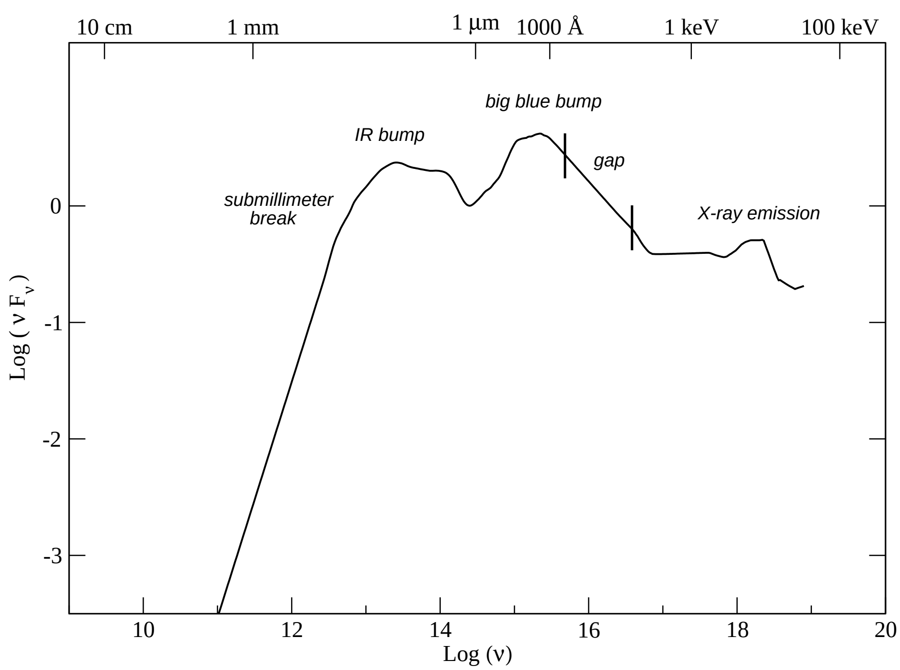

Figure 1.6: *A typical Spectral Energy Distribution (SED) for a radio quiet AGN is shown. The y axis is arbitrarily normalized, data were taken from (Elvis et al. 1994), together with an extrapolation in the 'gap'. The gap between* 1000 – 100 *Å (*10 – 10^2 *eV) is due to HI absorption from our own Galaxy; above* 100 μm *(*< 10^{-2} *eV) there is the 'submillimeter break' (see Section 1.3.2).*

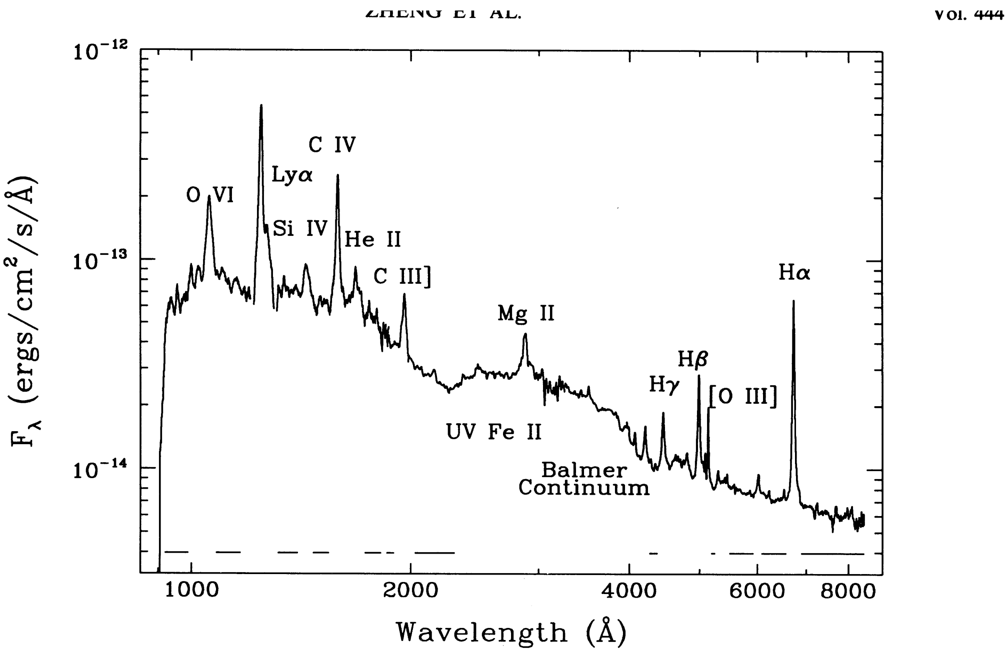

Figure 1.7: Merged UV/optical spectrum of the Seyfert 1 galaxy Mrk 335. Major emission features are labelled and the small blue bump can be seen between 2000Å and 4000 Å (from Zheng et al. 1995)

1.3.1 Optical/UV

The dominant feature in the UV/optical spectra of AGN is the big blue bump, as we can clearly see in Fig. 1.6 and 1.7, which can be attributed to thermal emission from a plasma at a temperature in the range $10^{5\pm1}$ K. The peak energy is around the Lyman edge (λ = 1216Å), and the spectrum can be well approximated by a power law both at lower and higher frequencies. The emission from an optically thick and geometrically thin accretion disc for a SMBH should peak in the UV (its temperatures are expected to be of the order of $\sim 10^5$ K.). The big blue bump is therefore most likely ascribed to thermal emission from the accretion disc. However, this association is not evident, since the exact shape of the optical/UV continuum is often strongly contaminated by starlight from the host galaxy, absorption by intervening materials and reddening by dust. Moreover, the superposition of the broad emission lines in this energy range makes this analysis very complex. In particular, a set of blended Balmer and Fe II emission lines together with the Balmer continuum make up the 'small blue bump', which alters the shape of the underlying continuum in the range between $\simeq$2000 Å and 4000 Å (see figure 1.7). It should also be remarked that in the extreme ultraviolet our own

Galaxy is opaque and no data are available in that 'gap' (see figure 1.6).

1.3.2 Infrared

The integrated IR emission (2-200 μm) accounts, on average, for the $\sim$ 30% of the bolometric luminosity of AGN and it is believed to be mainly due to reprocessing of the primary radiation from dust. The presence of the IR bump, with a minimum around 1μm (see Fig. 1.6), is ubiquitous in AGN (Sanders et al. 1989; Haas et al. 2005) and it leads to the conclusion that the emission must be thermal, since the required temperatures are in the right range ($\simeq$ 2000K) for hot dust in the nuclear regions (at higher temperatures dust grains would sublimate). The submillimeter break at the end of the far-IR band (see Fig. 1.6) can be easily reconciled with the rapid loss of efficiency of dust grains at long wavelengths. This would explain the sharp cutoff observed just shortward of 1 mm. The sublimation radius can be defined as the minimum distance from the AGN at which grains of a given composition can exist. Indeed, in the clumpy torus model proposed by Nenkova et al. (2008) the inner radius of the torus is defined by the dust sublimation temperature T_{sub} as follows:

$$R_d \approx 0.4 \left(\frac{L}{10^{45}\ \mathrm{erg\ s^{-1}}}\right)^{0.5} \left(\frac{1500\ \mathrm{K}}{\mathrm{T_{sub}}}\right)^{2.6}\ \mathrm{pc} \tag{1.24}$$

where L is the intrinsic AGN luminosity and $\mathrm{T_{sub}}$ is typically in the range 1000-1500 K. In more luminous AGN, R_d increases, and hence the opening angle of the torus must also increase. This leads to a luminosity dependence on the observed Type1-Type2 ratio: this is often referred to as the receding torus (Lawrence 1991; Simpson 2005).

The reprocessing dust model is also supported by infrared variability. An optical/UV variation should be followed by an IR variation, but with a significant time delay due to the larger scale where the dust is distributed. In the particular case of Fairall 9 this is exactly what was observed: a delay was measured of about 400 days (Clavel, Wamsteker & Glass 1989). This means that the minimum distance of dust is just below a parsec or so, in extremely good agreement with the expected sublimation radius for an object of such luminosity. The emerging scenario is a nucleus where the UV/optical continuum fully depletes the dust up to the sublimation radius. Beyond this radius, the same radiation heats the dust to a wide range of temperatures (depending on the distance from the central source), producing the observed IR bump around 10-30 μm. It should be noted, however, that a significant contribution of starlight to the dust heating has been proposed, especially in the far IR band (Prieto, Pérez García & Rodríguez Espinosa 2001).

1.3.3 Radio

The radio emission, in radio-quiet AGN, contributes very little to the bolometric luminosity; the luminosity can be 5-6 orders of magnitude lower than the UV/optical continuum. The emitting region is usually very compact, the radio spectra are very flat and become steeper at shorter wavelengths (see Lal & Ho 2010, and references therein). This a typical characteristic of non-thermal emission and hence synchrotron radiation is generally invoked as the mechanism responsible for the radio continuum. The flatness of the radio spectrum can be ascribed to a complex source structure and the presence of low-frequency cutoffs found in some objects can be explained in terms of synchrotron self absorption, even if the frequency dependence is not as steep as it should be.

1.3.4 X-rays

The X-ray properties of AGN have been intensively studied in the last decades, since the first X-ray missions in the mid-1970's. The X-ray emission from AGN extends from the Galactic absorption cut-off at ~ 0.1 *keV* up to ~ 300 *keV*. The intrinsic X-ray continuum is to first order a power law due to Comptonization of UV photons produced by the disc in a surrounding hot 'corona' (Liang & Price 1977; Liang 1979), possibly due to magnetic fields from the body of the disc itself (Haardt & Maraschi 1991; Zdziarski et al. 1994). However, many other components are present in this energy range, due to reprocessing of the primary continuum from circumnuclear material. We will discuss the main physical mechanisms in this energy range and the observational features that can be investigated in Chapter 2.

Chapter 2

The X-ray emission in AGN

In this chapter we will be briefly present the main mechanisms involved in the production and absorption of X-rays, the main physical mechanisms in this energy range and the observational features that can be investigated, in order to understand the physics behind AGN emission in this band. In particular the basic principles of atomic physics that lead to the production of spectral lines will be summarized.

2.1 Radiative processes

There are three main processes by which the radiation interacts with matter: Bremsstrahlung emission, Synchrotron radiation and Compton processes. Only Compton processes are important in understanding the X-ray emission of radio-quiet AGN, so we will briefly describe them in some more detail in the next section.

2.1.1 Compton processes

For low photon energies, $h\nu \ll mc^2$, the scattering of radiation from free electrons is the classical 'Thomson scattering'. It must be remembered that for Thomson scattering, when the incident photons are approximated as a continuous electromagnetic waves

$$E_i = E_f \tag{2.1}$$

$$\left(\frac{d\sigma_T}{d\Omega}\right)_{unpol} = \frac{r_0^2}{2}\left(1 + \cos^2\theta\right) \tag{2.2}$$

$$\sigma_T = \frac{8}{3}\pi r_0^2 \tag{2.3}$$

Here E_i and E_f are the incident and scattered photon energy, respectively, $d\sigma_T/d\Omega$ is the differential Thomson cross section for unpolarized incident radiation, θ the angle between the scattered wave and the incident wave, and $r_0 \equiv e^2/m_e c^2$ the classical electron radius. Since $E_i = E_f$ the scattering is called 'coherent' or 'elastic'. When the photon energies are higher ($\sim keV$), quantum effects arise, altering the kinematics of the scattering process and the cross section. The kinematic effects occur because the photon possesses a momentum $h\nu/c$ as well as an energy $h\nu$ and the scattering will no longer be elastic ($E_i \neq E_f$) because of the recoil of the charge. Making use of the conservation of momentum and energy, the energy of the scattered photon can be easily calculated

$$E_f = \frac{E_i}{1 + \frac{E_i}{mc^2}(1 - \cos\theta)} \tag{2.4}$$

The differential cross section for unpolarized radiation is shown in quantum electrodynamics to by given by the Klein-Nishina formula

$$\frac{d\sigma}{d\Omega} = \frac{r_0^2}{2}\frac{E_f^2}{E_i}\left(\frac{E_i}{E_f} + \frac{E_f}{E_i} - \sin^2\theta\right) \tag{2.5}$$

In the regime of Compton scattering, it may happen that a photon collides with a moving electron with a kinetic energy larger than the photon energy. In this case the energy transfer takes place in the opposite direction, from electron to photon, and the process is called 'Inverse Compton' (IC). In order to have an immediate idea about how the energy transfer acts, let us consider, in the rest frame of the laboratory, an hyper-relativistic electron, $\gamma \gg 1$, and a photon with initial energy E_i. In the rest frame of the electron, the photon energy before the collision is

$$E_i^{'} = E_i\gamma(1 - \beta\cos\theta) \tag{2.6}$$

where θ is the angle between the photon and electron trajectories in the laboratory rest frame, and $\beta = v/c$ is the dimensionless velocity of the electron. Assuming $E_i^{'} \ll mc^2$ [1],in the rest frame of the electron the scattering is described by the Thomson cross section and the energy of the photon remains almost the same, $E_f^{'} \simeq E_i^{'}$. On the other hand, in the rest frame of the laboratory the photon energy after the collision is

$$E_f = E_i^{'}\gamma(1 + \beta\cos\theta) \tag{2.7}$$

Comparing the above equation with the previous one, it is easy to see that the photon has a final energy γ^2-fold the initial value. This process therefore converts

[1]This approximation is applied, for example, to scattering between UV photons produced by the AGN accretion disk and relativistic electrons in the surrounding corona.

a low-energy photon to a high-energy one and it is very effective for $\gamma \gg 1$ electrons. Since the photon energy can be as high as, let's say, 100 keV and still be in the Thomson limit, it can be seen that photons of enormous energies ($\gamma \times 100$ keV) can be produced. The total power lost by the electron and thereby converted into increased radiation, can be shown (Blumenthal & Gould 1970) to be

$$P_{IC} = \frac{4}{3}\sigma_T c\gamma^2\beta^2 U_\gamma \left(1 - \frac{63}{10}\frac{\gamma < E_i^2 >}{mc^2 < E_i >}\right) \tag{2.8}$$

where

$$U_\gamma \equiv \int E_i n \, dE_i \tag{2.9}$$

is the initial photon energy density (n is the photon occupation number in the phase space). In equation 2.8, the term in brackets represents the corrections due to recoil, where $< E_i^2 >$ and $< E_i >$ are mean values integrated over U_γ.

The total IC power calculated in equation 2.8 concerns a single collision between an electron and a photon. When photon and electron distributions are considered, the calculations needed to obtain the power spectrum are arduous and sometimes can be solved only numerically. To begin with, considering that each collision increases the initial energy of the photon by a factor γ^2, it should be quite clear that the resulting final spectrum strongly depends on how many times the photons are scattered. Secondly, as hyper-relativistic electrons approach $\beta \lesssim 1$ ($\gamma \gg 1$), large relativistic corrections on the energy transfer are required. The best studied case, and the most common, is the repeated scattering by non-relativistic electrons. The electrons are assumed to be thermally distributed with $kT \ll mc$ while the photons are assumed to have small initial energies with respect to the thermal electron ones. In this case the average energy gain per collision (neglecting the recoil corrections) can be shown to be

$$\frac{\Delta E}{E_i} \approx 4\frac{kT}{mc^2} \ll 1 \tag{2.10}$$

For an optically thick medium, $\tau_T \gg 1$, the number of collisions made by a photon before escaping from the source is τ_T^2, where τ_T is the Thomson scattering optical depth[2]. For optically thin medium, $\tau_T \ll 1$, the number of collisions is τ_T. It is useful to introduce the so-called 'Compton parameter' which is defined, in the non-relativistic regime, as

$$y \equiv 4\frac{kT}{m_e c^2} \max\left(\tau_T, \tau_T^2\right) \tag{2.11}$$

[2] $\tau_T \approx \rho k_{es} R$, where ρ and R are the density and the size of the finite medium, respectively, and k_{es} is the electron scattering opacity, which for ionized hydrogen is $k_{es} = \sigma_T / m_p$.

This parameter describes the cumulative effect of many scatterings on the photon energy. The complete evolution of the spectrum produced by IC is described by the Kompaneets equation, a specialized form of a Fokker-Planck equation which can be shown to be a power law. In particular, for a non-thermal electron energy distribution, described by a power law with index α the outcoming spectrum in the optically thin regime is

$$J_{IC} \propto \left(\frac{\nu_i}{\nu}\right)^{\frac{\alpha-1}{2}} \tag{2.12}$$

The shape of the spectrum is, hence, identical to synchrotron emission.

2.2 Lines production

There are several ionization and recombination processes that are relevant in the X-ray band. Some of these processes also play directly a role in spectral line formation. We will first introduce some important ionization/excitation mechanisms and then the inverse processes of recombination/de-excitation that lead to production of spectral lines or, sometimes, continuum radiation.

2.2.1 Generating the vacancy

Collisional excitation and photoexcitation

A bound electron in a ion can be brought into a higher, excited energy level through a collision with a free electron or by absorption of a photon. Both these processes are referred as 'bound-bound' because there is no ionization, due to the electron/photon low energy[3]. When the excitation energy comes from a photon the process is called 'photoexcitation'. The dynamics of photoexcitation (and de-excitation) is very simple and will be expose later in this section (see 'radiative de-excitation' and 'resonant scattering'). When the source of energy is a free electron the excitation is called 'collisional'. The cross section Q_{ij} from level i to level j for collisional excitation can be conveniently parametrised as

$$Q_{ij}(U) = \frac{\pi a_0^2}{\omega_i}\frac{E_H}{E_{ij}}\frac{\Omega(U)}{U} \tag{2.13}$$

where $U = E/E_{ij}$ with E_{ij} the excitation energy from level i to j, E the energy of the exciting electron, E_H the Rydberg energy (13.6 eV), a_0 the Bohr radius and ω_i the statistical weight of the lower level i. The dimensionless quantity $\Omega(U)$ is

[3] When it is not important to distinguish between processes, it is customary to label ionization mechanisms as 'bound-free' processes and recombination mechanisms as 'free-bound' processes.

the so-called ‘collision strength’. Averaging the free electrons over a Maxwellian velocity distribution, it is possible to express the number of excitations per unit volume per unit time as

$$S_{ij} = S_0\overline{\Omega}(y)T^{-1/2}e^{-y} \tag{2.14}$$

where

$$\begin{aligned} y &\equiv E_{ij}/kT \\ S_0 &= \sqrt{\frac{8\pi}{m_e k}} a_0^2 E_H \end{aligned}$$

and

$$\overline{\Omega}(y) \equiv ye^y \int_1^\infty \Omega(U)e^{-Uy}dU$$

is the average collision strength. From equation (3.2) we can see that for low T there are exponentially few excitations (only the electrons in the energetic tail of the Maxwellian distribution have enough energy for excitation); for high T the number of excitations also approaches zero, because of the small collision cross section.

Collisional ionization

Collisional (or ‘direct’) ionization occurs when during the interaction of a free electron with an atom or ion, the free electron transfers part of its energy to one of the bound electrons, which is then able to escape from the ion. A necessary condition is that the kinetic energy E of the free electron must be larger than the binding energy I of the atomic shell from which the electron escapes. There are several formulae that describe the effective cross section Q as a function of E. The Lotz’s formula (1968) gives a correct order of magnitude of the cross section and has the proper asymptotic behaviour

$$uI^2Q = C \ln u \tag{2.15}$$

where $u = E/I$ and $C = an_s$, where n_s is the number of electrons in the shell and a a normalizing constant ($a = 4.5 \times 10^{-24}\ m^2\ keV^2$). For $E \to \infty$, the cross section $Q \sim (\ln E)/E \to 0$, meaning that energetic electrons are not very efficient in ionizing atoms because they pass too fast. As for collisional excitation it is possible to average the electrons over a Maxwellian distribution in order to obtain the total number of direct ionizations per unit volume per unit time, C_{DI}. It is interesting to consider C_{DI} in two relevant situation

$$kT \ll I: \qquad C_{DI} \simeq \frac{2\sqrt{2}C}{\sqrt{\pi m_e}} \frac{n_e n_i \sqrt{kT} e^{-I/kT}}{I^2} \tag{2.16}$$

$$kT \gg I: \qquad C_{DI} \simeq \frac{2\sqrt{2}C}{\sqrt{\pi m_e}} \frac{n_e n_i \ln(kT/I)}{I\sqrt{kT}} \tag{2.17}$$

As for collisional excitation, for low temperatures - equation 2.16 - the ionization rate goes exponentially to zero because only few energetic electrons have enough energy to ionize the atom, while for high temperatures - equation 2.17 - the ionization rate approaches zero because the cross section is small at high energies.

Photoionization

Photoionization occurs when an incident photon transfers all its energy to a bound electron allowing the electron to escape. In a similar way to what happens in direct ionization the photon energy, E, must be at least equal to the binding energy of the electron, I. For $E \gg I$ a rough approximation for the total cross section is given by

$$\sigma_{bf}(E) \propto \frac{Z^n}{E^3} \tag{2.18}$$

where Z is the atomic number of the atom and n is a number which varies between 4 and 5. For $E < I$ the cross section is zero, rises abruptly at threshold, $E = I$, and then roughly decreases as E^{-3}. For a given ionizing spectrum, $F(E)$ (photons per unit volume per unit energy), the total number of photoionizations are

$$C_{PI} = c\int_0^\infty n_i\sigma(E)F(E)dE \tag{2.19}$$

For *H-like* ions the total cross section can be written as

$$\sigma_{PI} = \left(\frac{64\pi ng}{3\sqrt{3}Z^2}\right)\alpha a_0^2\left(\frac{I}{E}\right)^3 \tag{2.20}$$

where n is the principal quantum number of the ejected electron, α the fine structure constant and a_0 the Bohr radius. The gaunt factor $g(E, n)$ is of the order of unit and varies slowly. Equation 2.20 is also applicable to ions in excited states.

2.2.2 Filling the vacancy

Collisional and radiative de-excitation

Collisional and radiative de-excitation are the inverse processes of collisional excitation and photoexcitation, respectively. If a bound electron of an atom or ion in an excited state, whatever the excitation mechanism, decays to a lower level emitting a photon, the process is referred to as 'radiative de-excitation'. The spectral lines produced in this way are only seen in gases at very low densities (typically less than a few thousand particles per cm^3). At higher densities, the antagonist process, the 'collisional de-excitation', suppresses lines production.

The rate coefficient S'_{ji} of collisional de-excitations from level j to level i is related to S_{ij}, the rate of excitations expressed by equation (3.2). The relation can be derived from the principle of detailed balance, and is given by

$$S'_{ji} = \frac{\omega_i}{\omega_j} S_{ij} e^{E_{ij}/kT} \tag{2.21}$$

where ω_i and ω_j are the statistical weights of level i and j respectively. In astrophysics, collisional de-excitation is important only for high density plasmas, where due to collisions higher levels are populated, or for metastable levels (levels that have only a small probability to decay radiatively). The so-called 'forbidden lines' are produced by radiative de-excitation of such metastable states. Their absence in the spectrum means that collisional de-excitation is the dominant process (see Section 2.2.3).

Auger effect & fluorescence

When a photon has an energy higher than the binding energy of the electrons in a shell of an ion, one of them can be ejected through photoelectric absorption (the phenomenon of photoionization seen before). The shell vacancy can then be filled by an electron from an outer shells and the energy resulting from the transition can be released in two different ways.

In the first case a photon is emitted and, by conservation, its energy equals the difference between the energy of the initial and the final state of the electron that makes the transition. This process is called 'fluorescence'. Depending on the quantum numbers of the involved electron, the transition acquires different denominations: e.g. for a vacancy in the *K-shell* (as usually happens for ionization by X-ray photons) if the electron came from the *L-shell*, the emitted photon is called $K\alpha$ and the transition is the one with the highest probability to occur; if the original shell was the *M*, the transition is called $K\beta$ (both transitions are, indeed, doublets, because of spin-orbit coupling effects). The total probability that the de-excitation happens via the emission of a photon, whatever the transition, is called 'fluorescence yield'. The fluorescence yield increases with nuclear charge and is largest for the innermost shells[4].

[4] It is not surprising that the $K\alpha$ fluorescence line of iron, which is the most abundant of heavy elements, is very prominent in a number of astrophysical sources, AGN included.

In the second case the energy released by the electron is gained by an outer electron, being allowed to leave the ion. This radiationless process is called ‘Auger effect’.

Radiative recombination

Radiative recombination is the inverse process of photoionization: a free electron is captured by an ion while emitting a photon. The released radiation is the so-called free-bound continuum emission. By the principle of the detailed balance there is a relation between the photoionization cross section $\sigma_{bf}(E)$ for photons with energy E, and the recombination cross section $\sigma_{fb}(v)$ for electrons with velocity v, namely the ‘Milne relation’

$$\frac{\sigma_{fb}}{\sigma_{bf}} = g_n \left(\frac{E}{mcv}\right)^2 \tag{2.22}$$

where g_n is the statistical weight of the quantum level into which the electron is captured. Averaging over a Maxwellian electron velocity distribution it is possible to calculate the recombination rate to the n-th quantum level, R_n, whose temperature dependence, in opposite limit situations, can be expressed as

$$kT \ll I : \qquad R_n \sim T^{-\frac{1}{2}} \tag{2.23}$$

$$kT \gg I : \qquad R_n \sim \ln(I/kT) \times T^{-3/2} \tag{2.24}$$

From equation (3.11), for $T \to 0$, $R_n \to \infty$ meaning that a cool plasma is hard to ionize. From equation (3.12), for $T \to \infty$, $R_n \to 0$ because $v \to \infty$ in (3.10) and because the sharp decrease of σ_{bf} at high energies. Radiative recombination is a a continuum emission because the energy of the emitted photon, by law of conservation, is

$$h\nu = E_e + I_n \tag{2.25}$$

where I_n is the ionization potential of the n-th level in which the free electron falls and E_e is the free electron energy and the latter can have, in principle, any value. Therefore the energy of the emitted photon is only down-limited ($h\nu > I_n$) and the emission produced in this matter is usually called ‘Radiative Recombination Continua’ (RRC). RRC lines plays a very important role in plasma diagnostic, as explained in the next section.

Resonant scattering

The last process of lines production is resonant scattering. Resonant scattering is a process where a photon is absorbed by an atom and then re-emitted as a line photon of the same energy into a different direction. As for strong resonance lines (allowed transitions) the transition probabilities are large, the time interval between absorption and emission is extremely short, and that is the reason why this process can be *de facto* regarded as a scattering process, as suggested by the name.

2.2.3 Ionization equilibria and plasma diagnostic

The knowledge of ion concentrations is required in order to calculate the X-ray emission or absorption from a plasma. These concentrations can be determined by solving the equations for ionization balance (or in more complicated cases by solving the time-dependent equations) where the ionization and recombination rates are very important. Two types of ionization equilibrium are particularly relevant for X-ray plasmas.

Collisional equilibrium

Here, the excitations and ionizations are dominated by electron-ion collisions. The electrons are hot, with characteristic temperatures comparable with the energies of the spectral lines observed. The emergent spectrum is nearly a unique function of the electron temperature distribution and the elemental abundances. These conditions apply in stellar coronae, in the intracluster media of clusters of galaxies, in elliptical galaxies, and in the shocked gas in old supernova remnants.

Photoionization equilibrium

In this case, the presence of an intense continuum radiation field has a significant effect on the ionization and thermal structure of the surrounding gas. The electrons are generally too cool to excite prominent X-ray lines. Instead, excited levels are populated by direct recombination and by radiative cascades following recombination onto higher levels, and by direct photoexcitation from the continuum. These conditions can apply in the circumsource media of accretion-powered sources, such as X-ray binaries and AGN.

The main spectroscopic differences between collisionally ionized and photoionized plasmas are due to the very different electron temperatures. For collisional ionization, the electron temperature is comparable with the ionization potential, while for photoionization, the photon field does most of the work, so the electron temperature can be much lower. Perhaps the most useful spectroscopic diagnostics for distinguishing collisional ionization from photoionization are radiative recombination continua (RRC). As we have seen in the previous section, the energy of the photon produced by recombination is given by the sum of the ionization potential and the electron energy - equation (3.13). As stated above, in the case of collisional ionization equilibrium (CIE), $kT_e \simeq I_n$ and the resulting recombination radiation line is broad, with a typical width of $\sim kT_e$. In the case of photoionization equilibrium (PIE), $kT_e \ll I_n$ and the recombination radiation line is narrow. When observing this effect with high resolution spectrometers, for a gas in CIE, RRC is too broad to be visible and hence the presence of a sharp RRC is a strong indicator of PIE. Other diagnostic tools deserving to be mentioned exist in X-rays spectroscopy, one of them linked to the *He-like K-shell* lines, probably the most important in X-ray spectra of cosmic sources. The main *K-shell* helium-like transitions are as follows

$$
\begin{aligned}
W &: 1s2p^1P_1 \rightarrow 1s^2\ {}^1S_0 \\
X &: 1s2p^3P_2 \rightarrow 1s^2\ {}^1S_0 \\
Y &: 1s2p^3P_1 \rightarrow 1s^2\ {}^1S_0 \\
Z &: 1s2p^3S_1 \rightarrow 1s^2\ {}^1S_0
\end{aligned}
$$

W is an electric dipole transition, also called the resonance transition, and is sometimes designated by r. X and Y are the so-called intercombination lines. These are usually blended (especially for the lower-Z elements), and are collectively designated by i. Z is the forbidden line, often designated by f. It is a relativistic magnetic-dipole transition, with a very low radiative-decay rate. Analyzing the line ratios it is possible to estimate the temperature and the density of the gas. For example the ratio $G = (X + Y + Z)/W$ is a decreasing function of electron temperature while the ratio $R = Z/(X + Y)$ is very sensitive to density. The density sensitivity comes from the fact that the ${}^3S_1$ level can be collisionally excited to the ${}^3P$ levels. At high enough electron density, the process successfully competes with radiative decay of the forbidden line. Therefore R drops off above a critical density, n_c. The critical density depends strongly on Z (the atomic number). For C^{4+}, $n_c \sim 10^9$ cm^{-3}, while, for Si^{12+}, $n_c \sim 10^{13}$ cm^{-3}.

2.3 The X-ray emission in AGN

2.3.1 The primary emission

The primary X-ray spectrum of Seyfert galaxies is a simple power law with spectral index 1.8-2.0 and a high-energy cutoff around 100-200 keV (Perola et al. 2002). In AGN, a radiatively-efficient accretion disc cannot account directly for the hard X-ray emission, since it mainly radiates in the UV/soft X. After the seminal work by Shakura & Sunyaev (1973) the most promising physical mechanism

to produce such components is Comptonization of UV seeds photons produced by the disc in a surrounding hot 'corona' (Liang & Price 1977; Liang 1979), possibly due to magnetic fields from the body of the disc itself (Haardt & Maraschi 1991; Zdziarski et al. 1994). The 'two-phase' model assumes a sandwich geometry where the hot corona (dominated by electron-positron pairs in thermal equilibrium at a temperature T_e) completely embeds the accretion disc, in this scenario the high-energy cutoff naturally arises as a function of T_e. The optical depth τ of the corona is defined by the compactness parameter l_c which depends on the height scale of the corona, the accretion disc radius and the overall luminosity of the object. The inverse Compton scattering of the UV seed photons emitted by the underlying disc on the hot electrons produces a X-ray power law spectrum, which photon index is a function only of T_e and τ.
However, this simple model fails to reproduce the observed X-ray spectra, since it is required that most of the gravitational energy must be dissipated in the corona rather than in the disc, implying a X-ray luminosity comparable to the one emitted in the UV band. It has been shown that, on the contrary, UV luminosity are much larger (Walter & Fink 1993). More complex geometries have been therefore proposed. For instance, Haardt, Maraschi & Ghisellini (1994) proposed and developed a 'patchy corona' model, where hot electrons partially cover the disc and are not distributed uniformly around it. The emission from the regions of the disc under the active clouds is then effectively dominated by the radiation produced by the corona, but the rest of the disc simply radiates as if the corona were not present.

2.3.2 The reprocessed emission

The interaction between the disc and the corona is a fundamental ingredient of the two-phase model. A substantial fraction of the X-ray photons (actually half of them in the plane parallel limit, if the corona emission is isotropic) is emitted in the direction of the accretion disc again. A large number of these photons are absorbed by the disc and then re-emitted as black body radiation, contributing once again as the seed photons to be Comptonized by the corona. Another fraction of the X-ray radiation interacting with the disc is Compton scattered and adds to the primary spectrum emitted by the corona. This gives rise to a characteristic reprocessed spectrum, very dependent from the ionization state of the disc. If it is highly ionized, Compton scattering becomes the main interaction mechanism, leading to a power law spectrum indistinguishable from the primary nuclear continuum. On the contrary, if matter is mostly neutral, photoelectric-absorption prevails at lower energies (Guilbert & Rees 1988; Lightman & White 1988). This last process is responsible for an emission spectrum where fluorescent narrow Kα lines from the most abundant metals are detected. The strongest

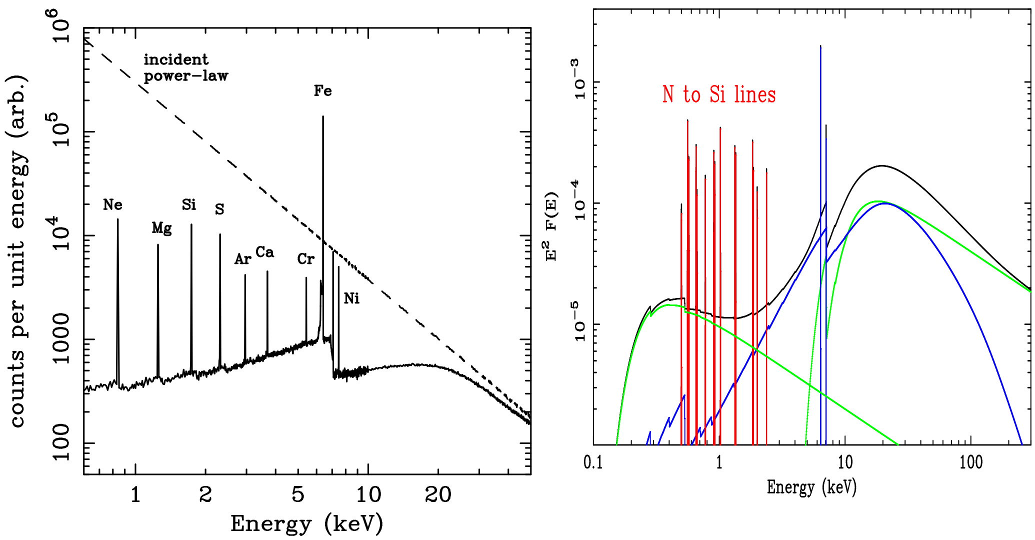

Figure 2.1: *Left panel*: Reflection of a power law X-ray spectrum from an optically thick neutral material. The incident continuum is shown as a dashed line, while the straight line is the reprocessed spectrum, including the Kα lines from the indicated elements, from (S. 1999). *Right panel*: The broadband spectrum of a Seyfert 2 galaxy. The primary continuum (green) is heavily absorbed by a column density $N_H > 10^{24}$ cm^{-2}, identified as the putative torus, partially blocking the line of sight. This material is responsible from the nearly neutral X-ray reflection (blue) from the visible side of the torus. Since the primary continuum flux is much lower with respect to unobscured objects several emission lines due to photoionized gas are detected (red), from Fabian & Miniutti (2005).

emission line is produced by iron, at 6.4 keV if the matter is mostly neutral, and up to 6.68 and 6.97 keV from more ionized material. This line comes together with a sharp ionization edge at 7.1 keV, which accounts for the absorbed photons above the photoionization threshold for neutral iron (this energy clearly shifts to higher values for ionized iron). Photoelectric absorption is an energy-dependent process, so that incident soft X-rays are mostly absorbed, while hard photons tend to be Compton scattered back out of the disc, producing a sort of hump peaking at $\sim$ 30 keV (George & Fabian 1991; Matt, Perola & Piro 1991). The typical X-ray reflection spectrum from a neutral and uniform density semi-infinite slab of gas is shown in Fig. 2.1 (top panel), where several emission lines are present below 10 keV and the Compton hump can be seen above 20 keV.

2.3.3 The soft excess

A soft, quasi-blackbody excess is often observed in the energy range below 1 keV in most spectra of Seyfert 1s. For a very complete review on this subject we refer the reader to Fabian & Ross (2010). So far, we described the scenario where the irradiation is weak and the gas dense, so it remains neutral, which is unlikely in the innermost regions of an AGN. It is expected that the irradiation from the corona is intense enough to ionize at least the surface of the accretion flow. There might also be sufficient radiation intrinsic to the accretion flow (e.g. thermal black body emission) which also ionizes the matter. Ross & Fabian (1993) calculated X-ray reflection spectra taking into account different parameters of the accretion disc, such as ionization state and temperature. In Fig. 2.2 we show ionized reflection models calculated for different accretion rates (15%, 20%, 25% and 30% of the Eddington limit), for a 10^8 $M_\odot$ black hole. Several models have been proposed in the last few years but the origins of such spectral features in the soft X-rays of AGN are still under debate. A blurred ionized reflection has been proposed by (Crummy et al. 2006): the soft X-ray lines in the reflection spectrum at standard solar abundances might overlap each other so that they relativistically blur into a mildly-structured soft hump. In this scenario the soft X-rays should be linked with the hard (>10 keV) X-rays and reflection components; i.e., a broad iron line and a bump at ~30 keV, are expected. Other authors proposed that the soft excess could result from warm Comptonization in an optically thick plasma (Petrucci et al. 2012; Done et al. 2012). In this case, a correlation between the UV and soft X-ray emission is expected. Finally, the effect of partial covering ionized absorption can also account for part of the observed soft excess without requiring material to be moving at extreme velocities (e.g. Miller, Turner & Reeves 2008).

2.3.4 Reflection and absorption from the torus

Most of the emission from AGN is somewhat, or at least in part, obscured. In the local universe optically obscured type 2 AGN outnumber unobscured type 1 AGN by a factor ~ 4, as shown by Maiolino & Rieke (1995a). Moreover, heavy absorption in the X-rays is very common, since about half of the optically selected Seyfert 2s in the local Universe are Compton-thick (Maiolino et al. 1998).

The geometry of the different absorbers distributed around the central engine is therefore crucial for the understanding of the mechanisms that fuel AGN. In the following we will describe the different emission features from the reprocessing of the nuclear radiation from the circumnuclear absorbing material.

In the previous sections we showed how reflection in X-rays is due to photoelectric absorption (dominant below ~ 4 keV) and Compton scattering (dominant from ~ 7 keV up to ~ 30 keV). The X-ray properties of obscured AGN strongly depend on

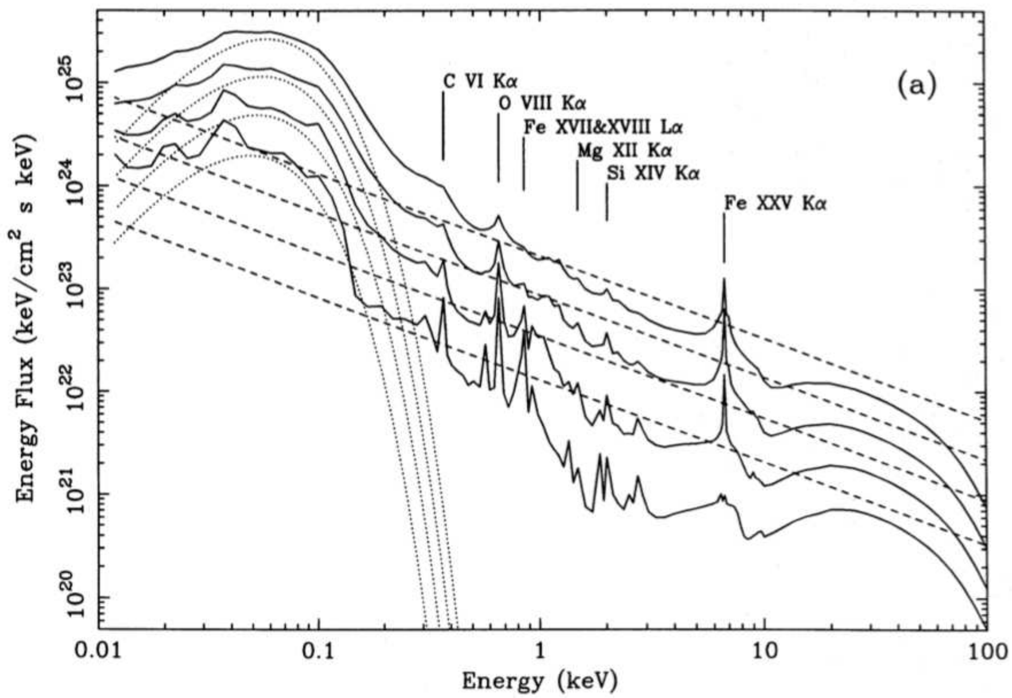

Figure 2.2: : Ionized reflection models calculated for different accretion rates (15%, 20%, 25% and 30% of the Eddington limit), for a 10^8 $M_\odot$ black hole. Solid curves show the spectrum emerging from the surface layer for each model. Dashed and dotted curves show the illuminating hard spectrum (a power-law of photon index 1.8) and the soft spectrum entering the surface layer from the disc below, respectively. From Ross & Fabian (1993).

the amount of absorbing column density: column densities above $\sigma_T^{-1} = 1.5\times10^{24}$ cm^{-2} (i.e. when the optical depth for Compton scattering equals unity) completely block the X-ray primary emission up to 10 keV or more and the source is classified as 'Compton-thick'. Column densities below this value (but still in excess of the Galactic one) produce a photoelectric cutoff at energies between 1 and 10 keV and in this case the object is classified as 'Compton-thin'. Otherwise, the source is completely unabsorbed and the spectrum unaltered. In Fig. 2.3 the emerging X-ray spectra for different absorbing column densities can be seen.

2.3.5 The reflection component

In Sect. refsubsec:um1 we described how, after the discovery of polarized broad lines in the optical spectra of NGC 1068 (Antonucci & Miller 1985; Miller &

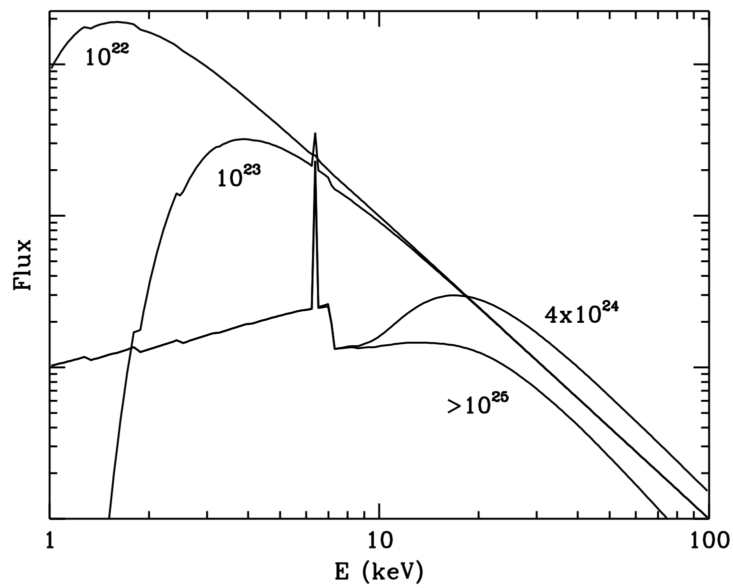

Figure 2.3: The X-ray spectrum of an obscured Seyfert Galaxy, for different column densities of the absorber, assumed to form a geometrically thick torus (from Matt, Guainazzi & Maiolino 2003).

Antonucci 1983), a torus was proposed as the most natural configuration for the circumnuclear absorber. If such torus is Compton-thick, it could be indirectly observed even if it does not intercept the line of sight. In fact, part of the nuclear radiation could hit the inner walls of the material and then be scattered towards the observer. The reprocessed spectrum should have the same shape as the Compton reflection component produced by the accretion disc. In Fig. 2.4 several reflection spectra are calculated as a function of the column density of the torus, from $2{\times}10^{22}$ cm^{-2} up to $2{\times}10^{25}$ cm^{-2}. However, as we will see in the next sections, both Compton-thin and Compton-thick absorbers can co-exist in the same source as already observed by several authors, e.g in NGC 1365 (Risaliti et al. 2005), NGC 6300 (Guainazzi 2002), UGC 4203 (Guainazzi et al. 2002) and NGC 5506 (Bianchi et al. 2003). Matt (2000) proposed a model where the torus is assumed always to be Compton-thick, while Compton-thin absorption comes from large

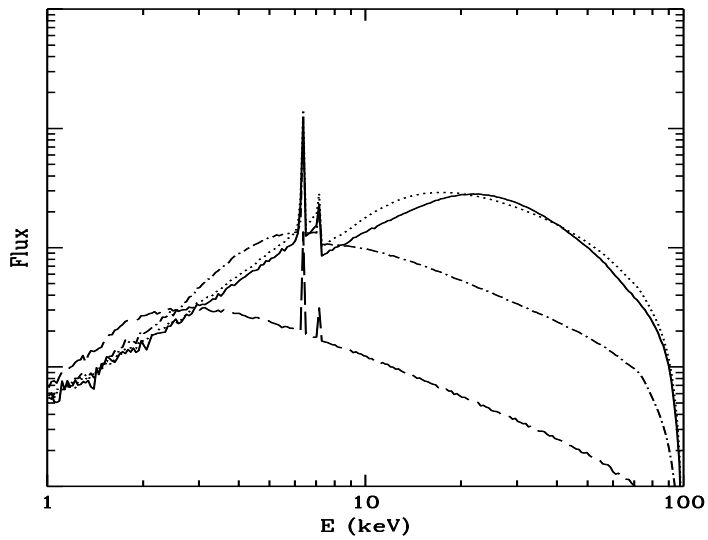

Figure 2.4: The reflection spectrum from the torus for different column densities: $2{\times}10^{22}$ cm^{-2} (dashed line), $2{\times}10^{23}$ cm^{-2} (dotted–dashed line), $2{\times}10^{24}$ cm^{-2} (dotted line), $2{\times}10^{25}$ cm^{-2} (solid line). The torus is assumed to be face-on, illuminated by a power law with photon index 2 and exponential cutoff at 100 keV (from Matt, Guainazzi & Maiolino 2003).

scale (hundred of parsecs) dust lanes, like the one observed with the HST by Malkan, Gorjian & Tam (1998).

2.4 The Iron Kα line emission

The optically thick material surrounding the central nucleus is also responsible for emission lines due to fluorescence. If an X-ray photon has an energy higher than the binding energy of the K-shell electrons of an ion, one of them can be expelled via photoelectric absorption. The vacancy is then filled by an electron from a different outer shell, with the release of a new photon, whose energy is equal to the difference between the two shells, or giving the same amount of energy to another electron (the so called ‘Auger effect’). If the electron came from the L-shell, the emitted photon is called Kα and the transition is that with the highest probability to occur; if the original shell was the M, the transition is called Kβ.

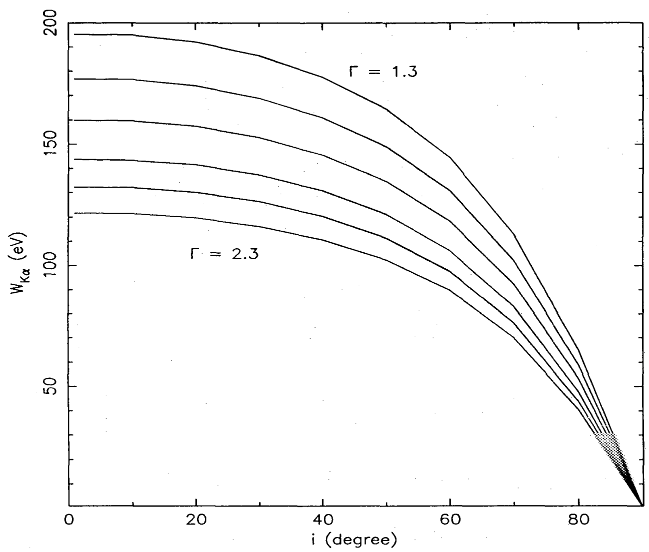

Figure 2.5: The EW of the iron line as a function of the inclination angle of the accretion disc, for incident power law photon index of (from the top) 1.3, 1.5, 1.7, 1.9, 2.1 and 2.3. The assumed geometry corresponds to R=1 (see George & Fabian 1991, for details).

Both transitions are doublets, because of spin-orbit coupling effects. The total probability that the de-excitation happens via the emission of a photon, whatever the transition, is called 'fluorescent yield', rising function of the atomic number Z (Bambynek et al. 1972). Iron is by far the most abundant among the heavy elements (e.g. Anders & Grevesse 1989), because it represents the final stage in thermonuclear fusion. Therefore, Kα iron lines are very prominent and crucial in a great variety of astrophysical sources.
The relevant energies for neutral iron are 6.391 and 6.404 keV for the Kα_1 and Kα_2 emission lines, respectively (Bearden 1967). The separation of these energies is smaller than the best energy resolution available in present X-ray satellites, it is then customary to adopt the value of 6.400 keV, as the mean weighted on the probability ratio 1:2 between the two transitions. Analogously, the weighted mean for the Kβ doublet is 7.058 keV (Bearden 1967).

2.4.1 The Equivalent Width

The Equivalent Width (EW) of an emission line is defined as:

$$\mathrm{EW} \equiv \int \frac{F_{\mathrm{L}}(E) - F_{\mathrm{C}}(E)}{F_{\mathrm{C}}(E)}\, dE \tag{2.26}$$

where F_L(E) is the observed flux of the line, while F_C(E) is the corresponding continuum level at the same wavelength. It strongly depends on the underlying continuum and therefore, for a given incident spectrum, it depends only on the physical properties of the material that produces the line. In several type 1 AGN the Iron Kα line is believed to be produced in the accretion disc. In the following we will briefly outline the main key parameters such as the geometry of the disc and the ionization structure of the emitting gas.
Let us assume a geometry with an accretion disc illuminated semi-isotropically from above: it is clear that when the material is seen edge-on the EW of the line is fainter than if it were face-on. The equation (from Ghisellini, Haardt & Matt 1994) that describes the dependence from the angle $\mu = \cos i$ between the normal to the reflecting surface and the line of sight can be written as :

$$EW(\mu) = \frac{EW_{\mu=1}}{\ln 2} \log\left(1 + \frac{1}{\mu}\right) \tag{2.27}$$

This is due to the different projected areas in the two cases and to the fact that, in the latter, the emitted photon would have lower probabilities to be absorbed and/or scattered again. If both the line and the Compton reflection component are produced by the same material, the EW of the iron line should correlate almost linearly with the amount of reflection, which is typically expressed in terms of the solid angle R=$\frac{\Omega}{2\pi}$ subtended by the reflector. In Fig. 2.5 the reader may find that, for a face-on disc with R=1, typical values for the iron line EW are about 150 eV, decreasing for larger angles and higher photon indexes. The ionization structure of a material can be described by the ionization parameter, which expresses the balance between the photoionization and the recombination rate:

$$\xi = \frac{4\pi F}{n} \tag{2.28}$$

where F is the incident flux and n the hydrogen number density. Matt, Fabian & Ross (1993, 1996) have performed detailed calculations on the reprocessed spectrum as a function of the ionization parameter of the reflecting material. For $\xi < 100$ erg cm s^{-1}, we are in the 'cold' reflection regime, with an Iron line at 6.4 keV. When $100 < \xi < 500$ erg cm s^{-1}, the available iron ions are FeXVII-FeXXIII. In this range the L-shell vacancy allows the resonant absorption of the Kα photons and the following de-excitation. The process of absorption and re-emission (the so called 'resonant scattering') will eventually end in a loss of the photon through the Auger effect, except for a very tiny fraction of the initial line flux. Therefore, the resulting EW is very weak. For $500 < \xi < 5000$ erg cm s^{-1}, iron is mainly FeXXV-FeXXVI: resonant scattering is still effective, but line photons are no longer lost, because the lack of L-shell electrons prevents the Auger effect to

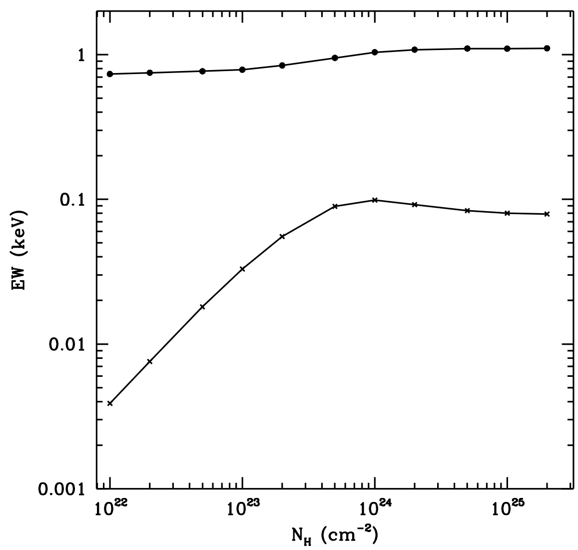

Figure 2.6: The EW of the iron line against the reflection continuum only (upper data) and the total continuum (lower data) as a function of the column density of a face-on torus (from Matt, Guainazzi & Maiolino 2003).

occur: strong lines at 6.68 and 6.97 keV are produced. In the end, when the value of the ionization parameter is even larger, iron ions are completely stripped and no line is expected.

All the above discussion is still valid if the iron line is produced by the torus instead of the disc, the main differences being in the relativistic effects which will be treated in section 2.4.2 for the standard accretion disc.

In heavily obscured sources ($N_H > 10^{24}$ cm^{-2}),where the primary continuum is completely absorbed well above the iron line energy, the EW of the Iron Kα line usually ranges between ~1-3 keV. In less obscured sources, it depends on the fraction of the intrinsic continuum emission absorbed at the line energy, for $N_H < 10^{24}$ cm^{-2}. It is useful to note that iron lines with EWs of about 100 eV are not necessarily produced by a Compton-thick material, as shown in figure 2.6, where values for Compton-thin matter are shown. The same figure display the expected EWs as calculated against the reflected continuum only, with values easily over-exceeding 1 keV.

A significant fraction of photons produced by the fluorescent emission of an iron Kα line can be Compton scattered once or more before escaping from the material where they are produced. This phenomenon has been widely studied in the past and it can be observed as a series of 'Compton Shoulders' on the red side of the line core (see Matt, Perola & Piro 1991; George & Fabian 1991; Leahy & Creighton 1993; Sunyaev & Churazov 1996). We refer the reader to Matt (2002), where the author extensively described the case of a single scattering, the first order Compton Shoulder, which is by far the strongest.

2.4.2 The profile of the Iron Line

The iron line profile is intrinsically narrow, apart from the natural thermal broadening (much lower than the resolution of X-ray instruments) and the Compton Shoulder described above. However, if it is produced in the accretion disc (as expected: see section 1.3.4), a number of effects contribute to forge a peculiar profile (see Fabian et al. 2000, for a review). Firstly, the line is broadened because of the rotation velocity of the accretion disc. Each radius produces a double-horned line profile, with the blue peak due to the region approaching the observer, the red one to that receding (first panel in figure 2.7). The effect is clearly higher for the inner radii of the disc, whose rotational velocities are larger. Since these velocities reach easily relativistic values, the blue peaks are beamed and thus enhanced with respect to the red ones. Moreover, the transverse Doppler effect also becomes important, shifting the overall profile to lower energies (second panel in figure 2.7). A comparable effect is due to gravitational redshift, as shown in the third panel of figure 2.7. The resulting profile is a good diagnostic tool both for the accretion disc and the central black hole's properties. First of all, it is very sensitive to the inclination angle of the disc with respect to the line of sight. When the disc is face-on, only transverse Doppler and gravitational redshift effect are clearly present, because there is no region of the disc which is actually moving in the direction of the line of sight. As the inclination angle rises, so do the velocity component along the line of sight of the approaching and receding regions of the disc, thus increasing the separation between the two peaks in the overall profile (see figure 2.8).

2.5 Ionized absorption

Very little is known about the flow patterns of gas in the innermost regions of AGN. Probing the gas kinematics (velocities) and dynamics (accelerations) around black holes is a fundamental to understand the geometry of the circumnuclear regions and the energy generation mechanism. Warm absorbers are an important diagnostic of the physical conditions within the central regions of active galaxies. For more detailed reviews on this topic we refer the reader to Komossa (2000),

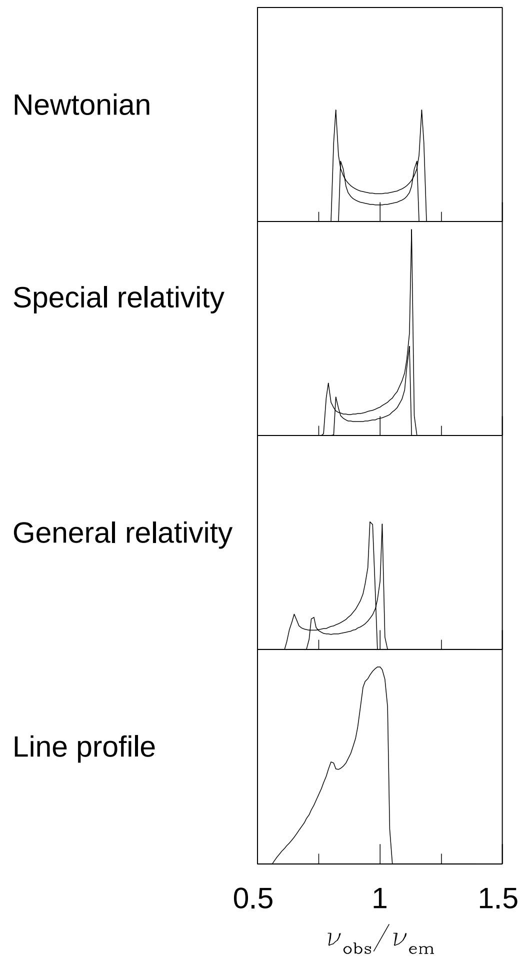

Figure 2.7: All the individual effects that contribute to forge the characteristic double-horned relativistic line (from Fabian et al. 2000)

Blustin et al. (2005) and Cappi (2006). The study of the ionized material provides a wealth of information about the nature of the warm absorber itself, its relation to other components of the active nucleus, and the intrinsic AGN X-ray spectral shape. Concerning the nature and location of the warm absorber, several different models have been suggested: (i) a relation of the WA to the BLR (a high-density component of the inner BLR, a BLR confining medium, winds from bloated stars, or a matter bounded BLR component; see Reynolds et al. 1995), (ii) an accretion disc wind (e.g. Konigl & Kartje 1994), (iii) a relation to the torus (e.g. Reynolds et al. 1997), or (iv) a relation to the NLR (see, e.g., the two-component WA model of Otani et al. 1996). The reason for the large variety of models discussed is that not all physical properties of the warm absorber (its density *n*, column density

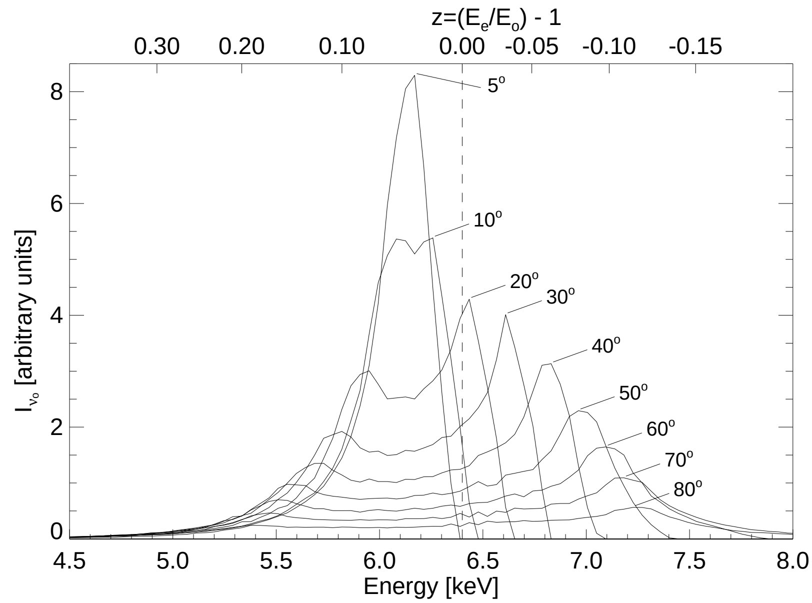

Figure 2.8: Iron line profiles as a function of the inclination angle of the accretion disc. The BH is assumed rapidly rotating (a=0.998) and the adopted line emissivity index is $\beta = 0.5$, with the disc extending from the last stable orbit (1.23 r_g) to 50 r_g (from Reynolds & Nowak 2003).

N_w, covering factor $\eta = \omega/4\pi$, distance r from the nucleus, elemental abundances Z, its velocity field, and the shape of the illuminating continuum) can be directly determined from X-ray spectral fits, but only certain combinations of these parameters.
About half of the X-ray spectra of local bright Seyfert galaxies show evidence of a warm absorber with column densities in the range $10^{22} - 10^{24}$ cm^{-2} (e.g Reynolds 1997). High-resolution grating observations performed with XMM-Newton and Chandra have shown that the warm absorber has a typical temperature of $\sim 10^6$ K and, in some cases, outflowing velocities of a few times 10^3 km s^{-1} (Krongold et al. 2003). The presence of narrow blue-shifted absorption lines at rest-frame energies higher than 7 keV in the spectra of a number of radio-quiet AGN are commonly identified with FeXXV and/or FeXXVI K-shell resonant absorption from a highly ionized zone of circumnuclear gas ($\log\xi \simeq 3 - 6$ erg s^{-1} cm). The blue-shifted velocities of the lines are also often quite large, reaching mildly relativistic values, up to $\sim 0.2 - 0.4$c and in some cases showing short term variability (Cappi et al. 2009). Very recently, X-ray evidence for ultra-fast outflows (UFOs), with blue-shifted velocities v$\geq 10^4$ km s^{-1} ($\simeq$0.033c), has been recently reported in a number of local AGN (Tombesi et al. 2010, 2011). The detection of these

UFOs is consistent with the observation of fast outflows in different classes of AGNs also in other wavebands, from the relativistic jets in radio-loud AGNs to the broad-absorption lines (BAL) in the UV and X-ray spectra of distant quasars (e.g Chartas, Brandt & Gallagher 2003).

2.6 Soft X-ray emission in obscured sources

A soft X-ray excess above the extrapolation of the absorbed nuclear emission is very common in nearby X-ray obscured AGN (Guainazzi, Matt & Perola 2005; Turner et al. 1997). High resolution spectroscopy of soft X-ray emission in obscured AGN reveals that it is dominated by strong emission lines. In fact, X-ray spectra of many obscured AGN exhibit strong emission lines in the soft X-ray band (0.5-3 keV), the so called 'soft excess'[5], due to the ubiquitous presence of warm gas surrounding the central nucleus. Emission from circumnuclear regions is much easier to observe in Seyfert 2s (and in particular in Compton-thick ones), where the nuclear radiation is obscured, than in unobscured Seyfert 1s, in which these components are heavily diluted by the photons from the nucleus.

Thanks to the unprecedented sensitivity and energy resolution of the grating detectors on-board Chandra and XMM-Newton, it is now possible for the first time to perform true spectroscopy of the reprocessed emission. Soft X-ray spectra in obscured AGN are dominated by He- and H-like transitions of metals from carbon to nitrogen, as well as by L-shell transitions from FeXVII to FeXXI (Sako et al., 2000, Sambruna et al., 2001 and Kinkhabwala et al., 2002). The detection of narrow radiative recombination continua (Liedahl et al., 1985) features, the large intensity ratio between the forbidden component of the OVII Ly-α triplet and the OVIII Ly-α, and the large integrated line luminosity ($L \geq 10^{40} ergs^{-1}$) indicate again that the AGN radiation field is the most likely culprit for the gas ionization balance (Guainazzi and Bianchi, 2007). This conclusion can be achieved only through measurements at the highest possible spectral resolution currently available.

The soft X-ray spectrum of Compton-thick Seyfert 2s had to await the high resolution spectrometers aboard XMM-Newton and Chandra to reveal its real nature, at least in the three brightest sources, where such an experiment was possible: NGC 1068 (Kinkhabwala et al. 2002; Brinkman A.C. et al. 2002; Ogle et al. 2003), Circinus (Sambruna et al. 2001b) and Mrk3 (Sako et al. 2000; Bianchi et al. 2005; Pounds K.A. & Page K.L. 2005).
The spectrum of the Seyfert 2 galaxy, NGC 1068, is shown in Fig. 2.9 at different energy-resolutions: in the bottom panel the spectrum taken with the moder-

[5]Despite the same name, this component has nothing to do with the 'soft excess' described in Sect. 2.3.3, which cannot be observed in obscured AGN

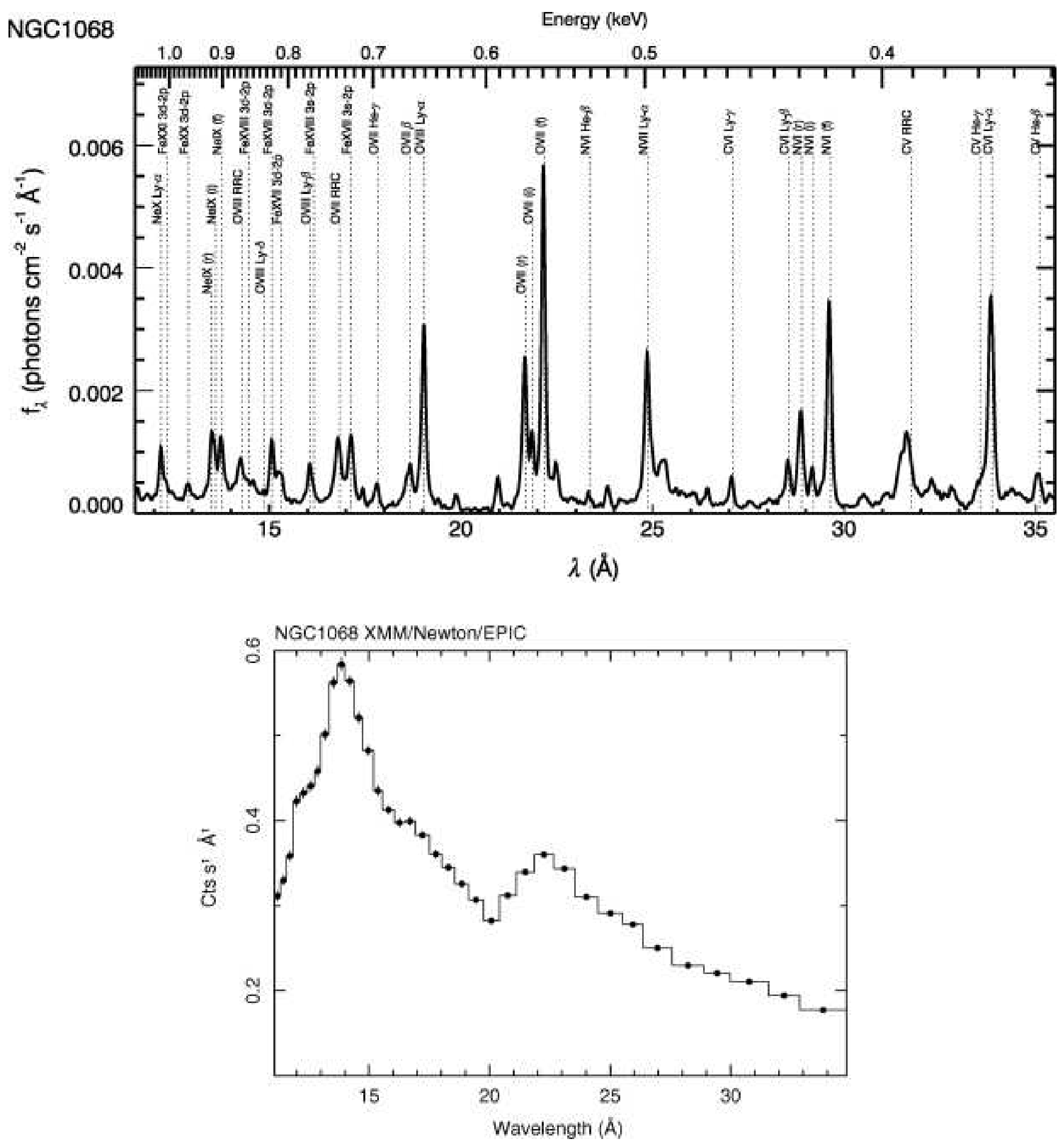

Figure 2.9: *The spectrum of the archetypal Seyfert 2 galaxies NGC 1068 at different energy-resolutions: in the* top panel *the spectrum (fluxed) taken with the high-resolution RGS cameras (E/ΔE ∼300; (der Herder et al., 2001)) and in the* bottom panel *the spectrum taken with the moderate energy-resolution (E/ΔE ∼15 (Struder et al., 2001) European Photon Imaging Camera (EPIC).*

ate energy-resolution (E/ΔE ∼15 (Struder et al., 2001) European Photon Imaging Camera (EPIC), and in the top panel the high-resolution RGS cameras (E/ΔE ∼300; (der Herder et al., 2001)). Despite the much larger collecting area, line features are irremediably blurred in the former. Indeed, the CCD, low-resolution soft X-rays spectra of NGC 1068 can be equally well fit by different scenarios (Turner et al., 1997 and Guainazzi et al., 1999), some of them totally ruled out by the high-resolution spectroscopic measurements (Brinkman et al., 2002).

The same three sources revealed that their soft X-ray emission was actually extended on hundreds of parsec, thus being clearly produced in a gas well beyond the torus (Young, Wilson & Shopbell 2001; Sambruna et al. 2001a; Sako et al. 2000). Moreover, the dimension and morphology of this emission closely resemble that of NLR, as mapped by the *[OIII]* λ 5007 emission line. These arguments, together with the fact that the NLR is also generally believed to be mainly constituted of gas photoionized by the nuclear continuum, led Bianchi, Guainazzi & Chiaberge (2006) to analyze the connection between soft X-ray emission and NLR. They selected a sample of 8 Seyfert 2 galaxies with extended *[OIII]* emission in their *HST* images, which were also observed by *Chandra*. They showed that all of them present a soft X-ray emission with extension and morphology highly correlated with that of the NLR. Figure 2.10 shows contours of the *Chandra* soft X-ray emission superimposed on the *HST [OIII]* images for 4 sources of their sample. Moreover, as said above, the most likely origin for this emission is from a photoionized gas and therefore they tested with the code `CLOUDY`[6] a simple scenario where the same gas photoionized by the nuclear continuum produces both the soft X-ray and the *[OIII]* emission. Solutions satisfying the observed ratio between the two components exist, and require the density to decrease with radius roughly like r^{-2}, similarly to what often found in the optical NLR.

Despite the important progress made possible by recent measurements with Chandra and XMM-Newton, the origin of the soft X-ray emission in obscured AGN is still unclear. Our understanding of the evolution of accretion onto supermassive black holes, and of its interaction with gas and stars in the dense nuclear environment would receive a burst by the knowledge of the origin of the soft X-ray emission.

In this scenario, Guainazzi & Bianchi (2007) produced CIELO-AGN (*Catalog of Ionized Emission Lines in Obscured AGN*) the first catalogue of soft X-ray emission lines in a sample of 69 sources which includes all the type ≥1.5 AGN (according to the NED optical classification) observed with the Reflection Grating Spectrometer (RGS) on board XMM-Newton, and whose data were public as of

[6]CLOUDY is a large-scale spectral synthesis code designed to simulate fully physical conditions within an astronomical plasma and then predict the emitted spectrum. See Ferland et al. 1998 et al. (1998) for details

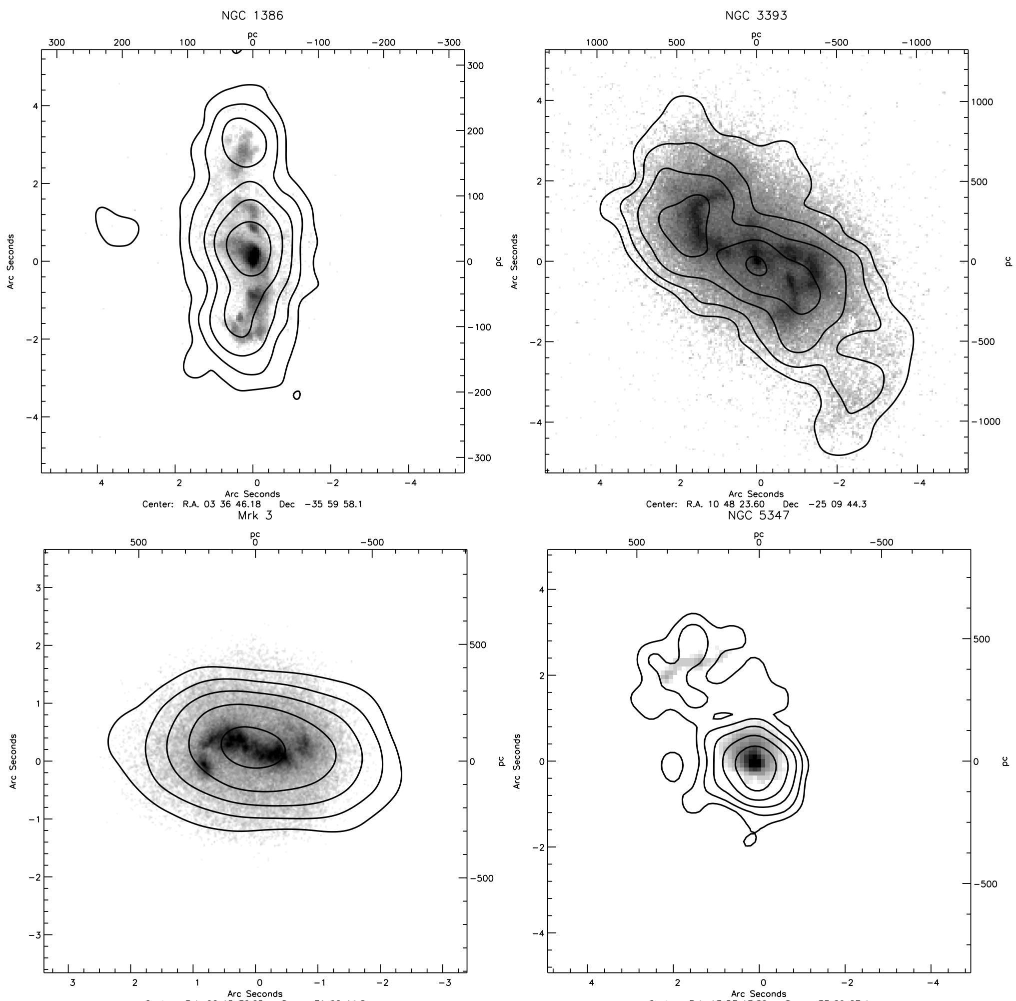

Figure 2.10: Soft X-ray (0.2-2 keV) ACIS/Chandra images of four obscured AGN in the Bianchi, Guainazzi & Chiaberge (2006) sample (contours), superposed to the HST/WFC2 O[III] filter images (greyscale).The contours correspond to five logarithmic intervals in the range of 1.5-50% (NGC 1386), 5-80% (Mrk 3), 5-90% (NGC 3393), and 2-50% (NGC 5347) of the peak flux.

September 2006.

Their analysis confirmed the dominance of emission lines over the continuum in the soft X-ray band of these sources, the presence of narrow Radiative Recombination Continua (RRC) and the important contribution from higher-order series lines (see Figure 2.11 and Figure 2.12).

In fact, they detected narrow RRC features from Carbon and Oxygen in 36% (25/69) of the objects of their sample and in 29% (26%) of the objects in their sample the RRC width is constrained to be lower than 50 (10) eV (Figure 2.11). The width of these features indicates typical plasma temperatures of the order of a few eV Kinkhabwala et al. (2002). These features are unequivocal signatures of photoionized spectra (Liedahl & Paerels 1996).

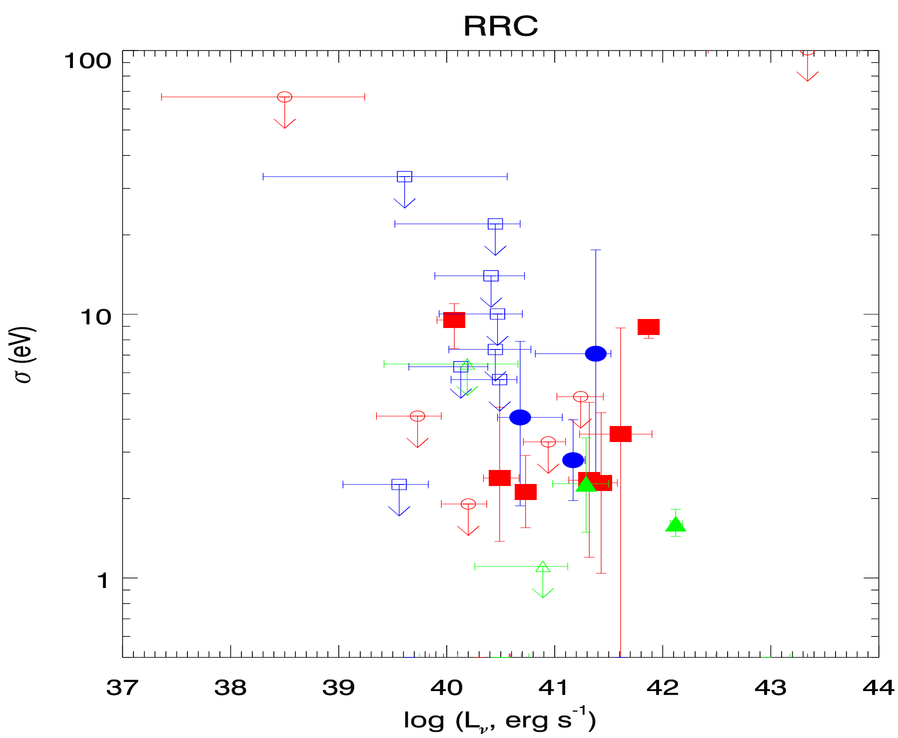

Figure 2.11: Luminosity versus intrinsic width for the RRC features detected in CIELO. *Filled* data points correspond to a measurement of the RRC width; *empty* data points correspond to RRC width upper limits. *Circles*: OVIII; *squares*: OVII; *triangles*: CV. Data points corresponding to upper limits on both quantities are not shown for clarity. Taken from Guainazzi & Bianchi (2007).

Another hint for photoionization is the prominence of the OVII forbidden line. In principle, diagnostics on the OVII triplet may be a good indicator of the ionization mechanism of the gas. Indeed, the predominance of the forbidden component is a sign of photoionization, and the significant detection of the resonant transition a hint that pure recombination is not the only mechanism to produce the emission lines, but photoexcitation has also an important role. In Fig. 2.12 we show the *CIELO* experimental results for the intensity of the O VII He-β against the f component of the O VII He-α triplet with the predictions of pure photoionization, and with models where radiative decay from photoexcitation and recombination from photoionization are self-consistently calculated (model `photoion`; Kinkhabwala et al. (2002)).

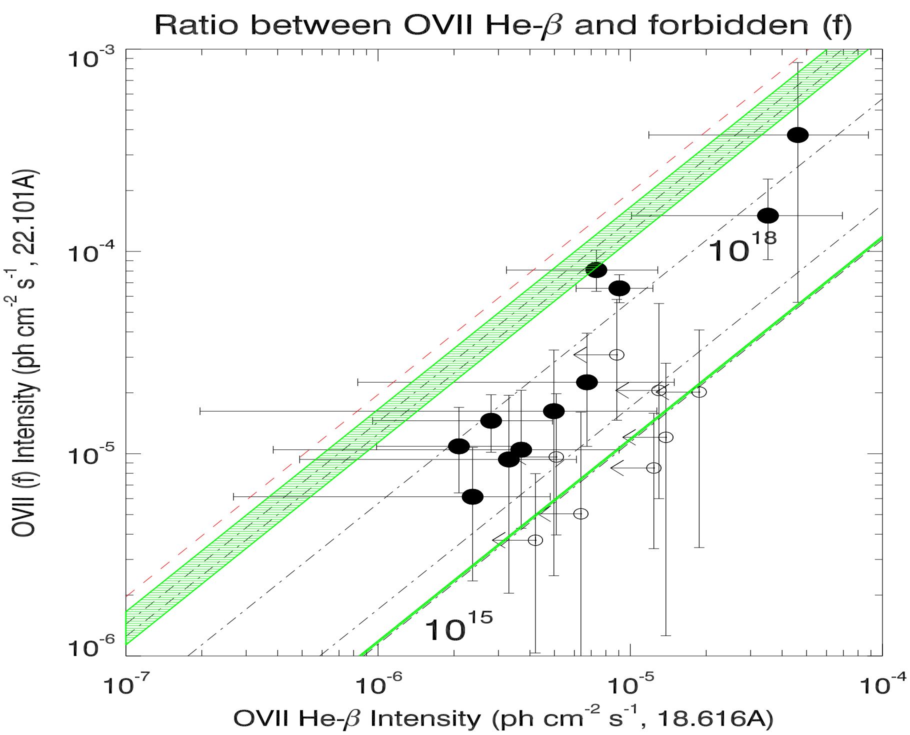

Figure 2.12: Intensity of O VII He-β line against the intensity of the f component of the He-α triplet in CIELO (only data points corresponding to a detection of the latter are shown; data points correspond to upper limits on the intensity of the former are shown as *empty symbols*). The *dashed-dotted lines* represent the prediction of the `photoion` code for O VII column densities increasing from $N_{OVII} = 10^{15}$ to 10^{20} cm^{-2} in steps of one decade, assuming $kT = 5$ eV and $v_{turb} = 200$ km s^{-1}. The *long-dashed line* represents the predictions for pure photoionization. The *shaded areas* represent the locii of the `photoion` predictions, when the turbulent velocity varies in the range 0–500 km s^{-1} at constant temperature and for the extreme values of the column density interval. The areas representing a variation of the temperature in the range 1–20 keV at constant velocity and column density are comparatively smaller, and therefore not shown. Taken from Guainazzi & Bianchi (2007).

The Guainazzi & Bianchi (2007) results support the scenario, whereby the active nucleus is responsible for the X-ray “soft excess” almost ubiquitously observed in nearby obscured AGN via photoionization of circumnuclear gas. They confirm on a statistical basis the conclusions drawn from the detailed study of the brightest spectra in CIELO sample.

Despite the results of CIELO, there are still many open issues related to the X-ray properties of these objects. High-resolution X-ray spectroscopy is crucial to the solution of this issue.

Chapter 3

CAIXA-A: a systematic analysis of high-resolution soft X-ray spectra of obscured AGN

A soft X-ray excess above the extrapolation of the absorbed nuclear emission is very common in nearby X-ray obscured AGN (Guainazzi, Matt & Perola 2005; Turner et al. 1997). As mentioned in Chapter 2, high resolution spectroscopy of soft X-ray emission in obscured AGN reveals that it is dominated by strong emission lines. The common spatial coincidence between the soft X-ray emission and the optical NLR suggests they can be one and the same medium, photoionized by the central AGN. However, there are still many open issues about the exact nature of this soft excess: the most effective way to address these questions is to analyze large numbers of AGN with good-quality X-ray spectra and to perform statistical studies, taking into account data in other wavelengths and other basic properties of the objects.

The European Space Agency's (ESA) X-ray Multi-Mirror Mission (XMM-*Newton*) was launched on December 10th 1999 (an overview of the *XMM-Newton* spacecraft and on board instruments can be consulted in Appendix A). The XMM-*Newton* public archive has since become the repository of an enormous amount of high-quality X-ray data and a precious legacy for future missions. In particular, our knowledge of the physics of AGN has dramatically improved thanks to the large sensitivity of the European Photon Imaging Camera (EPIC) pn charge-coupled device (CCD) arrays. At this time, a systematic and homogeneous study of the EPIC pn spectra of AGN represents a necessary step to fully take advantage of this highly successful X-ray mission. Moreover the Reflection Grating Spectrometer (RGS) on board XMM-Newton (den Herder et al. 2001) is the most suitable instrument currently flying for a systematic high-resolution X-ray spectroscopic study on a sizable sample of obscured AGN and then for the study of

the soft excess, due to its unprecedented effective area in the 0.2-2 keV band, as well as its good absolute aspect solution accuracy ($\simeq 8\ m$Å).
In this scenario, Guainazzi & Bianchi (2007) collected a sample of 69 nearby obscured AGN observed with the RGS on board XMM-Newton. The results of their research have been compiled into CIELO-AGN (*Catalog of Ionized Emission Lines in Obscured AGN*). CIELO-AGN comprises all the type ≥1.5 AGN (according to the NED optical classification) observed by XMM-Newton, and whose data were public as of September 2006. Their results support the scenario, whereby the active nucleus is responsible for the X-ray "soft excess" almost ubiquitously observed in nearby obscured AGN via photoionization of circumnuclear gas. They confirm on a statistical basis the conclusions drawn from the detailed study of the brightest spectra in the CIELO sample (see section 2.6 for more details on their results). The limitation of the CIELO approach lies in the fact that it has been used an optical selection and not an X-ray selection. As we shall see further below the optical classification does not match perfectly with the X-ray classification (see section 1.2).
With the aim to analyze large numbers of AGN with good-quality X-ray spectra and to perform statistical studies, Bianchi et al. (2009) published CAIXA, a Catalogue of AGN In the XMM-*Newton* Archive. CAIXA consists of all the radio-quiet X-ray unobscured ($\mathrm{N_H} < 2 \times 10^{22}$ cm^{-2}) AGN observed by XMM-*Newton* in targeted observations, whose data are public as of March 2007.
In this thesis, we have built the complementary catalogue of CAIXA: CAIXA-A, a Catalogue of AGN In the XMM-*Newton* Archive - Absorbed. CAIXA-A consists of all the radio-quiet, X-ray obscured ($\mathrm{N_H} > 2\times10^{22}$ cm^{-2}) AGN observed by XMM-Newton in targeted observations, whose data were public as of November 22, 2011. With its 109 sources, this is the largest catalog of high signal-to-noise X-ray spectra of obscured AGN. All the EPIC pn spectra and all the RGS spectra of the sources in CAIXA-A were extracted homogeneously, and a baseline model was applied in order to derive their basic X-ray properties. In this chapter, we describe the homogeneous spectral analysis of the X-ray data in CAIXA-A and present all the results derived by applying to the RGS spectra different methods of analysis.

To investigate the soft X-ray excess of obscured AGN, we need sources where the RGS band is not dominated by the primary continuum and the soft excess component can be modelled properly. Since recently quite a few studies have claimed the existence of objects for which optical and X-ray classifications do not match (see Sect. 1.2), we selected objects with $N_H > 2 \times 10^{22} cm^{-2}$, therefore relying on the X-ray rather than the optical classification. So, our selection criterion is based on the value of N_H. To calculate an accurate column density we need enough counts and a broad band: we selected our sources by analyzing the 0.5-10 keV EPIC pn spectra of all the AGN observed by XMM-Newton in targeted observations, whose data were public as of November 22, 2011, in order to derive their column densities N_H. To analyze the soft excess we need a very good spectral resolution coupled with a large effective area in the 0.2-2 keV band, so the RGS is the most suitable instrument (the Chandra High Energy Transmission Grating Spectrometer have better spectral resolution but lower effective area, see Appendix A: Fig. A.3).

3.1 The sample

As an update to the parent CAIXA sample, we performed a search for all AGN observations in the XMM-Newton Science Archive (XSA), whose data were public as of November 22, 2011 (16:00:00 UTC). All quasars nominally radio-loud were excluded from the list. For all the source in this list we searched the NASA/IPAC Extragalactic Database (NED) for published redshifts. All the sources with no measured redshift known prior to November 22, 2011 were excluded from the list. EPIC pn spectra with less than 200 (background-subtracted) counts in either of the (rest-frame) bands of 0.5-2 and 2-10 keV were rejected, because they do not possess enough independent bins to be fitted with our models (see Appendix B for an introduction to X-ray data analysis).

EPIC pn (Strüder et al. 2001) data were reprocessed, with SASv11. For the observations performed in Small Window mode, background spectra were generated using blank-field event lists, according to the procedure presented in Read & Ponman (2003). In all other cases, background spectra were extracted from source-free regions close to the target in the observation event file.

Source extraction radii and screening for intervals of flaring particle background were performed via an iterative process which leads to a maximization of the signal-to-noise ratio, similarly to what described in Piconcelli et al. (2004). Spectra were binned in order to oversample the intrinsic instrumental energy resolution by a factor not lower than 3, and to have spectral bins with at least 25 background-subtracted counts. This ensures the applicability of the χ^2 statistics.

All spectra were analyzed with XSPEC 12.8.0m. The cosmological parameters used throughout this paper are $H_0 = 70$ km s^{-1} Mpc^{-1}, $\Omega_\Lambda = 0.73$ and $\Omega_m = 0.23$ (i.e. the default ones in XSPEC 12.8.0m).

Our purpose is to select objects with $N_H > 2 \times 10^{22} cm^{-2}$, so that the RGS band is not dominated by the primary continuum and the soft excess component can be modelled properly. To do this we applied two different models to the pn spectra. The first kind of fit is with a single powerlaw:

$$F(E) = e^{-\sigma(E) N_H^G} \left[A e^{-\sigma(E) N_H^h} E^{-\Gamma_h} + 3 \times G \right] \tag{3.1}$$

and the second kind of fit is with two powerlaws:

$$F(E) = e^{-\sigma(E)N_H^G}\left[Ae^{-\sigma(E)N_H^s}E^{-\Gamma_s} + Be^{-\sigma(E)N_H^h}E^{-\Gamma_h} + 3\times G\right] \tag{3.2}$$

where $\sigma(E)$ is the photoelectric cross-section, adopting solar abundances as in Anderson & Ebihara (1982), N_H^G is the Galactic column density appropriate for each line of sight (after Dickey & Lockman 1990), $N_H^s < N_H^h$ are two local column densities at the redshift of the source, possibly coexisting if related to absorption on different scales, A and B are two normalization factors, Γ_s and Γ_h the spectral photon indexes for the soft an the hard spectrum, and G are three Gaussian emission lines at rest-frame energies fixed to 6.4, 6.7 and 6.96 keV, as appropriate for neutral, He- and H-like iron Kα, respectively.

We found three broad classes of sources: unobscured sources ($N_H < 2\times 10^{22}cm^{-2}$), obscured Compton-thin sources ($2\times 10^{22}cm^{-2} < N_H < 10^{24}cm^{-2}$) and obscured Compton-thick sources ($N_H \geq 10^{24}cm^{-2}$).

The main problem for the unobscured sources (Fig. 3.1*top*) is represented by significant residuals in the soft X-ray part of the spectrum, where the effects of absorption from ionized matter is not taken into account by our models. The lack of a proper modeling of warm absorbers in our model is dictated by the complexity of these components, which do not allow an automatic handling. However, we checked that the lack of a modelling of the warm absorption does not affect the measure of the cold column density, which is the main parameter used for the selection procedure. The addition of a second powerlaw is generally required by the fit as we can see in Fig. 3.1(*Bottom*), but there is no trace of cold absorption with $N_H > 2\times 10^{22}cm^{-2}$. In any case, residuals due to warm absorbers are still present.

Instead for the obscured Compton-thin sources ($2\times10^{22}cm^{-2} < N_H < 10^{24}cm^{-2}$) the residuals in the soft X-ray part of the spectrum represent the soft excess under investigation in this work (Fig. 3.2*top*). The addition of a second powerlaw is strongly required by the fit. In Fig. 3.2(*Bottom*) we show the double powerlaw model for IC4518A. In this case, the addition of a second powerlaw significantly improves the quality of the fit and the soft excess is modeled with a simple powerlaw, even if there are still residuals due to the most intense emission lines. The residuals in the hard band are an indication of the presence of a Compton reflection continuum, which is not included in our simple models.

Finally there are the Compton-thick sources ($N_H \geq 10^{24}cm^{-2}$). An example is shown in Fig. 3.3*Top*. The fit is clearly bad, also with the addition of a second powerlaw (as shown in Fig. 3.3*Bottom*) with several features in the 0.5–1 keV band and a very prominent iron K_α fluorescent line. Even if the best fit value for the local column density is less than $2\times 10^{22}cm^{-2}$, in these sources the spectral photon index for the hard spectrum is very flat. This photon index value suggests

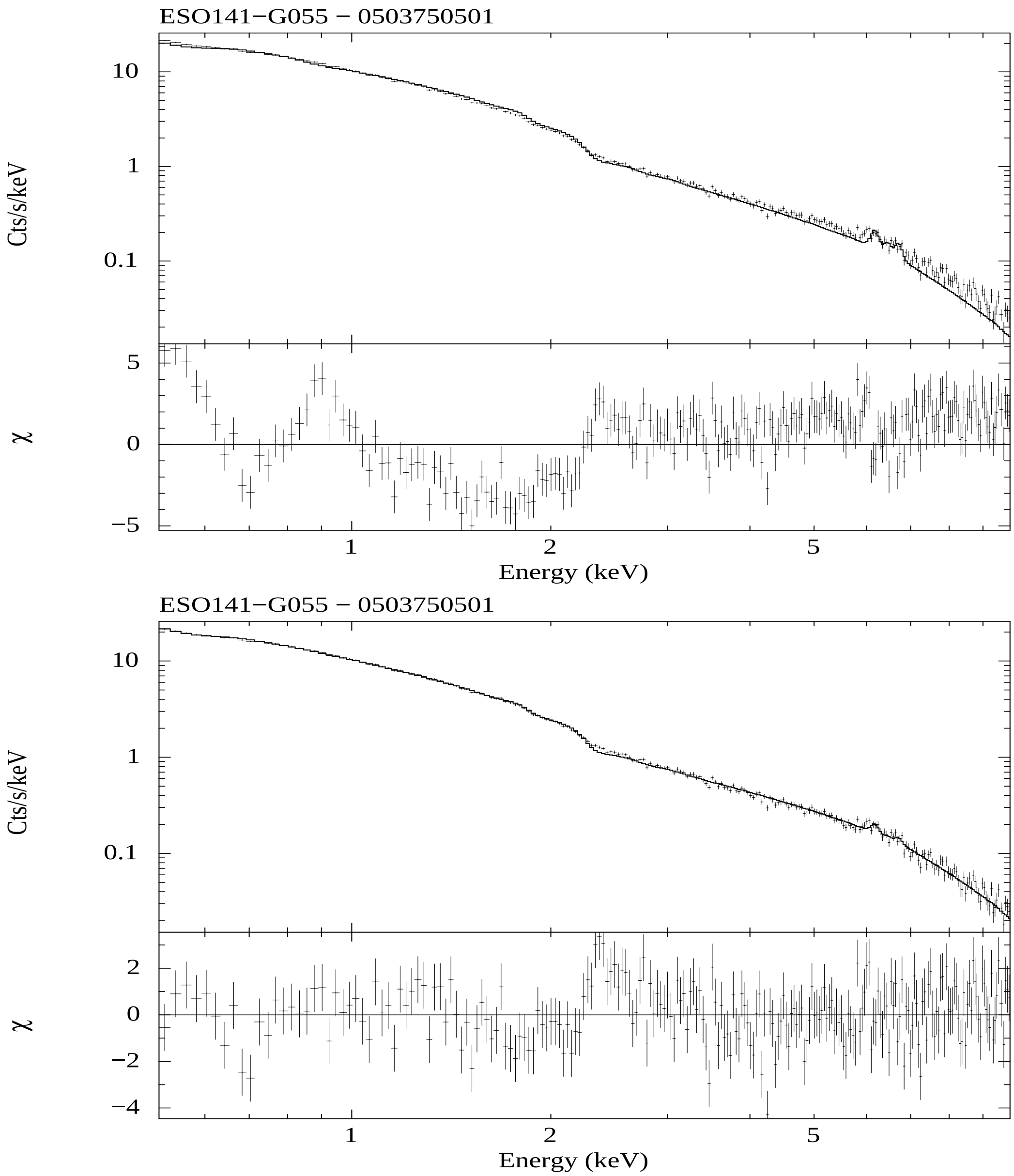

Figure 3.1: *Best fit data and model (*Top: *single powerlaw;* Bottom: *double powerlaw) for ESO141-G055, an unobscured ($N_H < 2 \times 10^{22} cm^{-2}$) source. The residuals at low energy are due to the warm absorbers.*

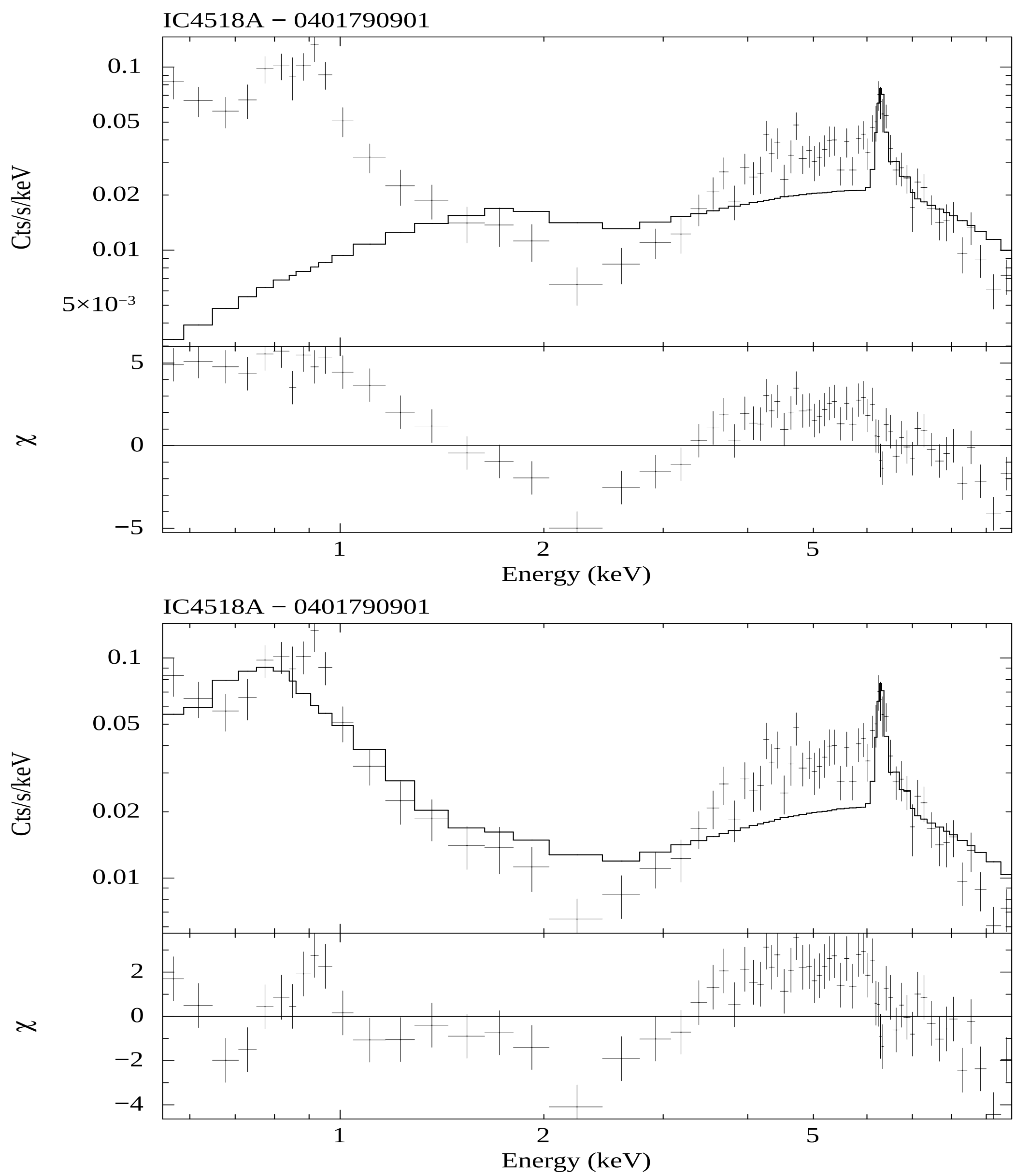

Figure 3.2: *Best fit data and model (*Top: *single powerlaw;* Bottom: *double powerlaw) for IC4518A: an obscured ($N_H > 2 \times 10^{22} cm^{-2}$, Compton-thin) source.* Top: *The excess at low energy is the soft excess.* Bottom: *In this case, the soft excess is modeled with a simple powerlaw, but there are still residuals due to the most intense emission lines.*

a reflection-dominated spectrum, the primary continuum being suppressed by a significant ($N_H > 10^{24} cm^{-2}$) absorption.

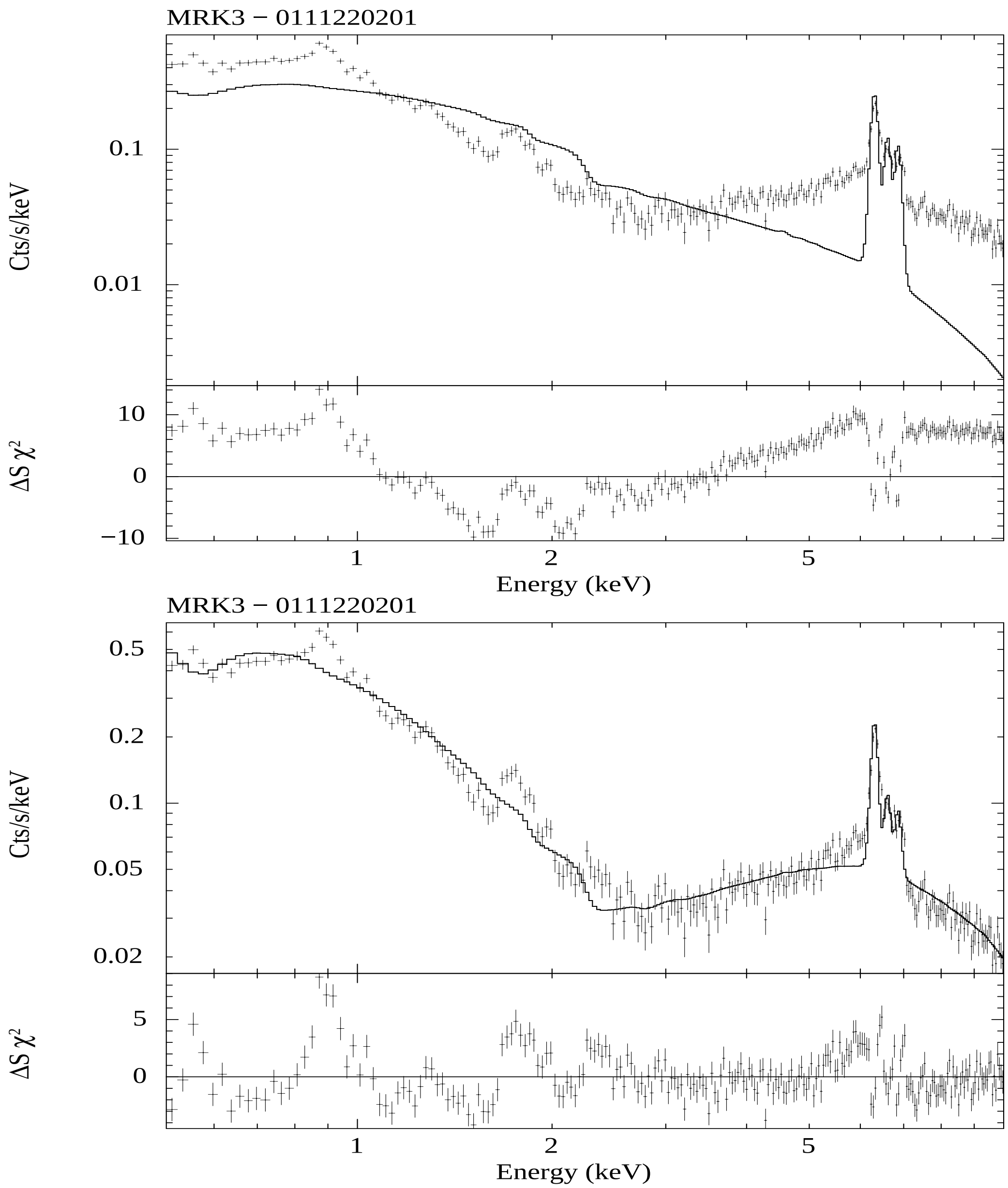

Figure 3.3: *Best fit data and model (*Top: *single powerlaw;* Bottom: *double powerlaw) for MRK3: an obscured Compton-thick sources ($N_H \geq 10^{24} cm^{-2}$). The excess at low energy is the soft excess.*

After the fitting procedure, we selected all the sources with $N_H > 2 \times 10^{22} cm^{-2}$ (measured in the 2-10 keV band) in at least one of the two models or that have a flat Γ_h in the second model ("Compton thick" sources) and/or that have a large EW of the neutral iron K_α. All sources with a local column density less than $2 \times 10^{22} cm^{-2}$ were instead excluded from the catalogue. An inspection by eye of all the spectra was eventually performed in order to remove any possible error introduced by automatic fitting and selection procedure presented above.

At the end of this selection procedure, the total catalogue comprises 171 observations of 109 radio-quiet X-ray obscured AGN. Therefore, CAIXA-A, the "Catalog of AGN In the XMM-Newton Archive - Absorbed " consists of all the radio-quiet, X-ray obscured ($N_H > 2 \times 10^{22} cm^{-2}$) AGN with known redshift observed by XMM-Newton, whose data were public as of November 22, 2011 and with more than 200 EPIC pn (background-subtracted) counts in either of the (rest-frame) bands of 0.5-2 and 2-10 keV.

Tab. 3.1 shows the list of sources in the sample, together with their right ascension and declination, redshift, XMM-Newton obsid and exposure time.

Table 3.1: XMM-Newton observations of CAIXA-A sources: right ascension and declination, redshift, XMM-Newton obsid, exposure time.

RA	DEC	SOURCE	z	XMM obsid	exposure time (ks)
49.5791	68.4921	2MASXJ03181899+6829322	0.0901	0312190501	6.40
59.2356	-40.696	2MASXJ03565655-4041453	0.0748	0551950601	7.93
114.936	-31.7174	2MASXJ07394469-3143024	0.0258	0501210201	29.12
126.18	29.9899	2MASXJ08244333+2959238	0.0253	0504102001	19.01
189.681	9.46018	2MASXJ12384342+0927362	0.0829	0504100601	17.44
180.241	6.80642	CGCG041-020	0.036045	0312191701	9.69
213.291	-65.3392	CIRCINUS	0.0014	0111240101	91.31
279.585	-65.4276	ESO103-G35	0.0133	0109130601	9.16
281.934	-63.157	ESO104-G11	0.0151	0405380501	26.73
248.809	-58.08	ESO137-G34	0.009	0307001901	17.38
252.834	-59.2348	ESO138-G01	0.00914	0405380201	15.64
				0405380901	11.10
87.1092	-47.7642	ESO205-3	0.0505	0554500301	34.38
196.609	-40.4146	ESO323-G077	0.015	0300240501	23.83
79.8992	-32.6578	ESO362-G018	0.013	0312190701	8.89
203.359	-34.0148	ESO383-G18	0.013	0307000901	12.06
44.0898	-32.1856	ESO417-G006	0.016291	0602560201	6.34
13.484	-70.6345	F00521-7054	0.0689	0301151601	10.33
119.5	39.3414	FBQSJ075800.0+392029	0.0960	0305990101	10.17
				0406740101	11.28
89.5083	-38.3346	H0557-385	0.0339	0404260101	24.53
				0404260301	52.64
43.9676	9.31183	IC1867	0.025728	0203610501	17.15
154.078	-33.5638	IC2560	0.0098	0203890101	71.95
224.422	-43.1321	IC4518A	0.0163	0401790901	8.81
1.00817	70.3217	IGRJ00040+7020	0.0960	0550450101	17.95
160.094	-46.4238	IGRJ10404-4625	0.0239	0401791201	10.47

180.698	-53.8355	IGRJ12026-5349	0.027966	0601740601	25.43
296.831	44.8284	IGRJ19473+4452	0.0539	0550451901	13.88
27.5112	-7.43013	IRAS01475-0740	0.0177	0200431101	8.95
73.3573	4.06158	IRAS04507+0358	0.030	0307000401	12.71
80.2558	-25.3626	IRAS05189-2524	0.042	0085640101	7.89
81.0271	-12.1666	IRAS05218-1212	0.049	0551950401	11.26
139.039	-62.3248	IRAS09149-6206	0.0573	0550452601	13.61
200.602	-16.7285	IRAS13197-1627	0.017	0206580101	38.33
237.673	-3.88843	IRAS15480-0344	0.0303	0600690201	42.19
279.243	-59.4024	IRAS18325-5926	0.0202	0022940101	3.51
45.1277	-11.4157	IRASF02581-1136	0.0300	0301150201	18.95
182.684	38.3362	KUG1208+386	0.0228	0601780901	8.79
28.2042	-3.44683	MCG-01-05-047	0.017197	0602560101	11.20
140.193	-8.05614	MCG-1-24-12	0.0196	0307000501	8.22
342.405	-19.274	MCG-3-58-7	0.031	0301150301	11.80
194.059	56.8737	MKN231	0.041	0081340201	17.02
162.379	22.9646	MKN417	0.032756	0312191501	8.97
182.309	47.0584	MRK198	0.02422	0601780801	21.57
205.296	30.3781	MRK268	0.0399	0554500701	23.11
				0554501101	18.48
206.175	55.8868	MRK273	0.03778	0101640401	17.97
93.9015	71.0375	MRK3	0.0135	0009220301	2.01
				0009220401	5.14
				0009220501	4.53
				0009220601	9.54
				0009220701	4.86
				0009220801	2.50
				0009220901	4.46
				0009221401	1.27
				0009221601	5.33
				0111220201	50.18
334.301	14.2391	MRK304	0.0658	0103660301	28.97
12.1964	31.957	MRK348	0.0150	0067540201	35.83
209.012	18.3721	MRK463	0.0504	0094401201	21.08
220.159	53.5044	MRK477	0.037726	0651100301	9.933
				0651100401	9.905
103.051	74.4271	MRK6	0.0188	0061540101	25.91
				0144230101	41.11
				0305600501	17.52
139.608	16.3053	MRK704	0.029	0300240101	14.88
174.927	31.9093	MRK744	0.0089	0204650301	16.29
115.674	65.1771	MRK78	0.0372	0307001501	7.26
40.27	-8.25576	NGC1052	0.005	0093630101	11.86
40.6696	-0.013281	NGC1068	0.0038	0111200101	35.06
				0111200201	35.31
43.8008	-0.183557	NGC1144	0.029	0312190401	8.73
45.9546	-1.10374	NGC1194	0.0136	0307000701	12.53
51.2029	-3.04228	NGC1320	0.0089	0405240201	13.36
53.4015	-36.1404	NGC1365	0.0055	0205590301	51.80

				0205590401	59.15
53.4015	-36.1404	NGC1365	0.0055	0505140201	108.19
54.1926	-35.9993	NGC1386	0.0029	0140950201	13.75
88.0474	-7.45621	NGC2110	0.0078	0145670101	44.54
102.536	60.8458	NGC2273	0.0061	0140951001	8.89
133.907	78.2231	NGC2655	0.005	0301650301	8.875
155.877	19.8651	NGC3227	0.0039	0101040301	31.20
				0400270101	97.59
2.77729	-12.1073	NGC34	0.0198	0150480501	12.70
181.596	52.7111	NGC4102	0.002823	0601780701	10.54
182.374	43.6853	NGC4138	0.0030	0112551201	8.80
182.636	39.4057	NGC4151	0.0033	0112310101	21.00
				0112830201	50.81
				0112830501	17.70
				0143500101	12.56
				0143500201	12.80
				0143500301	12.98
				0402660101	27.98
				0402660201	32.01
17.8651	-38.0835	NGC424	0.0117	0002942301	4.49
				0550950101	104.24
186.445	12.6621	NGC4388	0.008419	0110930701	7.35
186.454	33.5469	NGC4395	0.001064	0112521901	12.57
				0112522701	5.73
186.454	33.5469	NGC4395	0.0011	0142830101	94.62
188.903	-39.9093	NGC4507	0.0118	0006220201	36.00
				0653870201	15.67
				0653870301	13.10
				0653870401	13.05
				0653870501	13.08
				0653870601	17.31
18.5939	-55.3987	NGC454	0.012158	0605090301	24.20
191.666	54.5343	NGC4686	0.0167	0554500101	15.66
196.364	-49.4682	NGC4945	0.0019	0112310301	17.92
				0204870101	49.73
21.1119	33.7994	NGC513	0.019	0301150401	13.00
203.951	2.99892	NGC5231	0.021759	0601781201	13.84
204.567	4.54258	NGC5252	0.0230	0152940101	53.56
20.9766	-35.0655	NGC526A	0.019097	0109130201	9.27
				0150940101	41.50
205.535	35.6542	NGC5273	0.0035	0112551701	9.19
213.312	-3.20758	NGC5506	0.0062	0013140101	13.76
				0013140201	9.93
				0201830201	14.78
				0201830301	13.98
				0201830401	13.88
				0201830501	13.99
				0554170101	61.94
				0554170201	63.37

218.17	-44.1744	NGC5643	0.0040	0140950101	6.99
				0601420101	45.01
253.245	2.40093	NGC6240	0.0245	0101640101	22.32
				0101640601	8.95
				0147420201	20.01
				0147420301	2.53
				0147420401	10.70
				0147420501	7.18
				0147420601	5.04
330.508	-31.8697	NGC7172	0.0087	0147920601	10.88
				0202860101	52.10
				0414580101	27.71
331.755	10.2311	NGC7212	0.0266	0200430201	10.36
349.598	-42.3706	NGC7582	0.0053	0112310201	18.10
				0204610101	72.53
351.986	8.77904	NGC7674	0.0289	0200660101	7.91
352.266	3.53333	NGC7682	0.017	0301150501	16.06
30.0622	31.4294	NGC777	0.0167	0203610301	20.73
				0304160301	23.98
30.2769	-6.81552	NGC788	0.013603	0601740201	26.35
292.555	34.1797	NVSS193013+341047	0.0629	0602840101	12.91
172.319	-4.40211	PG1126-041	0.060	0202060201	28.72
				0556230701	17.45
				0556231201	8.66
				0606150101	94.10
213.451	44.0039	PG1411+442	0.0896	0103660101	22.71
234.16	54.5592	PG1535+547	0.0389	0150610301	24.22
				0300310301	14.41
				0300310401	15.62
				0300310501	18.79
318.719	6.12846	PG2112+059	0.4660	0300310201	64.47
				0500500701	50.05
337.127	-5.31521	PHL5200	1.981	0100440101	39.04
180.737	-20.9342	POX52	0.022	0302420101	90.45
125.755	-4.93486	SWIFTJ0823.4-0457	0.0218	0501210501	8.76
152.451	-42.8112	SWIFTJ1009.3-4250	0.0335	0501210101	21.08
143.965	61.3532	UGC05101	0.040	0085640201	26.50
44.9941	36.8206	UGC2456	0.012	0201770201	12.41
70.945	28.9718	UGC3142	0.0217	0401790101	8.78
90.6581	65.3712	UGC3386	0.0154	0554500601	24.39
109.879	59.3551	UGC3789	0.011091	0654800101	25.44
121.024	5.11385	UGC4203	0.0135	0002940701	1.85
173.157	52.9481	UGC6527	0.0274	0200430501	9.63
181.181	31.1773	UGC7064	0.024997	0601780601	27.78
23.1678	-13.552	XBSJ013240.1-133307	0.5620	0550960101	26.34

3.1.1 Optical classification versus X-ray absorption

The optical classification scheme which follows the orientation-based AGN unified model (Antonucci 1993) is expected to be strictly correlated with the X-ray absorption. However, recently quite a few studies have claimed the existence of objects for which optical and X-ray classifications do not match (see Sect. 1.2). It is commonly found in X-ray selected samples that ~10% - 30% of AGN which have only narrow lines in their optical spectra, suggesting extinction and thus classified as type 2, do not show absorption in their X-ray spectra (e.g. Panessa & Bassani 2002; Tozzi et al. 2006; Bianchi et al. 2012). On the other hand, there are more and more objects optically classified as type 1 which show significant amount of absorption in their X-ray spectra, a feature which is at odds with the presence of broad lines in the optical band (e.g. Garcet et al. 2007; Panessa et al. 2008).
A major issue about misclassification in X-ay and optical arises for the non-simultaneous data available in both wavelengths. However, a number of cases of unabsorbed type 2 and absorbed type 1 AGNs have been confirmed with an observational simultaneous campaign in X-rays and optical. The existence of a more complex structure surrounding the central engine of AGN rather than the one predicted by the unification model has been proposed and widely discussed in the past few years (Maiolino & Rieke 1995b; Elvis 2000; Matt 2000) and recently in Bianchi (2009); Risaliti & Elvis (2010); Elvis (2012). We refer the reader to Bianchi, Maiolino & Risaliti (2012) for a more detailed review on this issue.

In this section we explore the connection between optical classification and X-ray absorption in the CAIXA-A sample. For the optical classification we used the 13th edition of the Catalog of Quasars and Active Galactic Nuclei by Véron-Cetty & Véron (2010). As seen in Figure 3.4 the optical classification do not perfectly match with the X-ray classification even if most of the CAIXA-A sources are optically classified as Type 2 or intermediate objects, as expected.

In Figure 3.5 we show the position of the 109 CAIXA-A sources (red) with respect to the Véron-Cetty & Véron (2010) sources (Green) and the CIELO sources (Blue). Sources in our sample are more than those of CIELO because the catalog was updated until November 2011, while CIELO comprises only the observations whose data were public as of September 2006. In addition, the CIELO selection criteria excluded all the type <1.5 AGN (according to the NASA/IPAC Extragalactic Database (NED) optical classification), which constitute a not-negligible fraction (10,1%) of CAIXA-A, being X-ray obscured sources. Moreover, not all sources present in CIELO are also present in CAIXA-A. Only 33 CIELO-AGN (see Figure 3.6*Top*) are CAIXA-A sources too. The other 36 CIELO-AGN, due to their unabsorbed nature, (see Figure 3.6*Bottom*) were excluded from CAIXA-A. This is due to the new selection criteria used for the CAIXA-A catalogue, in

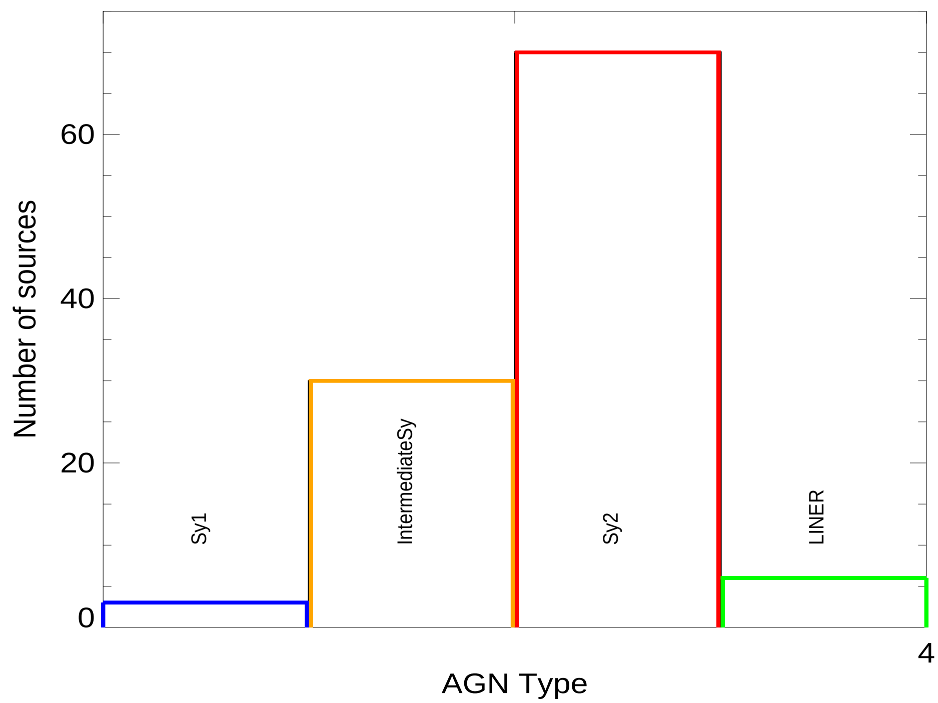

Figure 3.4: *Optical classification of the objects in CAIXA-A given by the Catalog of Quasars and Active Galactic Nuclei by Véron-Cetty & Véron (2010) (see Tab. 3.1). Sy1: Seyfert 1s (3 sources: IRAS09149-6206, UGC05101, NGC5231); Sy2: Seyfert 2s (70 sources, 64% of CAIXA-A sources); intermediate Seyfert galaxies (30 sources); LINERs(6 sources): NGC1052, NGC2655, NGC4102, NGC6240, NGC4686, UGC3386 (for the latter the optical classification is made by us based on the spectrum taken from Falco et al. (1999).*

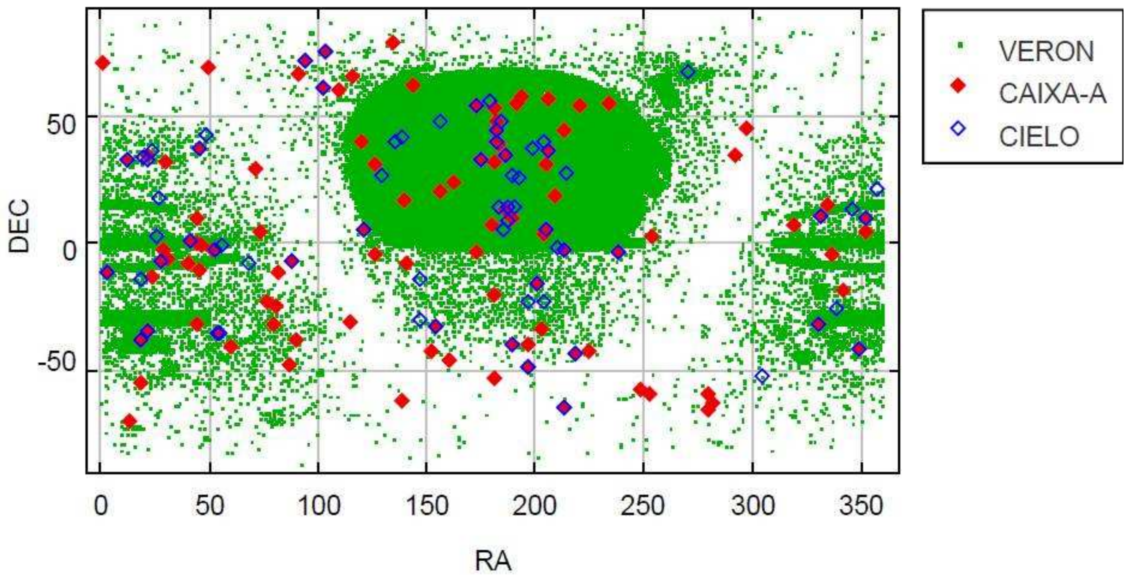

Figure 3.5: *The position (right ascensions and declinations) of The 109 CAIXA-A sources (Red) with respect to two known catalogue: Véron-Cetty & Véron (2010) sources (Green) and The 69 CIELO sources (Blue).*

particular to have used the X-ray classification and no longer an optical classification as occurred in CIELO[1]. Due to main goal of the analysis presented here, a criterion based on N_H is much more efficient with respect to the optical one (used in the CIELO sample). These 36 CIELO-AGN are optical type ≥1.5 sources, but they are X-ray unobscured ($N_H < 2\times10^{22}$ cm^{-2}) objects. Therefore these sources are dominated by the primary continuum below 2 keV, and their RGS spectrum cannot be used to investigate the soft excess in unobscured sources.

A detailed analysis of the EPIC-pn spectra of CAIXA-A is beyond the scopes of this work, and is deferred to a future work. In the following, only the RGS spectra will be analyzed.

3.2 The RGS spectra of CAIXA-A

For each observation, we have reprocessed RGS data starting with the *Observation Data Files*, using SASv11 (XMM Science Analysis System), and the most advanced calibration files available as of November 2011. Background spectra were generated using blank field event lists, accumulated from different positions on the sky vault along the mission. When more than one observation of the same

[1]How much of this misclassification is due to non-simultaneous observations is beyond the scopes of this work, and is deferred to a future work.

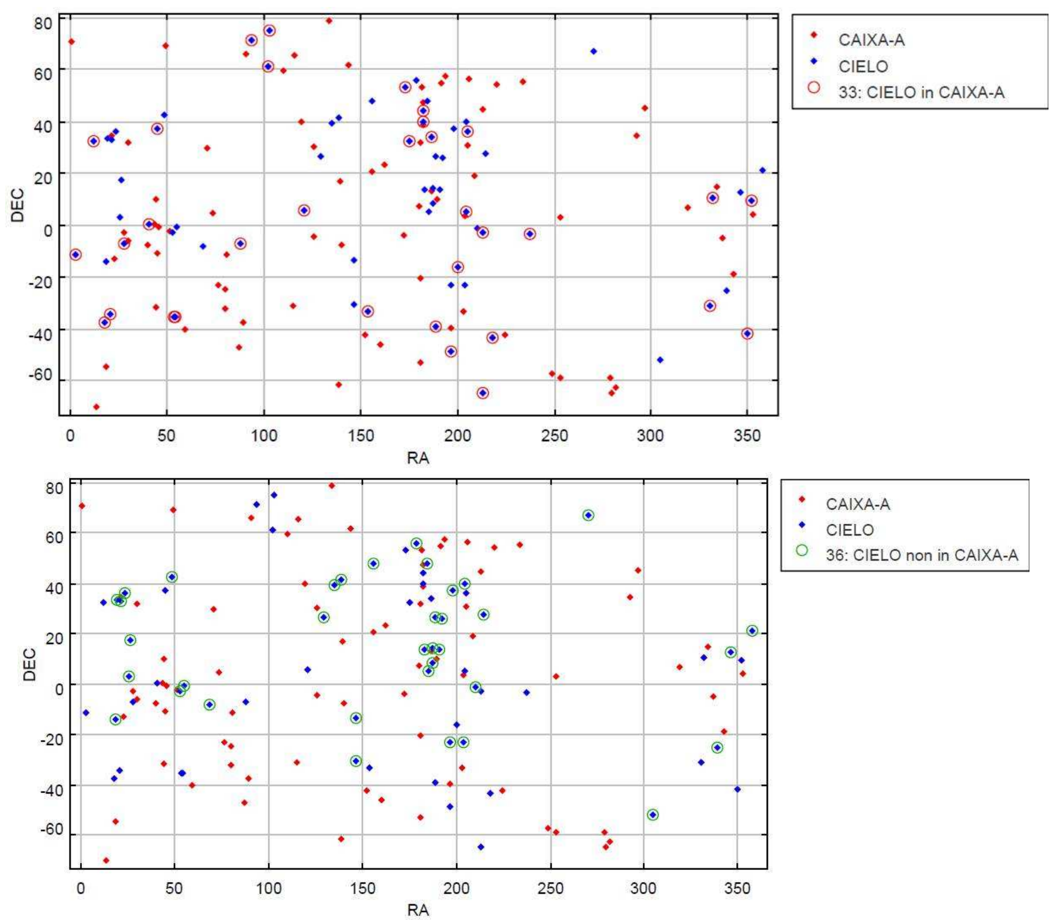

Figure 3.6: *The position (right ascensions and declinations) of The 109 CAIXA-A source (Red) with respect to the CIELO source (Blue). (*Top*) Red circle: the 33 sources both in CIELO that in CAIXA-A. (*Bottom*) Green circle: the 36 CIELO-AGN excluded from CAIXA-A.*

object was available, spectra of the same source from different observations were merged, together with their response matrices, after checking that no significant spectral variability occurred.

CAIXA-A includes poor to high quality RGS spectra: in Figure 3.7 we show for each source the percentage of net source count rates (combined RGS1+RGS2 in the 0.4 – 0.9 keV band[2]), with respect to the background and in Figure 3.8 we show for each source the total counts vs the percentage of net source count rates with respect to the background for combined RGS1+RGS2 in the 0.4 – 0.9 keV band. Since the background is modeled, it is possible that some sources posses a negative percentage, i.e. the total observed count rate is lower than the one expected by background alone. In these cases, we assigned a zero percentage. In Figure 3.9, 3.10, 3.11 we show the RGS spectra for spectra with different quality: also in poor-quality spectra, some lines are clearly present.

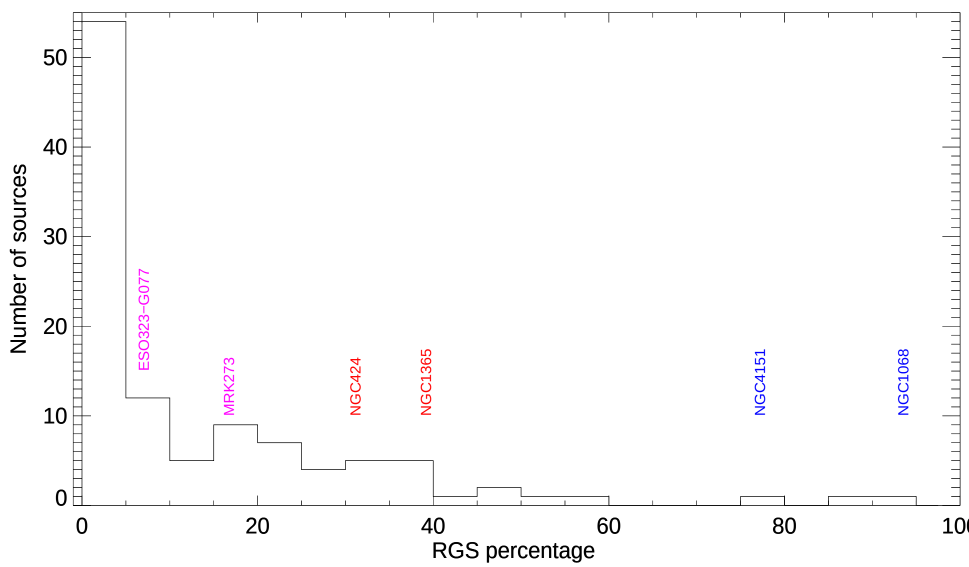

Figure 3.7: Percentage of net source count rates (RGS1+RGS2: 0.4 – 0.9 keV), with respect to the background. The effective area reaches the maximum in the 0.4-0.9 keV band so in this band we have a clearer idea of the quality of the spectra. Since the background is modeled there are sources with negative percentage: in these cases, we assigned a value of 0. Some representative sources are labeled for each quality of spectra. *Blue*: good quality spectra; *Red*: middle quality spectra; *Magenta*: poor quality spectra.

In order to extract as much information as possible, we performed the analysis of RGS spectra following three different approaches.

[2]The effective area reaches the maximum in the 0.4-0.9 keV band (see Fig A.3) so in this band we have a clearer idea of the quality of the spectra.

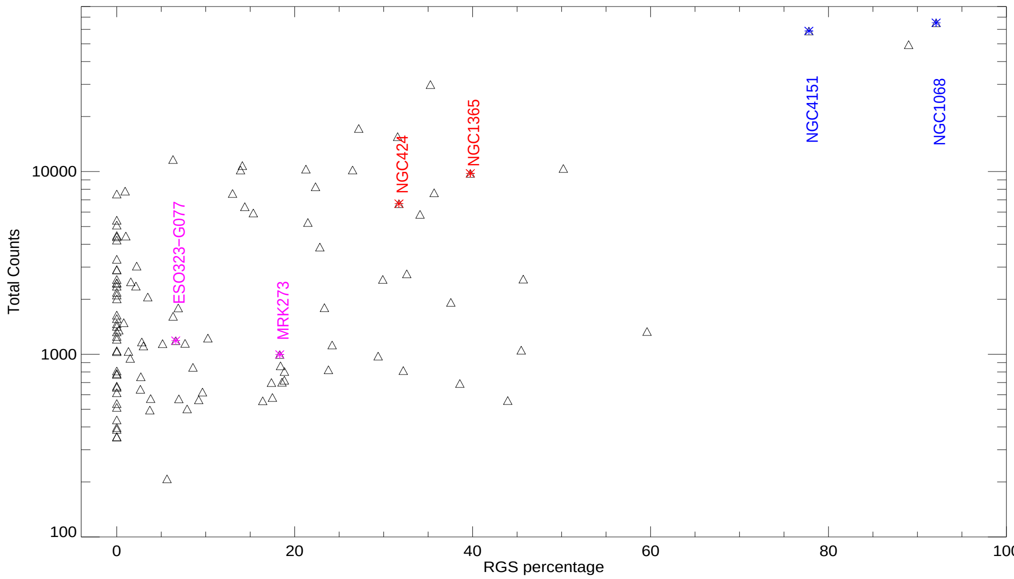

Figure 3.8: Total counts vs percentage of net source count rates with respect to the background for combined RGS1+RGS2 in 0.4 – 0.9 keV band. *Blue*: good quality spectra; *Red*: middle quality spectra; *Magenta*: poor quality spectra. The same representative sources labelled in Fig.3.7 are highlighted.

A *CIELO-like*: each spectrum was systematically searched for the presence of emission lines, modeling local continua with $\Gamma = 1$ power-laws and the transitions with Gaussian profiles with the lines energy fixed to laboratory transition energies.

B *Blind search for emission lines*: each spectrum was systematically searched for the presence of emission lines, modeling local continua with $\Gamma = 1$ power-laws and the transitions with Gaussian profiles with the energy of the lines as free parameters.

C *Self-consistent modelling*: self-consistent modelling of the soft X-ray emission lines with models using five different combinations of plasma.

Method A and B are similar. The difference between the two approaches is that in the first the energy of the lines is fixed to laboratory transition energies (following that described in Guainazzi & Bianchi (2007), so we called it *CIELO-like* analysis), while in the second method the energy of the lines is a free parameter, so we called it *Blind search for emission lines* analysis. The third approach analyzes RGS spectra reproducing the soft emission in terms of self-consistent models of plasma in photoionization equilibrium using the public photoioniza-

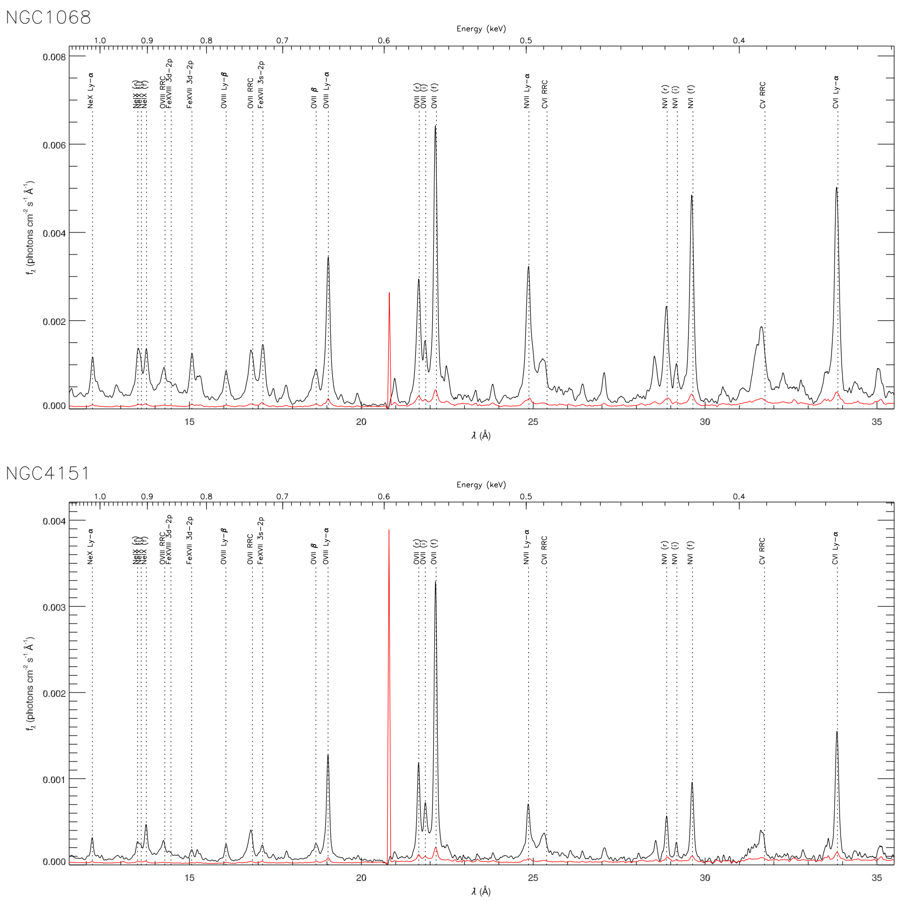

Figure 3.9: High-quality RGS spectra (see Figure 3.7) which exhibit the largest number of detected emission lines. *Top*: NGC1068, the best quality spectra in CAIXA-A; *bottom*: NGC4151. Spectra of the two RGS cameras (and error in red) have been smoothed with a 5-channels wide triangular kernel for illustration purposes only. The positions of the line transitions considered in Method A are labeled (see Tab.3.2).

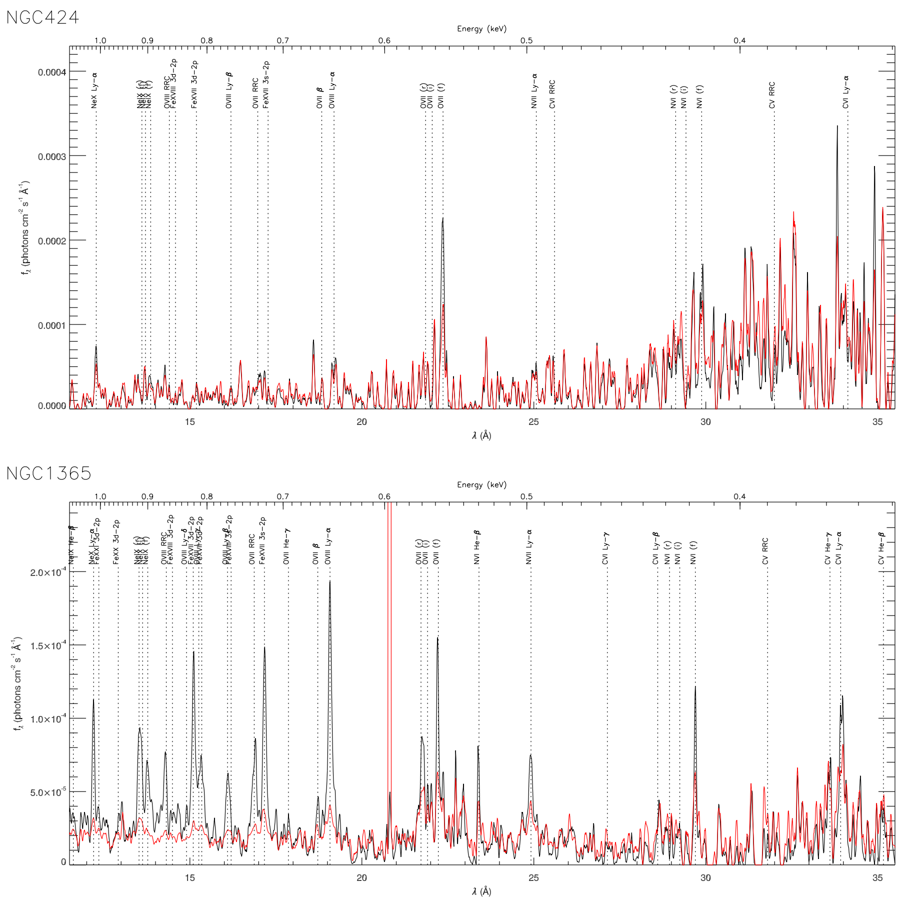

Figure 3.10: Poor-quality RGS spectra (see Figure 3.7) which exhibit some detected emission lines. *Top*: NGC424; *bottom* NGC1365. Spectra of the two RGS cameras (and error in red) have been smoothed with a 5-channels wide triangular kernel for illustration purposes only. The positions of the line transitions considered in Method A are labeled (see Tab.3.2).

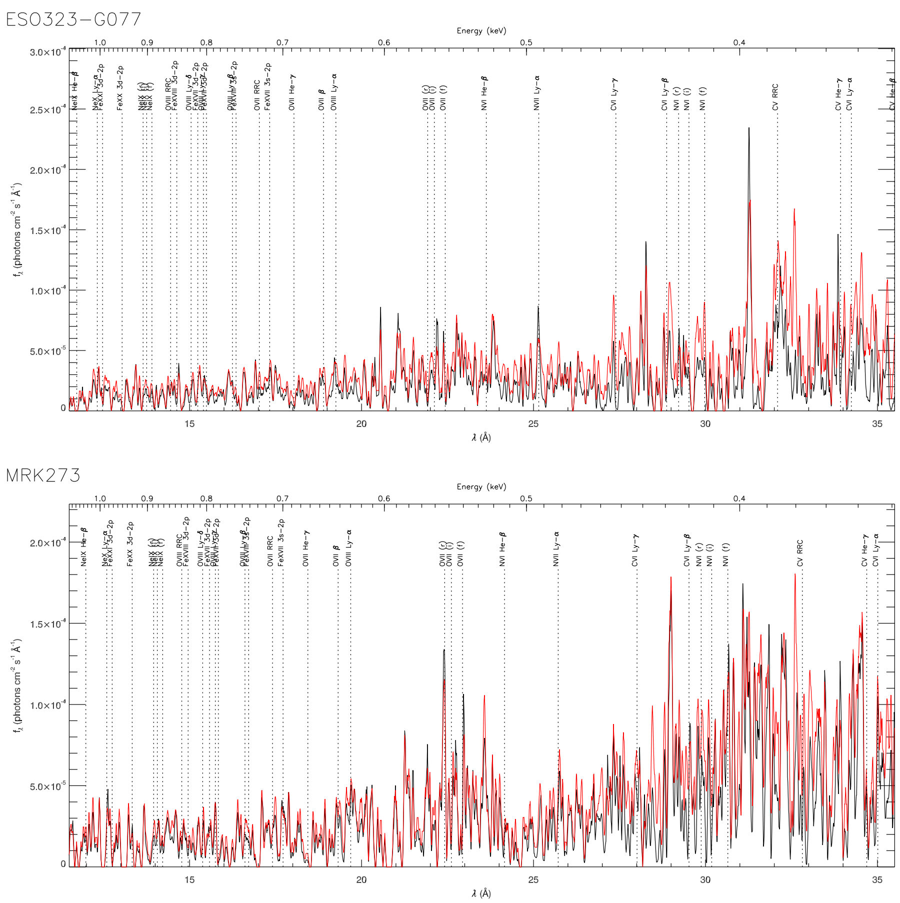

Figure 3.11: Poor-quality RGS spectra (see Figure 3.7) for ESO323-G077 (top) and MRK273 (bottom). Spectra of the two RGS cameras (and error in red) have been smoothed with a 5-channels wide triangular kernel for illustration purposes only. The positions of the line transitions considered in Method A are labeled (see Tab.3.2).

tion code CLOUDY[3] (Ferland (2000)) or collisional equilibrium using the XSPEC model APEC (an emission spectrum from collisionally-ionized diffuse gas calculated using the ATOMDB code[4]). We will refer to this method with *Self-consistent modelling* analysis.

The χ^2 statistic assumes that all the spectral channels are Gaussian distributed and that the estimate for the variance is uncorrelated with the observed counts. If there are small numbers of counts in a channel, as in most of our RGS spectra, these requirements will not be satisfied. An alternative statistic, the Cash (1979), should be used in this case. So we used the Xspec normalized version of this statistic (CSTAT) to determine the best-fit parameter and its uncertainties.

3.3 Method A: CIELO-like

Each spectrum was systematically searched for the presence of the brightest emission lines expected to arise from an ionized plasma. We simultaneously fit together the spectra of the two RGS cameras, using XSPEC version 12.8.0m. The fits to the data were performed on the unbinned spectra (Cash 1979, statistics) and the emission lines were modeled with Gaussian profiles, where the intrinsic width was always frozen to zero, also for the components of a multiplet. For the Radiative Recombination Continua (RRC) only the intrinsic width was considered as an additional free fit parameter. Laboratory energies are extracted from the CHIANTI database (Dere et al. 2001). We constrain the energy to vary in a small range of possible values near the laboratory transition energies chosen that have been selected from the most intense emission lines in the 0.3–1 keV band either arising in a photo- or collisionally ionized plasma (see Table 3.2 for the selected transitions).

"Local" fits to the data were performed on the spectra on ≃50 channels wide intervals (constructed centered on the laboratory transition energies chosen), using Gaussian profiles to account for any line features. Continua were modeled with $\Gamma = 1$ power-laws[5], leaving free in each fit the continuum normalization (Γ is the power-law photon index). Line luminosities have been corrected for Galactic photoelectric absorption using column densities after Dickey & Lockman (1990).

Fits of He-α triplets have been performed keeping the relative distance between the centroid energies of the components fixed to the value dictated by atomic physics. A line is considered to be detected when its flux is inconsistent

[3] http://www.pa.uky.edu/~gary/cloudy/

[4] More information can be found at http://atomdb.org/

[5] Since the model used to fit the continuum is not very sensitive to the photon index Γ, due to the very limited band width of each segment, it has been fixed to 1.

with 0 at the 1-σ level.

In Tab. 3.2 we list transition, laboratory wavelength and number of *CAIXA-A* sources for which a given transition has been detected (see also Figure 3.12). For each transition that we have looked for we have found at least 8 detections.

The three lines more detected in our analysis were the OVIII Ly-α (61), the FeXVII 3d-2p ($^1P_1$) (51) and the OVIII Ly-β (49). For all the triplets we looked for, the forbidden component has always more detections with respect to the resonant line and intercombination components. Radiative Recombination Continua (RRC) features from Carbon and Oxygen are detected in several sources. The predominance in the triplets of the forbidden lines and the good number of RRC indicates that photoionization plays an important role in the ionization balance of CAIXA-A sources. In Fig. 3.13 we show the number of detections for source: most sources have 9 detections, only a few (11 sources) have more than 15 detections and only 8 sources have no detections. The sources with no detections are all sources with poor quality spectra, as we can see in Fig. 3.14, while the sources with more then 15 detections have middle-to-hight quality spectra.

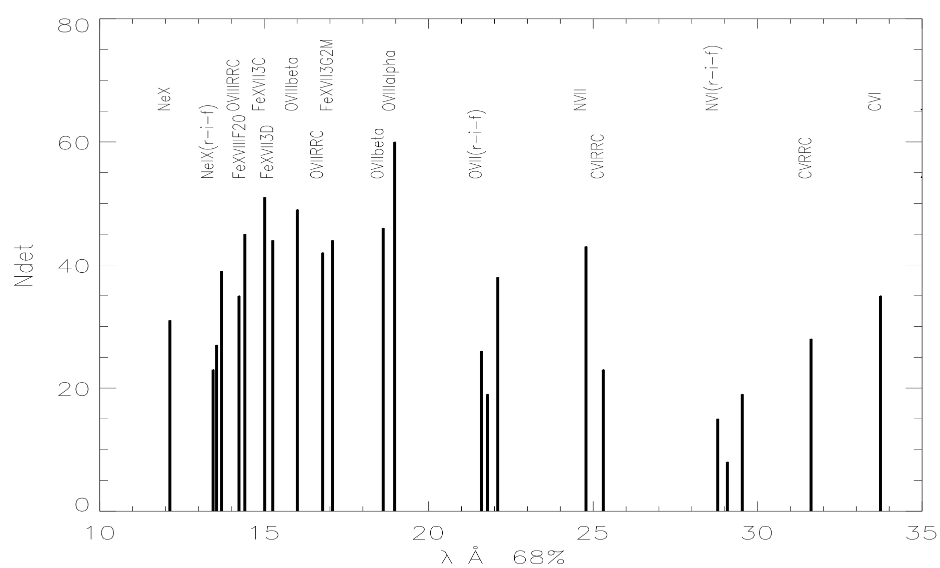

Figure 3.12: *Transition of CAIXA-A sources detected at the 1-σ level (see Tab. 3.2), when only a-priori selected transitions are looked for (Method A: see text for details).*

In Fig. 3.15, 3.16, 3.17 we show the RGS local fits spectra respectively for high-quality spectra (NGC1068 the best quality spectra in CAIXA-A, see Fig. 3.14; 23 detections), middle quality spectra (NGC424; 18 detections), and low quality spectra (ESO323-G077, 10 detections; MRK273, 12 detections).

Table 3.2: Number of *CAIXA-A* sources, N_{det}, for which a given transition (laboratory wavelength λ_{lab}) has been detected, if $N_{det} > 0$ at the 1-σ level.

Transition	λ_{lab} (Å)	E (KeV)	CAIXA-A N_{det}
NeX Ly-α	12.134[a]	1.0218	31
NeIX He-α (r)	13.447	0.9221	23
NeIX He-α (i)	13.553	0.9149	27
NeIX He-α (f)	13.699	0.9051	39
FeXVIII f20	14.207	0.8728	45
OVIII RRC	14.228	0.8714	35
FeXVII 3d-2p ($^1P_1$)	15.015	0.8257	51
FeXVII 3d-2p ($^3D_1$)	15.262	0.8125	44
OVIII Ly-β	16.006	0.7746	49
OVII RRC	16.771	0.7393	42
FeXVII 3s-2p (3G/M2)	17.076[b]	0.7262	44
OVII He-β	18.627	0.6656	46
OVIII Ly-α	18.967	0.6536	61
OVII He-α (r)	21.602	0.5739	26
OVII He-α (i)	21.803	0.5687	19
OVII He-α (f)	22.101	0.5611	38
NVII	24.785	0.5003	44
CVI RRC	25.306	0.4900	23
NVI He-α (r)	28.790	0.4307	15
NVI He-α (i)	29.083	0.4282	8
NVI He-α (f)	29.534	0.4259	19
CV RRC	31.622	0.3921	28
CVI Ly-α	33.737[c]	0.3675	35

[a]doublet: λ_1 = 12.1321 Å, λ_2 = 12.1375 Å [b]doublet: λ_1 = 17.0500 Å, λ_2 = 17.0970 Å [c]doublet: λ_1 = 33.7342 Å, λ_2 = 33.7396 Å

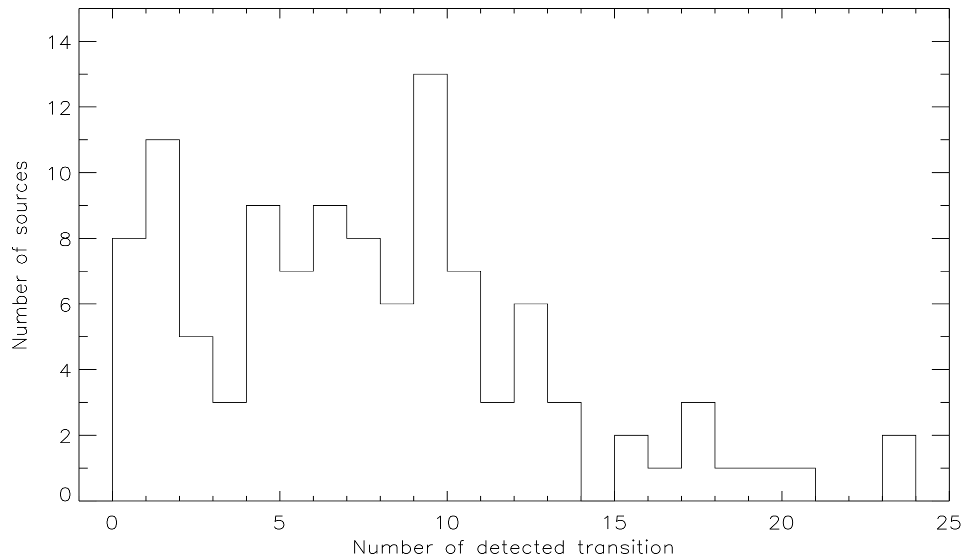

Figure 3.13: *Number of detections for source with Method A.*

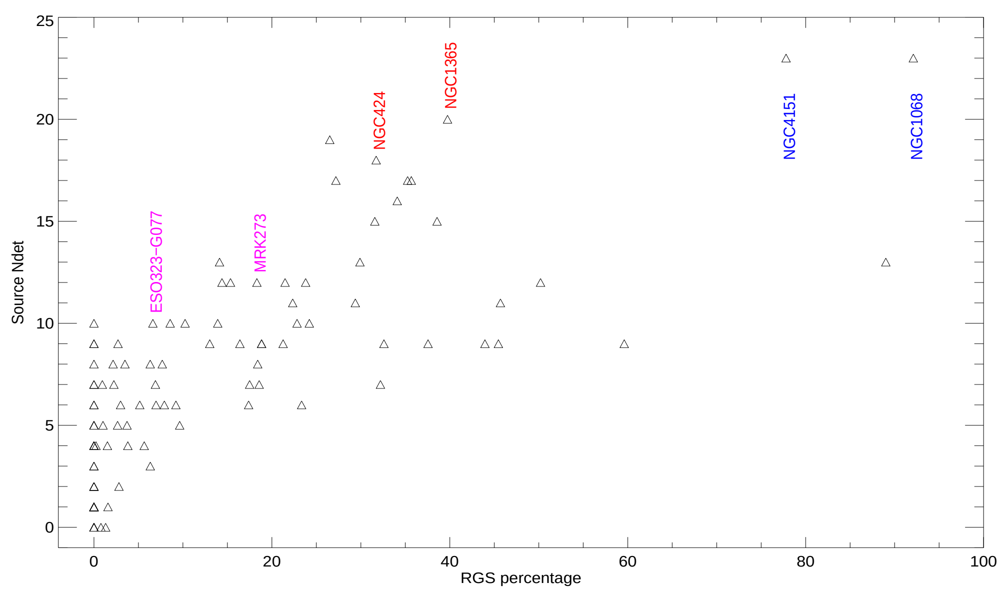

Figure 3.14: *Number of detections for source with Method A vs percentage of net source count rates for combined RGS* (0.4−0.9 *keV*)*, with respect to the background. The effective area reaches the maximum in the 0.4-0.9 keV band so in this band we have a clearer idea of the quality of the spectra.*

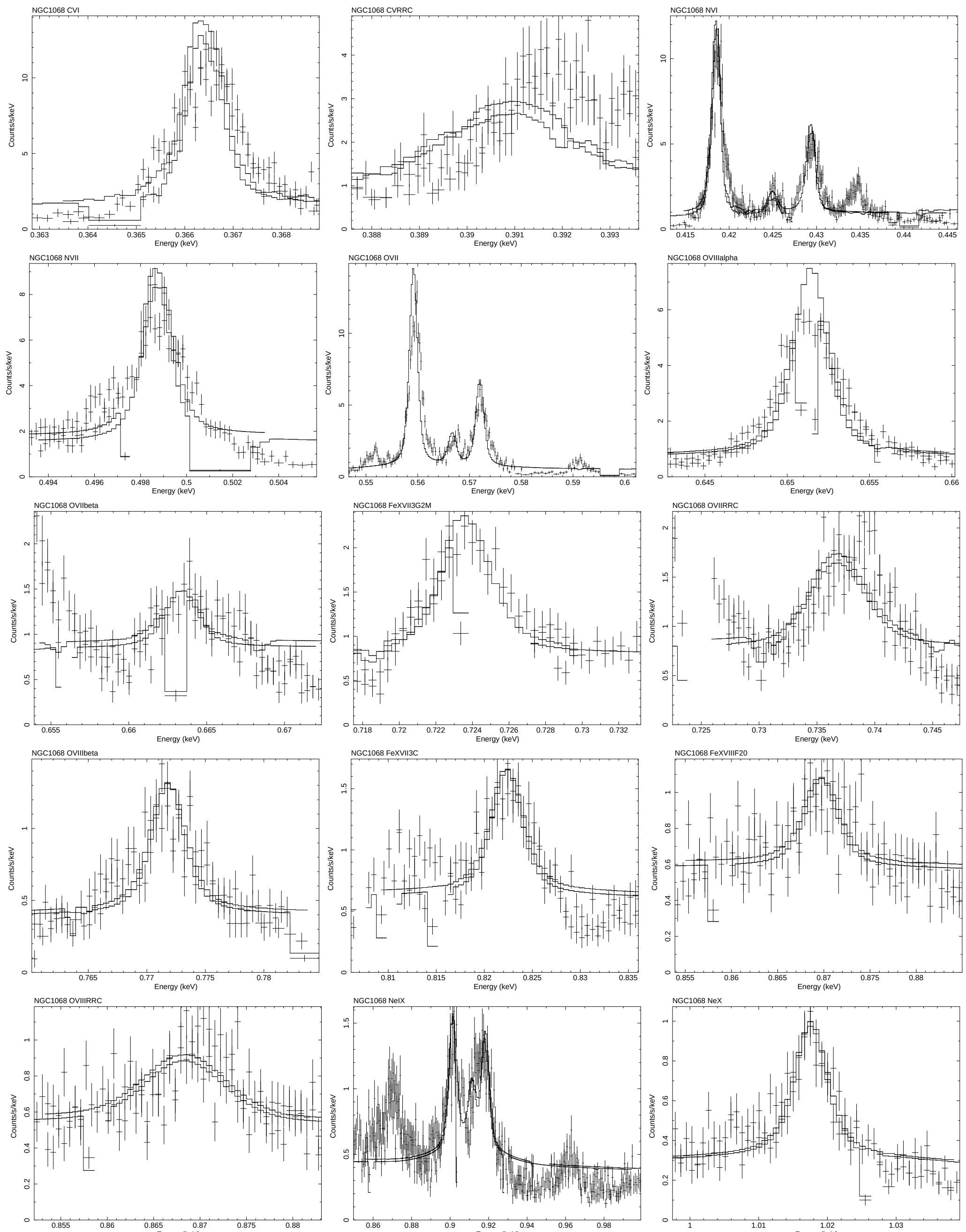

Figure 3.15: *Example of source with high quality spectrum (see Fig. 3.14): NGC1068 most significative detections with Method A. The spectra were binned to a minimum of 3 counts per spectral channel for visual clarity.*

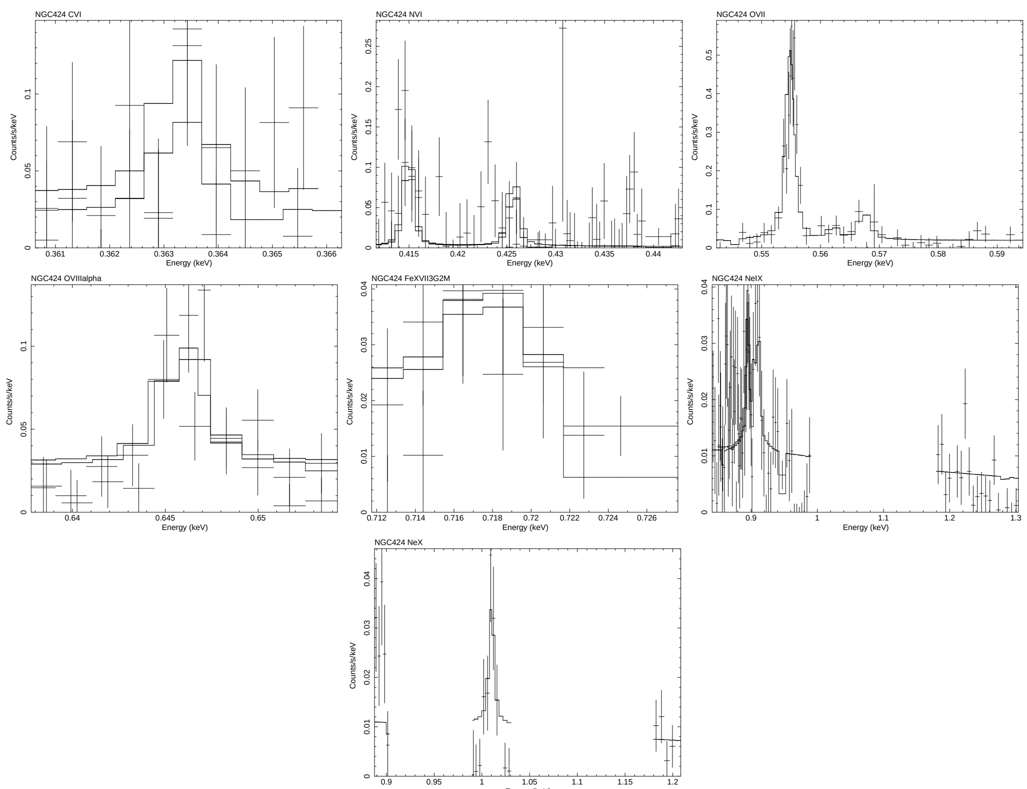

Figure 3.16: *Example of source with middle quality spectrum (see Fig. 3.14): NGC424 most significative detections with Method A. The spectra were binned to a minimum of 3 counts per spectral channel for visual clarity.*

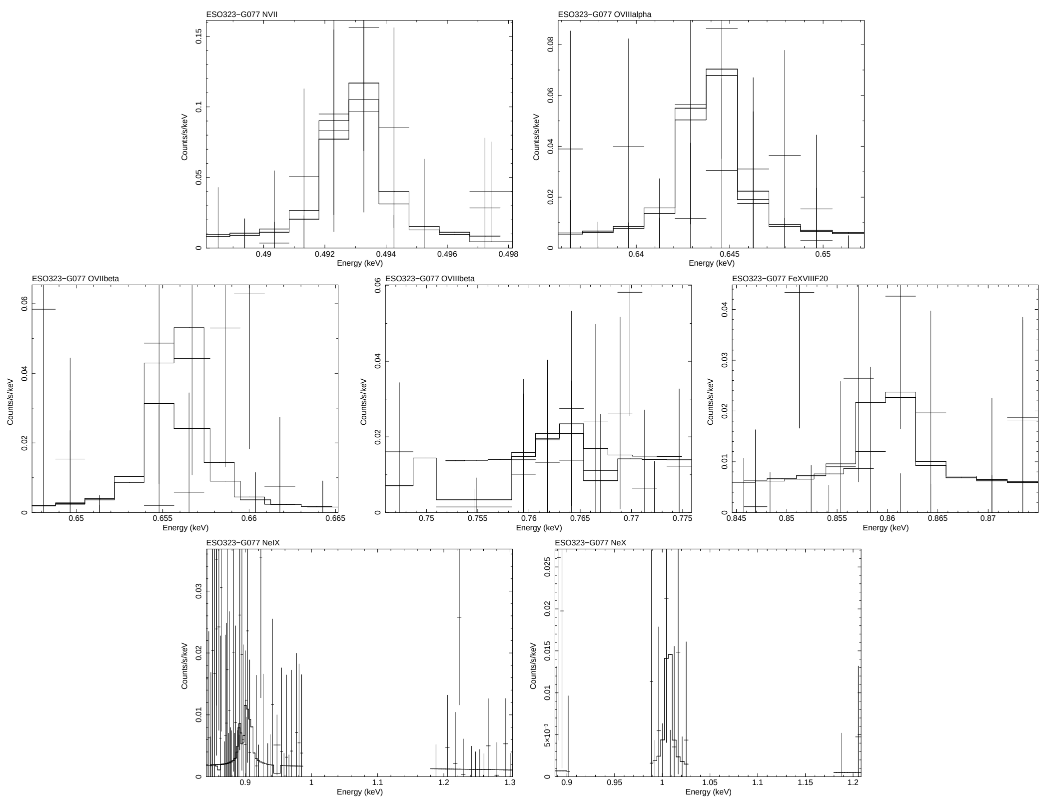

Figure 3.17: *Poor quality spectra: ESO323-G077 most significative detections with Method A. The spectra were binned to a minimum of 3 counts per spectral channel for visual clarity.*

The most intense RRC transitions expected in the RGS energy bandpass are: O VIII at 14.228Å, O VII at 16.771Å, C VI at 25.306Å and C V at 31.622Å. At least one of these RRC features is detected in 39% (42/109) of the objects of our sample: O VIII in 35/109 (Fig 3.18), O VII in 42/109 (Fig 3.19), C VI in 23/109 (Fig 3.20) and C V in 28/109 (Fig 3.21). Our result is very similar to that found in the CIELO sample by Guainazzi & Bianchi (2007) (see Fig. 2.11). In fact they detected RRC features in 36% (25/69) of the objects of their sample. The measurements of the RRC width, which represents a direct estimate of the temperature of the plasma (Liedahl & Paerels 1996), cluster in the range 1–10 eV (Fig 3.22). There is an obvious selection effect, favoring the detection of narrow features, but it is nonetheless a very significant common property of our sample. The association of high ionization emission lines with such a low-temperature plasma is strongly indicative of a plasma whose ionization state is governed by photoionization as opposed to collisional ionization.

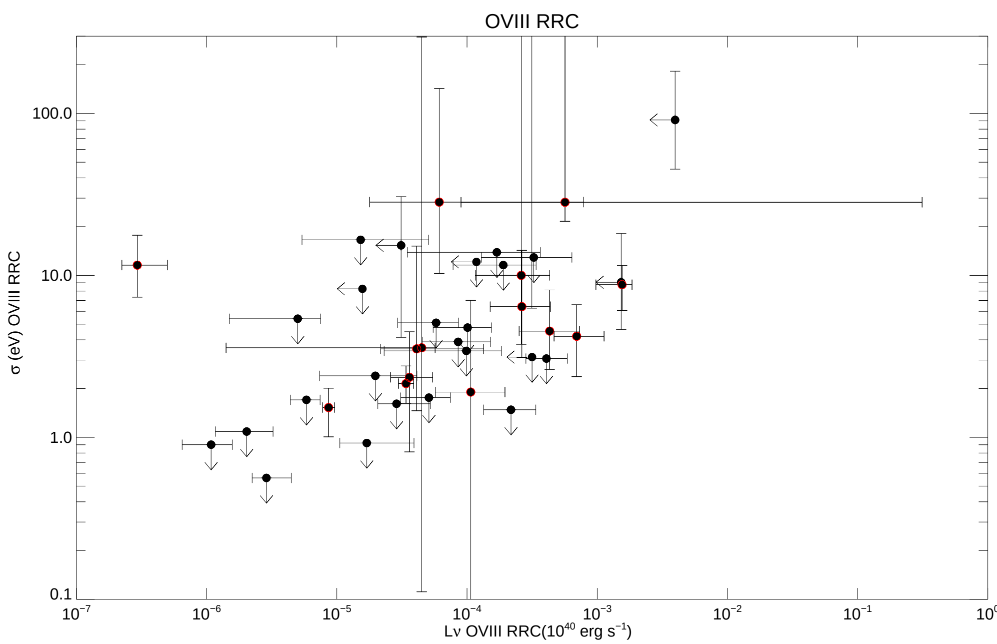

Figure 3.18: *Luminosity of O VIII RRC versus intrinsic width for the O VIII RRC features detected in our sample. Measures (15) are highlighted in red, all the other points (56) are upper limits (in either quantity). Unconstraining upper limits are not shown. We excluded the IRAS09149-6206 O VIII RRC sigma measure, because its value (> 10 keV) is unphysical.*

In addition to $n = 2p \rightarrow 1s$ transitions for H- and He-like atoms, *CAIXA-A* AGN contains a fair number of detections of discrete higher order resonance transitions ($np \rightarrow 1s$, $n > 2$). These transitions are selectively enhanced by photoexcitation.

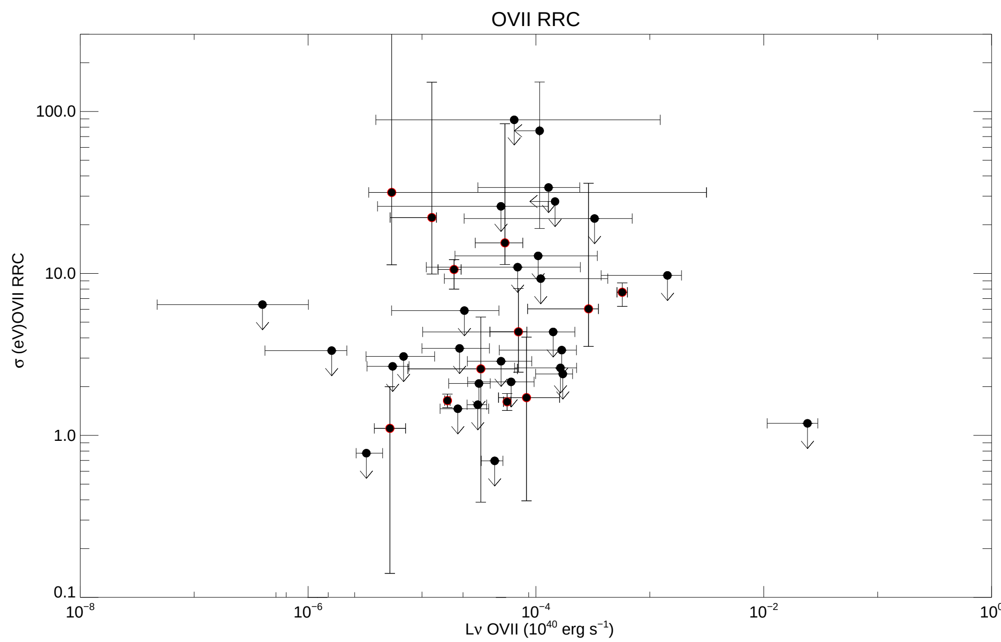

Figure 3.19: *Luminosity of* O VII*RRC versus intrinsic width for the* O VII*RRC features detected in our sample. Measures (12) are highlighted in red, all the other points (62) are upper limits (in either quantity). Unconstraining upper limits are not shown.*

Since the forbidden f transition in He-like triplets is unaffected by photoexcitation, the intensity ratio between higher order series and f transition intensities provides a potentially powerful diagnostic of the importance of resonant scattering in photoionized spectra (e.g. Kinkhabwala et al. 2002). An example of the application of this diagnostic test to *CAIXA-A* AGN is shown in Fig. 3.23, where we display the intensity of the O VII He-β against the forbidden component of the O VII He-α triplet[6]. In this plot, we compare the experimental results with the predictions of pure photoionization, and with models where radiative decay from photoexcitation and recombination from photoionization are self-consistently calculated (model `photoion`; Kinkhabwala et al. (2002)). We have produced a grid of models for different values of O VII column densities ($N_{OVII} \in$[10^{15},10^{20} cm^{-2}]), turbulence velocities ($v_{turb} \in$[0,500 km s^{-1}]), and temperatures ($kT \in$[1,20 keV]). Most of our values are in agreement with these photoionization models, with relatively low column densities and hence a significanti contribution from resonant scattering. We have two sources (MKN231 and NGC3227) with very high O VII He-β intensity values and some sources with very high intensity values of the forbidden component of the He-α triplet .

[6]For comparison see the results for CIELO (Guainazzi & Bianchi 2007) in Fig. 2.12.

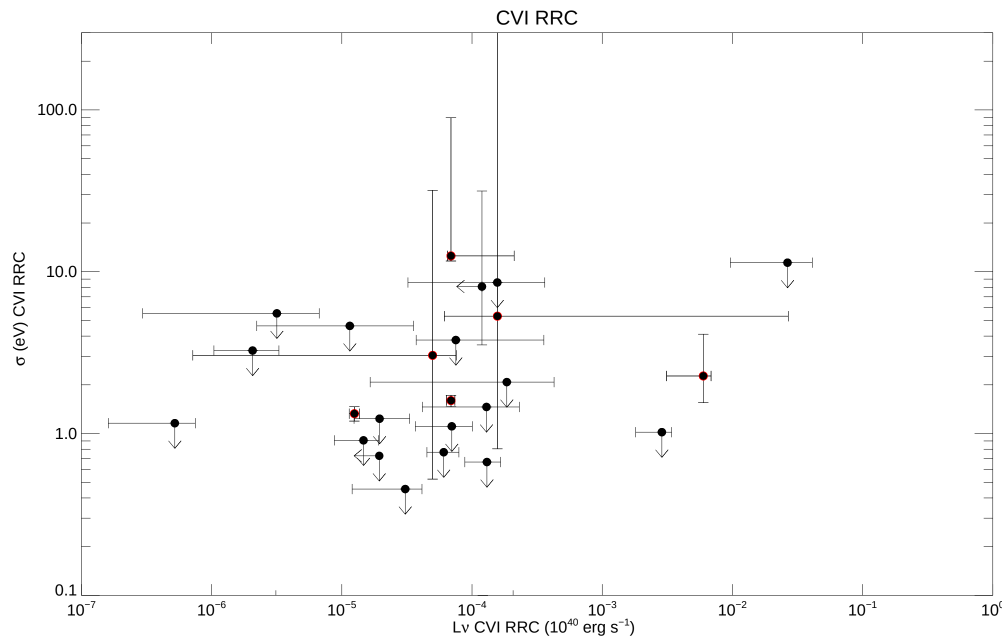

Figure 3.20: *Luminosity of* C VI *RRC versus intrinsic width for the* C VI *RRC features detected in our sample. Measures (6) are highlighted in red, all the other points (45) are upper limits (in either quantity). Unconstraining upper limits are not shown.*

High He-α forbidden versus He-β intensity ratio (larger then expected for pure photoionization) can be explained by the fact that the measurements on the He-β O VII transition at 18.6270Å could be contaminated by the nearby N VII RRC at 18.5872Å (e.g. Guainazzi & Bianchi 2007).

On the other hand, the O VII He-α forbidden line is significantly suppressed in collisionally ionised plasma, which could justify a low f versus He-β intensity ratio, as for MKN231 and NGC3227.

In Fig. 3.24 we plot the O VII f transition intensity against the intensity of the O VIII Ly-α. A ratio between the intensity of the forbidden component of the O VII triplet and the O VIII Ly-$\alpha \lesssim 1$ is a signature of photoionized plasma again because the forbidden component is strongly suppressed in a plasma in collisional equilibrium (e.g. Guainazzi & Bianchi 2007). As we can see in Figure 3.24 there are only three CAIXA-A sources that have this ratio greater than one: NGC6240, NGC1365 and NGC4395. The first two sources, NGC6240 and NGC1365, are known to have high-resolution X-ray spectra dominated by collisional ionization (Boller et al. 2003; Guainazzi et al. 2009). On the other hand the error for NGC4395 is greater than the errors estimated for all the other CAIXA-A sources and the O VIII Ly-α energy is very different from the laboratory energy (see Fig. 3.26). These issues prevent us from drawing any real physical mean-

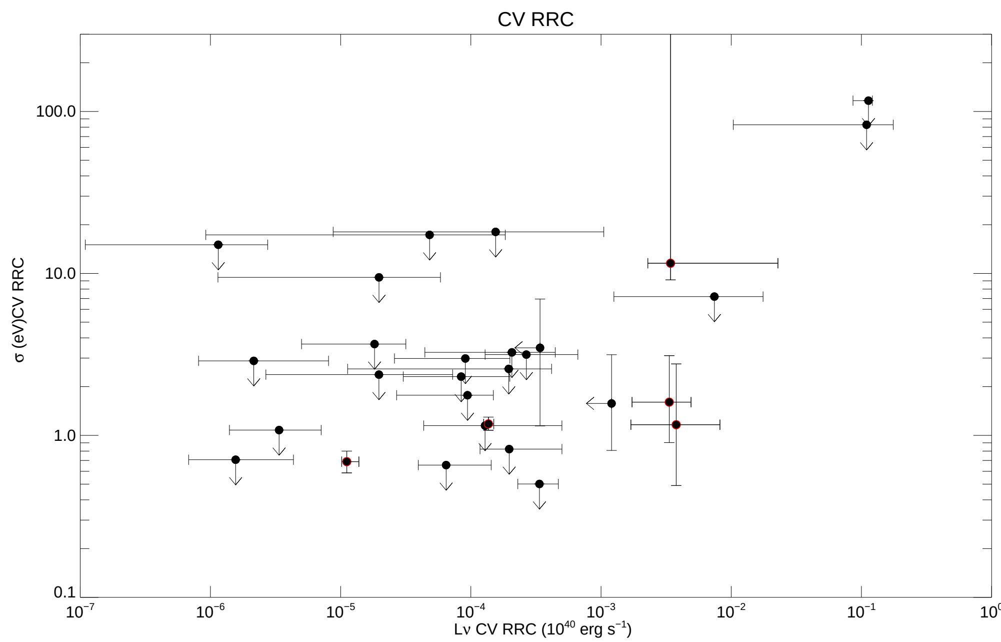

Figure 3.21: *Luminosity of C*V*RRC versus intrinsic width for the C*V*RRC features detected in our sample. Measures (5) are highlighted in red, all the other points (35) are upper limits (in either quantity). Unconstraining upper limits are not shown.*

ing of the OVII f/OVIIIα ratio in this source. We find no correlation between the OVII f/OVIIIα ratio and the total luminosity in these oxygen lines.

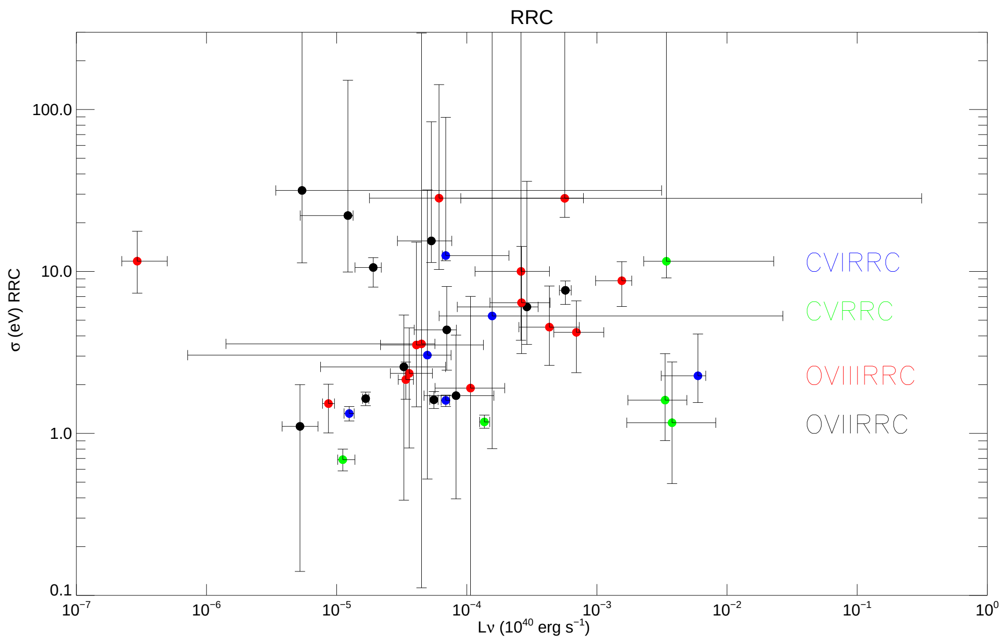

Figure 3.22: *Luminosity versus intrinsic width for all the RRC features detected in our sample.* Blue: Cvi*RRC;* Green: *C*V*RRC;* Red: *O*VIII*RRC;* Black: *O*VII*RRC. Upper limits are not shown. We excluded the IRAS09149-6206 O*VIII*RRC sigma measure, because its value (*$>$ 10 *keV) is unphysical.*

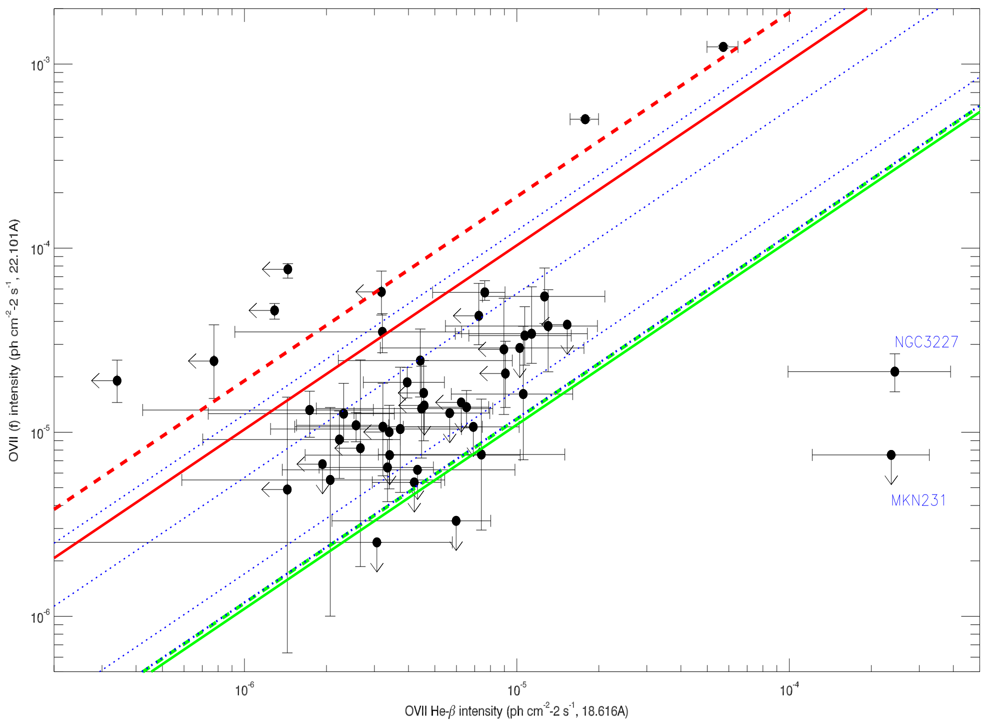

Figure 3.23: Intensity of OVII He-β line against the intensity of the forbidden component of the He-α triplet. The *red lines* represent the prediction for OVII column densities $N_{OVII} = 10^{20}$ cm^{-2}, assuming $kT = 20$ eV and $v_{turb} = 500$ km s^{-1} (*solid*) and $kT = 1$ eV and $v_{turb} = 50$ km s^{-1} (*dashed*). The *green lines* represent the prediction for OVII column densities $N_{OVII} = 10^{15}$ cm^{-2}, assuming $v_{turb} = 500$ km s^{-1} (*solid*) and $v_{turb} = 50$ km s^{-1} (*dashed*). The *blue lines* represent the prediction (from bottom to top) for OVII column densities $N_{OVII} = 10^{16}$ cm^{-2}, $N_{OVII} = 10^{17}$ cm^{-2}, $N_{OVII} = 10^{18}$ cm^{-2} and $N_{OVII} = 10^{19}$ cm^{-2}, assuming $kT = 5$ eV and $v_{turb} = 200$ km s^{-1}.

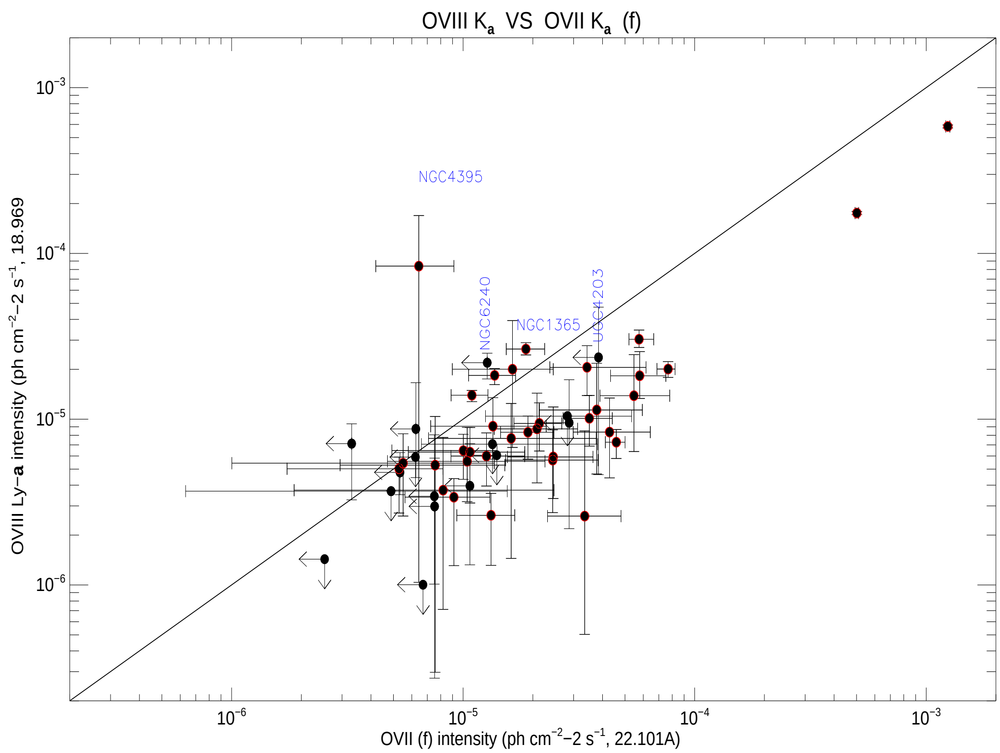

Figure 3.24: *Intensity of* O VII *He-β line against the intensity of the f component of the He-α triplet.*

Finally, we have as well checked whether the detected line energy centroids in each source were systematically shifted with respect to the laboratory energies in the following transitions: O VII He-α(f) (see Figure 3.25), and O VIII Ly-α (see Figure 3.26). Our analysis found none of these systematic shifts (see Figure 3.27). On the other hand, we found some occurrences of discrepancies between the best-fit centroid and the laboratory energies in individual lines. NGC4945 is the only source who shows significant systematic energy shifts (in the same direction) at the 1σ level for both lines, suggesting an inflowing gas (~ -1000 km s^{-1}). However, we refrain from attributing any astrophysical meaning to these discrepancies, which may be due to contamination by nearby transitions, residual errors in the aspect solution of the RGS cameras, or spurious detections.

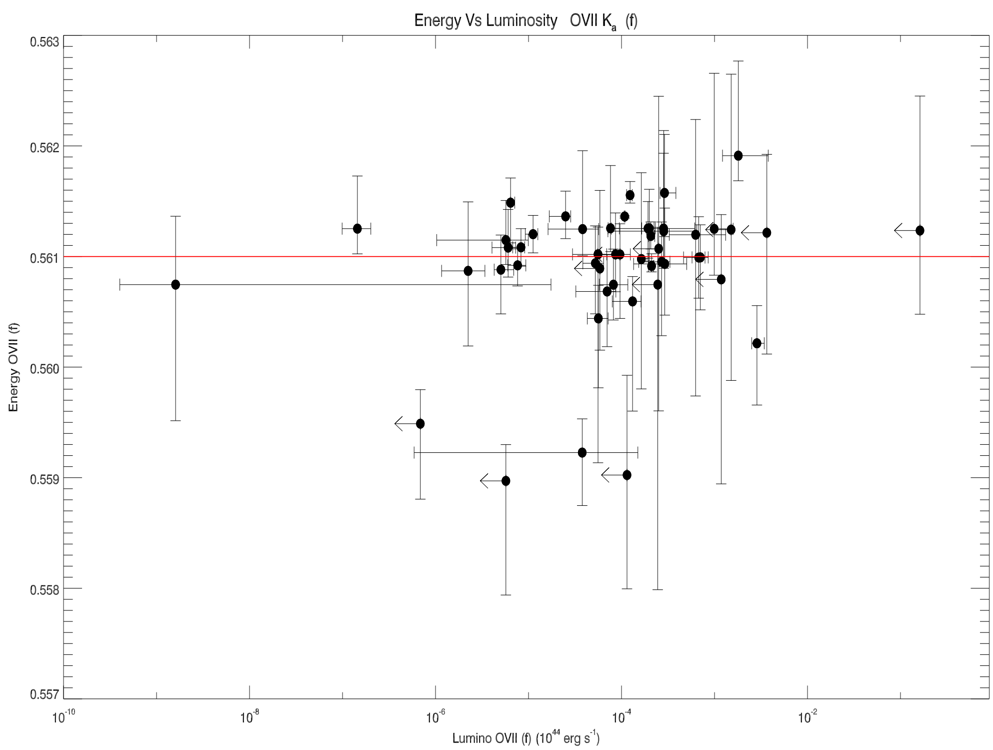

Figure 3.25: *O VII He-αf line energy centroids of CAIXA-A sources against luminosity. The red line represents the laboratory energy.*

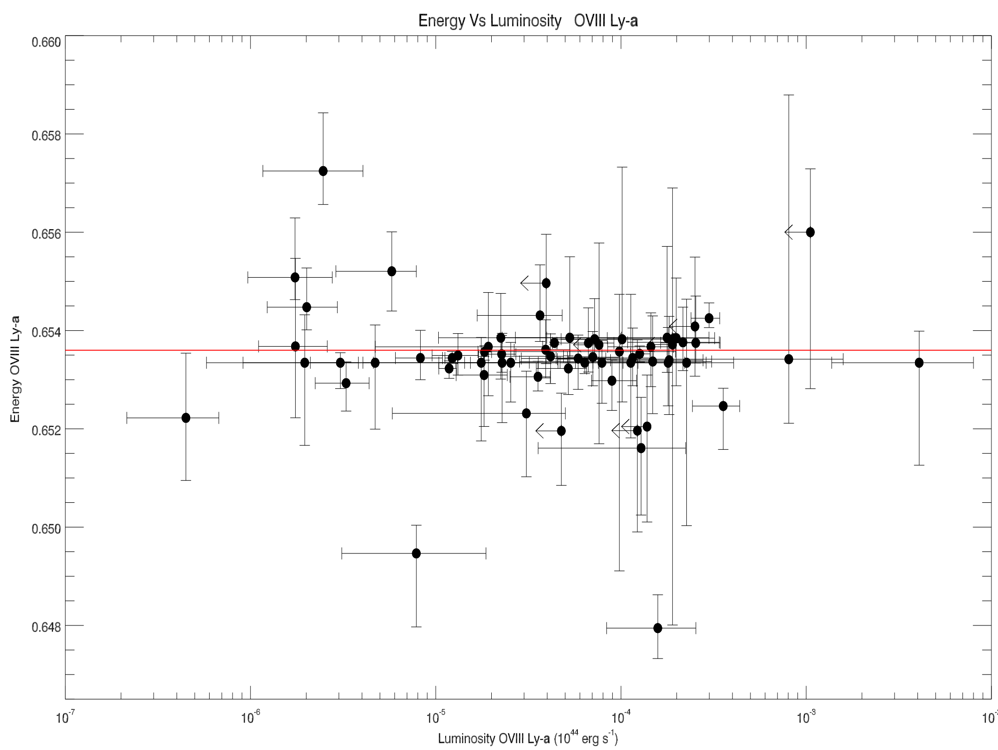

Figure 3.26: *O*VIII *Ly-α: line energy centroids shift. The red line represents the laboratory energy. We exclude NGC4395 because $E_{NGC4395}$ = 0.673593 eV against the laboratory energy that is 0.6536 eV (while the energy for the O*VII *He-α(f) is consistent with the laboratory energy).*

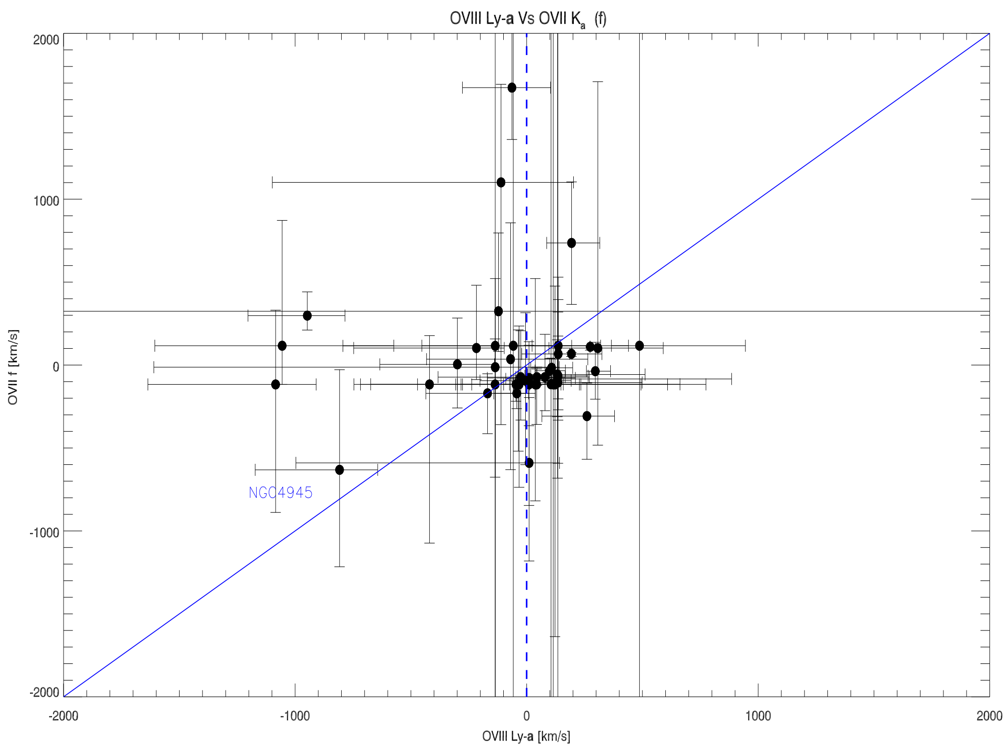

Figure 3.27: *Line energy centroids shift. NGC4945 is the only one source who shows significant systematic energy shifts (in the same direction) at the 1σ level for both lines.*

3.4 Method B: Blind search for emission lines

In this section, we present a new approach for the analysis of the CAIXA-A catalogue: each spectrum was again systematically searched for the presence of emission lines, but this time the energy of the emission lines was left as a free parameter. Each spectrum was divided into narrow bands. "Local" fits to the data were performed on unbinned spectra 100 channels intervals, using Gaussian profiles to account for any line features. Local continua were modeled with $\Gamma = 1$ powerlaws[7], leaving free in each fit the continuum normalization (Γ is the power-law photon index). No assumption was made *a priori* on the line centroid energies. Each interval of the spectrum was modelled as Gaussian line with energy that was left free to vary between the minimum and the maximum energy of the interval itself, and with normalization that was left free to vary between zero and 10^{-4} photons $cm^{-2}s^{-1}$. Then the χ^2 map is stored as a function of these two parameters, and the combinations of energy and normalization that give an improvement of 68%, 90%, 99% compared to the fit with the powerlaw only are marked. Line luminosities have been corrected for Galactic photoelectric absorption using column densities after Dickey & Lockman (1990).

In Figure 3.29, 3.30 we show the contour plots for two interesting parameters for our "local" fits for the archetypal Seyfert 2 galaxies NGC1068. Contour levels are drawn at predefined values of χ^2 (2.3, 4.61, and 9.21) with respect to the best-fit model, corresponding to the 68%, 90%, and 99% statistical confidence level for the two interesting parameters chosen (energy and flux). Superimposed on the plot you can see the locations of the emission lines searched for in the previous analysis (see Sect. 3.3).

As already said before, CAIXA-A spectra have different quality. As for Method A, generally we have more detections for sources with good RGS percentage of net count rates as shown in Fig 3.28, but we find some detections also for poor quality spectra at all confidence levels.

NGC1068 is the source with the best statistical quality in our catalogue (see Fig 3.28), but we got good results also with other sources, both those with middle statistical quality (as example NGC424 shown in Figure 3.32, 3.33), and those with poor statistical quality (MRK273 shown in Figure 3.34).

[7]Since the model used to fit the continuum is not very sensitive to the photon index Γ, due to the very limited band width of each segment, it has been fixed to 1.

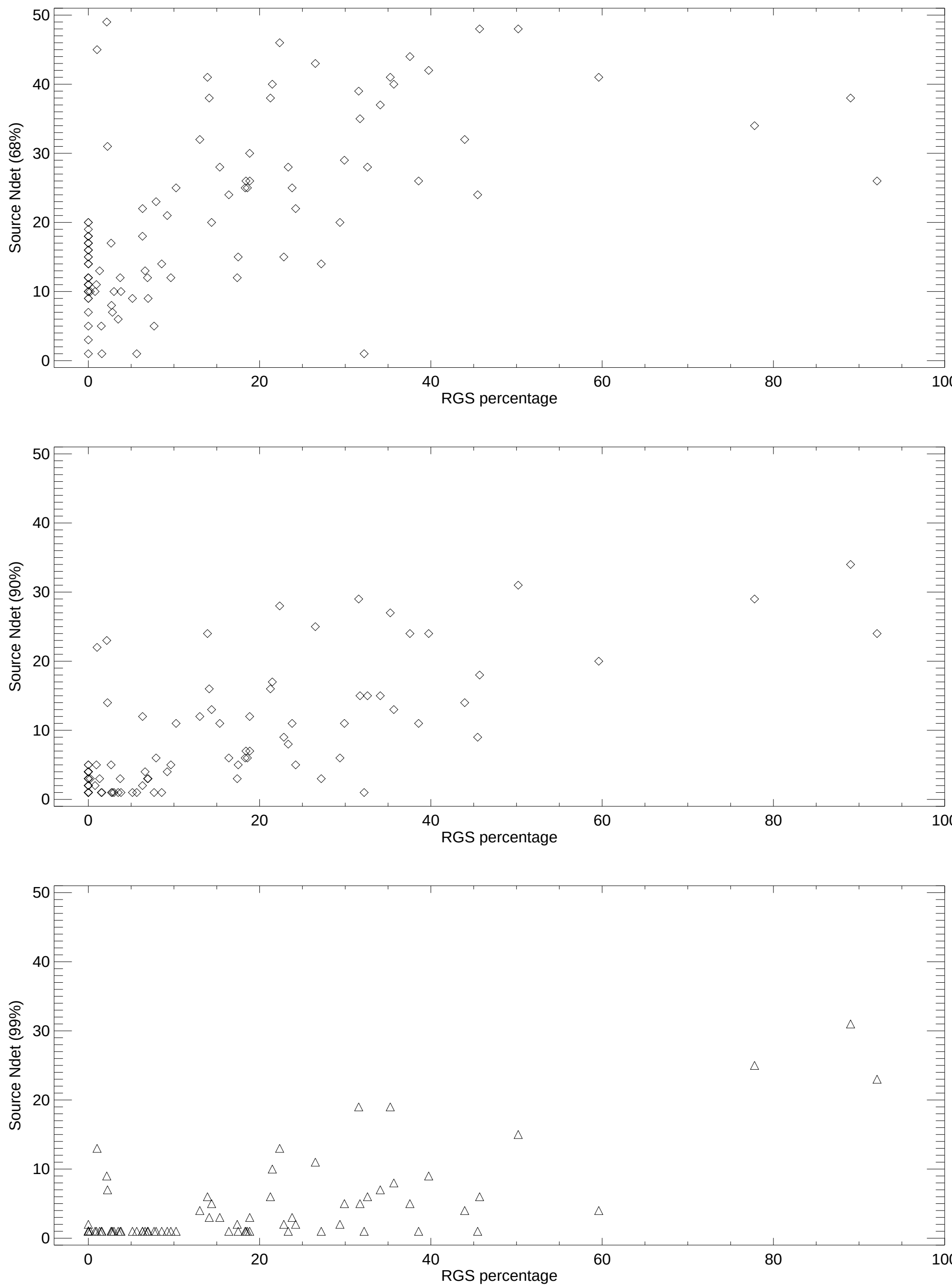

Figure 3.28: *Number of detections at the 68% (top), 90% (middle), 99% (bottom) confidence level for source with Method B vs percentage of net source count rates for combined RGS* ($0.4-0.9$ *keV), with respect to the background.*

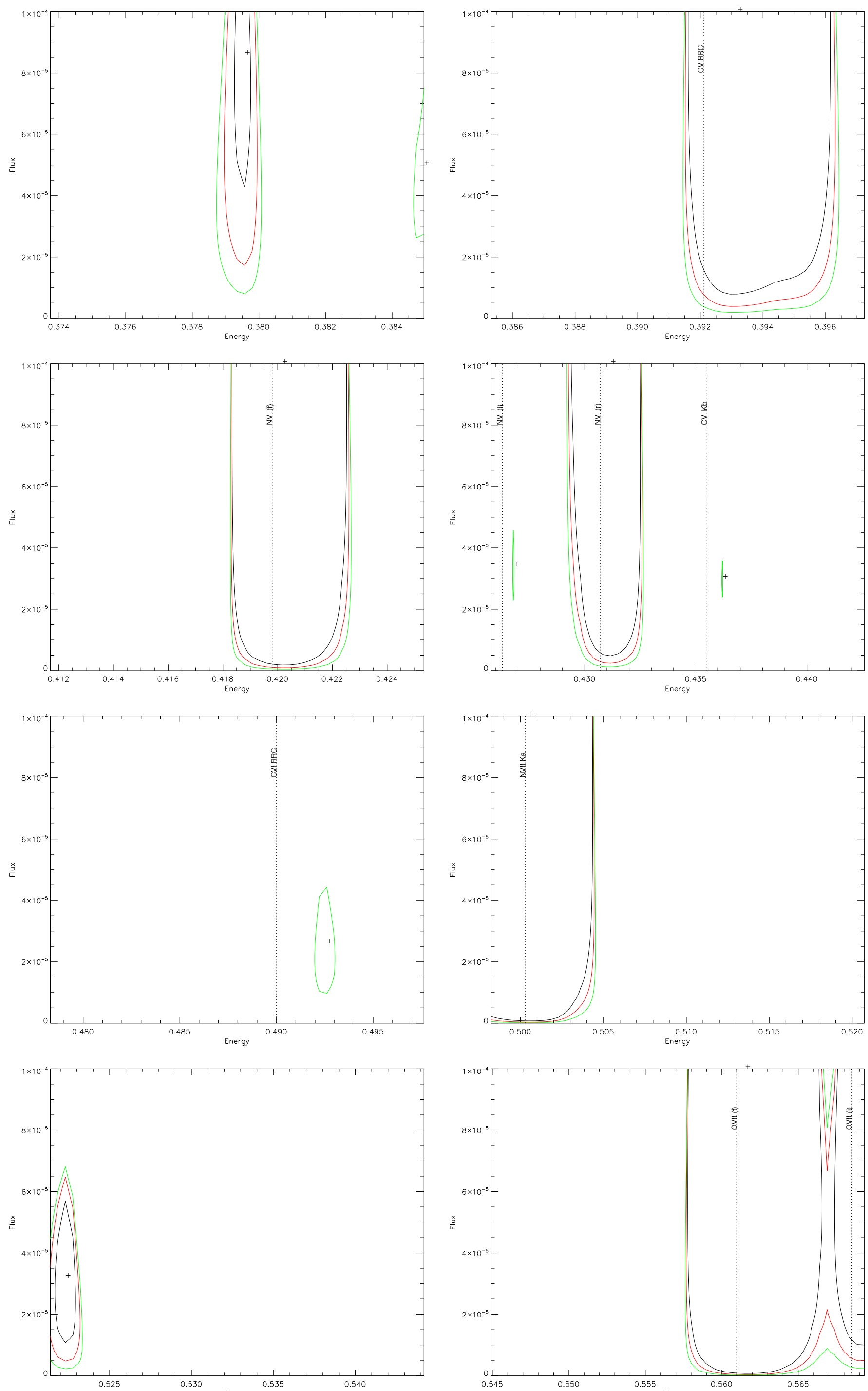

Figure 3.29: *NGC1068: centroid energy versus flux contour plots for the detected emission lines in the XMM-Newton RGS spectrum using Method B (see text for details). The contours refers to ΔC= 2.30, 4.61 and 9.21, i.e. confidence levels of 68, 90 and 99 per cent, respectively, for two interesting parameters. Ranges without detections at least at 90% confidence level are not shown.*

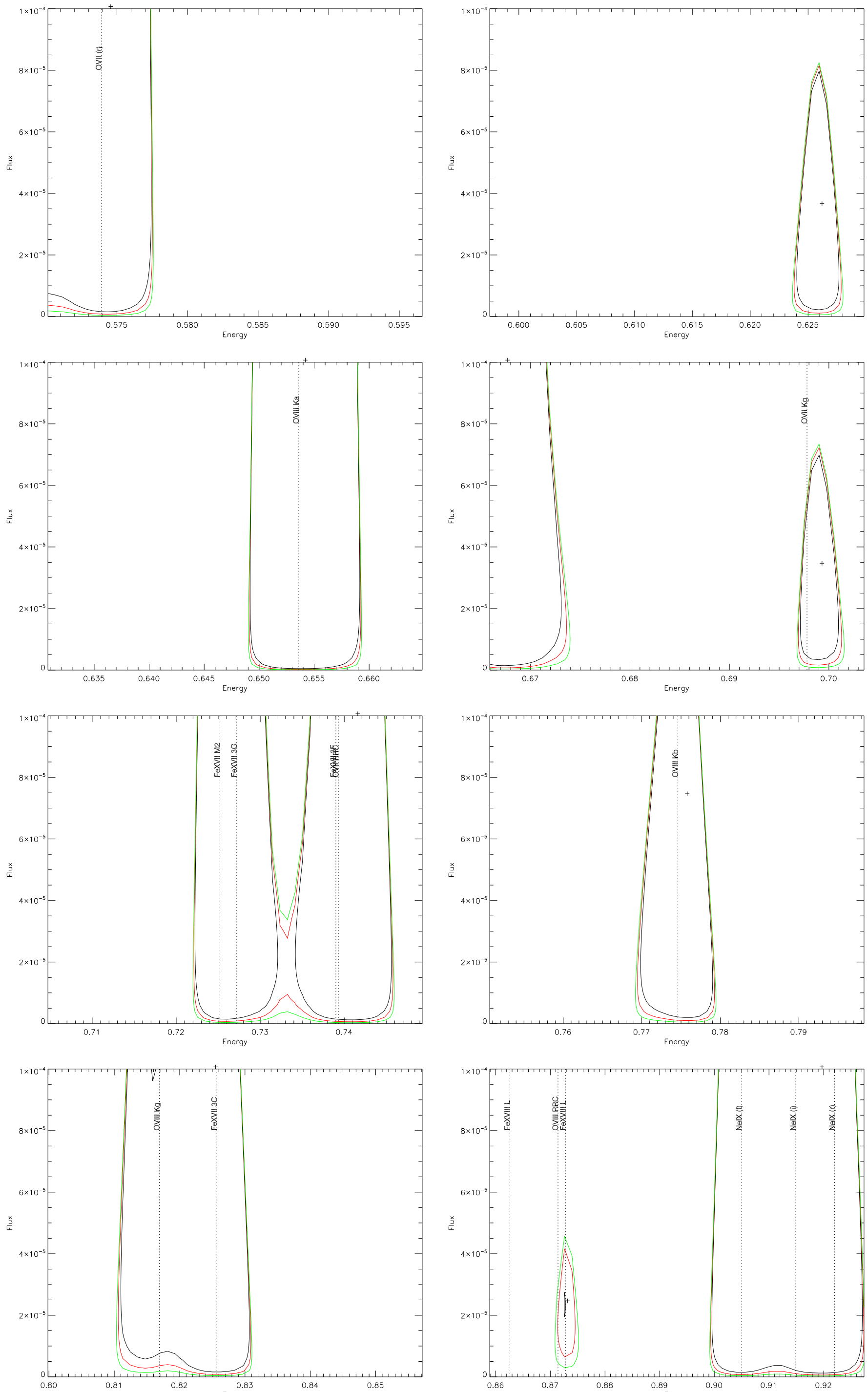

Figure 3.30: *As in Fig.3.29.*

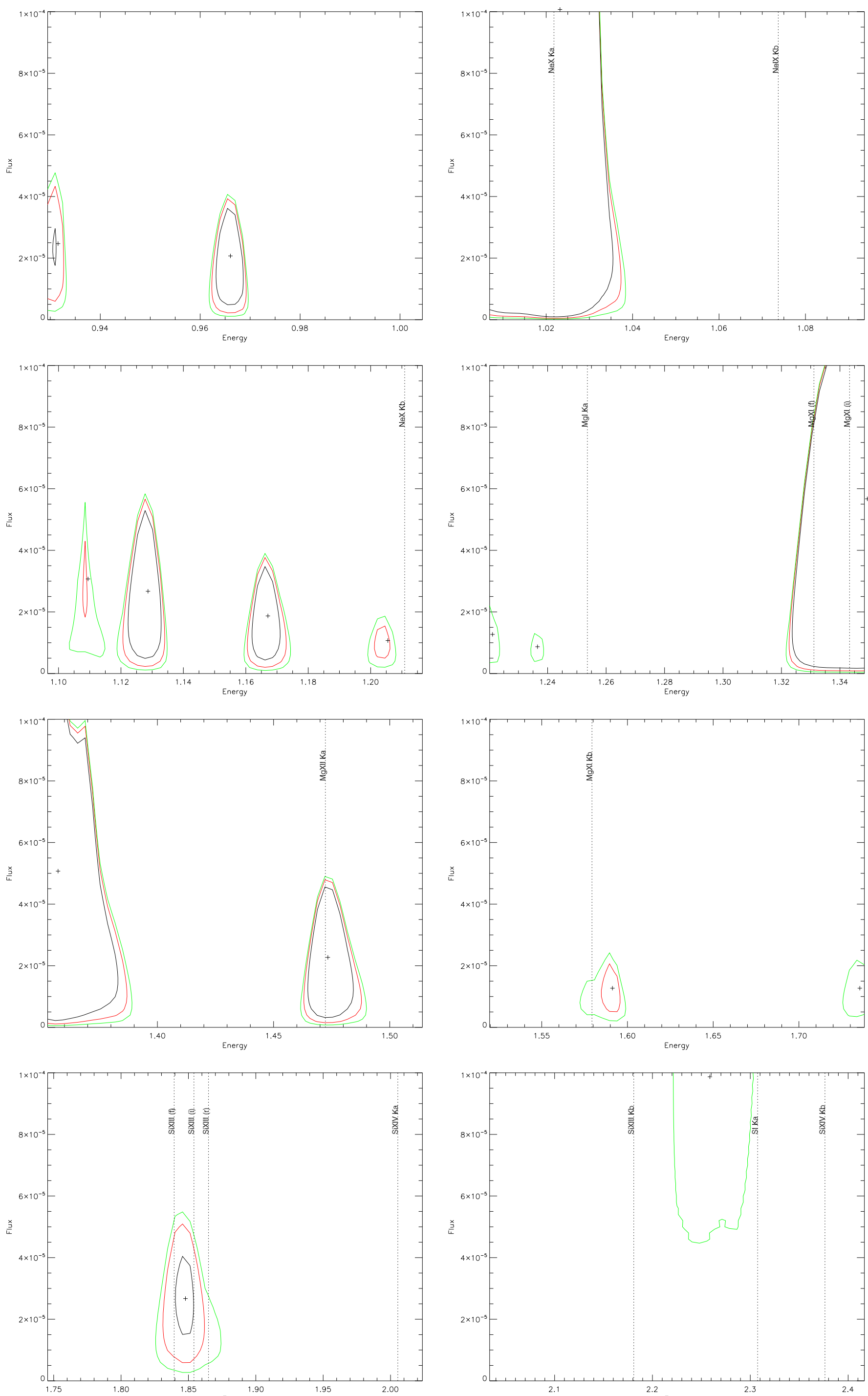

Figure 3.31: *As in Fig.3.29.*

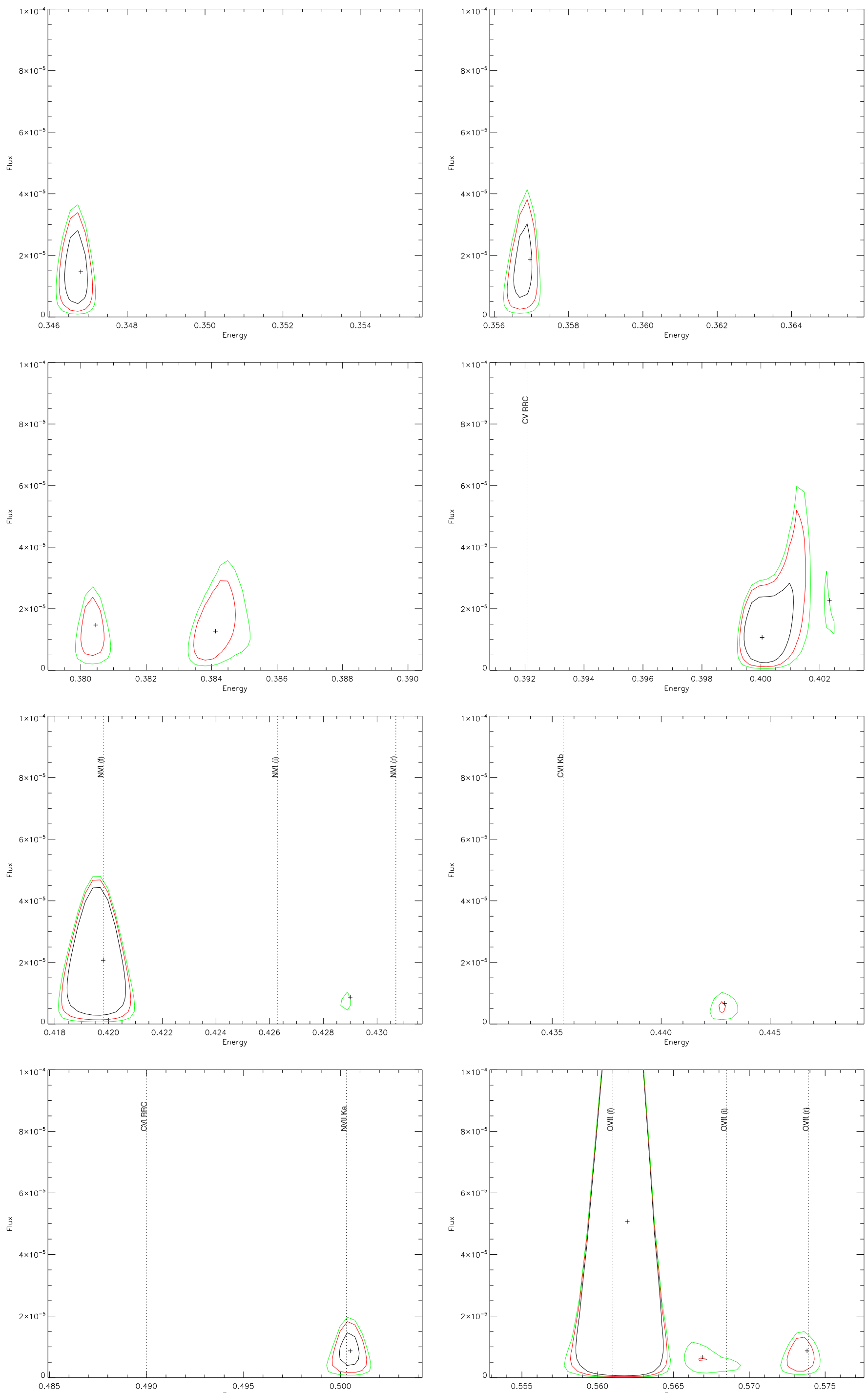

Figure 3.32: NGC424: centroid energy versus flux contour plots for the detected emission lines in the XMM-Newton RGS spectrum using Method B (see text for details). The contours refers to ΔC= 2.30, 4.61 and 9.21, i.e. confidence levels of 68, 90 and 99 per cent, respectively, for two interesting parameters. Ranges without detections at least at 90% confidence level are not shown.

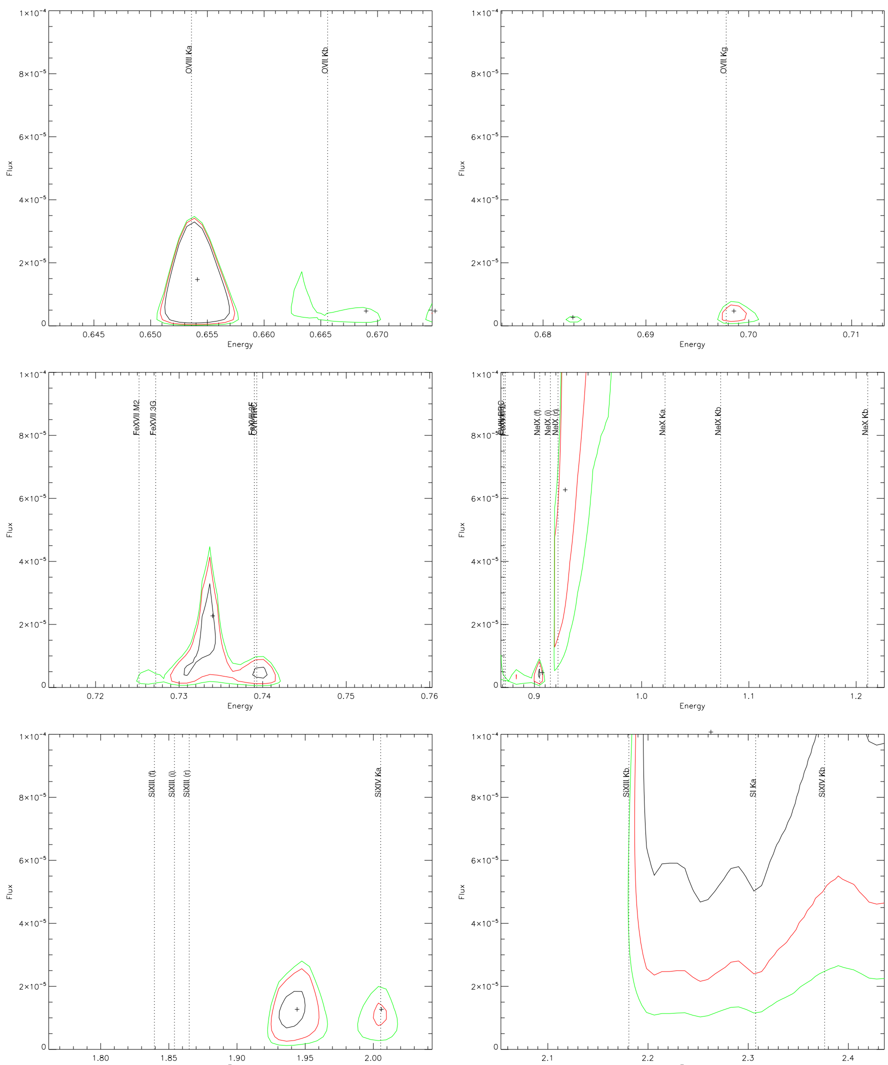

Figure 3.33: As in Fig.3.32.

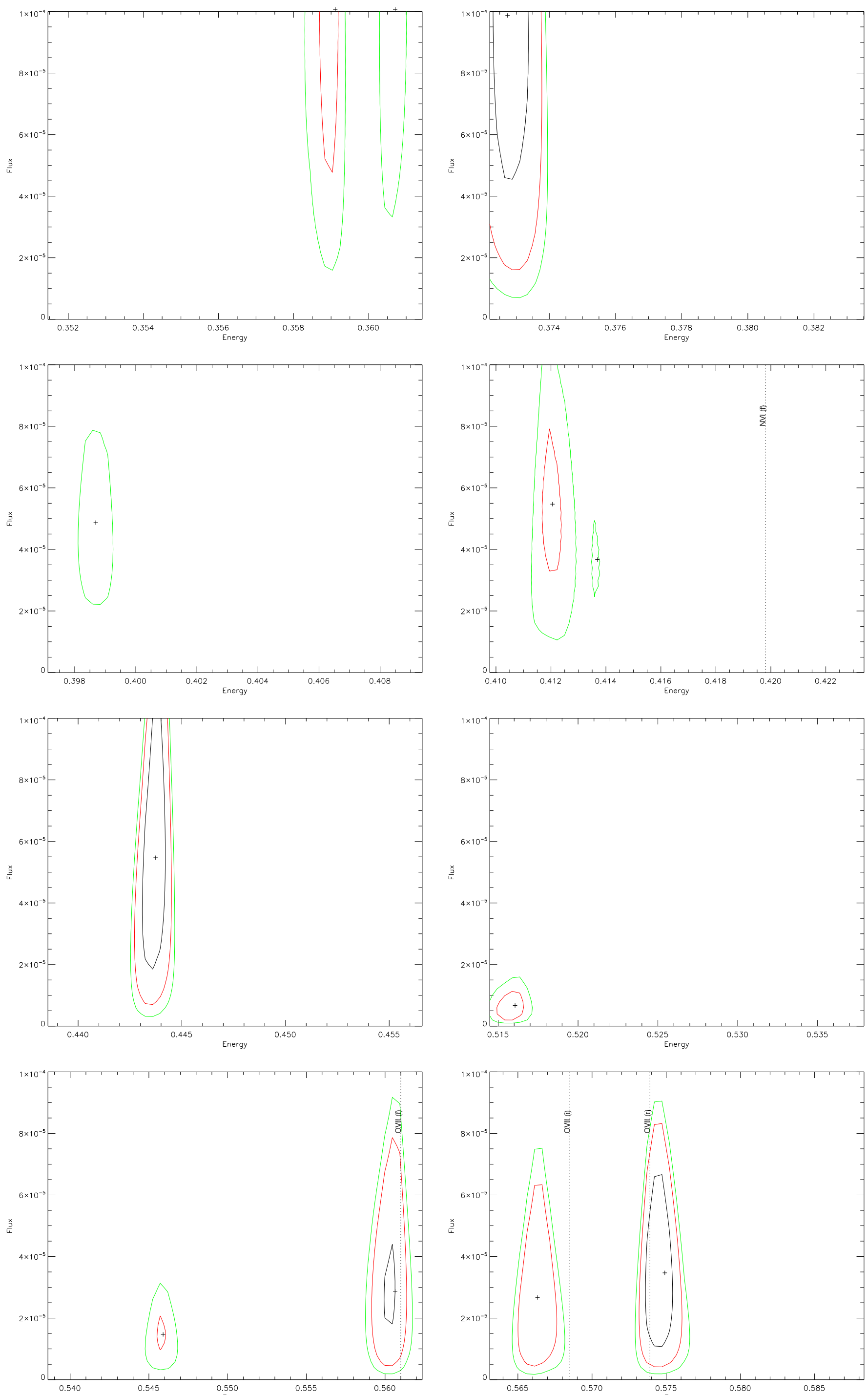

Figure 3.34: MRK273: centroid energy versus flux contour plots for the detected emission lines in the XMM-Newton RGS spectrum using Method B (see text for details). The contours refers to ΔC= 2.30, 4.61 and 9.21, i.e. confidence levels of 68, 90 and 99 per cent, respectively, for two interesting parameters. Ranges without detections at least at 90% confidence level are not shown.

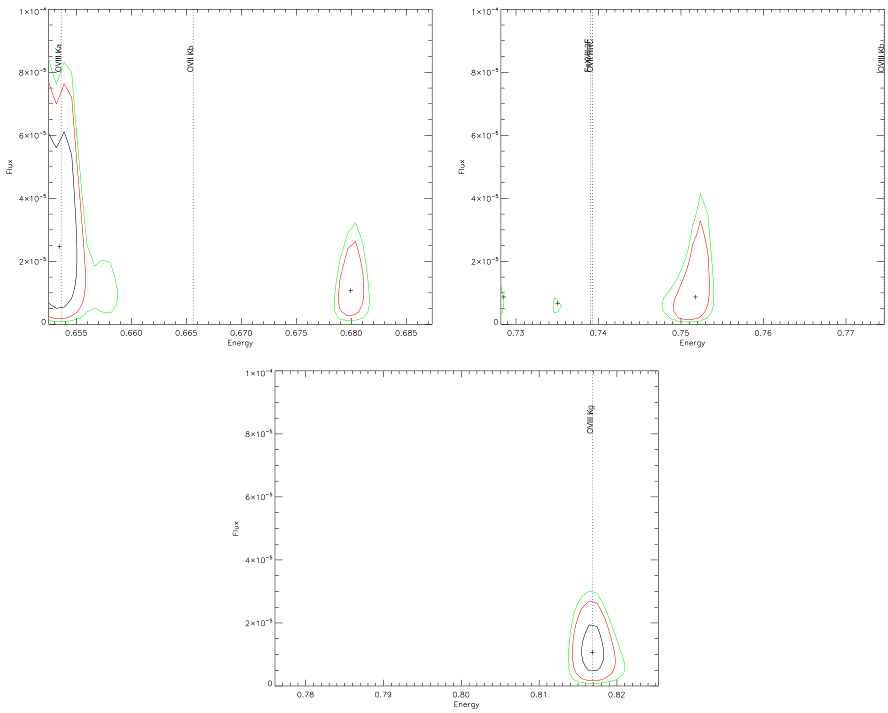

Figure 3.35: As in Fig.3.34.

In Tab. 3.3 we summarized the results of our analysis according to the different confidence levels. In Fig. 3.36 we show the number of detections for source according to the different confidence levels: all the CAIXA-A source have at least one detection at each confidence level (74 sources have 1 detection at 99% confidence level) and a few (6 sources) have more than 15 detections also at 99% confidence level (21 sources at 90% confidence level and 64 sources at 68% confidence level).

To test the robustness of our method and therefore to estimate the ”noise”, we made a simulated spectrum without emission lines for each source with the XSPEC *fakeit none* command. We simulated a simple power-law spectrum subjected to the Galactic photoelectric absorption (*wabs*, whose parameter is fixed to the hydrogen column of the corresponding source after Dickey & Lockman (1990)). The photon index of the powerlaw was kept fixed at 1, while the normalization has been fitted in order to reproduce the observed flux of each source. Background spectrum, response matrix and exposure time for each fake spectrum are those of the corresponding XMM-Newton RGS observation. Once obtained all the fake spectra we analyzed them with the same procedure used for the real spectra. So we obtained a number of detected lines that we reported in Tab. 3.3 according to the different confidence levels.

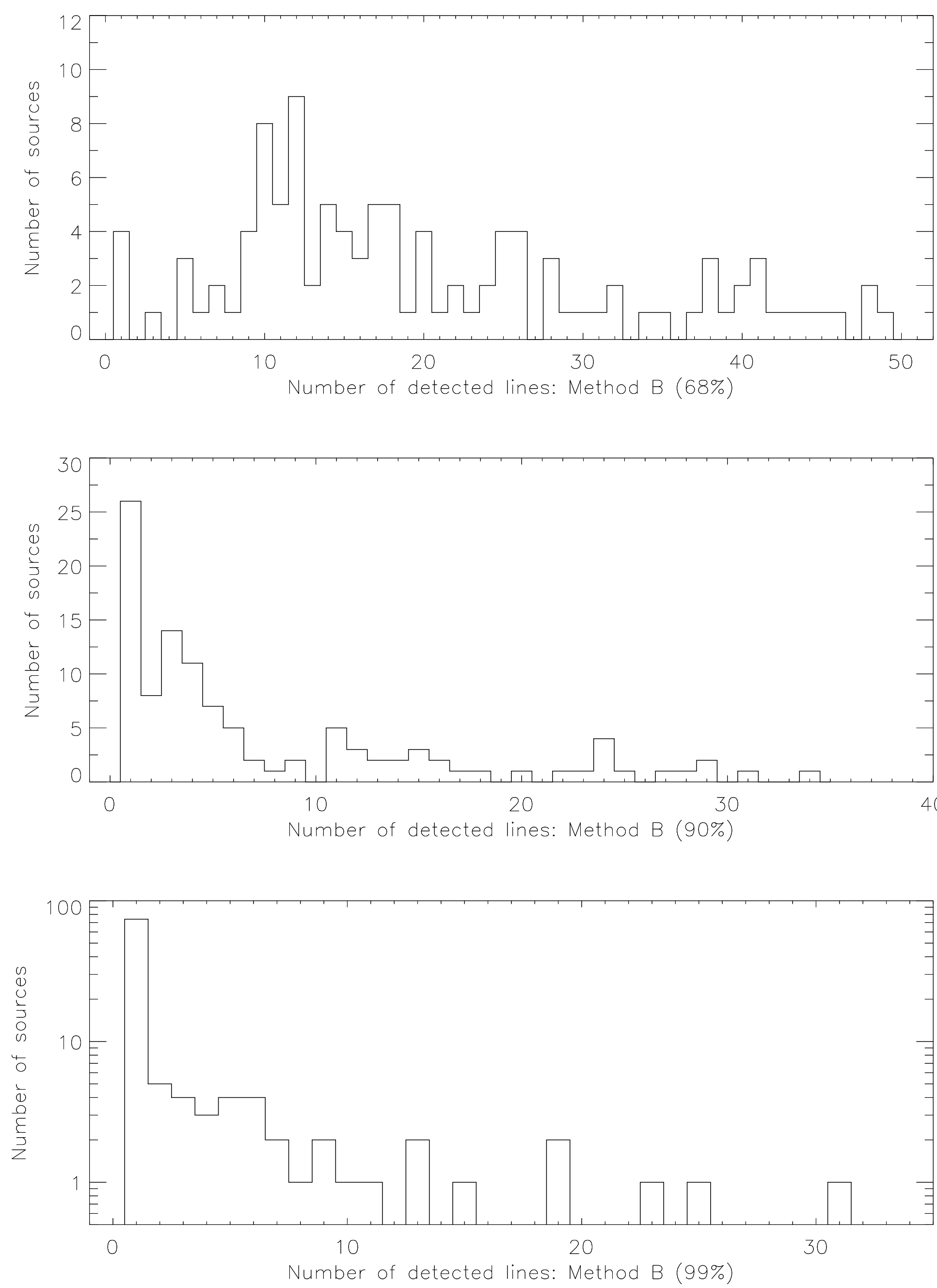

Figure 3.36: *Number of detections for source with Method B at 68%, 90% and 99% confidence levels.*

Table 3.3: Number of detected lines for the analysis with Method B of all the CAIXA-A catalogue for real and fake (simple-powerlaw) spectra. Last column is the result of the Kolmogorov-Smirnov test. See text for details.

Confidence level	Real	Fake	*prob*
68%	2557	1850	0.0084
90%	1265	527	0.24×10^{-7}
99%	569	56	0.00031

We compared the results of the analysis on the fake spectra with the results of the Method B analysis with the *KSTWO* idl routine that returns the Kolmogorov-Smirnov statistic and associated probability that two arrays of data values are drawn from the same distribution. To be more precise, given an array data1, and an array data2, this routine returns the Kolmogorov-Smirnov statistic *d*, and the significance level *prob* for the null hypothesis that two given data sets are drawn from the same distribution. Small values of prob show that the cumulative distribution function of data1 is significantly different from that of data2. The result of this test indicates that the two distributions are different (see Tab. 3.7) at each confidence level. The differences between the two numbers of detected lines (see Tab. 3.3) greatly increases when we pass from the 68% to 99% confidence level, so many of our detections are real.

In Figure 3.37 we show the total number of each detected lines (real spectra) for the 1-σ level (ΔC= 2.30), for the 90% confidence level (ΔC= 4.61) and for the 99% confidence level (ΔC= 9.21) against the energy of the lines. We obtained in this way a sort of spectrum representative of our 109 objects. Superimposed we plotted the results (smoothed with a 5-channels wide triangular kernel: we used the IDL *CONVOL*[8] command) for the fake spectra, in order to have an estimate of the noise.

Analyzing more in detail the results of the Method B (see zoomed figures from 3.38 to 3.43) we can say that:

- The most detected emission lines are O VIII α, O VII f, Fe XVII 3d-2p ($^1P_1$) for all confidence levels. These lines are also among the most detected lines with Method A.

- Diagnostics on the O VII triplet is a good indicator of the ionization mech-

[8]The CONVOL function convolves an array with a kernel, and returns the result. Convolution is a general process that can be used for various types of smoothing, signal processing, shifting, differentiation, edge detection, etc.

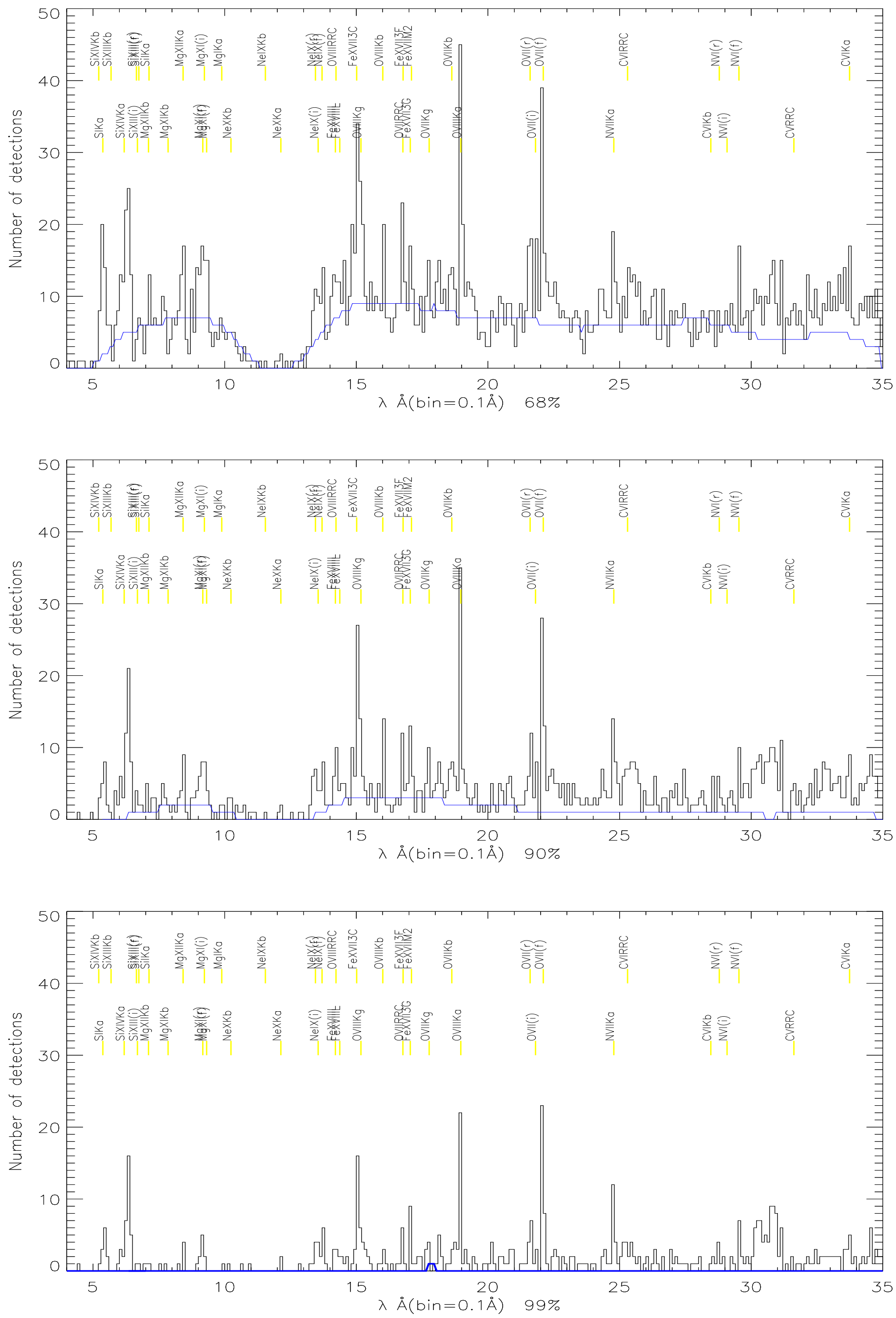

Figure 3.37: *Cumulative emission line detections with Method B at the 68% (top), 90% (middle), 99% (bottom) confidence level. The blue line is an estimate of the noise, extracted from simulations (see text for details). The positions of the line transitions considered for Method A are labeled.*

anism of the gas. Indeed, the predominance of the forbidden component in this analysis is a sign of photoionization, confirming what we found with Method A.

- Among the detected emission lines, we found a transition which can be readily identified with neutral S Kα at 2.308 keV (House 1969), likely arising from the same Compton-thick material responsible for the production of the features which dominate the high-energy part of the spectrum, that is the Compton reflection component and the neutral iron Kα line. Other fluorescence lines are not detected.

- At an energy between the SiXIV Kα and the SiXIII Kα triplet, there is an accumulation of several detections not clearly associated to known transitions (see Figure 3.37): this is probably a blend of the two adjacent sets of lines that automatic fits cannot entangle. Both Si lines are not fitted with Method A, where we consider only the most intense emission lines in the 0.3–1 keV band, while these Si lines are very intense only in the case of a gas with a little higher photoionization (or collisional ionization) than that which produces most of the lines considered.

- No unknown lines are significantly detected at any confidence level, except for a structure around 0.4 keV (31 Å). This structure should be due to a series of emission lines of SXIV. In the future we will investigate the potential diagnostic capabilities of these lines to disantangle the ionization equilibrium of the gas that produces them.

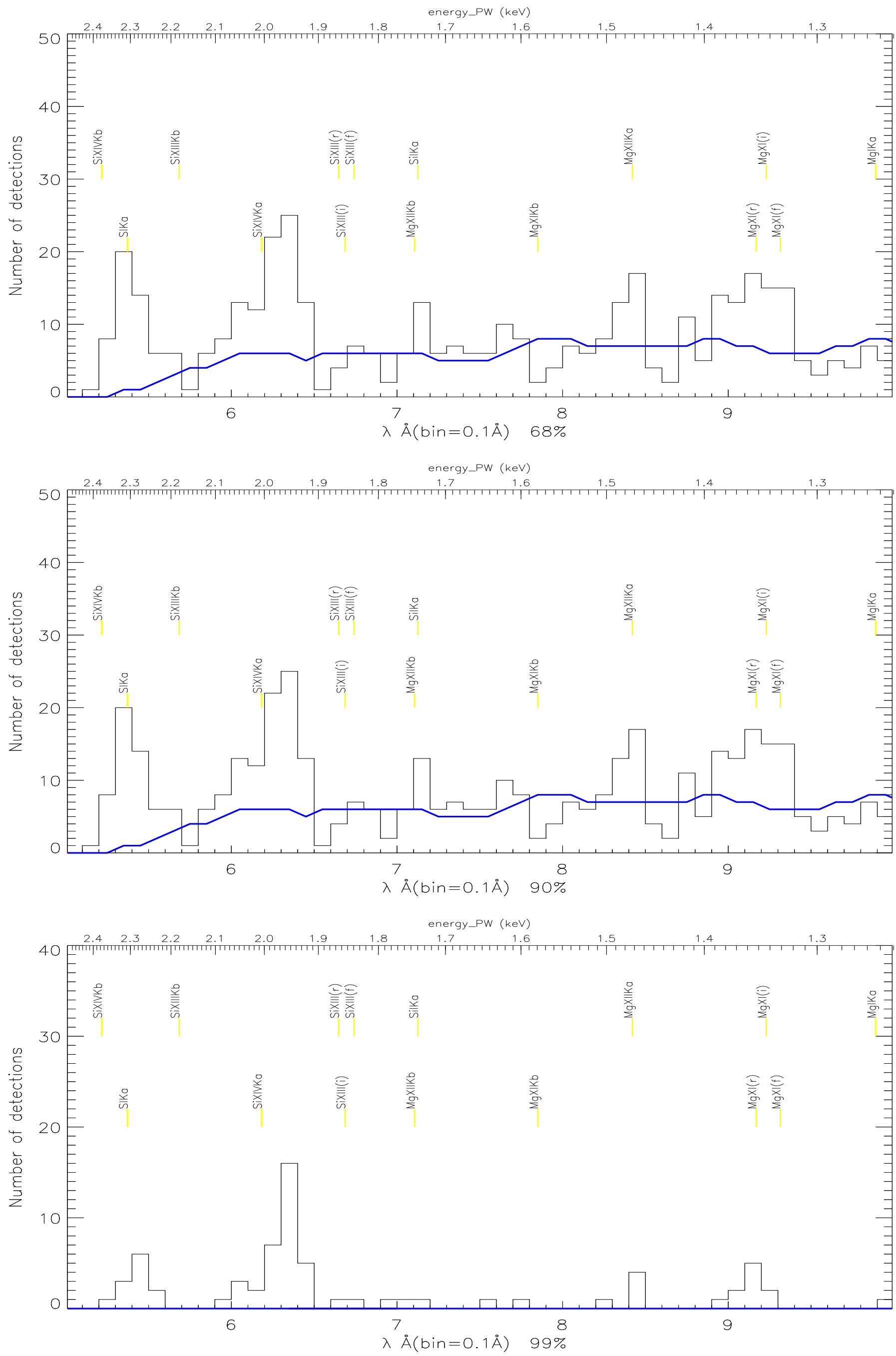

Figure 3.38: *Same as Fig.3.37, but for the energy range* 5 – 10Å.

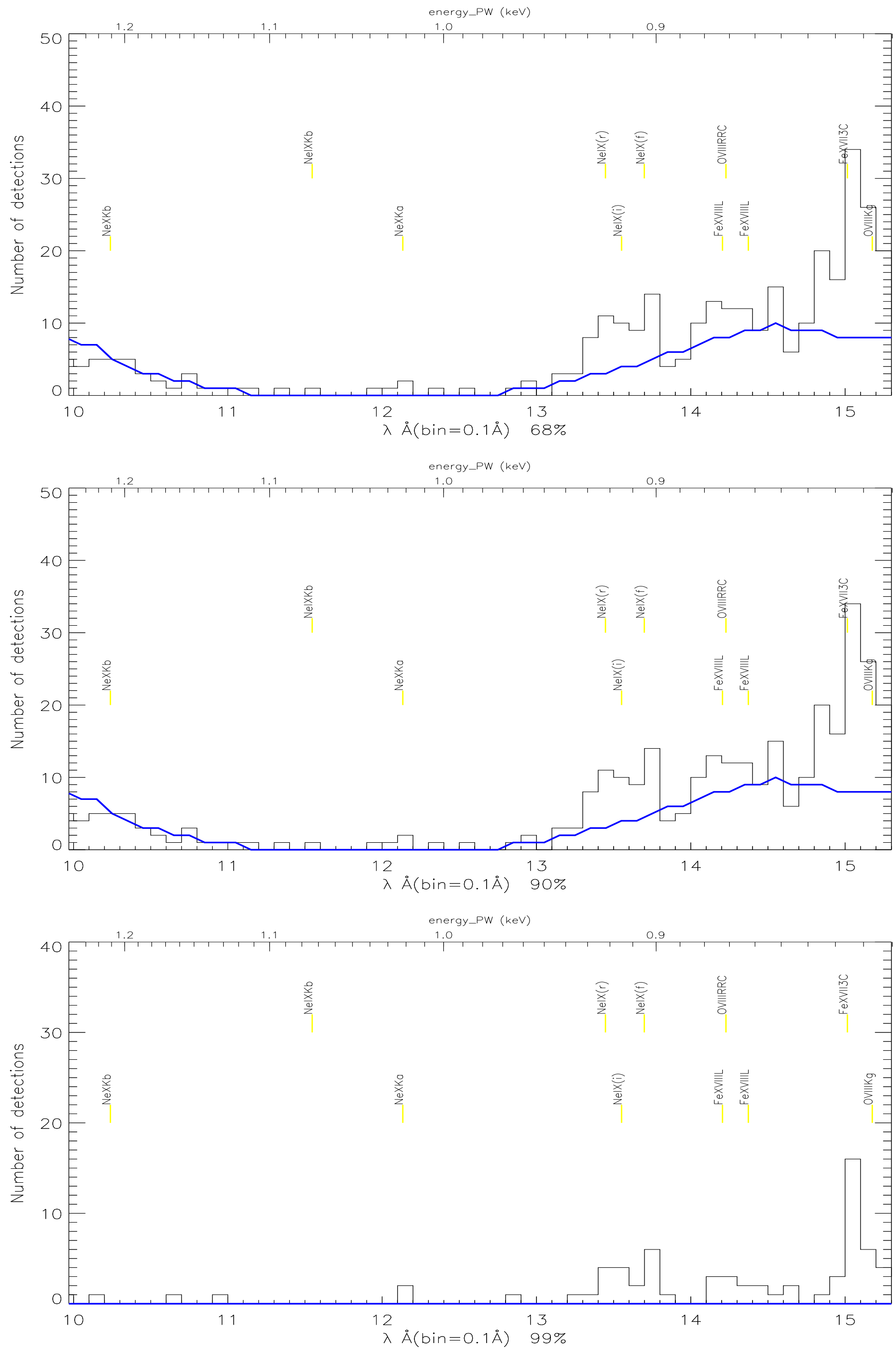

Figure 3.39: *Same as Fig.3.37, but for the energy range* 10 – 15Å.

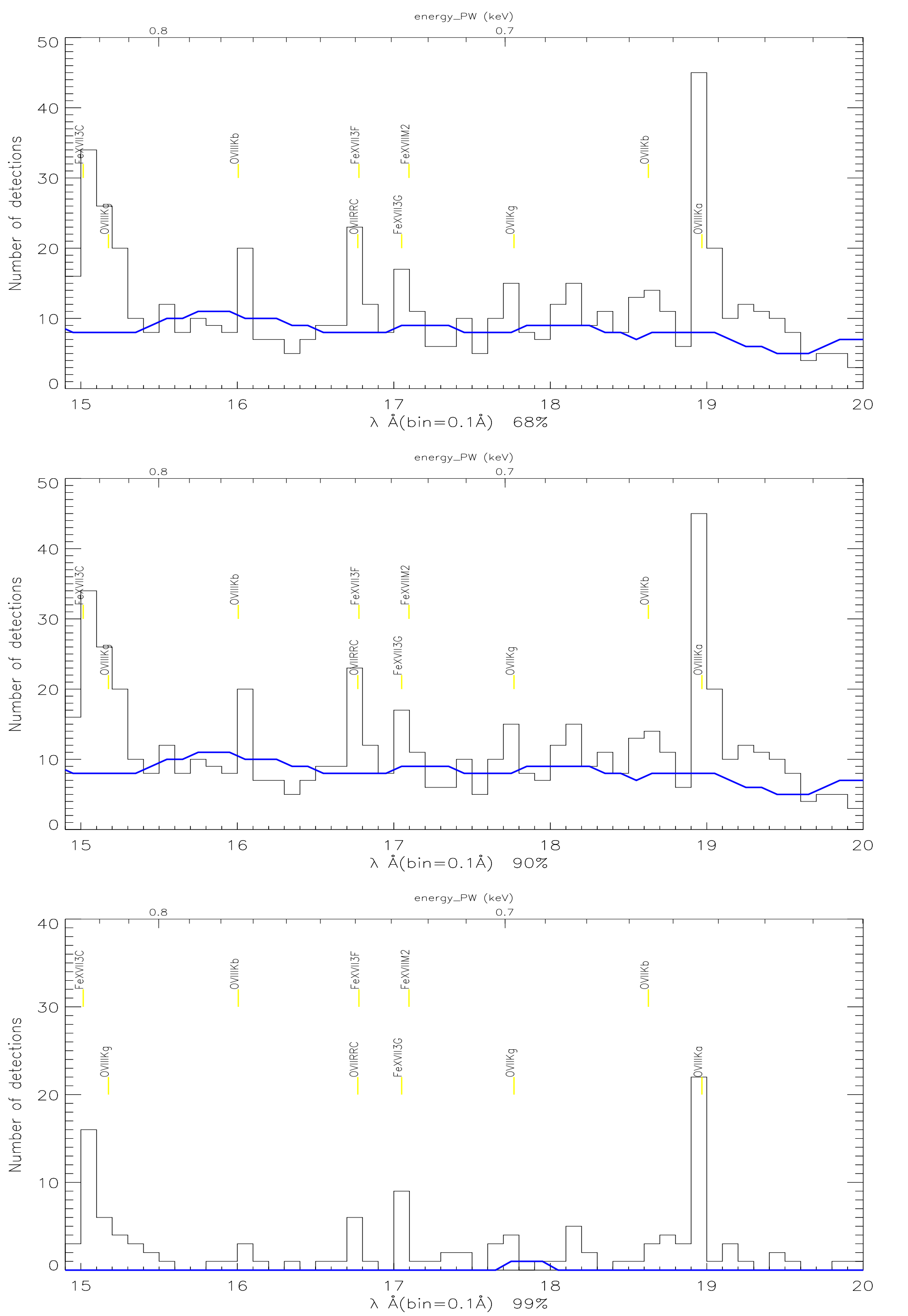

Figure 3.40: *Same as Fig.3.37, but for the energy range* 15 – 20Å.

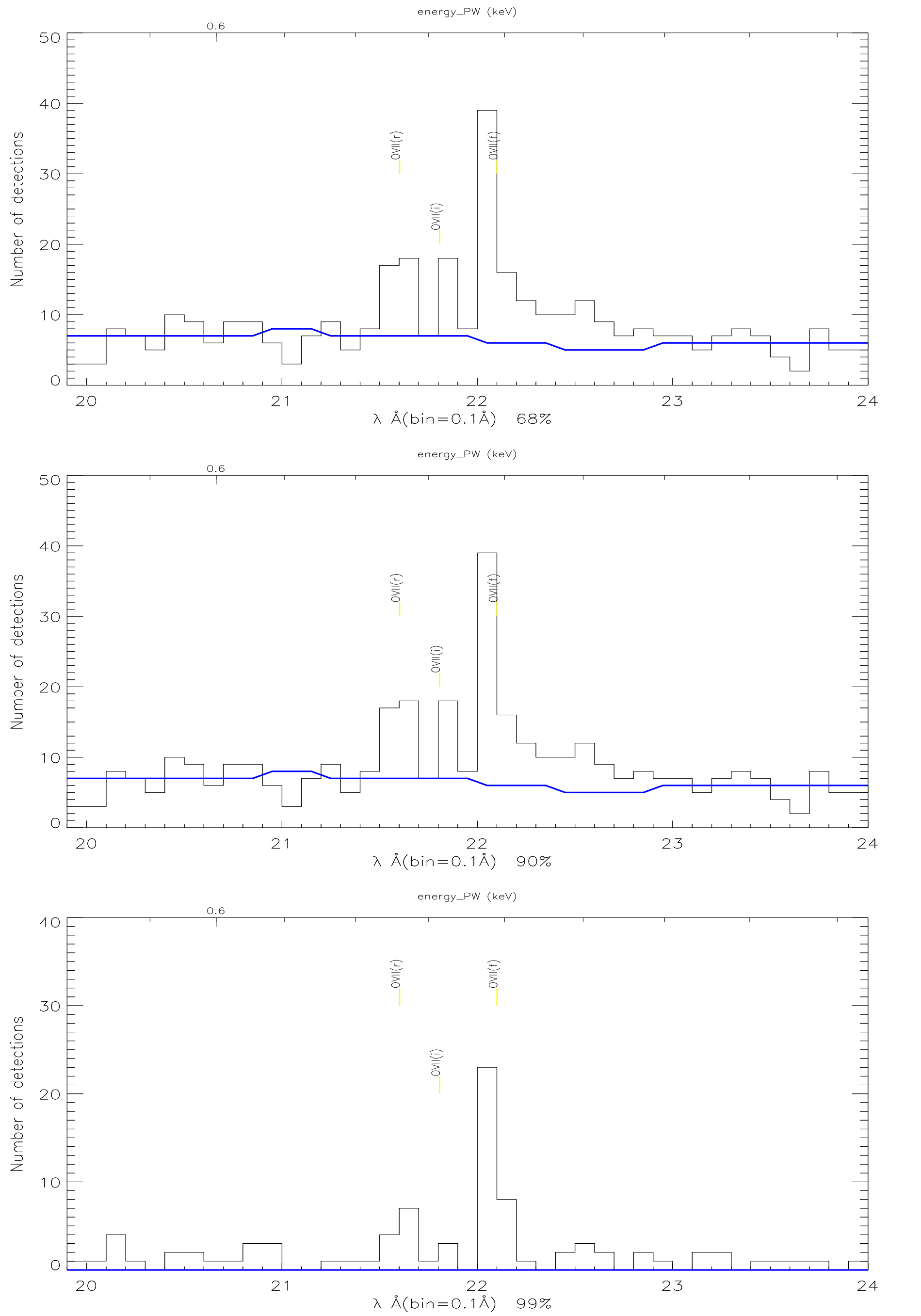

Figure 3.41: *Same as Fig.3.37, but for the energy range* 20 – 24Å.

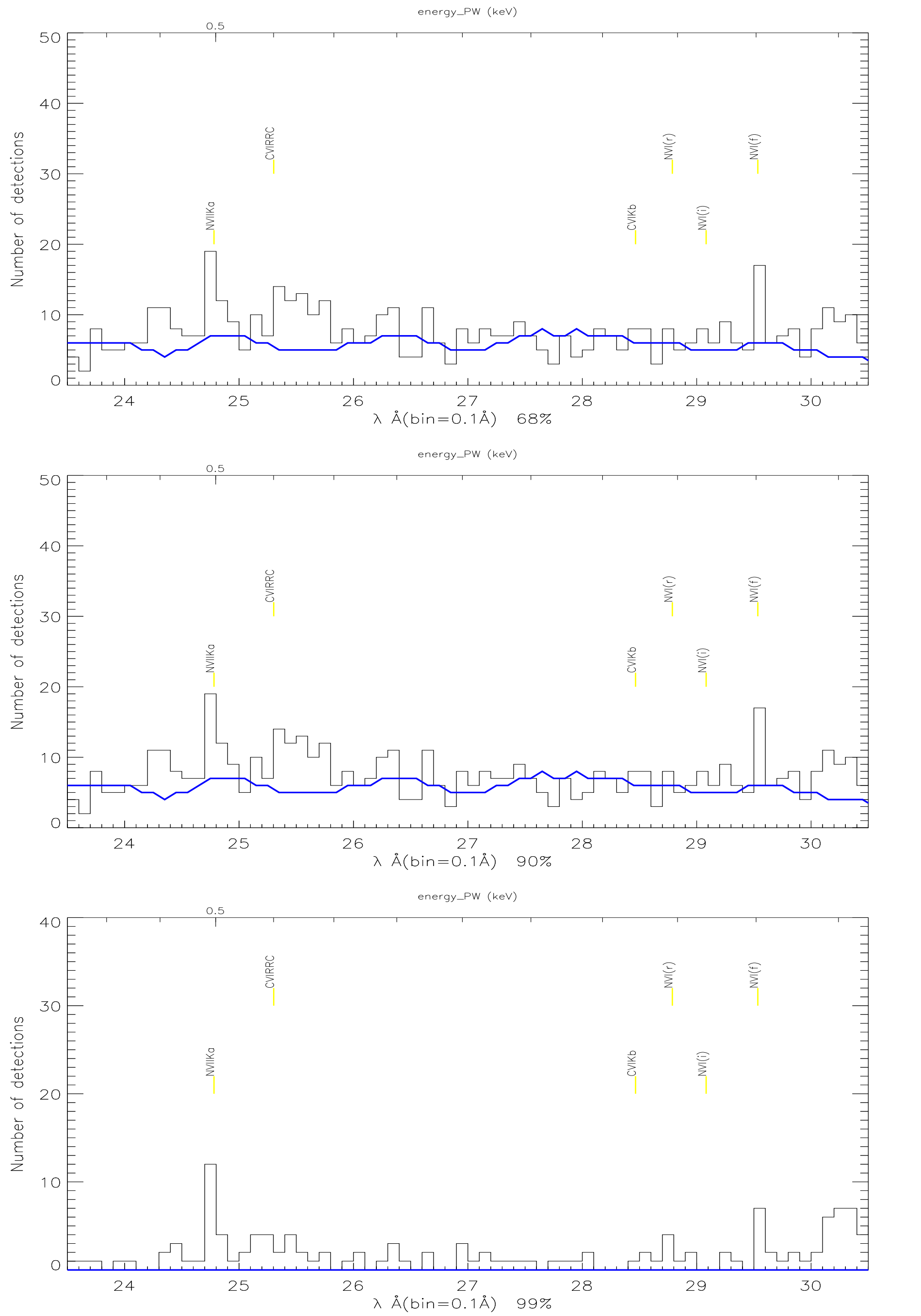

Figure 3.42: *Same as Fig.3.37, but for the energy range* 24 – 30Å.

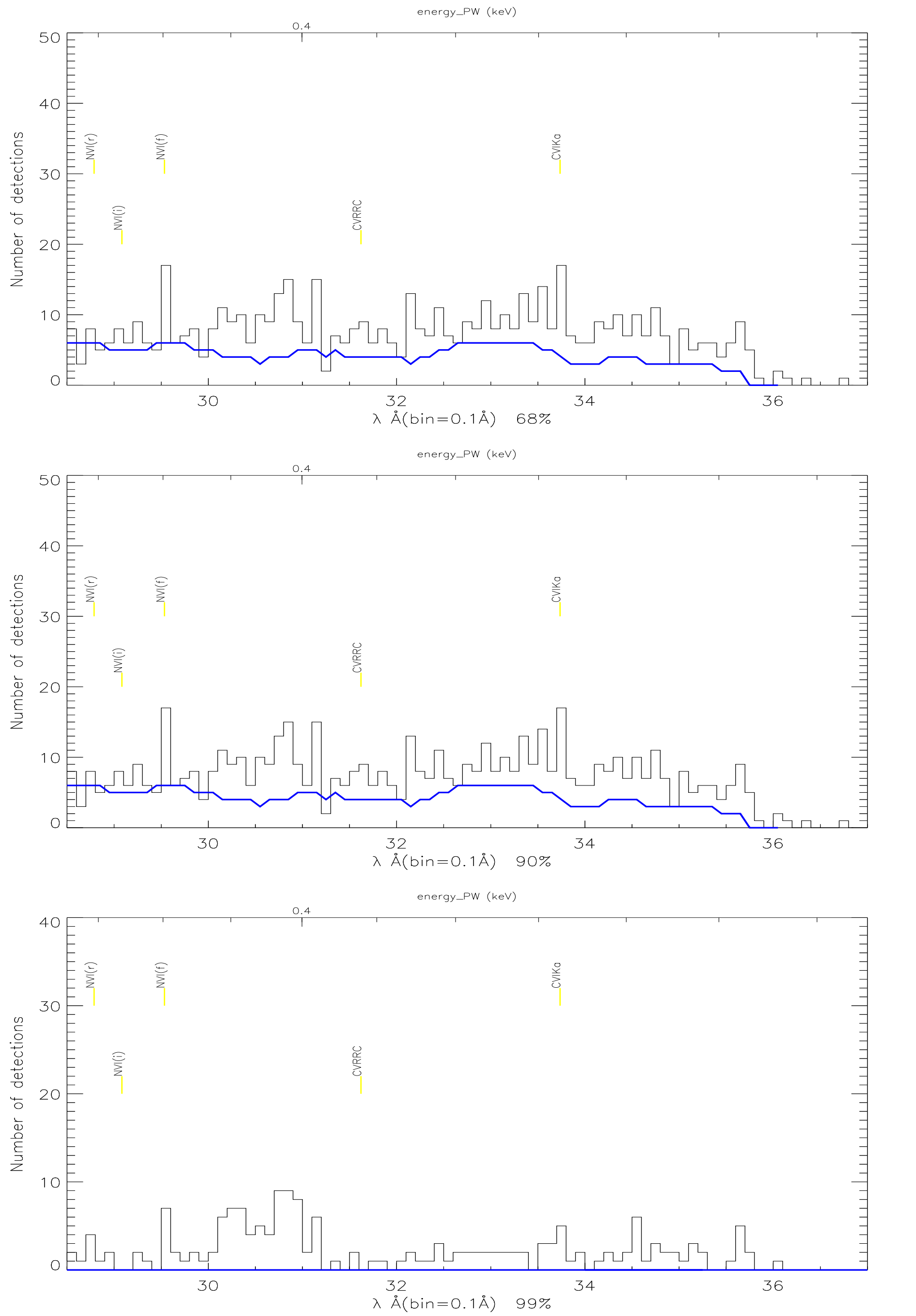

Figure 3.43: *Same as Fig.3.37, but for the energy range* 30 – 37Å.

3.5 Method C: Self-consistent plasma models in collisional and photoionization equilibrium

After the phenomenological fits performed in the last two sections, we proceeded to a self-consistent modelling of the soft X-ray emission lines detected in the RGS spectra of CAIXA-A. The basic atomic processes in astrophysical X-ray emitting plasmas are two-body collisional excitation and ionization, photoexcitation and ionization, spontaneous radiative decay, and two-body recombination (see Sect.2.2.1). A consequence of this is that the plasmas can be separated into two categories depending on the temperature T_e of the gas and the ionization energy of the ions that constitute it:

1. Collisional: $k_B T_e \sim$ ionization energy of plasma ions.

2. Photoionized: $k_B T_e <<$ ionization energy of plasma ions .

In this section, we analyze our data with five different combinations of plasma. The five baseline models we used to fit the 0.4-0.9 keV[9] spectra can be roughly expressed by the five following general formulas:

- a single photoionized plasma:

$$C : F(E) = e^{-\sigma(E) N_H^G}[Ph_C], \tag{3.3}$$

- a single collisionally-ionized plasma:

$$A : F(E) = e^{-\sigma(E) N_H^G}[Co_A], \tag{3.4}$$

- a collisionally-ionized plasma plus a photoionized phase:

$$AC : F(E) = e^{-\sigma(E) N_H^G}[Ph_C + Co_A], \tag{3.5}$$

- two different collisionally-ionized plasma:

$$AA : F(E) = e^{-\sigma(E) N_H^G}[Co_{A1} + Co_{A2}], \tag{3.6}$$

- two photoionized phases:

$$CC : F(E) = e^{-\sigma(E) N_H^G}[Ph_{C1} + Ph_{C2}], \tag{3.7}$$

[9]The choice of the 0.4-0.9 keV band corresponds to the region of largest effective area of both RGS units together (see Fig.A.3).

where $\sigma(E)$ is the photoelectric cross-section (abundances as in Anders & Grevesse 1989), N_H^G is the Galactic absorbing column density along the line of sight to the source (Dickey & Lockman 1990); Co_A is emission from a a collisionally ionized plasma, as modelled by APEC, the Astrophysical Plasma Emission Code, which uses atomic data in the companion Astrophysical Plasma Emission Database (APED) to calculate spectral models for hot plasmas. The APEC parameters are the normalization, the electron temperature, and the plasma metallicity. We fixed the plasma metallicity to 1 and we fit the model with normalization and electron temperature as free parameters. Ph_C is the emission from a photoionized gas reproduced with self-consistent CLOUDY[10] (Ferland 2000) models as described in Bianchi et al. (2010) and Marinucci et al. (2011). The main ingredient is the ionization parameter U (Osterbrock et al. (2006)), defined as:

$$U = \frac{\int_{\nu_R}^{\infty} \frac{L_\nu}{h\nu} d\nu}{4\pi r^2 c n_e} \tag{3.8}$$

where c is the speed of light, r the distance of the gas from the illuminating source, n_e its density and ν_R the frequency corresponding to 1 Rydberg. The incident continuum has been modeled as in Korista et al. (1997), a constant electron density $\mathrm{n_e} = 10^5$ cm^{-3} has been used and elemental abundances can be found as in Table 9 of CLOUDY documentation[11]. The resulting grid parameters are $\log U = [-2.00 : 4.00]$, step 0.25, and $\log N_\mathrm{H} = [19.0 : 23.5]$, step 0.1. Only the reflected spectrum, arising from the illuminated face of the cloud, has been taken into account in our model. We also produced tables with different densities ($\mathrm{n_e} = 10^3 - 10^4$ cm^{-3}): all the fits presented in this thesis resulted to be insensitive to this parameter, as expected since we are always treating density regimes where line ratios of He-like triplets are insensitive to density (Porquet & Dubau (2000)). In Fig. 3.44, 3.45, 3.46 , 3.47, 3.48 we show examples of best fits respectively for ModelC, ModelA, ModelAC, ModelAA, ModelCC.

Up to now we used all spectra for our analysis because we were looking for individual lines, but it is known that, if the data used in the fit are not particularly good, one may be able to find many different models for which adequate fits can be found. For this kind of analysis we need spectra of good quality, therefore we selected only those sources that had at least 20% background-subtracted mean count rates for combined RGS (RGS1+RGS2) between $0.4 - 0.9$ keV[12].

In Fig. 3.8 we show the total counts against the percentage of background-subtracted count rates in 0.4 – 0.9 keV band: 29 spectra are above the 20% threshold, and will be analyses in this section. In Tab. 3.4 we listed the 29 CAIXA-A

[10] http://www.pa.uky.edu/~gary/cloudy/

[11] Hazy 1 version 08, p. 67: `http://viewvc.nublado.org/index.cgi/tags/release/c08.00/docs/hazy1_08.eps?revision=2342&root=cloudy`

[12] The effective area reaches the maximum in the 0.4-0.9 keV band, see Fig A.3.

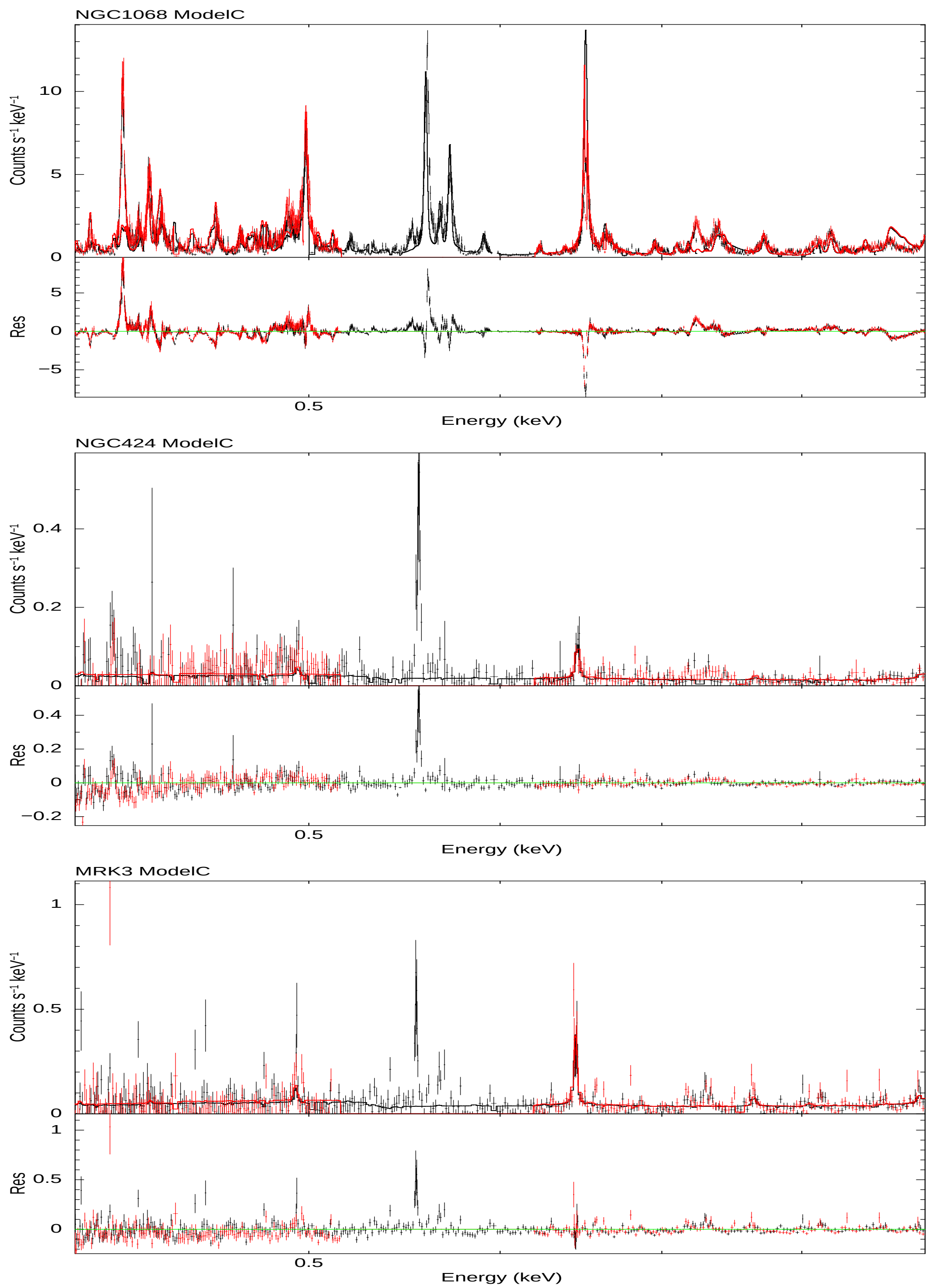

Figure 3.44: Example of best fits for ModelC for RGS1 (black) and RGS2 (red) between 0.4 and 0.9 keV. In the lower panel the plot of the residua is shown.

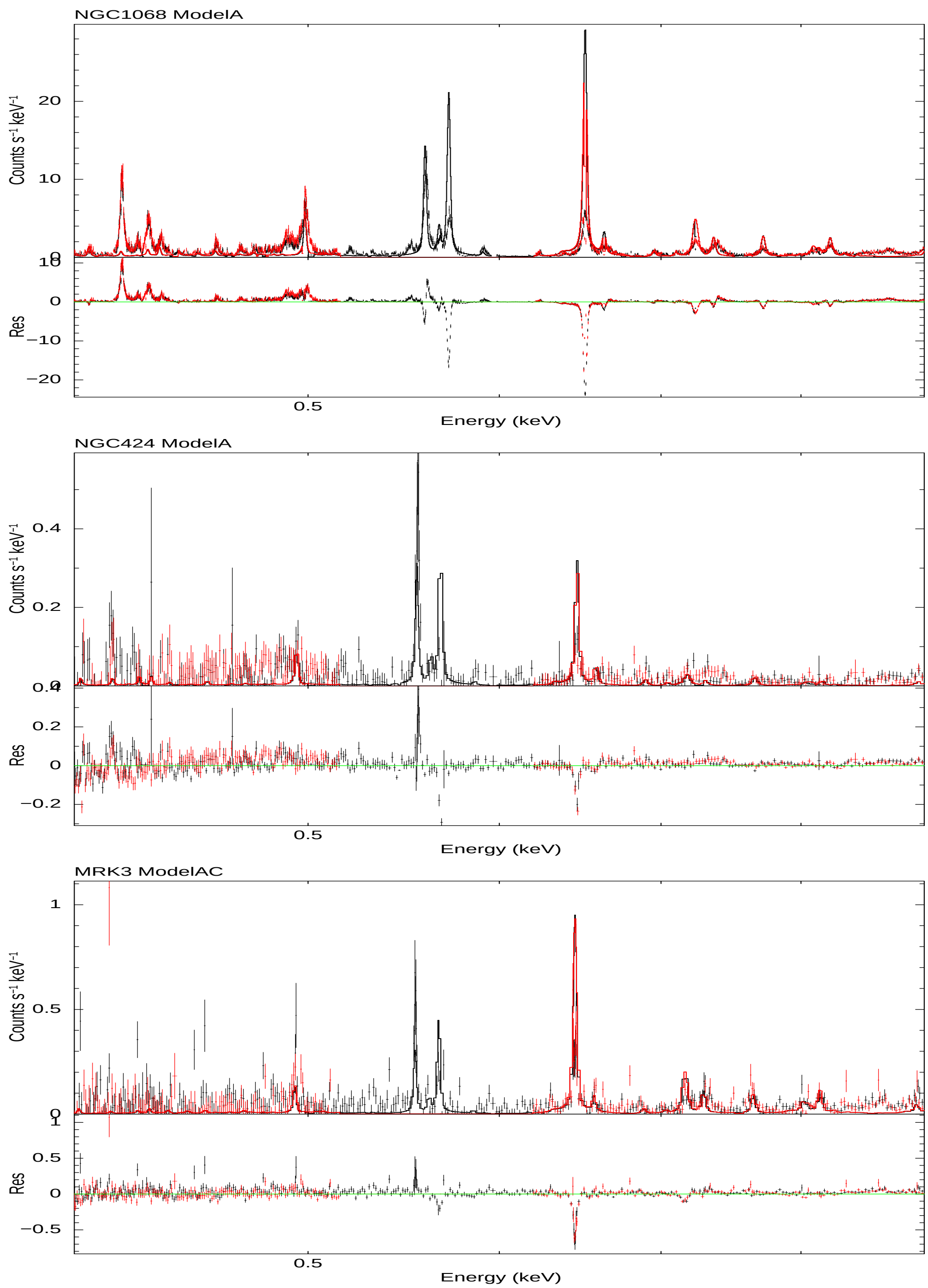

Figure 3.45: Example of best fits for ModelA for RGS1 (black) and RGS2 (red) between 0.4 and 0.9 keV. In the lower panel the plot of the residua is shown.

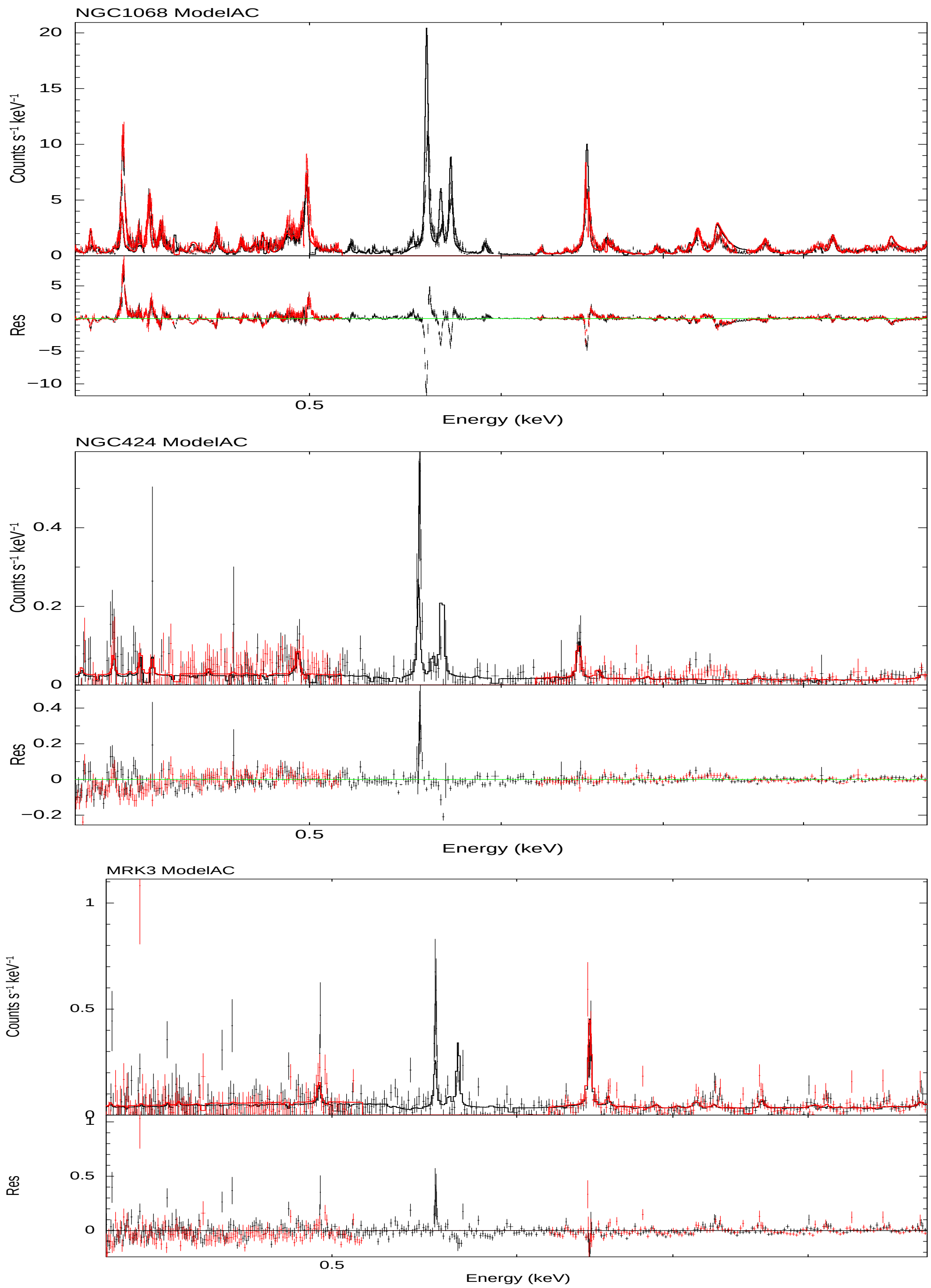

Figure 3.46: Example of best fits for ModelAC for RGS1 (black) and RGS2 (red) between 0.4 and 0.9 keV. In the lower panel the plot of the residua is shown.

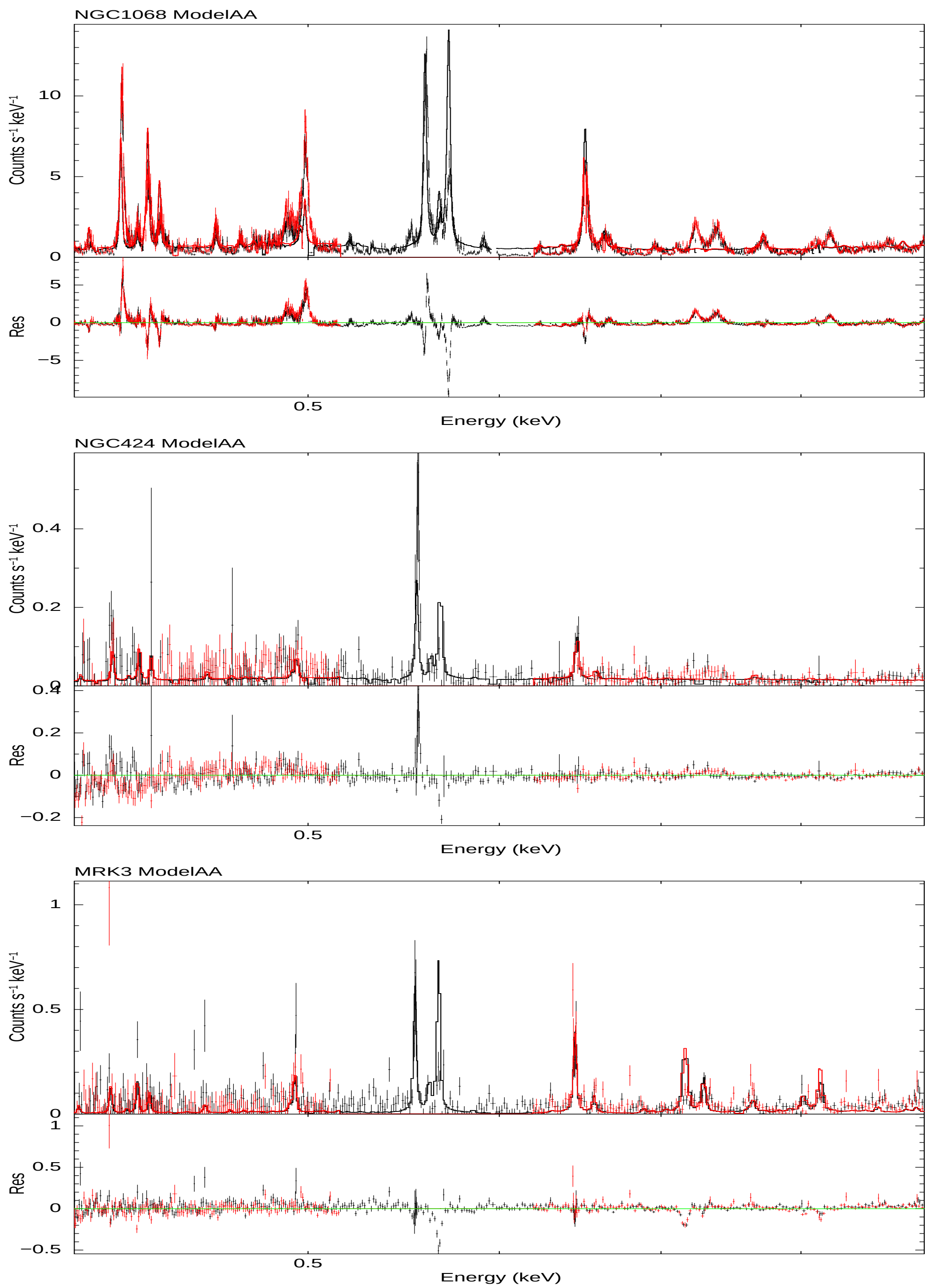

Figure 3.47: Example of best fits for ModelAA for RGS1 (black) and RGS2 (red) between 0.4 and 0.9 keV. In the lower panel the plot of the residua is shown.

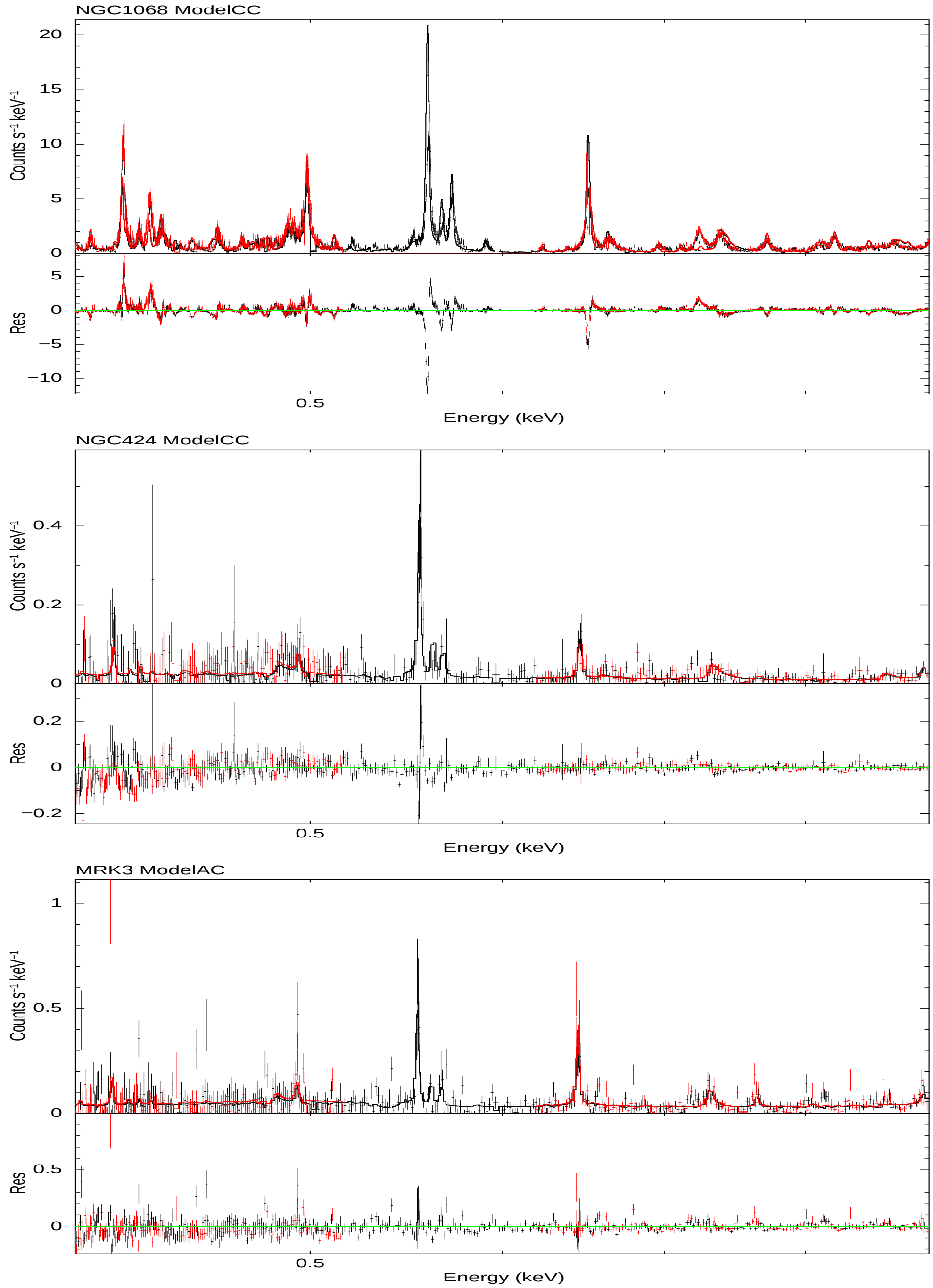

Figure 3.48: Example of best fits for ModelCC for RGS1 (black) and RGS2 (red) between 0.4 and 0.9 keV. In the lower panel the plot of the residua is shown.

sources with at least 20% background-subtracted mean count rates for combined RGS (RGS1+RGS2) in $0.4 - 0.9$ keV band.

Despite this choice, we have a small numbers of counts in a channel, so we can't use the χ^2 statistic: we used the Xspec normalized version of this statistic (CSTAT) to determine the best-fit parameter and its uncertainties.

Parameter values and confidence regions only mean anything if the model actual fits the data. The standard way of assessing this is to perform a test to reject the null hypothesis that the observed data are drawn from the model. Thus we calculate some statistic T and if $T_{obs} > T_{critical}$ then we reject the model at the confidence level corresponding to $T_{critical}$. Ideally, $T_{critical}$ is independent of the model so all that is required to evaluate the test is a table giving $T_{critical}$ values for different confidence levels. This is the case for χ^2 which is one of the reasons why it is used so widely. However, for other test statistics (like the Cash statistics we are using) this may not be true and the distribution of T must be estimated for the model in use, then the observed value compared to that distribution. This is done in XSPEC using the goodness command. The model is simulated many times and a value of T calculated for each fake dataset. These are then ordered and a distribution constructed. This distribution can be plotted using plot goodness. Now suppose that T_{obs} exceeds 90% of the simulated T values, we can reject the model at 90% confidence.

It is worth emphasizing that goodness-of-fit testing only allows us to reject a model with a certain level of confidence, it never provides us with a probability that this is the correct model. The XSPEC "goodness" command simulates (Monte-Carlo simulation) spectra based on the model and writes out the percentage of these simulations with the fit statistic less than that for the data. The fit is good when about 50% of the simulated spectra have the value of Cstat less than that of the data in question. So if the observed spectrum was produced by the model then this number should be around 50%.

To test the goodness of our fits we have tried different statistics: PGSTAT (for Poisson data with Gaussian background), PCHI (Pearson chi-square statistic for Poisson data), KS (Kolmogorov-Smirnov), CVM (Cramer-von Mises), AD (Anderson-Darling) and RUNS (Wald-Wolfowitz: the runs statistic tests for runs of consecutive positive or negative residuals)[13].

The results of "goodness of fit" with the statistic PGSTAT, the statistic KS, the statistic CVM, the statistic AD and the statistic RUNS were around 100% for most of our spectra regardless of the model used. Instead the results of "goodness of fit" with the statistic PCHI were different from 100% for 12 sources as we reported in Tab. 3.5, where we compare the goodness of fit for the different models. Some

[13] We refer the reader to http://heasarc.gsfc.nasa.gov/xanadu/xspec/manual/XSappendixStatistics.html for more detailed descriptions of the implementation of these statistics.

Table 3.4: CAIXA-A sources with at least 20% background-subtracted mean count rates for combined RGS (RGS1+RGS2) in $0.4 - 0.9$ keV band.

source	z	RGS %
NGC1068	0.0038	91.5
NGC3227	0.0039	88.5
NGC4151	0.0033	77
NGC5273	0.0035	59
MRK704	0.029	51.5
NGC4395	0.001064	49.5
IRAS09149-6206	0.0573	45
UGC4203	0.0135	45
NGC4388	0.008419	43.5
NGC1365	0.0055	39
ESO362-G018	0.013	38
NGC34	0.0198	37
NGC4507	0.0118	35.5
NGC6240	0.0245	34.5
ESO138-G01	0.00914	33.5
NGC5643	0.0040	32
NGC424	0.0117	31
NGC5506	0.0062	31
2MASXJ12384342+0927362	0.0829	29
IRAS13197-1627	0.017	29
MRK3	0.0135	26.5
NGC7582	0.0053	26
MRK463	0.0504	24
FBQSJ075800.0+392029	0.0960	23
NGC1386	0.0029	23
NGC4102	0.002823	22.5
IRAS18325-5926	0.0202	22
NGC4945	0.0019	21
NGC7172	0.0087	21

examples of comparison between the data and fitted distributions are shown in Fig. 3.49 and in Fig. 3.50: for sources with middle quality spectra (as NGC424, Fig. 3.50) the goodness of fit is able to distinguish the best model; instead for high quality spectrum the goodness of fit fails to distinguish the best model because our automatic fits are too simple to well reproduce the NGC1068 and NGC4151 spectra.

Table 3.5: Results of "goodness of fit" with the statistic PCHI for CAIXA-A sources with at least 20% background-subtracted mean count rates for combined RGS (RGS1+RGS2) count rates (P) in $0.4-0.9$ keV band.

Source	MODEL	Cstat	d.o.f.	Goodness
NGC1068	C	21974.1	2916	100
NGC1068	A	51758.4	2917	100
NGC1068	CC	15079.6	2913	100
NGC1068	AA	19695.6	2915	100
NGC1068	AC	14996.5	2914	100
NGC3227	C	5700.57	2943	100
NGC3227	A	7758.75	2944	100
NGC3227	CC	5660.98	2940	100
NGC3227	AA	7611.34	2942	100
NGC3227	AC	5314.56	2941	100
NGC4151	C	28086.8	2984	100
NGC4151	A	28539.1	2985	100
NGC4151	CC	6017.97	2981	100
NGC4151	AA	20489	2983	100
NGC4151	AC	10787.2	2982	100
NGC5273	C	2897.29	2902	100
NGC5273	A	3411.42	2903	100
NGC5273	CC	2876.15	2899	100
NGC5273	AA	2925.17	2901	100
NGC5273	AC	2877.03	2900	100
MRK704	C	3283.72	2919	100
MRK704	A	3584.17	2920	100
MRK704	CC	3240.08	2916	100
MRK704	AA	3277.07	2918	100
MRK704	AC	3259.54	2917	100
NGC4395	C	3809.05	3004	93.41
NGC4395	A	6943.59	3005	100
NGC4395	CC	3782.33	3001	91.91
NGC4395	**AA**	**3673.7**	**3003**	**89.62**

NGC4395	AC	3771.96	3002	91.79
IRAS09149-6206	C	2611.37	2925	100
IRAS09149-6206	A	2799.52	2926	100
IRAS09149-6206	CC	2603.16	2922	100
IRAS09149-6206	AA	2625.49	2924	100
IRAS09149-6206	AC	2606.53	2923	100
UGC4203	C	3356.07	2932	100
UGC4203	A	3995.61	2933	100
UGC4203	CC	3351.04	2929	100
UGC4203	AA	3910.68	2931	100
UGC4203	AC	3352.74	2930	100
NGC4388	C	1983.19	2941	100
NGC4388	A	2022.05	2942	100
NGC4388	CC	1961.26	2938	100
NGC4388	AA	1949.36	2940	100
NGC4388	AC	1961.96	2939	100
NGC1365	C	4571.95	2953	100
NGC1365	A	4187.71	2954	100
NGC1365	CC	4415.19	2950	100
NGC1365	**AA**	**3684.15**	**2952**	**99.98**
NGC1365	AC	3653.93	2951	100
ESO362-G018	C	2162.85	2932	100
ESO362-G018	A	2185.38	2933	100
ESO362-G018	CC	2096.22	2929	100
ESO362-G018	AA	2103	2931	100
ESO362-G018	AC	2113.13	2930	100
NGC34	C	3170.46	2916	100
NGC34	A	3459.36	2917	100
NGC34	CC	3159.2	2913	100
NGC34	AA	3215.94	2915	100
NGC34	AC	3164.86	2914	100
NGC4507	A	4472.56	3000	100
NGC4507	C	4191.78	2999	100
NGC4507	AA	4026.65	2998	100
NGC4507	**CC**	**3654.5**	**2996**	**93.05**
NGC4507	AC	3804.37	2997	97.28
NGC6240	**C**	**3731.41**	**2967**	**99.96**
NGC6240	A	7846.33	2968	100
NGC6240	CC	3689.39	2964	99.98
NGC6240	AA	6419.56	2966	100

NGC6240	AC	3678.36	2965	99.98
ESO138-G01	C	3429.02	2932	97.32
ESO138-G01	A	4185.14	2933	100
ESO138-G01	**CC**	**3410.11**	**2929**	**92.75**
ESO138-G01	AA	3498.46	2931	99.53
ESO138-G01	AC	3407.13	2930	92.91
NGC5643	C	1961.38	2950	89.13
NGC5643	A	1953.22	2951	93.14
NGC5643	**CC**	**1953.9**	**2947**	**85.42**
NGC5643	AA	1953.22	2949	93.42
NGC5643	AC	1953.22	2948	93.44
NGC424	C	3826.22	2941	95.95
NGC424	A	4201.08	2942	98.22
NGC424	CC	3507.33	2938	63.19
NGC424	AA	3621.66	2940	61.7
NGC424	**AC**	**3618.73**	**2939**	**56.88**
NGC5506	**C**	**4242.91**	**2959**	**99.92**
NGC5506	A	5206.61	2960	99.98
NGC5506	CC	4180.59	2956	99.97
NGC5506	AA	4223.03	2958	99.98
NGC5506	AC	3773.59	2957	99.95
2MASXJ12384342+0927362	C	2527.32	2921	100
2MASXJ12384342+0927362	A	2593.65	2922	100
2MASXJ12384342+0927362	CC	2519.77	2918	100
2MASXJ12384342+0927362	AA	2521.94	2920	100
2MASXJ12384342+0927362	AC	2524.53	2919	100
IRAS13197-1627	C	3445.74	2892	100
IRAS13197-1627	A	3483.45	2893	100
IRAS13197-1627	CC	3381.51	2889	100
IRAS13197-1627	AA	3301.53	2891	100
IRAS13197-1627	AC	3340.24	2890	100
MRK3	C	4383.17	3003	100
MRK3	A	5489.83	3004	100
MRK3	CC	4132.75	3000	100
MRK3	AA	5120.16	3002	100
MRK3	AC	4184.69	3001	100
NGC7582	C	3811.22	2972	99.99
NGC7582	A	4056.36	2973	99.99
NGC7582	CC	3639.57	2969	99.1
NGC7582	AA	3718.7	2971	99.79

NGC7582	**AC**	**3580.77**	**2970**	**99.09**
MRK463	C	2602.86	2900	100
MRK463	A	2613.25	2901	100
MRK463	CC	2596.05	2897	100
MRK463	AA	2600.02	2899	100
MRK463	AC	2583.54	2898	100
FBQSJ075800.0+392029	C	3155.89	2939	95.28
FBQSJ075800.0+392029	A	3213.26	2940	99.88
FBQSJ075800.0+392029	**CC**	**3128.85**	**2936**	**87.37**
FBQSJ075800.0+392029	AA	3142.93	2938	95.4
FBQSJ075800.0+392029	AC	3131.7	2937	88.95
NGC1386	C	2364.86	2929	100
NGC1386	A	2351.99	2930	100
NGC1386	CC	2328.58	2926	100
NGC1386	AA	2334.56	2928	100
NGC1386	AC	2326.93	2927	100
NGC4102	C	3468.3	2921	100
NGC4102	A	3477.73	2922	100
NGC4102	CC	3467.37	2918	100
NGC4102	AA	3572.13	2920	100
NGC4102	AC	3459.6	2919	100
IRAS18325-5926	C	3139.67	2881	100
IRAS18325-5926	A	3103.1	2882	100
IRAS18325-5926	CC	3132.79	2878	100
IRAS18325-5926	AA	3218.42	2880	100
IRAS18325-5926	AC	3112.71	2879	100
NGC4945	C	3493.06	2924	45.32
NGC4945	A	3657.17	2925	96.7
NGC4945	CC	3489.69	2921	39.59
NGC4945	AA	3601.29	2923	90.1
NGC4945	**AC**	**3468.42**	**2922**	**35.4**
NGC7172	C	3638.77	2953	99.74
NGC7172	A	4170.54	2954	99.99
NGC7172	CC	3611.15	2950	99.52
NGC7172	AA	4109.05	2952	100
NGC7172	**AC**	**3610.3**	**2951**	**99.37**

When the goodness of fit is able to distinguish the best model, there is a preference for models with at least one photoionized component (see Tab. 3.5). The

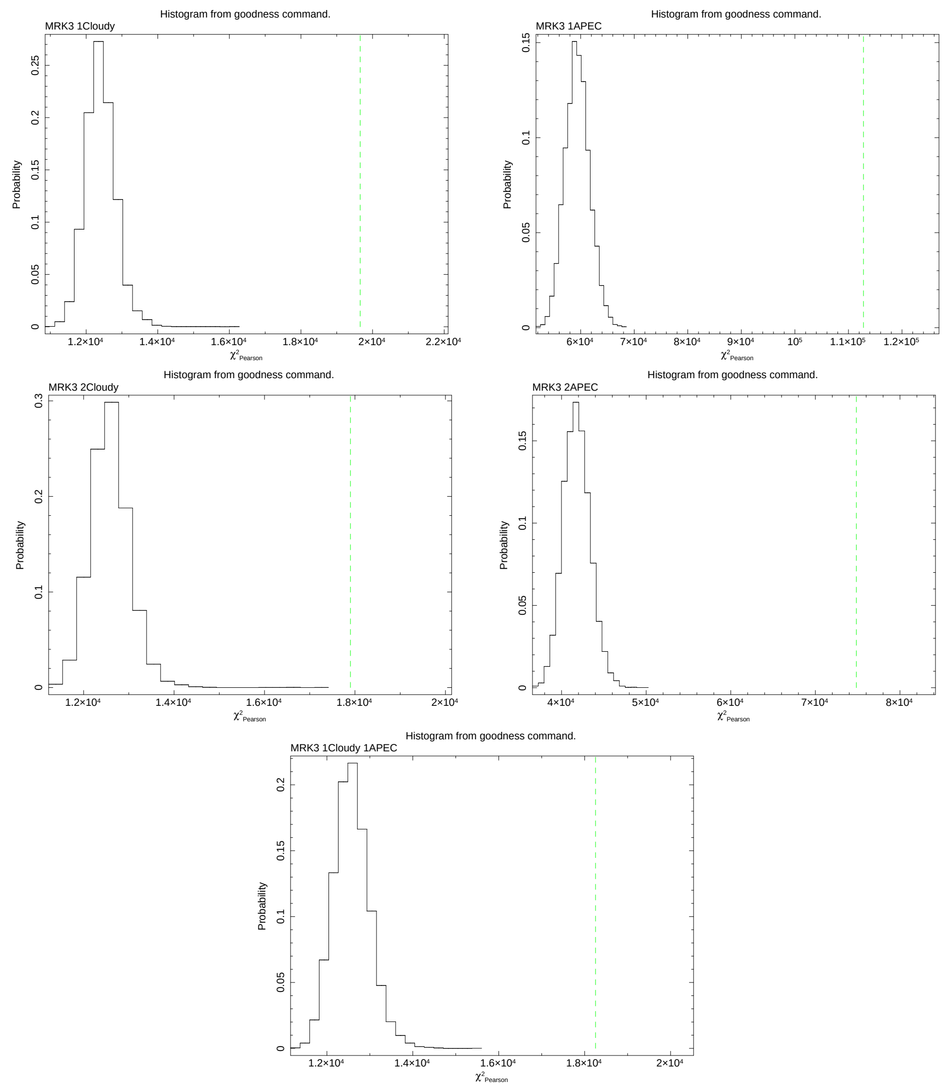

Figure 3.49: Comparison between the data and fitted distributions for MRK3. Model C, A, CC, AA, AC. The histogram shows the fraction of simulations with a given value of the statistic and the dotted line marks that for the observed data. The goodness of fit fails to distinguish the best model.

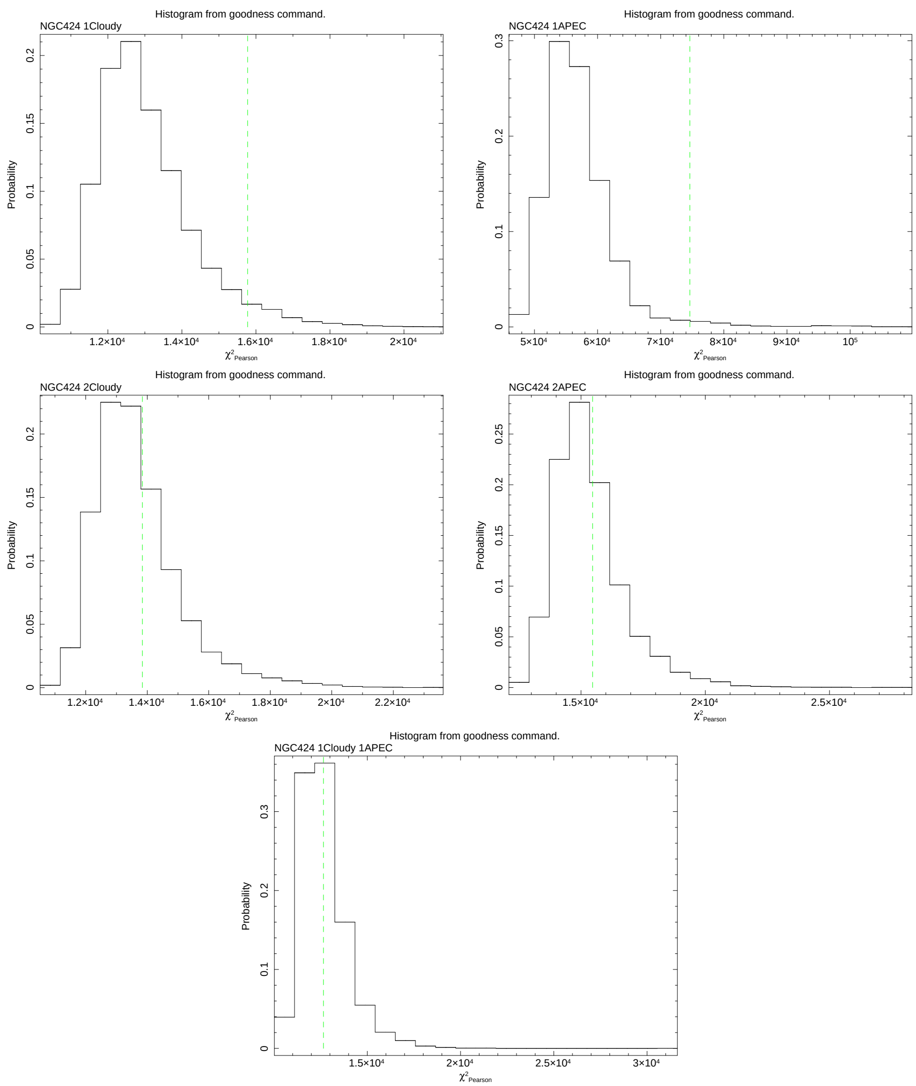

Figure 3.50: The result of the command plot goodness for NGC424: (from *top* to *bottom*) Model C, A, CC, AA, AC. The histogram shows the fraction of simulations with a given value of the statistic and the dotted line marks that for the observed data. There is no reason to reject the model.

soft excess in CAIXA-A sources seems to be dominated by emission from photoionizated gas as suggested by our previous analysis. The only exceptions are NGC4395 and NGC1365 where the model with two collisionally-ionized phases is preferred, in agreement with the OVIII/OVII ratio > 1 as found with Method A (section 3.3) see Figure 3.24. Referring to Table 3.5, there is a preference for models with two components (10/12 sources: two components of collisionally-ionized plasma for 2/10 sources, two components of photoionization for 4/10 sources, a component of collisionally-ionized plasma plus a component of photoionization for 4/10 sources) or for the model with emission from a single photoionization plasma (2/12 sources).

We have not found any kind of correlation between the parameters of the fits, then we will display only the distributions of the parameters of best fit for each model. Errors on the parameters are very large, so these distributions are very uncertain.

In all the models with at least a photoionized component, a peak at logU=2.5 is clearly present in the distributions of the ionization parameters (see Figure 3.51(a)). A second peak at logU=4 appears in Model AC (Figure 3.51(c)), while a larger distribution of ionization parameters is found for Model CC (Figure 3.51(b)).

The distributions of the column density N_H for ModelC and ModelAC are similar, and seem to suggest that resonant scattering is relevant because peaks at low values (Figure 3.52(a) and 3.52(c)). For ModelCC, the distribution of the column densitity N_H (Figure 3.52(b)) is larger, with a peak at a significantly higher N_H.

In Figure 3.53(a) we show the distribution of the temperature for ModelA. The peak is at low temperature. The result for the ModelAC (Fig. 3.53(b)) is similar, but with a tail at lower temperature. The distribution of the temperature for ModelAA (Figure 3.53(c)) is instead, larger.

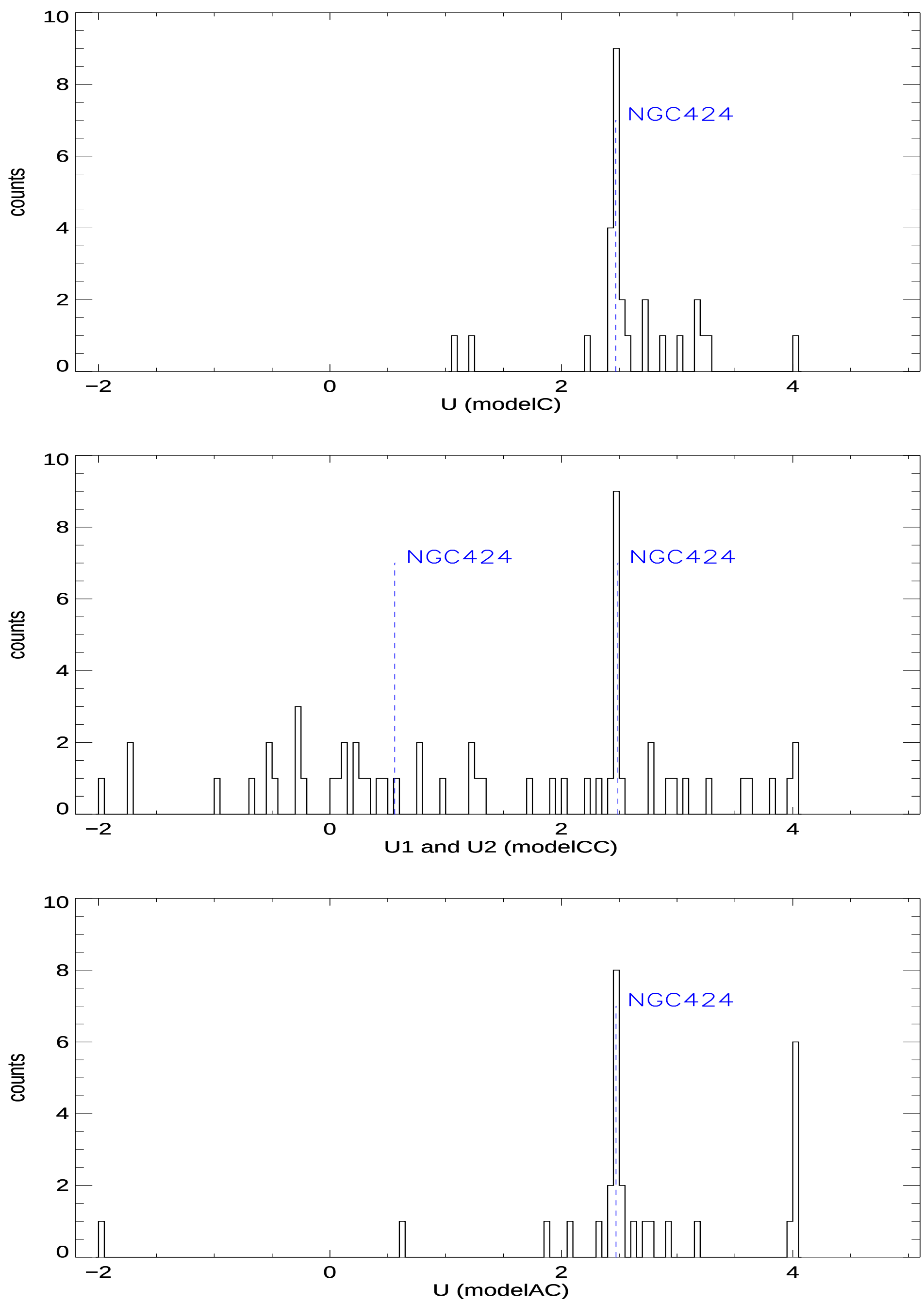

Figure 3.51: *Distribution of the ionization parameters for ModelC (top), for ModelCC (middle) and for ModelAC (bottom). The values for NGC424 is labelled.*

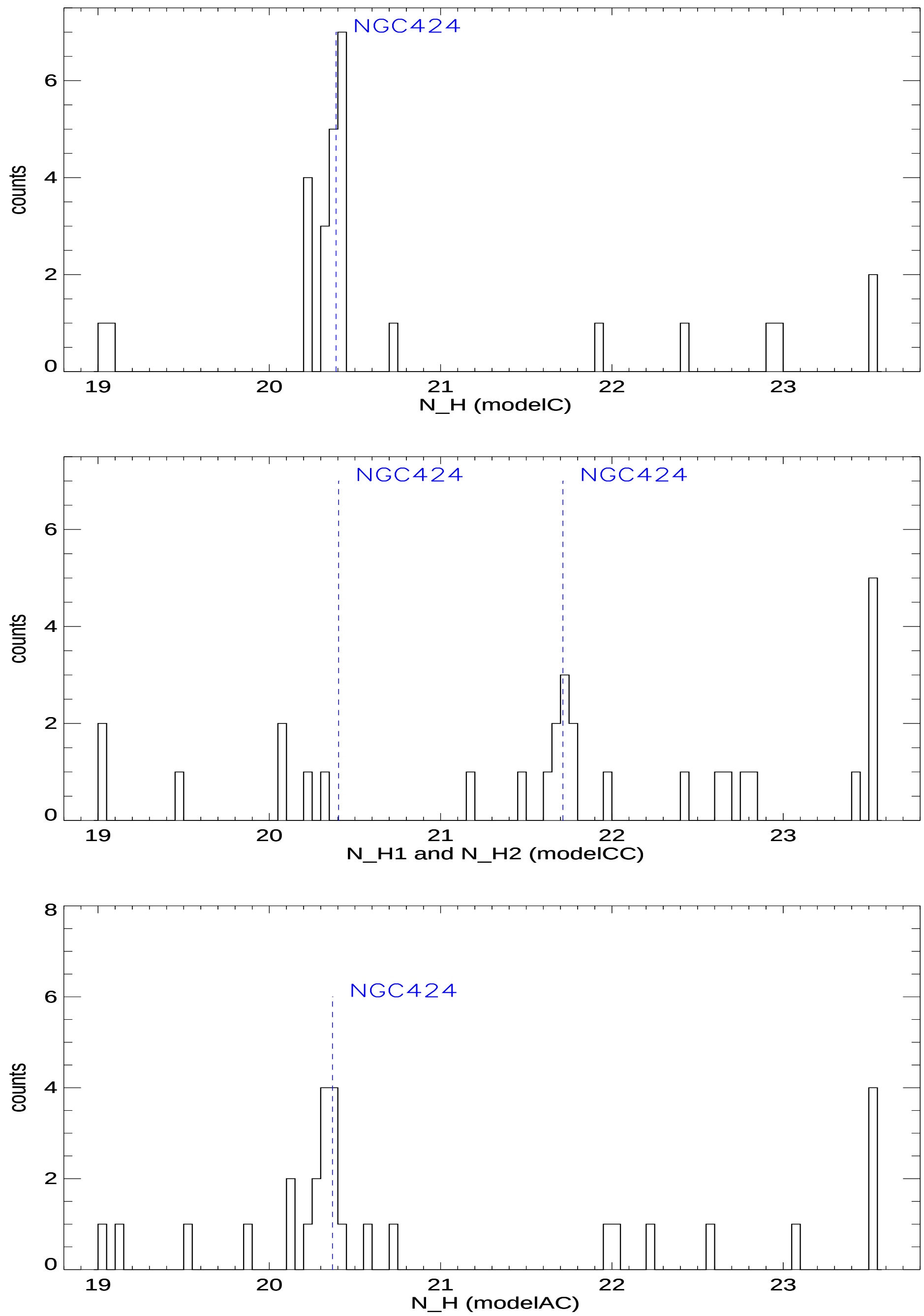

Figure 3.52: *Distribution of the column densitity N_H for ModelC (top), for ModelCC (middle) and for ModelAC (bottom). The values for NGC424 is labelled.*

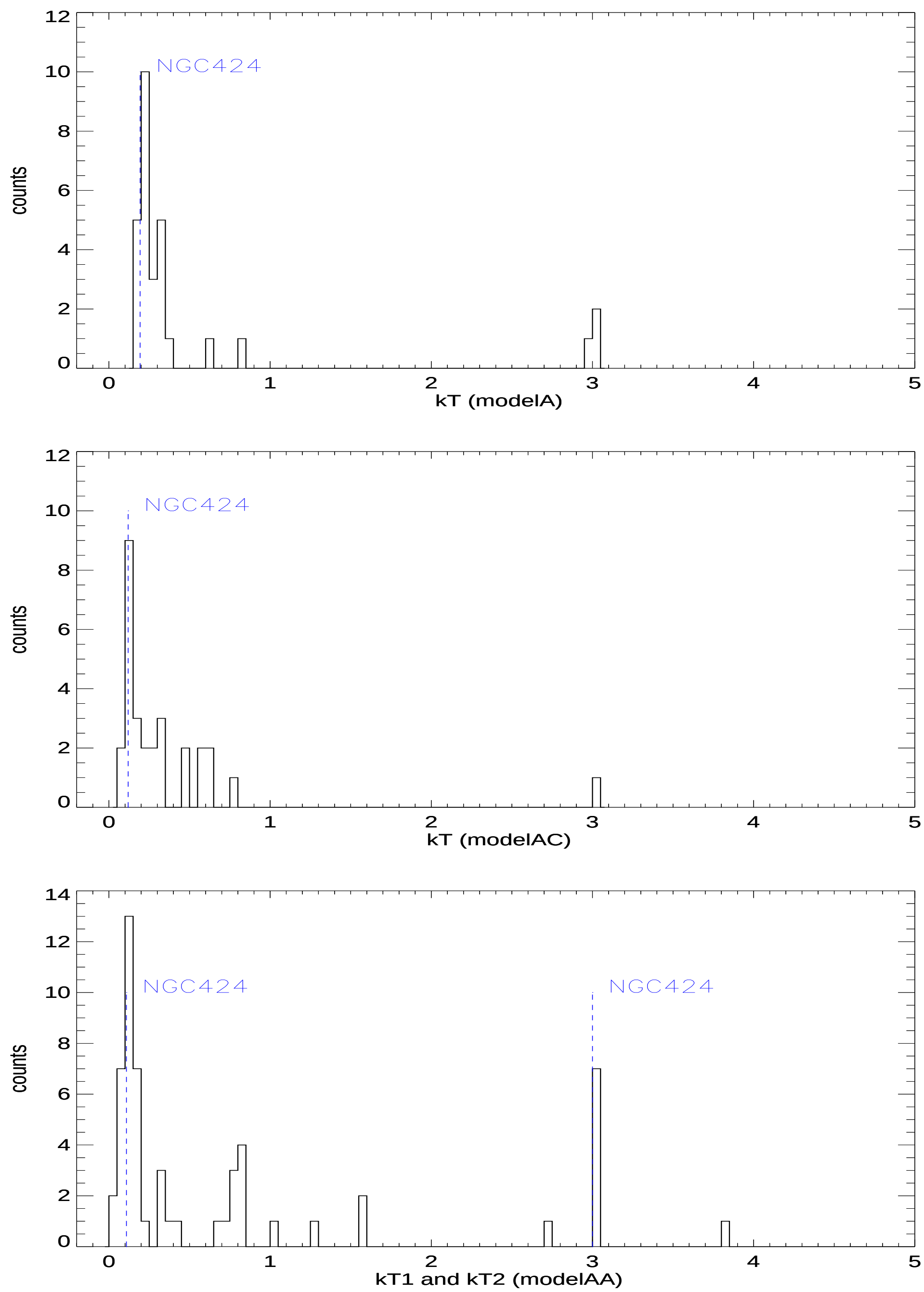

Figure 3.53: *Distribution of the temperature for ModelA (top), for ModelAC (middle) and for ModelAA (bottom). The values for NGC424 is labelled.*

Table 3.6: NGC424 best fit parameters.

MODEL	U1	U2	N_H1	N_H2	KT1	KT2
C	2.47067	-	20.3896	-	-	-
A	-	-	-	-	0.193229	-
AA	-	-	-	-	0.108466	2.885
CC	0.560052	2.4887	21.714	20.4045	-	-
AC	2.4724	-	20.3688	-	0.119261	-

In each figure we marked the NGC424 best fit values which are representative of the distributions of all Models (see also Tab. 3.6). Moreover, Marinucci et al. (2011) applied a similar self-consistent model at the source NGC424. At first, they tried to fit the 8Å – 35Å spectrum of NGC424 using a single photoionized phase and they obtained a rather good fit. Even if the fit was acceptable, they added another photoionized phase and the fit improves. They introduced a further photoionized phase with a higher photoionization parameter, but the fit is not sensitive to the new component, so they tried to introduce a collisional component with slightly better results. In our analysis we obtained more or less the same results for this source. In fact for NGC424 the goodness of fit indicates a preference for the Model AC (56.88), even if the goodness for Model CC (63.19) is not bad.

As a further test to check which models better reproduce the data, we simulated spectra for each source with the XSPEC ”fakeit none” command for all the different models we used in the *Method C* analysis: **FakeC**, **FakeA**, **FakeAA**, **FakeCC**, **FakeAC**. The ionization parameters U_1 and U_2, the N_H1 N_H2 and the temperature kT_1 and kT_2 was fixed to the best fit values of NGC424 for the corresponding models (see Tab. 3.6). Redshift, background, response matrix and exposure time for each fake spectrum are those of the corresponding source. We investigated all this fake spectra with the *Free-lines* analysis (Method B, Sect. 3.4). This method is similar to what has been done before and are designed to compare the distributions of detected lines observed with that expected for an homogeneous population of objects whose lines are produced by known models. The results are shown in Fig. 3.54 for the *FAKEC* spectra, in Fig. 3.55 for the *FAKEA* spectra, in Fig. 3.56 for the *FAKECC* spectra, in Fig. 3.57 for the *FAKEAA* spectra, in Fig. 3.58 for the *FAKEAC* spectra. Superimposed we plotted the results for the fake-simple-powerlaw spectra smoothed with a 5-channels wide triangular kernel, in order to give an estimate of the noise (see Sect. 3.4).

We compared the results of the analysis on the fake spectra with the results of the Method B analysis with the Kolmogorov-Smirnov statistic, as we did before

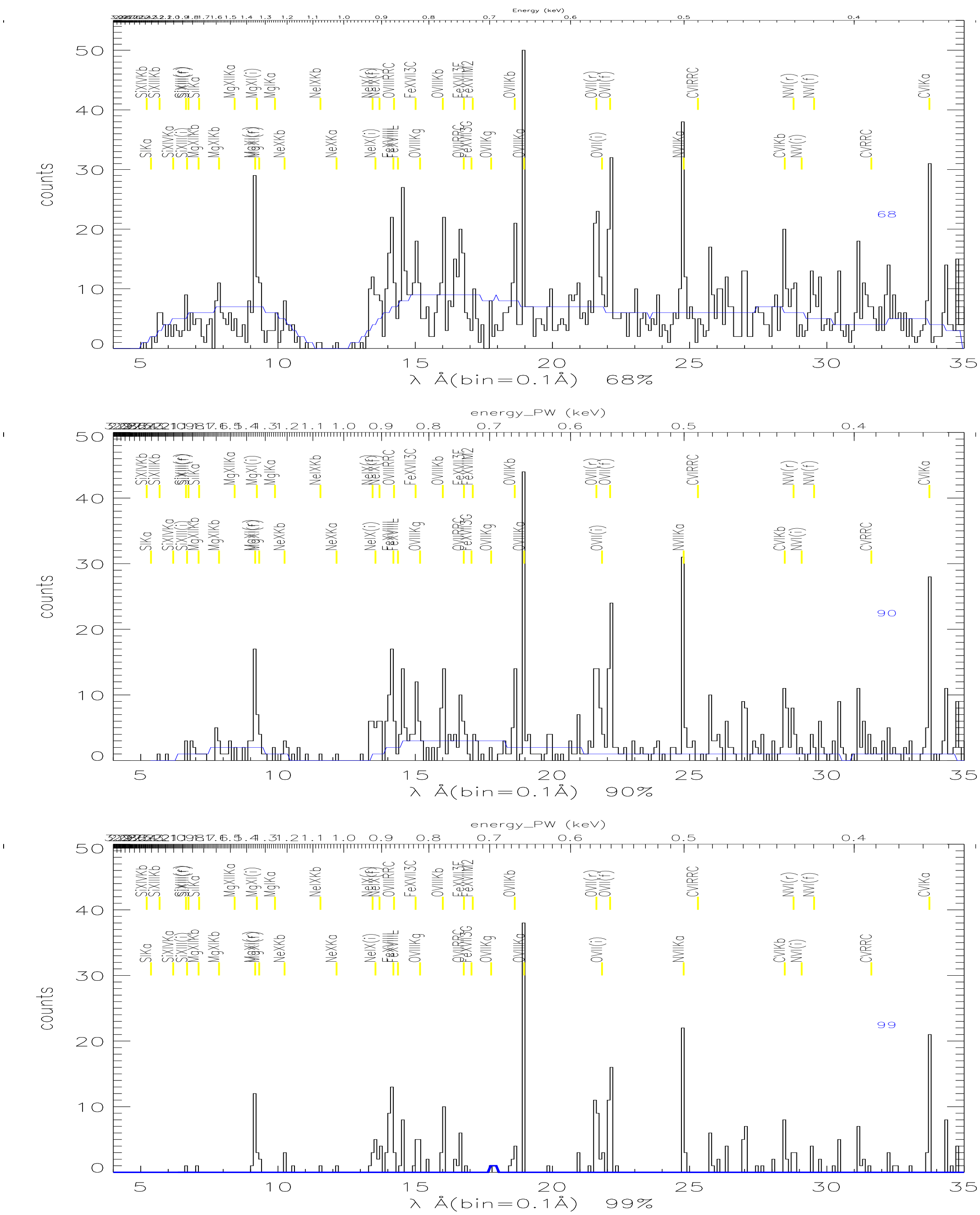

Figure 3.54: *Cumulative emission line detections for FAKEC sources detected at the 68% (top), 90% (middle), 99% (bottom) confidence level. The blue line is an estimate of the noise, extracted from simulations (see text for details). The positions of the most intense line transitions in this band are labeled.*

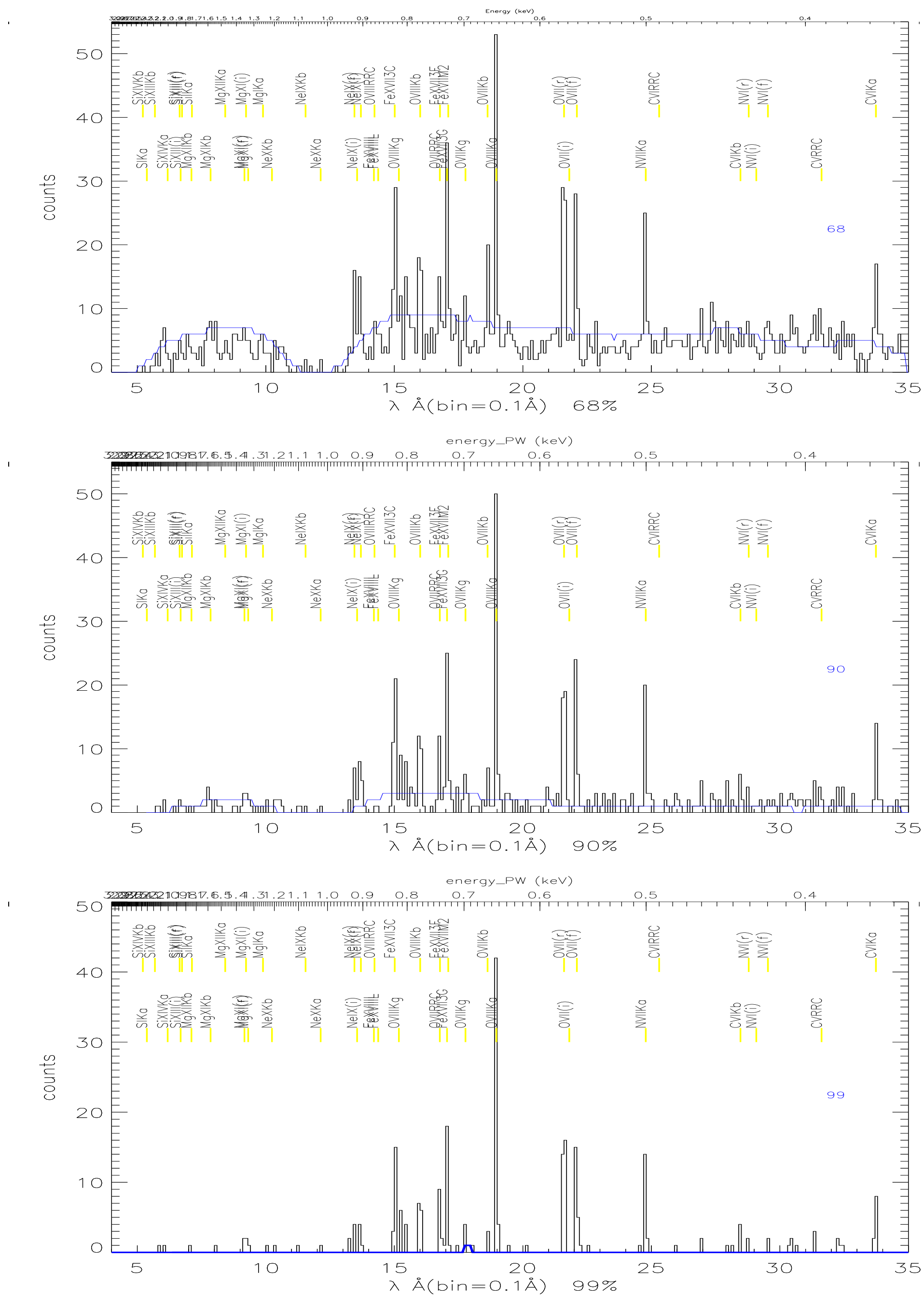

Figure 3.55: *Cumulative emission line detections for FAKEA sources detected at the 68% (top), 90% (middle), 99% (bottom) confidence level. The blue line is an estimate of the noise, extracted from simulations (see text for details). The positions of the most intense line transitions in this band are labeled.*

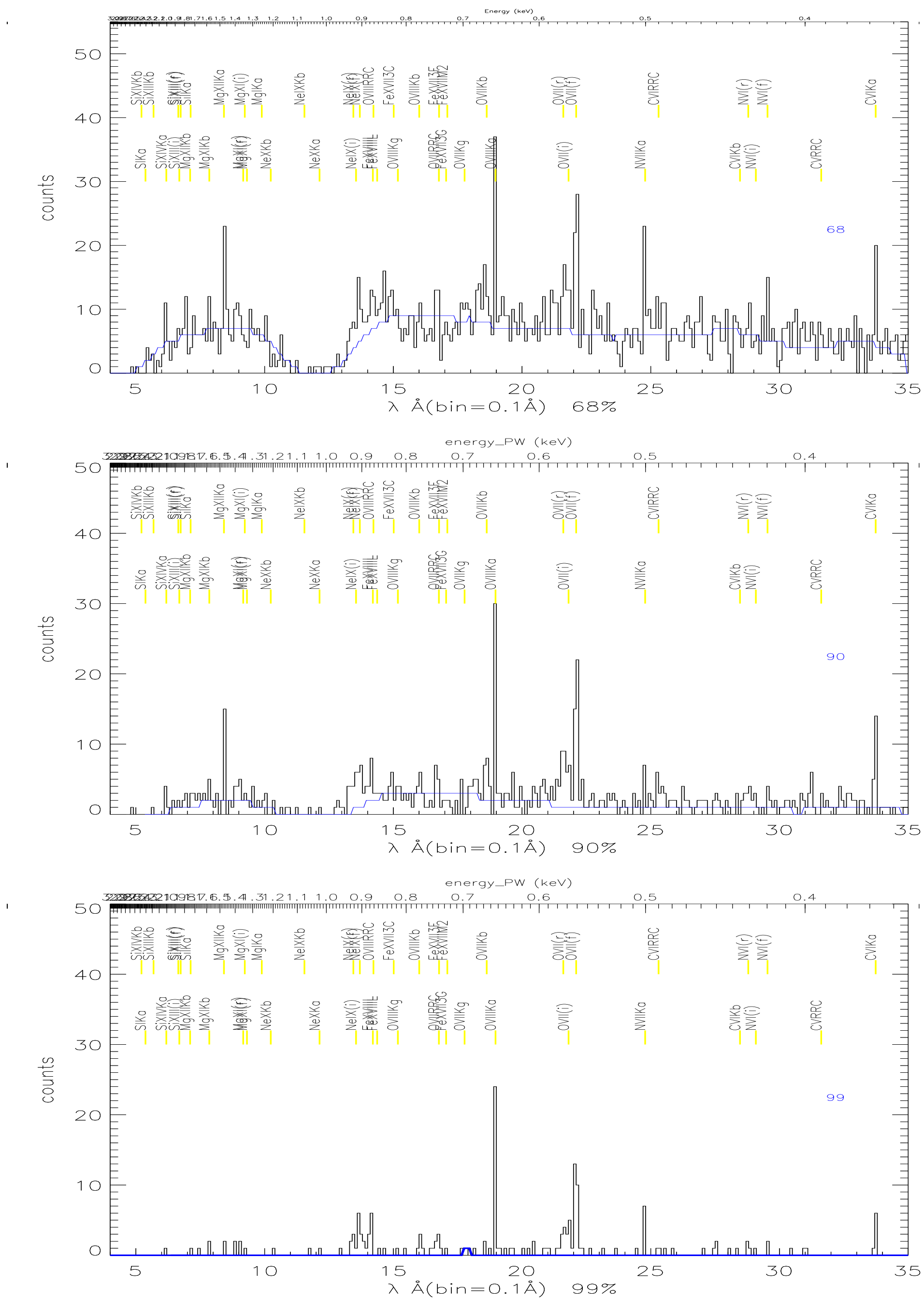

Figure 3.56: *Cumulative emission line detections for FAKECC sources detected at the 68% (top), 90% (middle), 99% (bottom) confidence level. The blue line is an estimate of the noise, extracted from simulations (see text for details). The positions of the most intense line transitions in this band are labeled.*

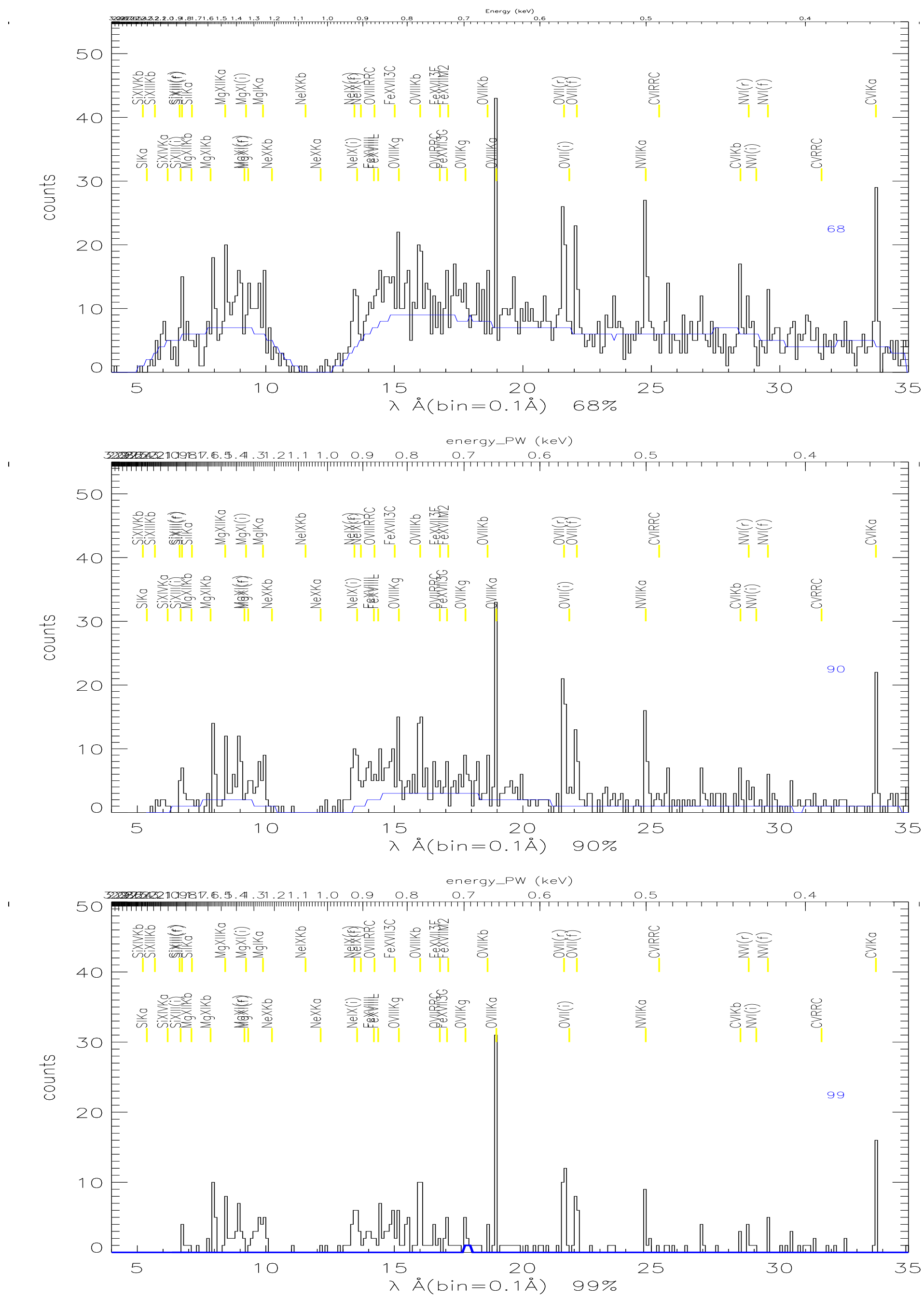

Figure 3.57: *Cumulative emission line detections for FAKEAA sources detected at the 68% (top), 90% (middle), 99% (bottom) confidence level. The blue line is an estimate of the noise, extracted from simulations (see text for details). The positions of the most intense line transitions in this band are labeled.*

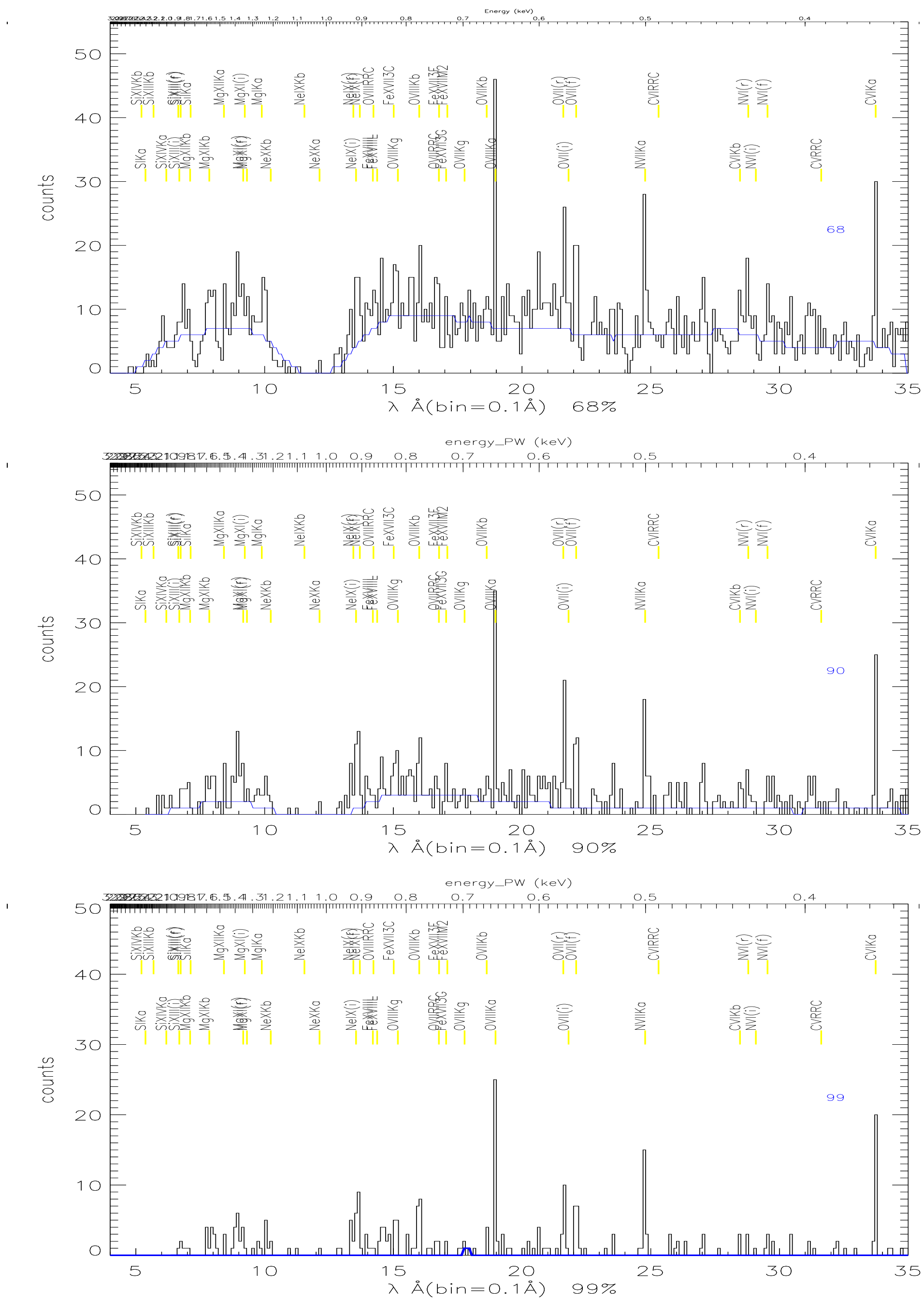

Figure 3.58: *Cumulative emission line detections for FAKEAC sources detected at the 68% (top), 90% (middle), 99% (bottom) confidence level. The blue line is an estimate of the noise, extracted from simulations (see text for details). The positions of the most intense line transitions in this band are labeled.*

for the simple powerlaw fake spectra.

According to Table 3.7, regarding the models with a single component this test indicates the distributions obtained by Method B are most closely related to the distributions obtained by the analysis of the fake spectra simulated with a single photoionized phase model (FakeC) as soon as we move to higher confidence levels. Generally speaking the distribution function of collisionally-ionized plasma models are significantly different from that of real data. Indeed we obtained the smallest values of probability (hence the largest difference between the real and the simulated distributions) for the model with two collisionally-ionized plasma components at each confidence level, meanwhile it is always required at least a photoionized phase component, likely due to the fact that in real data there is a strong presence of O VII f lines. Anyway, compared to the models with a single component, the addition of another photoionized phase seems to improve the agreement between real and fake data only at the 68% confidence level. In fact the two models with the two photoionized phases or the photoionized phase plus the collisionally-ionized phase are practically indistinguishable for 90% and 99% confidence level. It should be noted, however, that we have assigned to each fake spectra the NGC424 best fit values: further investigations are needed in order to estimate any bias introduced by this choice.

Finally, we searched for differences between the results of the analysis on the fake spectra and the results of the Method B analysis on real data: we subtracted the cumulative emission line detections obtained with Method B (Fig. 3.37) from the cumulative *FAKEC* emission line detections (Fig. 3.59), from the cumulative *FAKEA* emission line detections (Fig. 3.60), from the cumulative *FAKEAA* emission line detections (Fig. 3.61), from the cumulative *FAKECC* emission line detections (Fig. 3.62) and from the cumulative *FAKEAC* emission line detections (Fig. 3.63) at the 68%, 90%, 99% confidence level.

In all cases, the lines of Si, present in the data, are underestimated by all the models on fake data: evidently these lines are associated with a plasma with a U/kT higher than those that produce the rest of the lines. Moreover, there are several differences depending on the model that we used to build the fake spectra. The agreement between real data and FAKECC is very good as we can see in Fig.3.62: there are not big residua except for the Fe XVII 3d-2p ($^1P_1$) lines, and the Si lines present in all comparisons made. Once again our analysis favors photoionization as dominant process for CAIXA-A sources, even if the presence of some Fe XVII 3d-2p ($^1P_1$) lines suggests contribution from a gas in collisional equilibrium. Nevertheless also in the case of a collisionally-ionized plasma plus a photoionized phase (FAKEAC) we found more Fe XVII 3d-2p ($^1P_1$) lines in real data as we can see in Fig.3.63 even if the difference decreases with respect to the comparison with FAKECC. Always referring to Fig.3.63 our results on real data show less C VI Kα than that expected in the case of a collisionally-ionized

Table 3.7: Comparison between the results of the analysis on the fake spectra with the results of the Method B analysis.

Confidence level	d	*prob*
	Fake0: POWERLAW	
68%	0.0502857	0.0084
90%	0.148401	0.24×10^{-07}
99%	0.287723	0.00031
	Fake1: CLOUDY	
68%	0.0577186	0.0013
90%	0.0745134	0.0076
99%	0.1051495	0.014
	Fake2: APEC	
68%	0.0600550	0.0016
90%	0.130184	1.6×10^{-06}
99%	0.258184	6.7×10^{-11}
	Fake3: APEC+APEC	
68%	0.0788158	7.7×10^{-07}
90%	0.185280	2.2×10^{-16}
99%	0.294687	5.2×10^{-18}
	Fake4: CLOUDY+CLOUDY	
68%	0.0450200	0.019
90%	0.134879	1.2×10^{-07}
99%	0.259208	1.02×10^{-08}
	Fake5: CLOUDY+APEC	
68%	0.0452045	0.015
90%	0.140279	3.3×10^{-09}
99%	0.189543	7.7×10^{-07}.

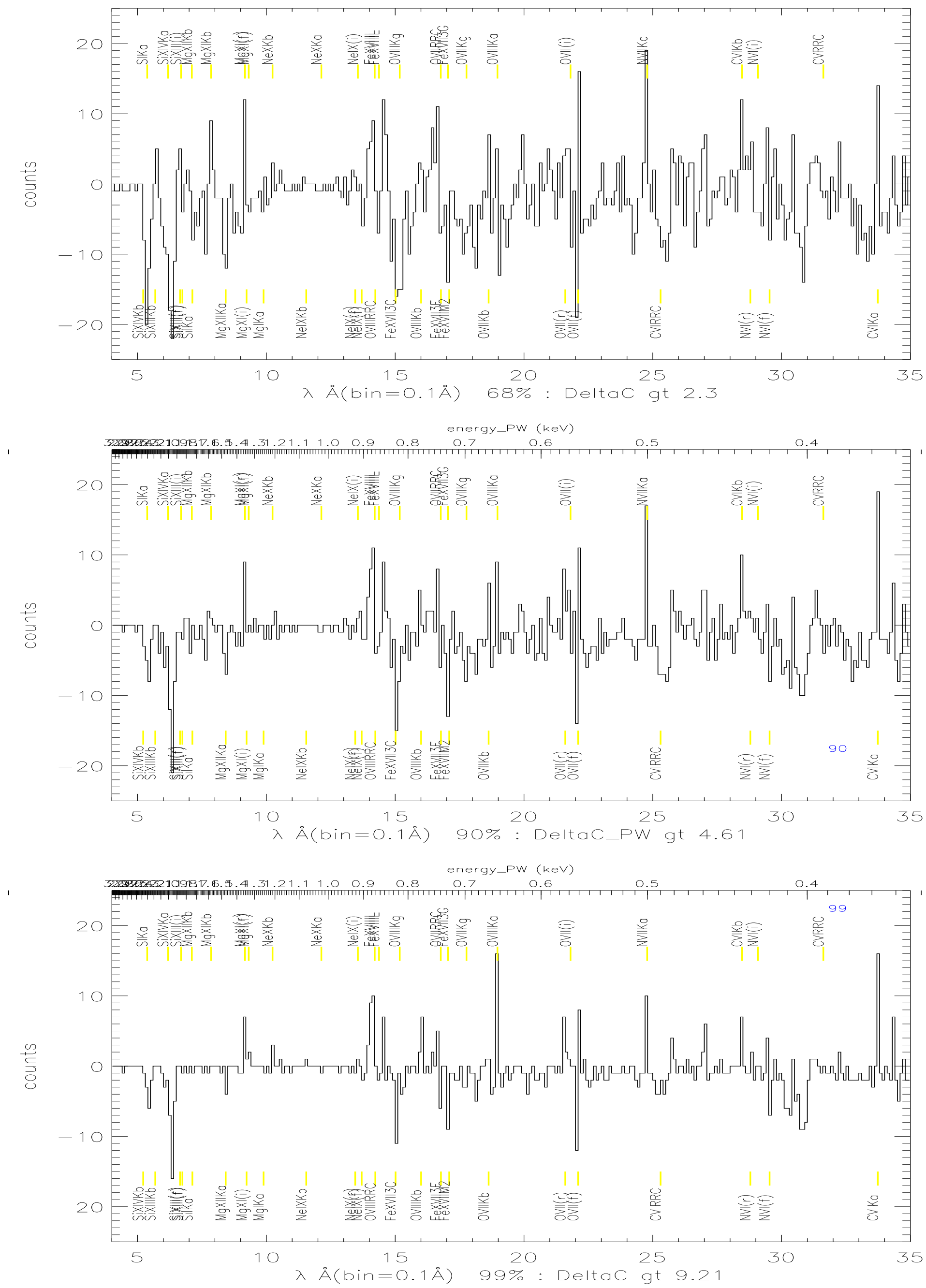

Figure 3.59: *Differences between transition of FAKEC sources detected and transition of CAIXA-A sources detected with Method B at the 68% (top), 90% (middle), 99% (bottom) confidence level. The positions of the most intense line transitions in this band are labeled.*

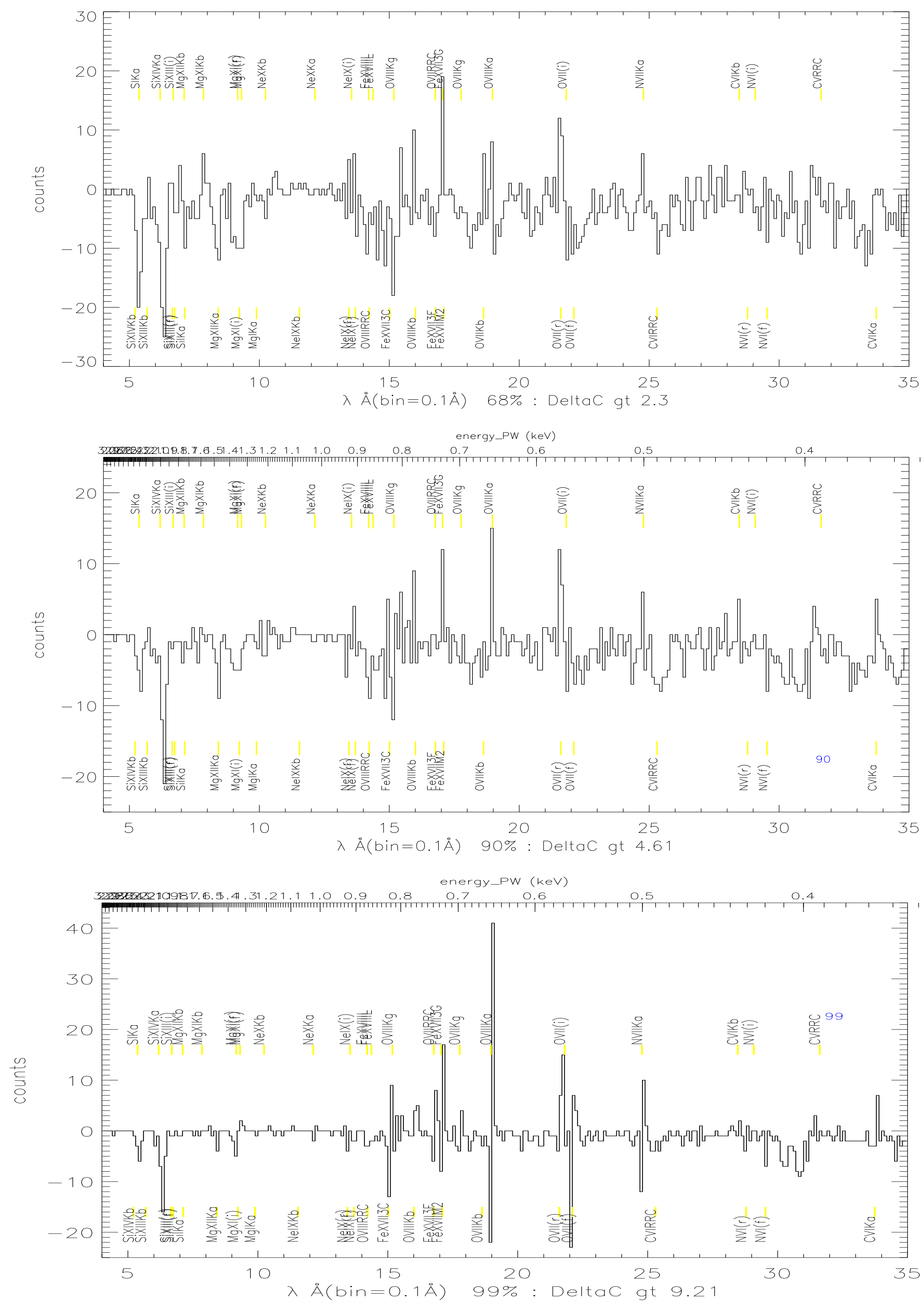

Figure 3.60: *Differences between transition of FAKEA sources detected and transition of CAIXA-A sources detected with Method B at the 68% (top), 90% (middle), 99% (bottom) confidence level. The positions of the most intense line transitions in this band are labeled.*

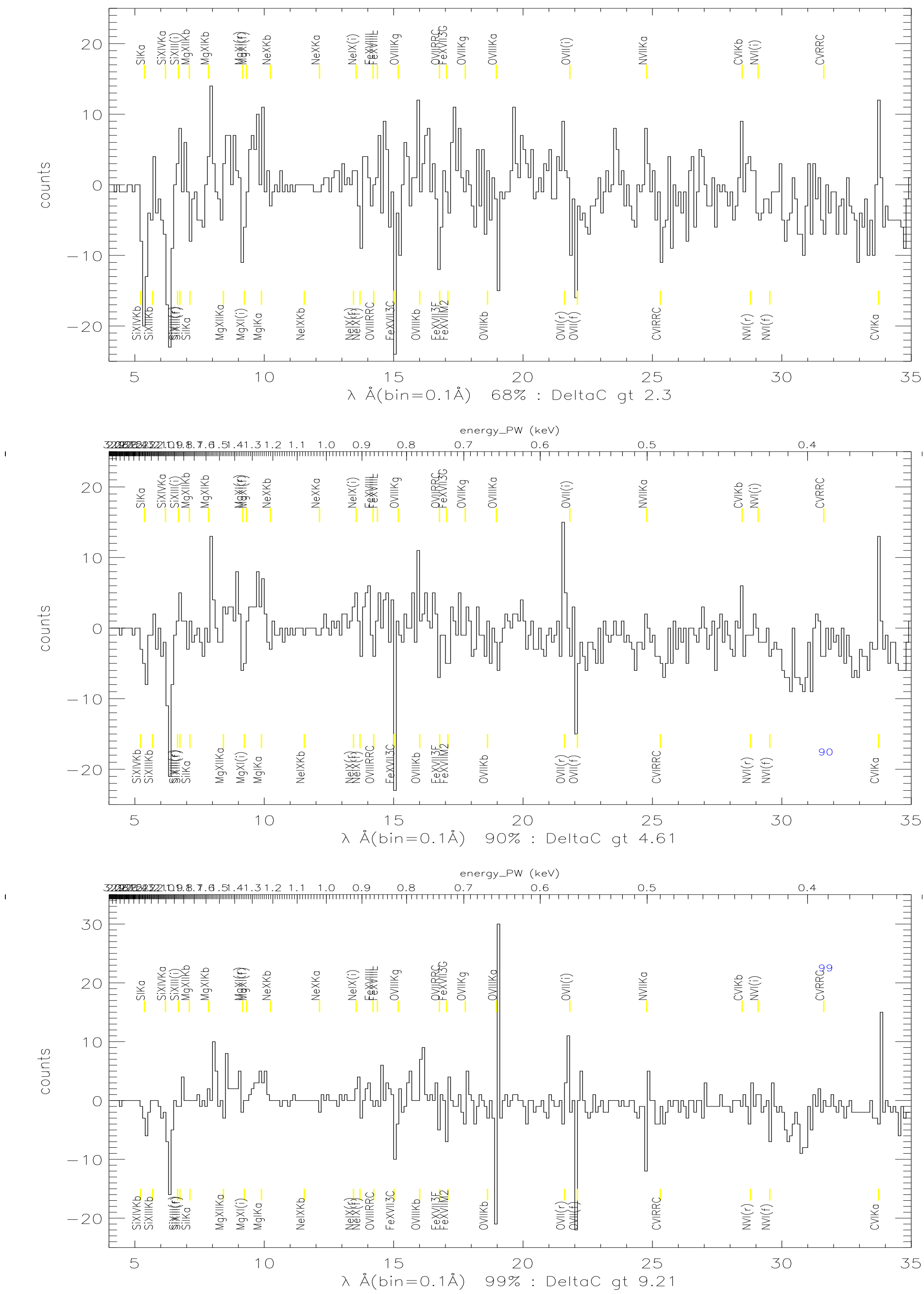

Figure 3.61: *Differences between transition of FAKEAA sources detected and transition of CAIXA-A sources detected with Method B at the 68% (top), 90% (middle), 99% (bottom) confidence level. The positions of the most intense line transitions in this band are labeled.*

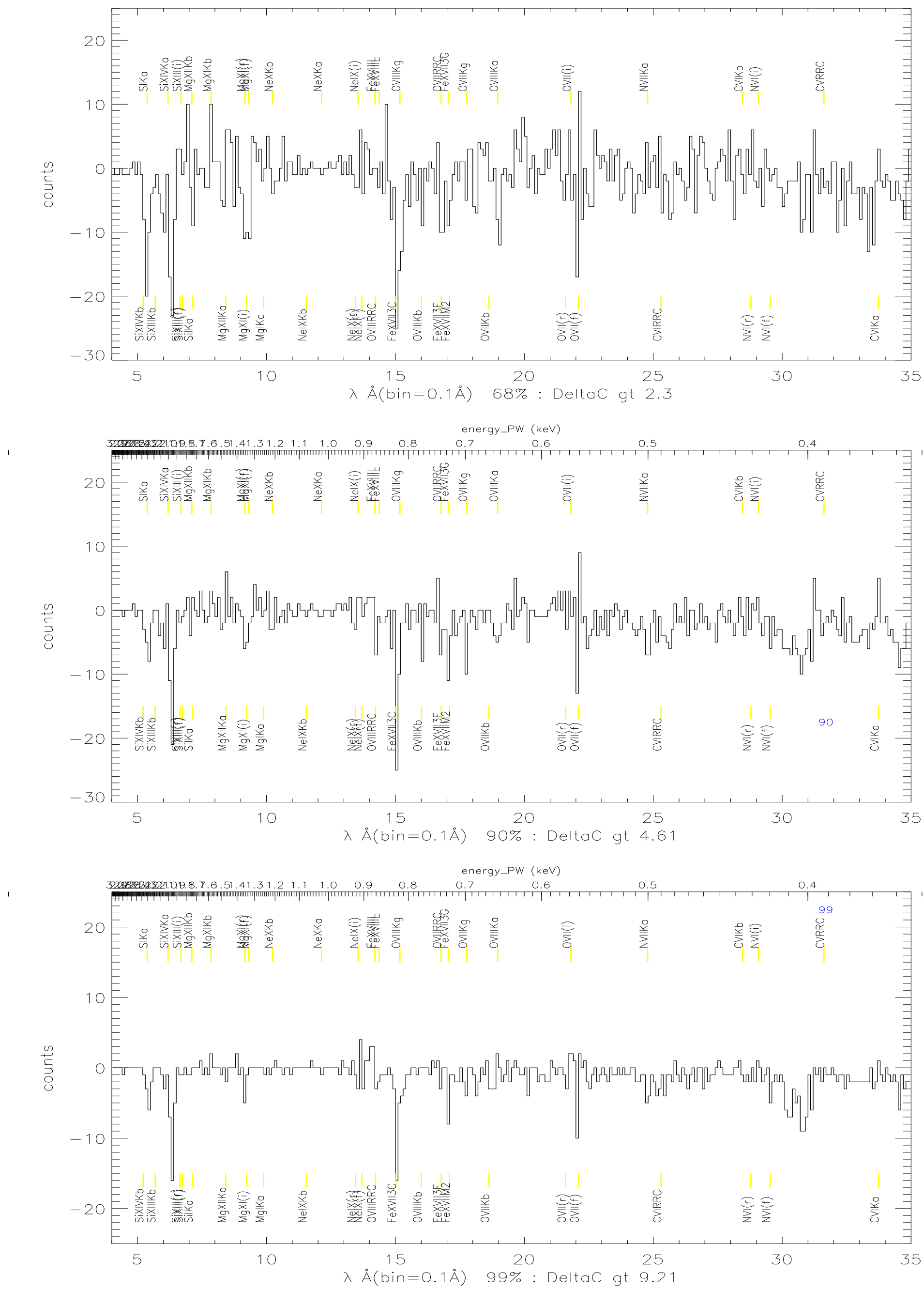

Figure 3.62: *Differences between transition of FAKECC sources detected and transition of CAIXA-A sources detected with Method B at the 68% (top), 90% (middle), 99% (bottom) confidence level. The positions of the most intense line transitions in this band are labeled.*

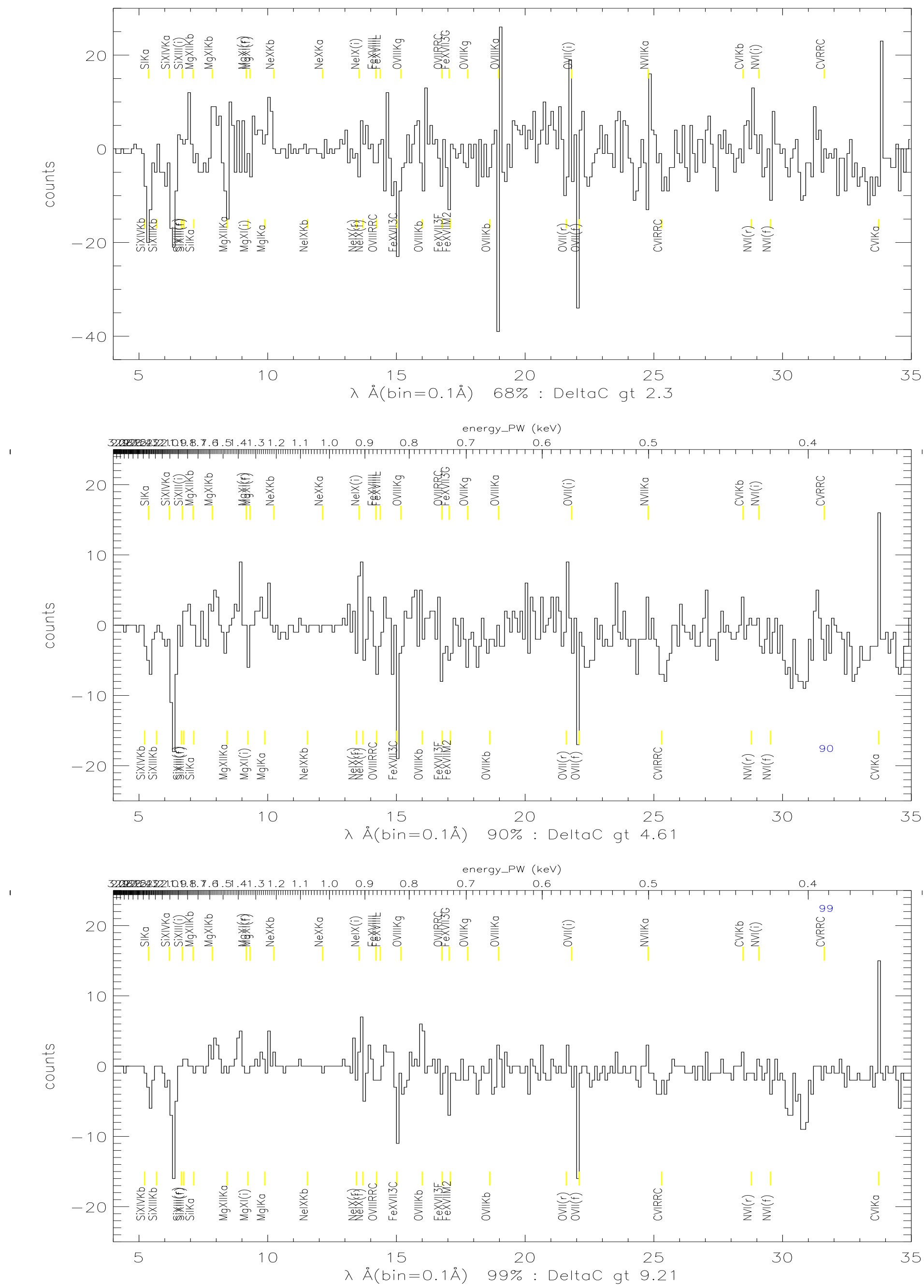

Figure 3.63: *Differences between transition of FAKEAC sources detected and transition of CAIXA-A sources detected with Method B at the 68% (top), 90% (middle), 99% (bottom) confidence level. The positions of the most intense line transitions in this band are labeled.*

plasma plus a photoionized phase. There are residua also for O VII forbidden component: once again an indication of photoionization. In the case of FAKEC we have a good agreement (Fig.3.59), even if the differences between transitions of FAKEC sources and CAIXA-A sources indicate that in real data there are much less O VIII Ly-α, O VIII RRC and C VI Kα than that expected in the case of a single photoionized plasma. As indicated in table 3.7 the agreement between real data and FAKEA is worse than in the previous case. The main differences between the real data and the FAKEA (Fig.3.60) are in the O VIII Ly-α lines and in the O VII forbidden component. In fact, in the case of a collisionally-ionized plasma the forbidden component is generally suppressed, contrary to what we observe in the real data. These differences are equally found in the comparison with FAKEAA (Fig.3.61). Moreover, in the case of two different collisionally-ionized plasma we expect more C VI Kα than that we found in real data.

Chapter 4

Conclusions

The aim of this thesis was to investigate the soft X-ray excess of obscured active galactic nuclei (AGN). With this aim we have built CAIXA-A (Catalogue of AGN In the XMM-*Newton* Archive - Absorbed), a sample of all the radio-quiet, X-ray obscured ($N_H > 2{\times}10^{22} cm^{-2}$) AGN observed by XMM-Newton in targeted observations, whose data were public as of November 22, 2011. With its 109 sources, this is the largest catalog of high signal-to-noise X-ray spectra of obscured AGN.

To investigate the soft X-ray excess of obscured AGN, we need sources where the soft X-ray band is not dominated by the primary continuum and the soft excess component can be modelled properly. Our selection criterion is based on the value of N_H. To calculate an accurate column density we need a lot of counts and a broad band: we selected our sources by analyzing the broad band (0.5-10 keV) EPIC pn spectra of all the AGN observed by XMM-Newton in targeted observations, whose data were public as of November 22, 2011, in order to derive their column densities N_H. To analyze the soft excess we need good effective area in the 0.2-2 keV band and a good resolution, so the RGS is the most suitable instrument. In most of our RGS spectra there are small numbers of counts in a channel, so we used the Xspec normalized version of the Cash (1979) statistic to determine the best-fit parameter and its uncertainties.

In order to extract as much information as possible, we performed the analysis of high-resolution RGS spectra following different approaches. Each spectrum was systematically searched for the presence of emission lines, modeling continua with power-laws and the transitions with Gaussian profiles (Method A). Firstly, the energy of the lines was fixed to laboratory transition energies (following that described in Guainazzi & Bianchi (2007)). Our results can be summarized as follows:

– For each transition that we have looked for we have found at least 8 detections.

– The three more detected lines in our analysis were O VIII Ly-α (61 detections), Fe XVII 3d-2p ($^1P_1$) (51 detections) and O VIII Ly-β (49 detections).

– For all the triplets we looked for the forbidden component has always more detections with respect to the resonant and intercombination lines. The predominance in the triplets of the forbidden lines indicates that photoionization plays an important role in the ionization balance of CAIXA-A sources.

– Radiative Recombination Continua (RRC) features from Carbon and Oxygen are detected in several sources. At least one of the RRC features looked for is detected in 39% (42/109) of the objects of our sample: O VIII in 35/109, O VII in 42/109, C VI in 23/109 and C V in 28/109. Our result is very similar to that found in the CIELO sample by Guainazzi & Bianchi (2007), in fact they detected RRC features in 36% (25/69) of the objects of their sample. The measurements of the RRC width, which represents a direct estimate of the temperature of the plasma (Liedahl & Paerels (1996)), clusters in the range 1–10 eV. The association of high ionization emission lines with such a low-temperature plasma is strongly indicative of a plasma whose ionization state is governed by photoionization as opposed to collisional ionization.

– Most of our values of O VII f versus He-β intensity ratio are in agreement with the predictions of photoionization models, when the effect of resonant scattering is taken into account.

– All our values for the ratio between the intensity of the forbidden component of the O VII triplet and the O VIII Ly-α is $\lesssim 1$, except for NGC4395 (but the error for this source is larger than the errors estimated for all the other CAIXA-A sources) and two sources in the literature with very intense contribution of collisionally ionized plasma, NGC6240 and NGC1365. A ratio between the intensity of the O VII triplet f component and the O VIII Ly-$\alpha \lesssim 1$ is a signature of photoionized plasma.

– Our analysis found no systematic shifts of the detected line energy centroids.

After this fixed energy analysis whose results are in agreement with those described in Guainazzi & Bianchi (2007) for the smaller CIELO sample, each spectrum was divided into narrow bands. Each interval of the spectrum was modelled with a powerlaw and a Gaussian line with energy that was left free to vary between the minimum and the maximum energy of the interval itself (Method B). Our results can be summarized as follows:

- The most detected transition lines are O VIII α, O VII f, Fe XVII 3d-2p ($^1P_1$), for all confidence levels, in good agreement with the results found with the previous method.

- Diagnostics on the O VII triplet reveals the predominance of the forbidden component, as we found with Method A analysis. This is a signature of photoionization.

- Among the detected emission lines, we found a transition which can be readily identified with neutral S Kα at 2.308 keV (House 1969), likely arising from the same Compton-thick material responsible for the production of the features which dominate the high-energy part of the spectrum, that is the Compton reflection component and the neutral iron Kα line. Other fluorescence lines are not detected.

- At an energy between the Si XIV Kα and the Si XIII Kα triplet, there is an accumulation of several detections not clearly associated to known transitions: this is probably a blend of the two adjacent sets of lines that automatic fits cannot disentangle. Both Si lines are not fitted with Method A, where we consider only the most intense emission lines in the 0.3–1 keV band, while these lines are very intense only in the case of a gas with a higher ionization parameter (or temperature) than that which produces most of the lines considered.

- No unknown lines are significantly detected at any confidence level, except for a structure around 0.4 keV (31 Å). This structure should be due to a series of emission lines of S XIV. In the future we will investigate the potential diagnostic capabilities of these lines to disentangle the ionization equilibrium of the gas that produces them.

To test the robustness of our method (to estimate the noise) we made a simulated spectrum without emission lines for each CAIXA-A source and we analyzed them with the same procedure used for the real spectra. The numbers of detected lines in this case was much lower than the numbers of detected lines for CAIXA-A source spectra. Moreover the differences between the two numbers of detected lines greatly increases when we pass from the 68% to 99% confidence level, so many of our detections are real.

While the first part of our work is focused on a phenomenological study of the CAIXA-A spectra, in the second one we investigated the spectra with self-consistent plasma models in collisional and photoionization equilibrium. The different baseline models includes five different combinations of photo- or collisionally ionized plasma (Method C). For this kind of analysis we need spectra of good quality, therefore we selected only the 29 CAIXA-A sources that had at least 20% of counts with respect to the background for combined RGS (RGS1+RGS2) between 0.4 – 0.9 keV.

Since the Cash statistics cannot indicate the quality of the fit, we computed its goodness using Monte Carlo probability calculations. The results of "goodness of fit" were able to disentangle between different models for 12/29 high quality spectra sources. More generally, there is a preference for models with at least one photoionized component, except for NGC1365 and NGC4395, where the presence of a collisional component is required, in agreement with the ratio O VIII/O VII > 1 found with Method A analysis. In any case, the CAIXA-A sources seems to be dominated by the photoionization as suggested by our previous analysis.

As a further step, we simulated spectra for each source for all the different models we used in *Method C*, analyzing them with *Method B*. This analysis was designed to compare the distributions of detected lines observed with that expected for an homogeneous population of objects whose lines are produced by known models. We compared the results of the analysis on the fake spectra with the results of Method B with the Kolmogorov-Smirnov statistic.

– Regarding the models with a single component, this test indicates that the observed distributions obtained by Method B are most closely related to the distributions obtained by the analysis of fake spectra simulated with a single photoionized phase model as soon as we move to higher confidence levels. Generally speaking the distribution functions of collisionally-ionized plasma models are significantly different from that of real data, hence the largest difference between the real and the simulated distributions.

– Indeed we obtained the largest difference for the model with two collisionally-ionized plasma components at each confidence level, meanwhile it is always required at least a photoionized phase component likely due to the fact that in the real data there is a strong presence of O VII f lines.

– Anyway, compared to the models with a single component, the addition of another photoionized phase seems to improve the agreement between real and fake data only at the 68% confidence level. Moreover, the two models with the two photoionized phases or the photoionized phase plus the collisionally-ionized phase are practically indistinguishable.

Finally, we searched for differences between the results of the analysis on the fake spectra and the results of Method B on real data: we subtracted the cumulative emission line detections obtained with Method B from the cumulative emission line detections of all fake spectra. In all cases, the lines of Si, present in the data, are underestimated by all the models on fake data: evidently these lines are associated with a plasma with a U/kT higher than those that produce the rest of the lines. The agreement between real data and the model with two photoionized components is very good: there are not big residua except for the FeXVII 3d-2p ($^1P_1$) lines, and the Si lines present in all comparisons made. Once again our analysis favors photoionization as dominant process for CAIXA-A sources, even if the presence of some FeXVII 3d-2p ($^1P_1$) lines suggests contribution from a gas in collisional equilibrium. Nevertheless also in the case of a collisionally-ionized plasma plus a photoionized phase we found more FeXVII 3d-2p ($^1P_1$) lines in real data even if the difference decreases with respect to the comparison with the model without a collisional phase. Our results on real data show less CVIKα than that expected in the case of a collisionally-ionized plasma plus a photoionized phase. There are residua also for the OVII forbidden component: once again an indication of photoionization. In the case of the model with a single photoionized plasma we have a good agreement, even if the differences with respect to CAIXA-A sources indicate that in real data there are much less OVIII Ly-α, OVIIIRRC and CVIKα than that expected in the case of a single photoionized plasma. The agreement between real data and the model with a single collisional component is worse than in the previous case. The main differences between the real data and this model are in the OVIII Ly-α lines and in the OVII forbidden component. In fact, in the case of a collisionally-ionized plasma the forbidden component is generally suppressed, contrary to what we observe in the real data. These differences are equally found in the comparison with two collisional components. We also have more CVIKα than that we found in real data.

In conclusion, we addressed different, complementary, approaches to study the soft excess of obscured AGN: a phenomenological analysis and a self consistent modeling of CAIXA-A spectra. High resolution spectroscopy of soft X-ray emission in obscured AGN reveals that it is dominated by strong emission lines, with a low level of continuum. Several diagnostic tools both on few bright sources and on a large sample (CIELO) agree on its origin in a photoionized gas, with photoexcitation playing an important role. The analysis of CAIXA-A sources revealed that the ‘soft excess’ observed in all the CAIXA-A spectra was due to the blending of bright emission lines, mainly from He- and H-like transitions of light metals and L transitions of Fe, with low or no continuum. The predominance in the triplets of the forbidden lines and the good number of RRC indicates that photoionization plays an important role in the ionization balance of CAIXA-A sources. In fact, the RRC width indicates typical plasma temperatures of the order of a few eV. These features are unequivocal signatures of photoionized spectra (Liedahl & Paerels 1996). The observational evidence discussed in this thesis are in agreement with a picture where the observed lines should be produced in a gas photoionized by the AGN, with little contribution from any collisionally ionized plasma. This confirms and extends the work of Guainazzi & Bianchi (2007) who studied the soft excess of less than seventy sources (the CIELO sample). In our case, this picture is based on the study of a significantly larger number of objects selected relying on the X-ray rather than the optical classifications. Moreover, these objects were analyzed with different methods whose results are in agreement with each other.

Therefore, this study allows us to confirm that the results extracted from the detailed study of high-quality spectra of the brightest objects can be extended to the whole population of obscured AGN.

Moreover, our work demonstrates the significance of studies which investigate the spectra with self-consistent plasma models in collisional and photoionization equilibrium (Bianchi et al. 2010; Marinucci et al. 2011, applied similar self-consistent models to Mrk 573 and NGC424 respectively), whose approach is complementary to a phenomenological study of the CAIXA-A spectra, allowing the measure of the main properties of the material responsible for the soft X-ray emission (column density, ionization parameter) and its relation to the circumnuclear environment, putting them in the general context of our understanding of the AGN structure.

4.1 Future perspectives

Our work can be improved by including all the XMM-Newton observations whose data were public after November 22, 2011 until today to increase the RGS spectra quality, in particular to increase the number of sources that had at least 20% of counts with respect to the background for combined RGS (RGS1+RGS2) between $0.4-0.9$ keV and so to increase the number of sources which can be analyzed with a self-consistent modelling of the soft X-ray emission.

The currently operating X-ray space observatories perform X-ray spectral imaging with the use of CCDs. When available, cryogenic X-ray microcalorimeter arrays will far outperform CCDs in terms of spectral resolution, energy bandwidth and count rate.

A microcalorimeter provide very high resolution ($E/\Delta E$ =40 to 1000) spectra (comparable to that obtained with the gratings) but with a much higher efficiency than that of the gratings and over a very wide energy band of 0.3 to 10 keV.

With the expected launch of ASTRO-H in 2015 a new era for X-ray astronomy will begin. Among all other instruments, it will take onboard the Soft X-ray Spectrometer (SXS), thanks to its microcalorimeter an unprecedent energy resolution in the energy range between 0.5 and 12 keV will be reached.

ASTRO-H is an international X-ray observatory, which is the 6th in the series of the X-ray observatories from Japan. It is currently planned to be launched in 2015. Astro-H (formerly known as ”NeXT”) is a facility-class mission to be launched on a JAXA H-IIA into low Earth orbit. The core instrument is the Soft X-ray Spectrometer (SXS). The SXS consists of two components, the X-Ray Telescope (XRT), and the X-ray Calorimeter Spectrometer (XCS). The XRT is a lightweight mirror of the same heritage as the BBXRT, ASCA, and Suzaku missions. The XCS is a 6x6 array of similar design as the Suzaku XRS. In order to obtain high energy resolution, the XCS cooling system must cool the array to 50 ~mK.

The Soft X-ray Spectrometer combines a lightweight Soft X-ray Telescope (SXT) paired with a X-ray Calorimeter Spectrometer (XCS), providing non-dispersive 7 eV resolution in the 0.3-10 keV bandpass. The SXS represents a significant advance over all current high-resolution spectrometers, as shown in Fig. 4.1 and 4.2 which show a comparison with other present X-ray satellites)

The Advanced Telescope for High-energy Astrophysics (*Athena+*) is being proposed to ESA as the L2 mission, for a launch in 2028.

The Athena+ payload comprises three key elements:

- A single X-ray telescope with a focal length of 12 meters and an unprecedented effective area (2 m^2 at 1 keV). The X-ray telescope employs Silicon Pore Optics (SPO) has an excellent effective area-to-mass ratio and can achieve high angular resolution ($< 5''$) and a flat response across the field of view.

- The X-ray Integral Field Unit (X-IFU), an advanced actively shielded X-ray microcalorimeter spectrometer for high-resolution imaging, utilizing Transition Edge Sensors cooled to 50 mK.

- The Wide Field Imager (WFI), a Silicon Active Pixel Sensor camera with a large field of view, high count-rate capability and moderate resolution spectroscopic capability.

With such a mission configuration Athena+ will truly provide transformational capabilities, as illustrated in Fig. 4.3. It will provide an improvement factor > 100 in high spectral resolution throughput (e.g. compared to *ASTRO-H* microcalorimeter and XMM-Newton gratings).

The unprecedented spectral resolution, together with the large effective area, of future X-ray missions such as Astro-H and, especially, ATHENA (they will fly with a X-ray microcalorimeter on board) will further our ability to analyze the soft X-ray excess of obscured AGN, examine many more AGN with greater s/n, so that our understanding of the nature of this component will be largely improved.

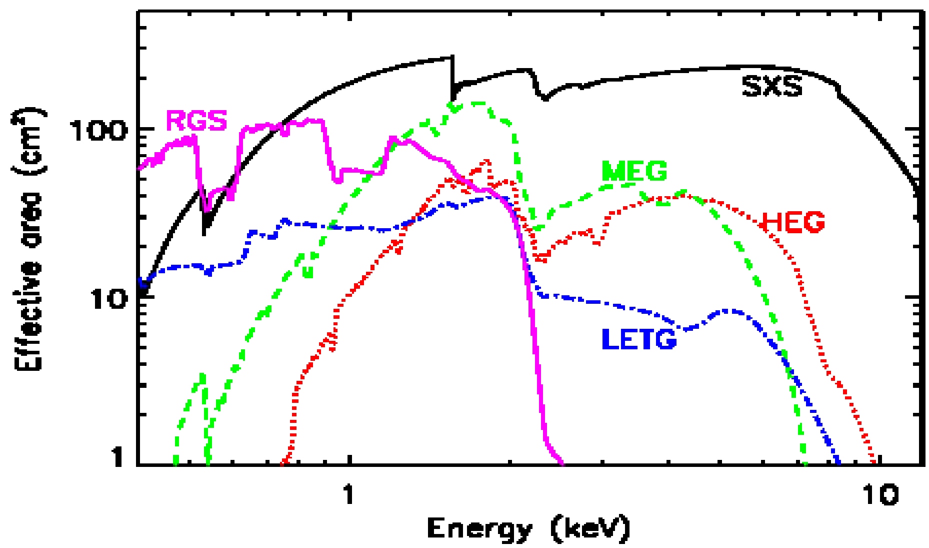

Figure 4.1: SXS Effective Area (black) compared to other high-resolution X-ray spectrometers. Pink: RGS, the spectrometer used in our work. (http://heasarc.gsfc.nasa.gov/docs/astroh/)

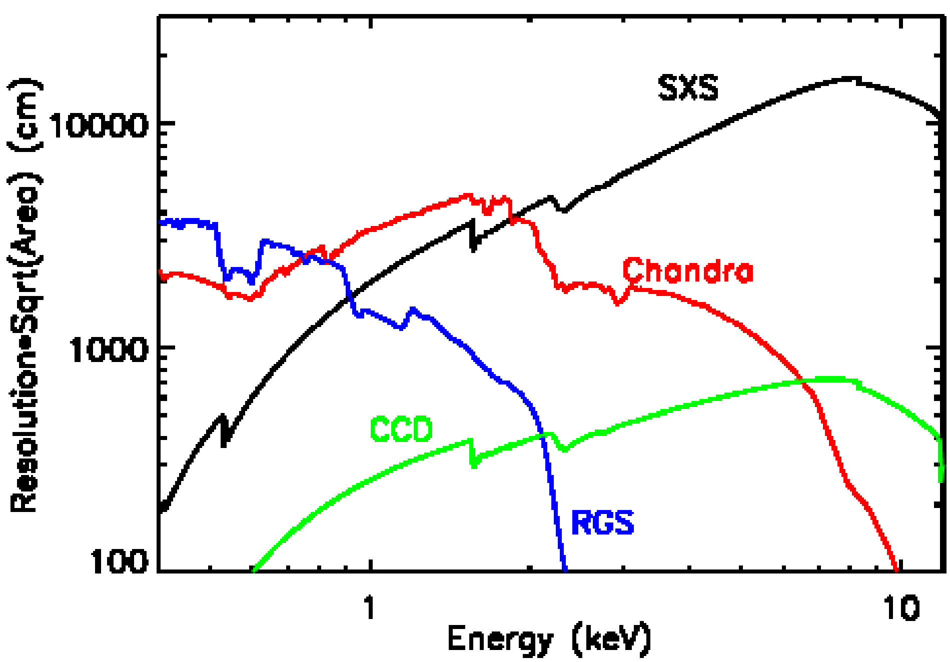

Figure 4.2: Black: SXS Line resolution power (defined as resolution*sqrt(area)), compared to other high-resolution missions, plus a typical imaging CCD. Blue: RGS, the spectrometer used in our work. (http://heasarc.gsfc.nasa.gov/docs/astroh/)

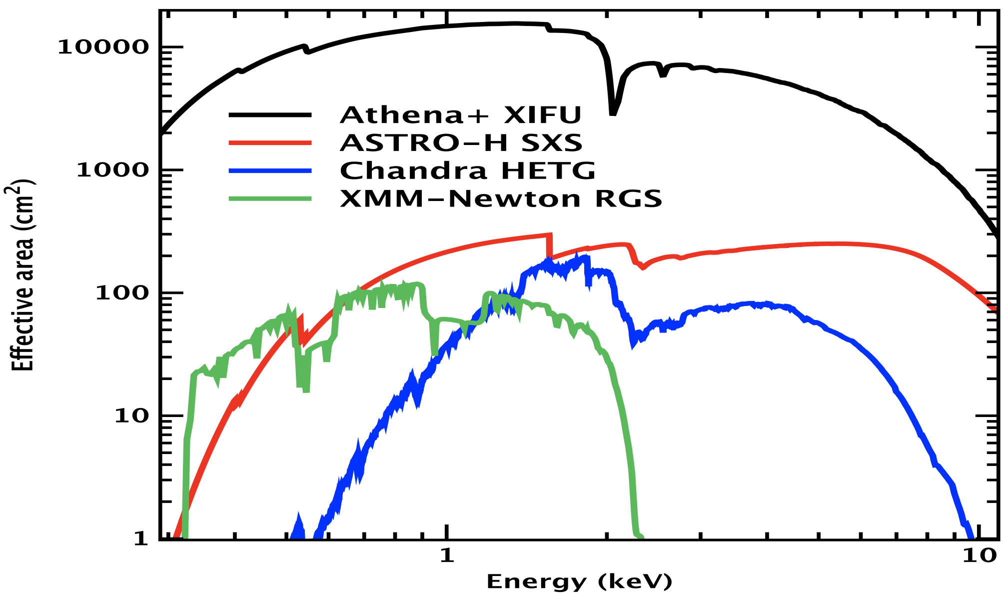

Figure 4.3: Effective area curves for high resolution X-ray spectrometers, operational and planned. Green: RGS, the spectrometer used in our work. (Barret et al. 2013)

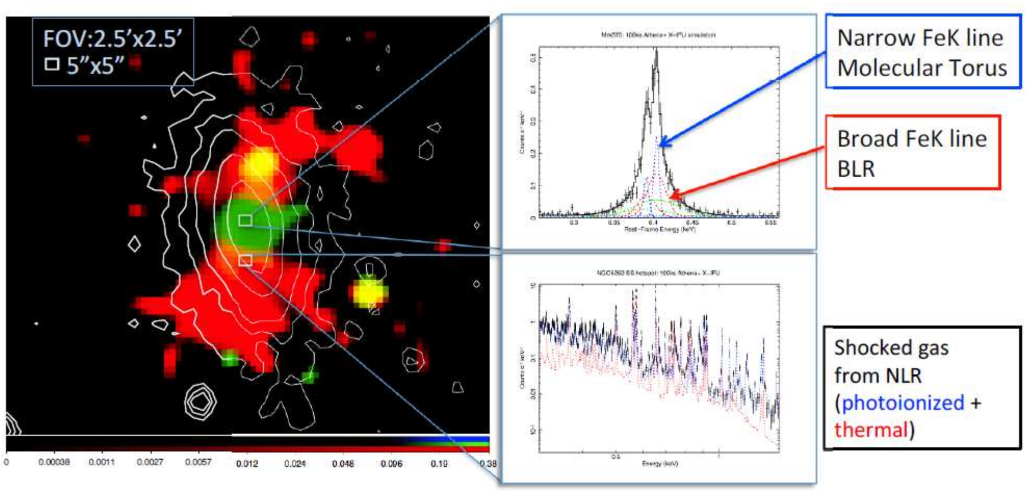

Figure 4.4: (*Left*) Athena+ simulated color-coded image of the nearby Seyfert 2 galaxy NGC 5252 (from the Chandra image in Dadina et al. 2010). The soft X-rays are known (Dadina et al. 2010) to trace the [OIII] ionization cones forming a biconical outflow/illumination pattern driven by the AGN which impacts all over the S0 host galaxy (DSS optical contours indicated in white). (*Right-top*) Athena+ X-IFU simulated spectrum of the FeK emission line of NGC 5252 assuming the sum of a broad plus a narrow line component, from the BLR and molecular torus respectively (see also Matt, Dovciak, et al., 2013, Athena+ supporting paper). (*Right-bottom*) Athena+ X-IFU simulated spectrum of a part of the plume of ionized emission south of the nucleus and attributed to 25% of shock (thermal) emission plus 75% of photoionized emission. (Cappi et al. 2013)

Appendix A

XMM-Newton

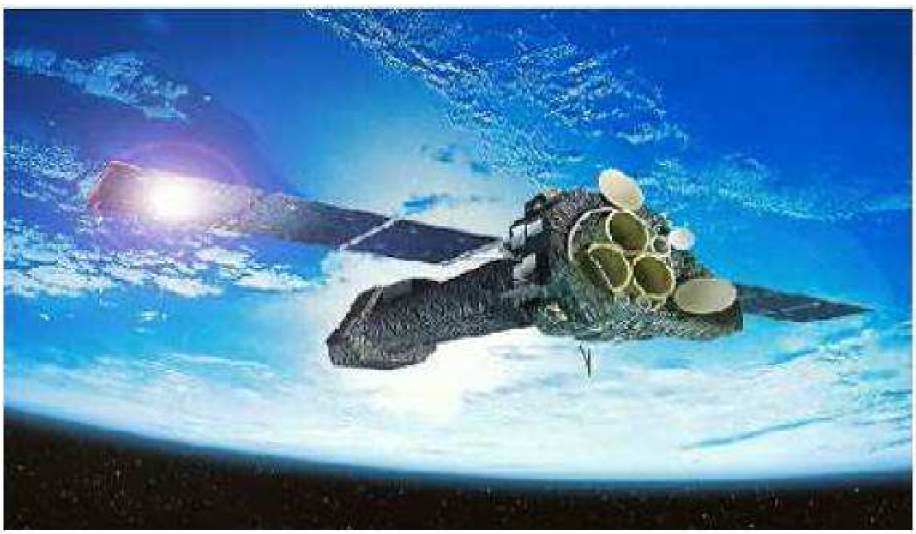

The *X-ray Multi-Mirror Mission* (*XMM*) is the second Cornerstone of the European Space Agency Horizon 2000 Science Programme. Renamed *XMM-Newton*, it was launched with an Ariane 5 spacecraft from Kourou, French Guyana, on 10 December 1999, and put into an highly elliptical orbit, with an apogee of about 114000 km and a perigee of about 7000 km. This choice for the orbit allows for long, continuous exposures unaffected by Earth blockage and avoids degradation to the Charge Coupled Device (CCD) cameras, since the spacecraft does not pass through the Earth's proton belt. The satellite weighs 3800 kg, is 10 m long and 16 m in span with its solar arrays deployed. It holds three X-ray telescopes, developed by Media Lario of Italy, each of which contains 58 Wolter-type concentric mirrors. The payload carried by the *XMM* consists of three scientific instruments: the Reflection Grating Spectrometer (RGS), the European Photon Imaging Camera (EPIC), and the Optical Monitor (OM) (see Table A.1)

Instrument	Main Purpose	Energy Range/ Bandwidth	Spectral Resolution (E /ΔE)	Spatial Resolution (arcsec)	Sensitivity	Total Mass/Power
EPIC	High-throughput non-dispersive imaging/ spectroscopy	0.1 - 15 keV 1 - 120 Å	5 - 60	14 (Half Energy Width)	10^{-14} erg/cm² sec	235 kg 240 W
OM	Optical/UV imaging	160 - 600 nm	50 -100 (with grisms)	1	< 24 magnitude	82 kg 60 W
RGS	High-resolution dispersive spectroscopy	0.35 - 2.5 keV 5 - 35 Å	200 - 800 (400/800 at 15 Å in 1st/2nd order)	N.A.	3 x 10^{-13} erg / cm² s	248 kg 140 W

Table A.1: *Main characteristics of the XMM instruments. (from Bagnasco et al., 1999)*

An exploded view of the *XMM* payload, with the main elements labelled, is shown in Figure A.1.

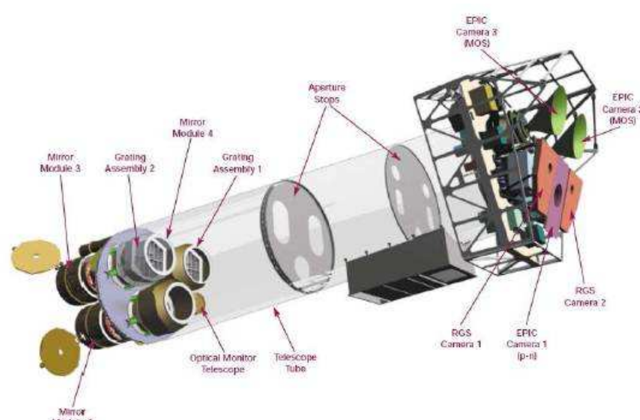

Figure A.1: *The main elements of the XMM payload. (from Bagnasco et al., 1999)*

Three Mirror Modules, co-aligned with the OM telescope, and equipped with two RGS grating assemblies, lie at the heart of the *XMM* telescope. Each Mirror Module, with a focal length of 7.5m, provides an unprecedented collecting area, thanks to its 58 nested Wolter-I-type shells, designed to operate in the soft X-ray energy band between 0.1 and 10 keV (1-100 $\AA$). The *XMM* telescope is completed by three EPIC cameras, placed in the foci of the three Mirror Modules, and by two RGS cameras, suitably positioned to collect the spectrum created by the two grating assemblies. A Telescope Tube (TT), which is equipped with two aperture stops for stray-light suppression and with an outgassing baffle for cleanliness and decompression purposes, separates the Cameras from the Mirror Modules.

A.1 The Reflection Grating Spectrometer (RGS)

The conceptual idea behind the RGS instrument is depicted schematically in Figure A.2. The incoming X-ray radiation, collected and focused by the Mirror Mod-

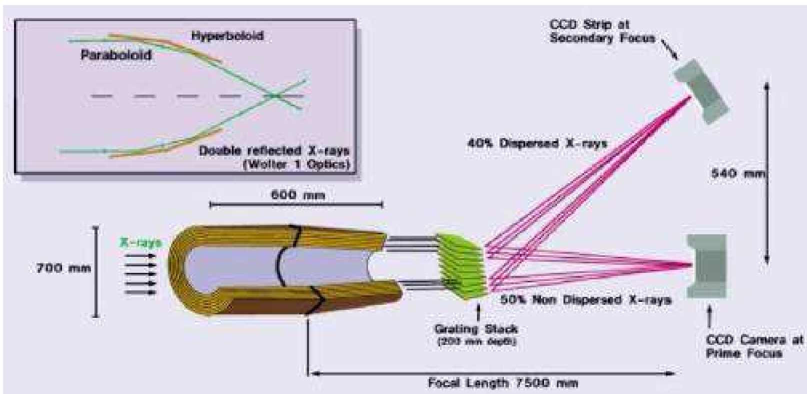

Figure A.2: *Schematic of the concept underlying the RGS instrument. (from Bagnasco et al., 1999)*

ule, is partly intercepted by a set of reflection gratings which, like a prism, disperse the various wavelengths at different angles so that a spectrum can be collected and analysed by a strip of CCD detectors. The X-ray radiation that passes undispersed through the set of gratings is focused onto the EPIC cameras for imaging purposes.

The grating array is made up of a stiff lightweight monolithic beryllium structure, which houses 182 reflection gratings. In order to achieve its X-ray dispersing capabilities, each reflection grating features more than 600 grooves/mm ruled on a 200 micron-thick gold layer, deposited on top of a 20 cm $\times$ 10 cm silicon-carbide substrate. Linear and angular positioning accuracies between gratings of the order of a few microns and a few arcseconds have been achieved by means of sophisticated manufacturing techniques, like precision diamond grinding and interferometric alignment.

The diffracted X-rays are detected with a strip of CCD detectors. The choice of ‘back-illuminated’ CCD technology enables a high quantum efficiency to be achieved throughout the $5 - 35\ \AA$ instrument bandwidth. Each CCD has 768×1024 pixels, 27×27 microns in size. A strip of nine of these devices have been chosen so that the 253 mm-long spectrum created by the grating array can fit onto the detector focal plane.

Several parameters determine the RGS effective area per dispersion order: the properties of all optical components in the light path, the CCD quantum efficiency and the source and order filtering criteria. All these components are functions of wavelength and source position angle. Figure A.3 displays the calculated effective area of both RGS units together (upper panel), and individual RGS1 and RGS2 overlayed one on top of the other (lower panel). The calculations have been performed taking into account all the factors listed above. The broad gaps in Figure A.3 are due to the inoperative CCDs while absorption edges are due to the existence of passive layers in the X-ray path consisting of various atomic species.

A.2 European Photon Imaging Camera (EPIC)

The EPIC instrument is made up of three independent instrument chains, each one consisting of a camera unit with a CCD detector assembly, an analogue electronic unit for camera control and signal conditioning, a digital signal-processing unit, and a data-handling unit, responsible for overall instrument control, data formatting, and interfacing to the spacecraft. The three CCD cameras, positioned in the primary foci of the Mirror Modules, can be configured in a wide range of observation modes, which affect their sensitivity, and their spatial, spectral and time resolution. In this way, a large variety of time-correlated imaging and spectral measurements of one or more celestial objects can be gathered in a single observation.

Two cameras consist of an arrangement of seven metal-oxide (MOS) CCD arrays covering the 30 arcmin field of view of each Mirror Module. Each MOS CCD features an imaging area of 600×600 pixels, 40 microns in size, capable of detecting X-rays in an energy band ranging from 0.1 to 15 keV, with a maximum timing resolution of 1 ms.

The third CCD camera differs from the first two MOS cameras mainly in terms of the semiconductor technology used, and the CCD size, number and layout. Twelve back-illuminated CCDs are all generated on a single 10 cm-diameter wafer and constitutes the EPIC pn CCD. Each of them is organised as a 64×200 matrix of 150 micron-sized pixels. The use of pn technology has resulted in a higher quantum efficiency than comparable instruments. Typical full-frame readout times of 48 ms can be achieved, with a maximum timing resolution of 40 μs.

An important factor influencing the EPIC effective area, specifically in the low energy part of the passband, is the choice of the optical blocking filter. These filters are used, because the EPIC CCDs are not only sensitive to X-ray photons, but also to IR, visible and UV light. Therefore, if an astronomical target has a high optical flux, there is a possibility that the X-ray signal becomes contaminated by those photons. Each EPIC camera is equipped with a set of three separate filters, named ‘thick’, ‘medium’ and ‘thin’. It is necessary for the observer to select the filter which maximises the scientific return, by choosing the optimum optical blocking required for the target of interest. Figure A.4 displays the effective area

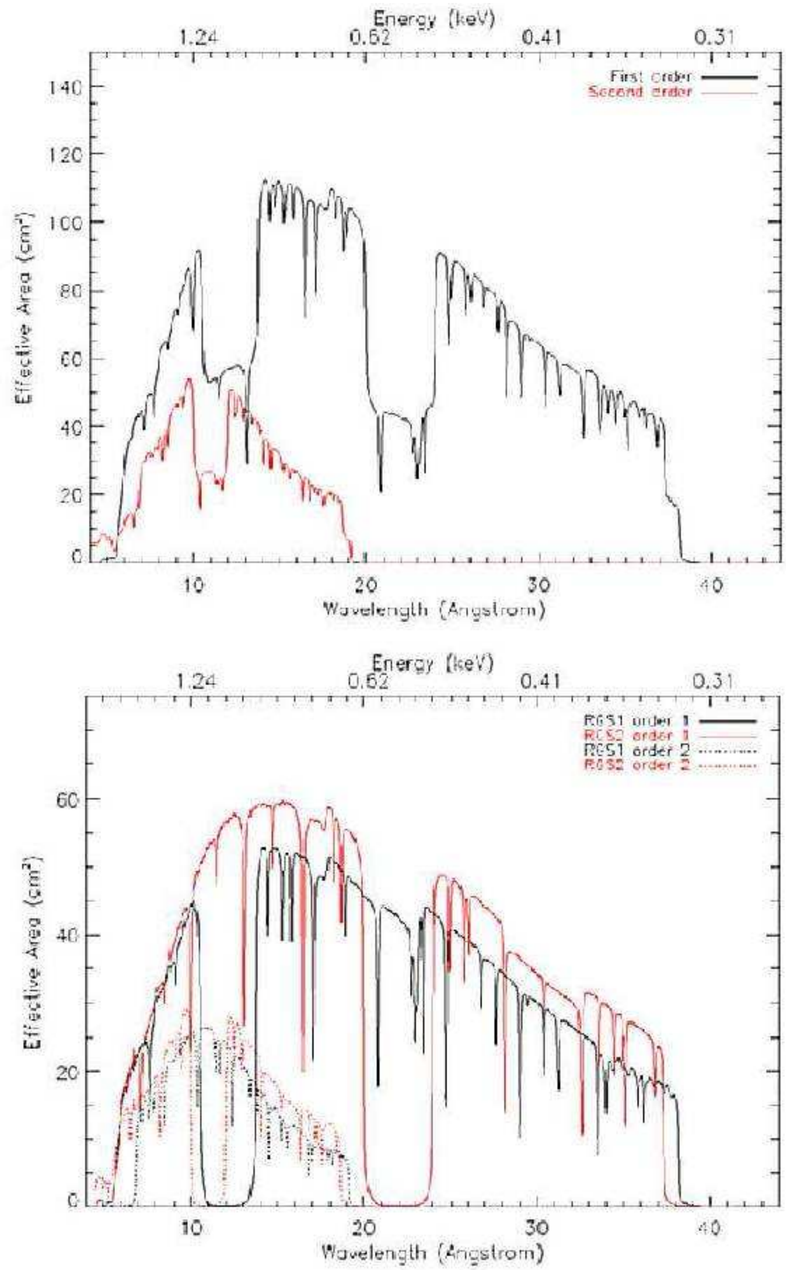

Figure A.3: *Effective area of both RGS units together (upper panel), and individual RGS1 and RGS2 overlayed one on top of the other (lower panel) as a function of energy and wavelength (top and bottom horizontal scales, respectively).*

of EPIC MOS camera (upper panel) and EPIC pn camera (lower panel) and the impact of the different filters on the soft X-ray response.

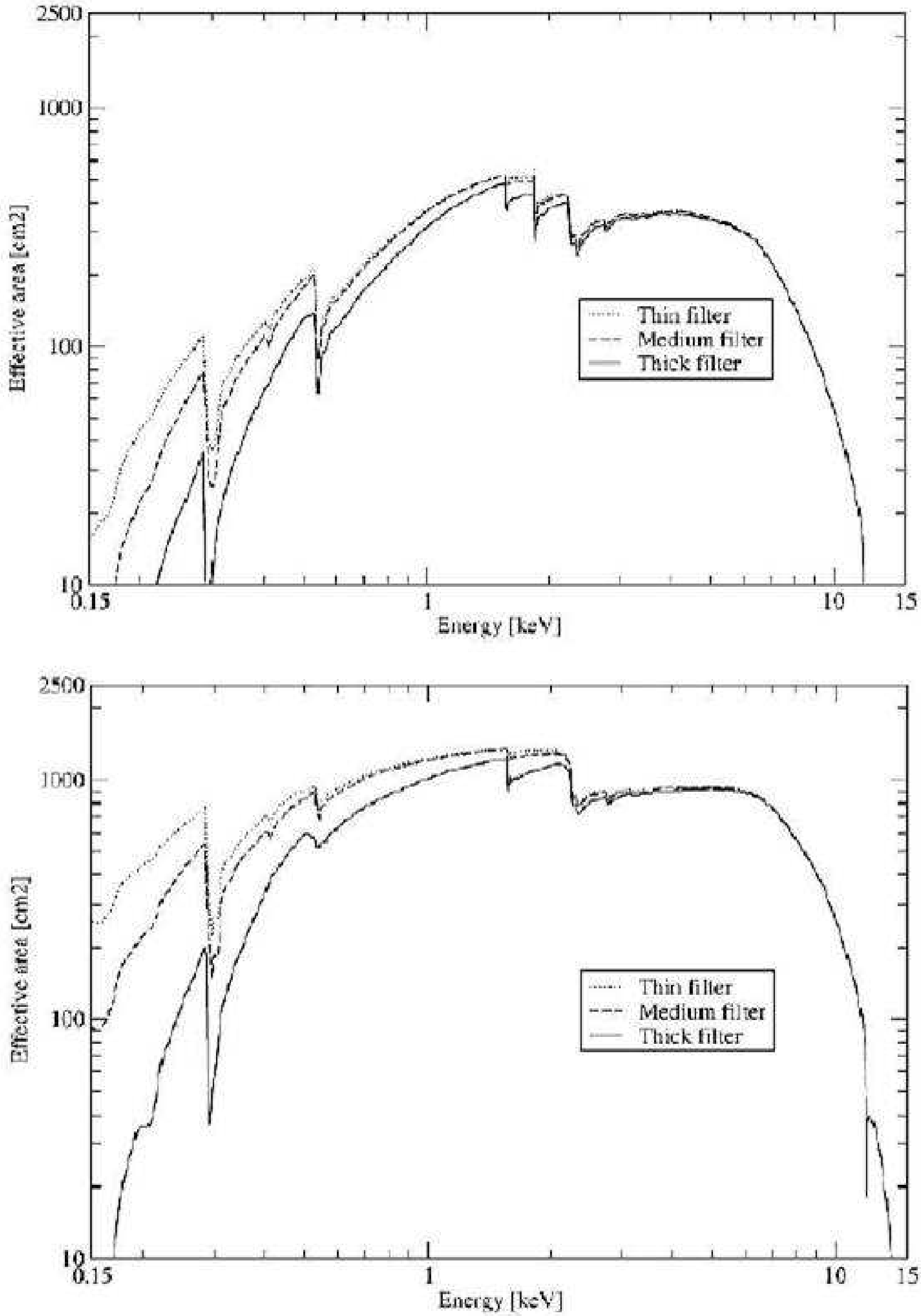

Figure A.4: *The EPIC MOS (upper panel) and EPIC pn (lower panel) effective area for each of the optical blocking filters.*

Appendix B

Xspec

Although we use a spectrometer to measure the spectrum of a source, what the spectrometer obtains is not the actual spectrum, but rather photon counts, C, within specific instrument channels, I. This observed spectrum is related to the actual spectrum of the source $f(E)$ by

$$C(I) = \int_0^\infty f(E)R(I,E)dE$$

where $R(I,E)$ is the instrumental response and is proportional to the probability that an incoming photon of energy E will be detected in channel I. Ideally, then, we would like to determine the actual spectrum of a source, $f(E)$, by inverting this equation, thus deriving $f(E)$ for a given set of $C(I)$. Regrettably, this is not possible in general, as such inversions tend to be non-unique and unstable to small changes in $C(I)$. The usual alternative is to choose a model spectrum, $M(E)$, that can be described in terms of a few parameters (i.e., $M(E, p1, p2, ...)$), and match, or 'fit' it to the data obtained by the spectrometer. For each $M(E)$, a predicted count spectrum, $C_p(I)$, is calculated and compared to the observed data $C(I)$. Then a 'fit statistic' is computed from the comparison and used to judge whether the model spectrum fits the data obtained by the spectrometer. The model parameters then are varied to find the parameter values that give the most desirable fit statistic. These values are referred to as the best-fit parameters. The model spectrum, $M_b(E)$, made up of the best-fit parameters is considered to be the best-fit model. The most common fit statistic in use for determining the 'best-fit' model is χ^2, defined as follows

$$\chi^2 = \sum_n \frac{\left[C(I) - C_p(I)\right]^2}{[\sigma(I)]^2}$$

where n is the number of channels and $\sigma(I)$ is the (generally unknown) error for channel I - e.g., if $C(I)$ are counts then $\sigma(I)$ is usually estimated by $\sqrt{C(I)}$. The

χ^2 statistic provides a well-known-goodness-of-fit criterion for a given number of degrees of freedom, d, which is calculated as the number of channels minus the number of model parameters, $d = n - p$, and for a given confidence level. If χ^2 exceeds a critical value, tabulated in many statistics texts, one can conclude that $M_b(E)$ is not an adequate model for $C(I)$. As a general rule, one wants the 'reduced χ^2', $\tilde{\chi}^2 = \chi^2/d$, to be approximately equal to 1 ($\chi^2 \simeq d$). A $\tilde{\chi}^2$ that is much greater than 1 indicates a poor fit, while a $\tilde{\chi}^2$ that is much less than one indicates that the errors on the data have been over-estimated. Even if the best-fit model, $M_b(E)$, does pass the 'goodness-of-fit' test, one still cannot say that it is the only acceptable model. For example, if the data used in the fit are not particularly good, one may be able to find many different models for which adequate fits can be found. In such a case, the choice of the correct model to fit is a matter of scientific judgment. For a given best-fit parameter, the range of values within which one can be confident the true value of the parameter lies is called the 'confidence interval'. The confidence interval for a given parameter is computed by varying the parameter value until the χ^2 increases by a particular amount above the minimum, or 'best-fit' value. The amount that the χ^2 is allowed to increase (also referred to as the critical) depends on the confidence level one requires, and on the number of parameters whose confidence space is being calculated. `Xspec` uses a a modified Levenberg-Marquardt fitting algorithm (based on `curfit` from Bevington, 1969) to find the best-fit values of the model parameter. The algorithm used is local rather than global, so be aware that is possible for the fitting process to get stuck in a local minimum and not find the global best-fit. The process also goes much faster (and is more likely to find the true minimum) if the initial model parameters are set to sensible values.

Acknowledgements

I would like to thank all the people who helped me during these three years to make this thesis possible. In particular Stefano Bianchi, for his advices and patience. I am grateful to Matteo Guainazzi, who helped me to begin the analysis in this thesis and Andrea Marinucci, for his precious comments and suggestions.

Bibliography

Anders E., Grevesse N., 1989, Geochim. Cosmochim. Acta, 53, 197

Antonucci R., 1993, ARA&A, 31, 473

Antonucci R. R. J., Miller J. S., 1985, ApJ, 297, 621

Bambynek W., Crasemann B., Fink R. W., Freund H. U., Mark H., 1972, Rev. Mod. Phys., 44, 716

Barret D. et al., 2013, in SF2A-2013: Proceedings of the Annual meeting of the French Society of Astronomy and Astrophysics, Cambresy L., Martins F., Nuss E., Palacios A., eds., pp. 447–453

Bearden J. A., 1967, Rev. Mod. Phys., 39, 78

Bianchi S., 2009, XMM-Newton Proposal, 42

Bianchi S., Balestra I., Matt G., Guainazzi M., Perola G. C., 2003, A&A, 402, 141

Bianchi S., Chiaberge M., Evans D. A., Guainazzi M., Baldi R. D., Matt G., Piconcelli E., 2010, MNRAS, 405, 553

Bianchi S., Guainazzi M., 2007, 924, 822

Bianchi S., Guainazzi M., Chiaberge M., 2006, A&A, 448, 499

Bianchi S., Guainazzi M., Matt G., Fonseca Bonilla N., Ponti G., 2009, A&A, 495, 421

Bianchi S., Maiolino R., Risaliti G., 2012, Advances in Astronomy, 2012

Bianchi S., Miniutti G., Fabian A. C., Iwasawa K., 2005, MNRAS, 360, 380

Bianchi S. et al., 2012, MNRAS, 426, 3225

Blumenthal G. R., Gould R. J., 1970, Reviews of Modern Physics, 42, 237

Blustin A. J., Page M. J., Fuerst S. V., Branduardi-Raymont G., Ashton C. E., 2005, A&A, 431, 111

Boller T., Keil R., Hasinger G., Costantini E., Fujimoto R., Anabuki N., Lehmann I., Gallo L., 2003, A&A, 411, 63

Brinkman A.C. et al., 2002, A&A 396, 761-772

Cappi M., 2006, Astronomische Nachrichten, 327, 1012

Cappi M. et al., 2013, ArXiv e-prints

—, 2009, A&A, 504, 401

Cash W., 1979, ApJ, 228, 939

Chartas G., Brandt W. N., Gallagher S. C., 2003, ApJ, 595, 85

Clavel J., Wamsteker W., Glass I. S., 1989, ApJ, 337, 236

Crummy J., Fabian A. C., Gallo L., Ross R. R., 2006, MNRAS, 365, 1067

den Herder J. W. et al., 2001, A&A, 365, L7

Dere K. P., Landi E., Young P. R., Del Zanna G., 2001, ApJS, 134, 331

Dickey J. M., Lockman F. J., 1990, ARA&A, 28, 215

Done C., Davis S. W., Jin C., Blaes O., Ward M., 2012, MNRAS, 420, 1848

Elvis M., 2000, ApJ, 545, 63

—, 2012, Journal of Physics Conference Series, 372, 012032

Elvis M. et al., 1994, ApJS, 95, 1

Fabian A. C., Iwasawa K., Reynolds C. S., Young A. J., 2000, PASP, 112, 1145

Fabian A. C., Miniutti G., 2005, ArXiv Astrophysics e-prints

Fabian A. C., Ross R. R., 2010, Space Sci. Rev., 157, 167

Falco E. E. et al., 1999, PASP, 111, 438

Ferland G. J., 2000, Revista Mexicana de Astronomia y Astrofisica Conference Series, 9, 153

Fiore F. et al., 2001, MNRAS, 327, 771

—, 2002, 258, 205

Garcet O. et al., 2007, A&A, 474, 473

George I. M., Fabian A. C., 1991, MNRAS, 249, 352

Ghisellini G., Haardt F., Matt G., 1994, MNRAS, 267, 743

Guainazzi M., 2002, MNRAS, 329, L13

Guainazzi M., Bianchi S., 2007, MNRAS, 374, 1290

Guainazzi M., Matt G., Fiore F., Perola G. C., 2002, A&A, 388, 787

Guainazzi M., Matt G., Perola G. C., 2005, A&A, 444, 119

Guainazzi M., Risaliti G., Nucita A., Wang J., Bianchi S., Soria R., Zezas A., 2009, A&A, 505, 589

Guilbert P. W., Rees M. J., 1988, MNRAS, 233, 475

Haardt F., Maraschi L., 1991, ApJ, 380, L51

Haardt F., Maraschi L., Ghisellini G., 1994, ApJ, 432, L95

Haas M., Siebenmorgen R., Schulz B., Krügel E., Chini R., 2005, A&A, 442, L39

House L. L., 1969, ApJS, 18, 21

Kinkhabwala A. et al., 2002, ApJ, 575, 732

Komossa S., 2000, ArXiv Astrophysics e-prints

Konigl A., Kartje J. F., 1994, ApJ, 434, 446

Korista et al., 1997, ApJ 487, 555

Krolik J. H., Begelman M. C., 1988, ApJ, 329, 702

Krongold Y., Nicastro F., Brickhouse N. S., Elvis M., Liedahl D. A., Mathur S., 2003, ApJ, 597, 832

Lal D. V., Ho L. C., 2010, AJ, 139, 1089

Lawrence A., 1991, MNRAS, 252, 586

Leahy D. A., Creighton J., 1993, MNRAS, 263, 314

Liang E. P. T., 1979, ApJ, 231, L111

Liang E. P. T., Price R. H., 1977, ApJ, 218, 247

Liedahl D. A., Paerels F., 1996, ApJ, 468, L33

Lightman A. P., White T. R., 1988, ApJ, 335, 57

Maiolino R., Marconi A., Salvati M., Risaliti G., Severgnini P., Oliva E., La Franca F., Vanzi L., 2001, A&A, 365, 28

Maiolino R., Rieke G. H., 1995a, ApJ, 454, 95

—, 1995b, ApJ, 454, 95

Maiolino R., Salvati M., Bassani L., Dadina M., della Ceca R., Matt G., Risaliti G., Zamorani G., 1998, A&A, 338, 781

Malkan M. A., Gorjian V., Tam R., 1998, ApJS, 117, 25

Marinucci A., Bianchi S., Matt G., Fabian A. C., Iwasawa K., Miniutti G., Piconcelli E., 2011, A&A, 526, A36

Matt G., 2000, A&A, 355, L31

—, 2002, MNRAS, 337, 147

Matt G., Fabian A. C., Ross R. R., 1993, MNRAS, 262, 179

—, 1996, MNRAS, 278, 1111

Matt G., Guainazzi M., Maiolino R., 2003, MNRAS, 342, 422

Matt G., Perola G. C., Piro L., 1991, A&A, 247, 25

et al. F., 1998, PASP 110, 761-778

Miller J. S., Antonucci R. R. J., 1983, ApJ, 271, L7

Miller L., Turner T. J., Reeves J. N., 2008, A&A, 483, 437

Narayan R., Yi I., Mahadevan R., 1995, Nature, 374, 623

Nenkova M., Sirocky M. M., Nikutta R., Ivezić Ž., Elitzur M., 2008, ApJ, 685, 160

Ogle P. M., Brookings T., Canizares C. R., Lee J. C., Marshall H. L., 2003, A&A, 402, 849

Osterbrock et al., 2006, Osterbrock and Ferland

Otani C. et al., 1996, PASJ, 48, 211

Panessa F., Bassani L., 2002, A&A, 394, 435

Panessa F. et al., 2008, Mem. Soc. Astron. Italiana, 79, 268

Perola G. C., Matt G., Cappi M., Fiore F., Guainazzi M., Maraschi L., Petrucci P. O., Piro L., 2002, A&A, 389, 802

Petrucci P. O. et al., 2012

Piconcelli E., Jimenez-Bailón E., Guainazzi M., Schartel N., Rodríguez-Pascual P. M., Santos-Lleó M., 2004, MNRAS, 351, 161

Porquet D., Dubau J., 2000, A&AS, 143, 495

Pounds K.A., Page K.L., 2005, MNRAS 360, 1123-1131

Prieto M. A., Pérez García A. M., Rodríguez Espinosa J. M., 2001, A&A, 377, 60

Pringle J. E., 1981, ARA&A, 19, 137

Read A. M., Ponman T. J., 2003, A&A, 409, 395

Reynolds C. S., 1997, MNRAS, 286, 513

Reynolds C. S., Fabian A. C., Nandra K., Inoue H., Kunieda H., Iwasawa K., 1995, MNRAS, 277, 901

Reynolds C. S., Nowak M. A., 2003, Phys. Rep., 377, 389

Reynolds C. S., Ward M. J., Fabian A. C., Celotti A., 1997, MNRAS, 291, 403

Risaliti G., Elvis M., 2010, A&A, 516, A89

Risaliti G., Elvis M., Fabbiano G., Baldi A., Zezas A., 2005, ApJ, 623, L93

Ross R. R., Fabian A. C., 1993, MNRAS, 261, 74

S. R. C., 1999, in ASP Conf. Ser, 161

Sako M., Kahn S. M., Paerels F., Liedahl D. A., 2000, ApJ, 543, L115

Sambruna R. M., Brandt W. N., Chartas G., Netzer H., Kaspi S., Garmire G. P., Nousek J. A., Weaver K. A., 2001a, ApJ, 546, L9

Sambruna R. M., Netzer H., Kaspi S., Brandt W. N., Chartas G., Garmire G. P., Nousek J. A., Weaver K. A., 2001b, ApJ, 546, L13

Sanders D. B., Phinney E. S., Neugebauer G., Soifer B. T., Matthews K., 1989, ApJ, 347, 29

Schmidt M., 1963, Nature, 197, 1040

Schödel R., Bower G. C., Muno M. P., Nayakshin S., Ott T., 2006, Journal of Physics Conference Series, 54

Schödel R. et al., 2002, Nature, 419, 694

Shakura N. I., Sunyaev R. A., 1973, A&A, 24, 337

Shapiro S. L., Teukolsky S. A., Lightman A. P., 1983, Physics Today, 36, 89

Simpson C., 2005, MNRAS, 360, 565

Strüder L. et al., 2001, A&A, 365, L18

Sunyaev R. A., Churazov E. M., 1996, Astronomy Letters, 22, 648

Tombesi F., Cappi M., Reeves J. N., Palumbo G. G. C., Braito V., Dadina M., 2011, ApJ, 742, 44

Tombesi F., Cappi M., Reeves J. N., Palumbo G. G. C., Yaqoob T., Braito V., Dadina M., 2010, A&A, 521, A57

Tozzi P. et al., 2006, A&A, 451, 457

Tran H. D., 2001, ApJ, 554, L19

—, 2003, ApJ, 583, 632

Turner T. J., George I. M., Nandra K., Mushotzky R. F., 1997, ApJS, 113, 23

Véron-Cetty , Véron , 2010, A&A 518, A10

Walter R., Fink H. H., 1993, A&A, 274, 105

Young A. J., Wilson A. S., Shopbell P. L., 2001, ApJ, 556, 6

Zdziarski A. A., Fabian A. C., Nandra K., Celotti A., Rees M. J., Done C., Coppi P. S., Madejski G. M., 1994, MNRAS, 269, L55

Zheng W. et al., 1995, ApJ, 444, 632